2011

Thermophysical Characterization of Nanofluids Through Molecular Dynamic Simulations

John Shelton
University of South Florida, js980172@yahoo.com

Thermophysical Characterization of Nanofluids

Through Molecular Dynamic Simulations

by

John T. Shelton

A dissertation submitted in partial fulfillment
of the requirements for the degree of
Doctor of Philosophy
Department of Mechanical Engineering
College of Engineering
University of South Florida

Major Professor: Frank Pyrtle, III, Ph.D.
Venkat R. Bhethanabotla, Ph.D.
Ivan Oleynik, Ph.D.
Jose Porteiro, Ph.D.
Muhammad M. Rahman, Ph.D.

Date of Approval:
October 26, 2011

Keywords: Thermal Conductivity, Shear Viscosity, Density, Nonequilibrium Thermodynamics, LAMMPS

Dedication

To Mom and Dad.

Acknowledgments

Firstly, I would like to thank my major professor, Dr. Frank Pyrtle, III, for giving me an opportunity to pursue this work under his guidance and support throughout my doctoral studies. I would also like to thank Dr. Venkat R. Bhethanabotla, Dr. Ivan Oleynik, Dr. Jose Porteiro, and Dr. Muhammad M. Rahman, for being members of my dissertation committee, as well as for their valuable suggestions, their unending patience and much-needed guidance as I stumbled through this PhD research project. I am grateful for the financial assistance of the National Science Foundation Florida Georgia LSAMP project (HRD 021675), the National GEM Consortium, and the Sloan Foundation.

I would also like to thank my many USF mentors, Dr. Richard Pollenz, Dr. Vonzell Agosto, Dr. Ajit Mujumdar, Dr. Lusk, Dr. Nathan Crane, and Dr. Sylvia Thomas for their guidance to help me grow professionally as an academic. I have reserved a special thanks to Mr. Bernard Batson for his support from my arrival at USF until the final months where his assistance was able to pushed me over the top and prepare me for the final portion of my dissertation and lay the foundation for future research opportunities.

The student members of Bridge to the Doctorate program at the University of South Florida have been a tremendous support group for which I am truly grateful. To the staff at the office of Mechanical Engineering, members of the rest of the University of South Florida family, the community of Tampa Bay, and my support groups from my

undergraduate institution at North Carolina Agricultural and Technical State University, I say a big thank you for your support.

Lastly, I would like to say a special thank you to my mom and dad, Jonathan and Isidora Shelton. Their unending support so that my hard work would reach fruition is invaluable and immeasurable. I can only humbly say a gracious “Thank you!” from the bottom of my heart and I only hope to give a fraction of that support in return.

Table of Contents

List of Tables

List of Figures

Abstract

Using equilibrium molecular dynamics simulations, an analysis of the key thermophysical properties critical to heat transfer processes is performed. Replication of thermal conductivity and shear viscosity observations found in experimental investigations were performed using a theoretical nanoparticle-fluid system and a novel colloid-fluid interaction potential to investigate the key nanofluid parameters. Analysis of both the heat current (thermal conductivity) and stress (shear viscosity) autocorrelation functions have suggested that the dominant physical mechanisms for thermal and momentum transport arises from enhancements to the longitudinal and transverse acoustic modes energy transfer brought about by the increased mass ratio of the nanoparticle to the fluid. This conclusion was further supported by analysis of the local density fluctuations surrounding increasing nanoparticle diameters where the longitudinal acoustic mode characteristics for density fluxes were seen to be enhanced by the presence of the heavier platinum nanoparticles. It is then concluded that the key macroscopic characteristic in obtaining the largest thermal energy transfer enhancement is through the mass of the nanoparticle relative to the base fluid. Also, the small local density effects in the nanofluid are greatly affects the viscosity calculations. These conclusions provide the theoretical framework for many of the experimental results obtained.

Chapter 1 – Introduction and Scope

Current engineering fluids used in thermal management systems are becoming increasingly unable to meet the design specifications for cooling heat generating sources found in advancing new technologies. Therefore, significant effort has been made to engineer new fluids that are able to meet these demanding requirements [1-5]. One of the interesting results obtained from these efforts has been the development of *nanofluids*, which are traditional thermal management fluids that contain nanoparticle suspensions. In an attempt to understand the interesting heat transfer characteristics found when using nanofluids, an even larger amount of interest has been expressed in understanding the effect that nanoparticle suspensions have on the thermophysical properties of the base fluid, specifically thermal conductivity and shear viscosity. Both experimental and theoretical approaches to an understanding of this effect have been proposed, with varying degrees of approval from within the research community. Of the theoretical approaches that have been taken, molecular dynamics modeling has yielded interesting results. Therefore, it is the focus of this dissertation.

1.1 Nanofluids

The development of nanofluids was first proposed in 1995 by Stephen Choi at Argonne National Lab [6]. In the theoretical nanofluid proposed, the heat transfer characteristics of the base fluid are enhanced by the suspension of nano-sized metallic particles, while not suffering from issues associated with the use of millimeter or

micrometer sized particle suspensions [7]. Since then, additional types of nanofluids composed of metal-oxide [7-10] and nonmetal [11-13] nanoparticle suspensions have been proposed and investigated for their heat transfer characteristics in thermal management applications.

The preparation of nanofluids for experimental use has varied among investigators, but generally can be described as either a one- or two-step process. In one-step processes, the nanofluid is developed directly in the fluid either by a method of condensation of nanoparticle vapor into a low-vapor-pressure liquid (e.g., the vacuum-submerged arc nanoparticle synthesis system), or through a method of vacuum evaporation onto a running oil substrate. In two-step processes, nanoparticles (most often metal-oxides) are preprocessed and then later dispersed into the base fluid by means of ultrasonication. Once the nanofluid has been prepared, dispersion of the nanoparticle may be enhanced with the addition of a surfactant or increasing acidity levels. A limited, yet comprehensive, investigation by Buongiorno, et al. [14] has demonstrated that the preparation process had little effect on the thermophysical properties. However, Buongiorno stated that it was not an exhaustive investigation and could not cover all possible methods for preparation.

Observable physical characteristics of nanofluids are dependent on the nanoparticle size, composition, and concentration. Nanoparticle suspensions can consist of particles whose diameters vary in size from approximately 11 nm [15] to as much as 250 nm [8]. Once suspended in the base fluid, the resulting nanofluid exhibits observable physical properties determined by the composition of the nanoparticle suspension. While current research does not provide quantifiable data of the turbidity of nanofluids,

qualitative examination of the specimens generated for experimental investigations suggest definitive relationships between the nanoparticle suspension and the observed physical properties of the resulting nanofluid. For example, a nanofluid with 1% bohemite alumina blade suspensions [16] was generally transparent with slight physical manifestation of the presence of nanoparticles. However, a nanofluid with 1% spherical alumina suspensions [9] was opaque and displayed the white cloudy characteristics of the alumina powder. With investigations looking at concentrations of nanoparticles that vary from as little as 0.00023% [17] to as much as 8% [18], investigators can determine which thermophysical characteristics play important roles in increasing their effectiveness in heat transfer applications.

1.2 Heat Transfer Investigations Using Nanofluids

Of the many applications considered where nanofluids could be used, the most common one is in thermal management. From use in heavy vehicle radiators or microchannel heat exchangers, the potential of nanofluids as effective heat transfer fluids is promising. Early performance results have shown enhancements in the heat transfer coefficient for all aspects of single phase internal flow through a pipe, with as much as a 47% increase within the entrance region and as much as a 39% increase within the fully developed region [19, 20].

On the other hand, performance results for phase change heat transfer using nanofluids have yet to arrive to a definitive conclusion. Examples of enhancement can be found with: a) Witharana [21], who demonstrated that an approximately 21% increase in the heat transfer coefficient is attained when boiling water with gold nanoparticle suspensions, and b) Kim, et al. [8], who was also was able to demonstrate an almost 80%

increase in the critical heat flux using silica nanofluids. However, examples can also be found that show a decrease in the heat transfer performance using nanofluids. These include: a) Bang, who established that the increasing concentration of alumina nanoparticles caused the water boiling curve to shift to the right, thereby demonstrating a decreasing heat transfer coefficient [22], and b) Witharana, who calculated from experimental results decreases in the boiling heat transfer coefficient for water and ethylene glycol containing silica nanoparticles [21].

An interesting result of the analyses of both single phase and phase change heat transfer is the performance dependency on the thermophysical properties of the nanofluid. It has been shown through correlations to convective transport models that heat transfer performance is directly related to such thermophysical properties as the thermal conductivity, shear viscosity, and density of the nanofluid [10, 22-24]. Therefore, much emphasis has been placed on fully understanding how nanoparticles affect the thermophysical properties of the base fluid and how these adjustments affect overall heat transfer performance.

1.3 Experimental Investigations of Thermophysical Properties

Eastman et al. [25] was the first to present thermophysical property enhancement with an almost 60% increase in the thermal conductivity of water with the insertion of 5% concentration copper oxide nanoparticles. Since then, a high concentration of experimental research in the thermophysical properties of nanofluids has focused on thermal conductivity characterization. However, a brief overview of various recent thermal conductivity measurements obtained by different investigators for the Al_2O_3/H_2O nanofluid highlight reasons for continued discussion on how the thermal conductivity

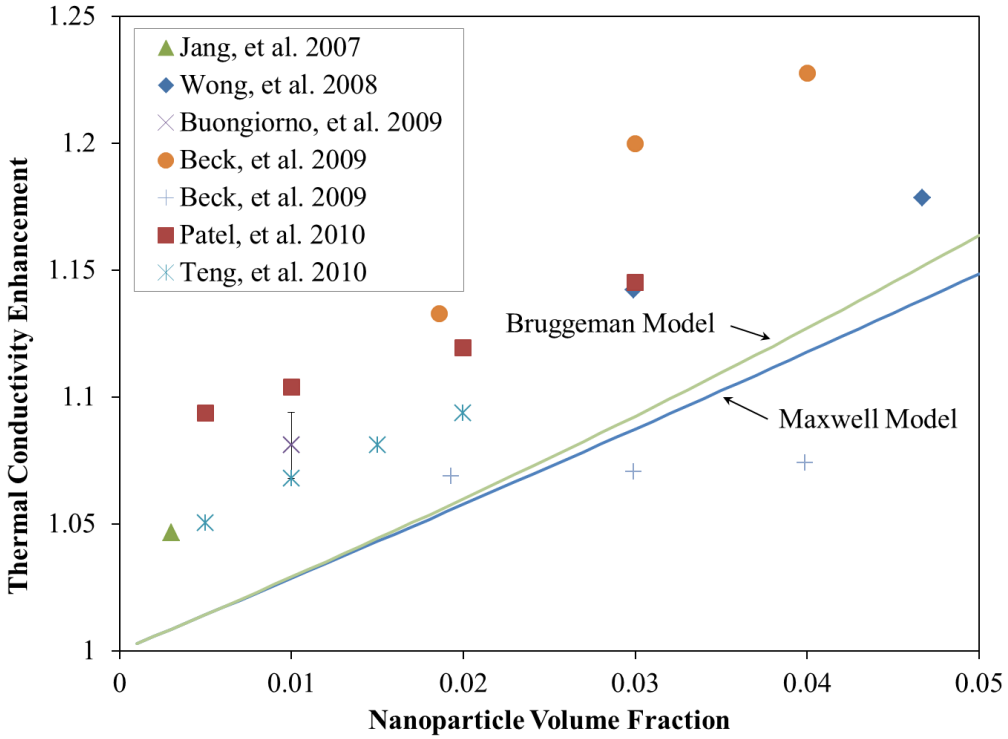

Figure 1.1 Thermal conductivity enhancements of various measurements of aluminum oxide nanofluids at various volume fractions.

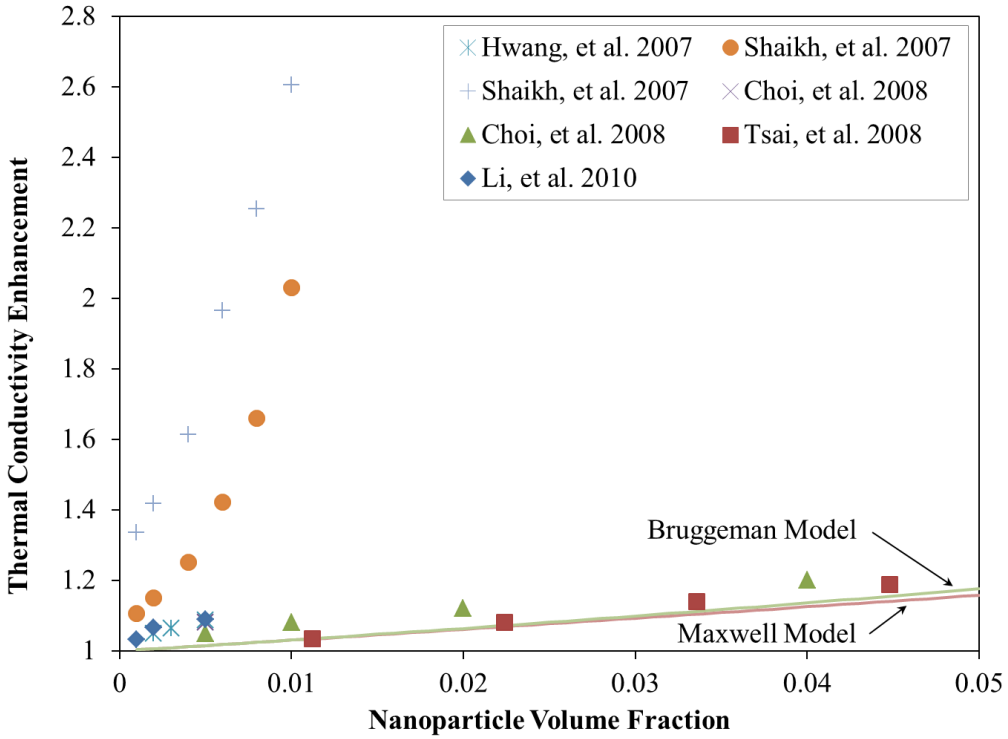

Figure 1.2 Thermal conductivity enhancements of nanofluids with different nanoparticle types and base fluids at various volume fractions.

enhancements seen in nanofluids vary amongst investigations, as shown in figure 1.1 [14, 15, 26-29]. While a general correlation can be seen between nanoparticle volume fraction and thermal conductivity enhancement, the range in values obtained from different investigators of the same nanofluid increases to a maximum of approximately 15% at a nanoparticle volume fraction of 0.04. A similar linear relationship can be observed in other nanofluids where the nanoparticle is spherically shaped, regardless of the base fluid type [30, 31]. Figure 1.2 further presents the complication in finding a consistent relationship between nanoparticle volume fraction and thermal conductivity enhancement when varying nanoparticle type in a fluid that is oil-based. Spherically-shaped nanoparticles in oil-based fluids continues to exhibit enhancements that could be predicted by effective medium theories as was seen with the water-based aluminum oxide nanofluids mentioned earlier [32-34]. However, when the aspect ratio of the nanoparticle increased, as is the case for nanotubes, a parabolic relationship between the volume fraction and the thermal conductivity enhancement is observed [35, 36].

Additional factors that could affect the thermal conductivity values obtained from experimentation are the measurement technique, nanoparticle composition, and nanoparticle/fluid interaction. Results from the benchmark study by Buongiorno et al. [14] did demonstrate that measurement technique does affect the obtained thermal conductivity value, but less of a factor in its enhancement. A brief analysis of figure 1.1 supports the assertion that differences in both the thermal conductivity values and their relationship to volume fraction can be seen when measured using the KD2 apparatus [29], transient hot wire method [26-28], or the temperature oscillator method [15]. Also, while figure 1.2 clearly demonstrates that the type of nanoparticle suspension

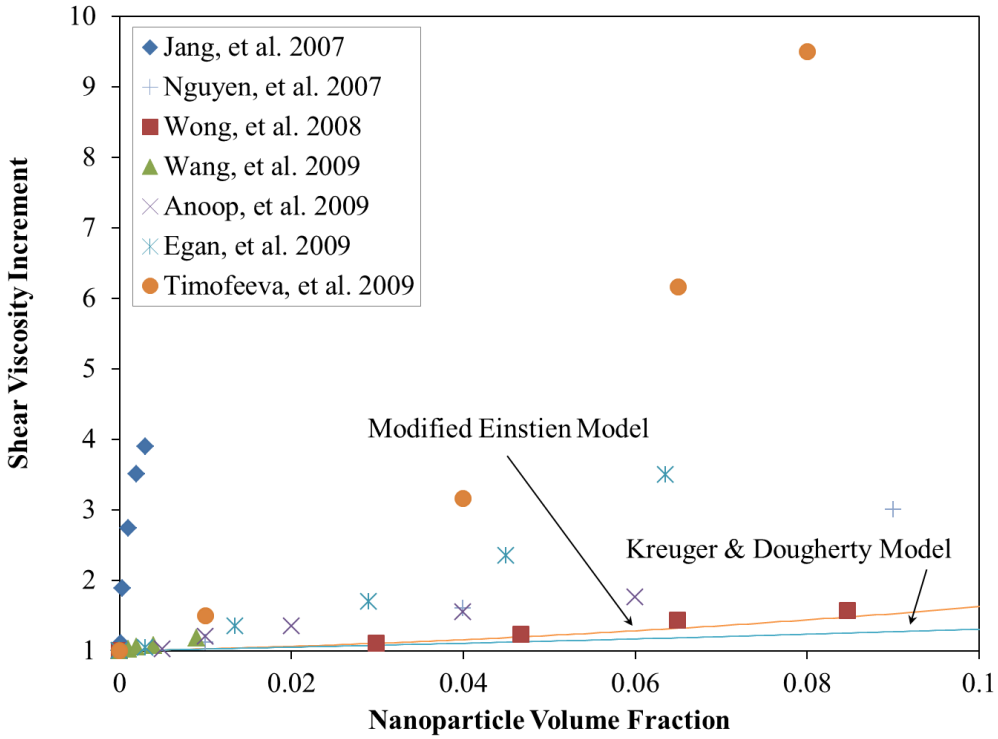

Figure 1.3 Shear viscosity increments of various measurements of aluminum oxide nanofluids at various volume fractions.

significantly affects the measured thermal conductivity, it has been shown that the constitutive property of the suspension itself is not a significant factor. This observation was demonstrated experimentally by Hong et al. [37] where their work with iron nanoparticles manifested higher thermal conductivity enhancements of ethylene glycol that that of the copper nanoparticles used in the work of Eastman et al. [38]. Finally, Patel et al. [17] was further able to demonstrate that enhancing the nanoparticle surface/base fluid interaction through nanoparticle coating positively affected the thermal conductivity of the overall nanofluid.

Investigators have also reported interesting experimental viscosity measurements of nanofluids in recent years, with some of the results displayed in figure 1.3 [16, 26, 27, 39-42]. Among the most significant results is that very small concentrations of

Table 1.1 Rheological regions for nanofluids [43].

Region	***Concentration***	***Characteristics***
1	$0\% < \phi < 0.001\%$ vol.	Newtonian fluid
2	$0.001\% < \phi < 0.05\%$ vol.	Non-Newtonian fluid with shear thinning characteristics
3	$0.5\% < \phi < 0.1\%$ vol.	Viscoelastic fluid with low and high shear viscosities accessible
4	$\phi > 0.1\%$ vol.	Viscoelastic solid with a yield stress or a high shear viscosity fluid when the yield stress is exceeded

nanoparticles can, in some cases, double the overall nanofluid viscosity [44, 45]. Thus, its usefulness as a heat transfer fluid is diminished, even with the enhancements in thermal conductivity mentioned earlier. Other results [43] showed that nanofluid viscosity characteristics are nanoparticle-concentration dependent and yield four distinct rheological regions, as can be seen in table 1.1. Several other researchers [16, 46, 47] have shown that nanofluid viscosity is also dependent on nanoparticle size, shape, temperature, use of surfactant, and pH value. Nguyen [41] also found that, in addition to being temperature dependent, at higher temperatures the viscosity of nanofluids exhibited an undesirable and unpredictable hysteresis behavior.

Experimental investigations into the density of nanofluids are a relatively recent area of research and published results have been debated less than those of measured thermal conductivity and viscosity. General observations of Vajjha [48, 49] have shown that increasing the concentration of metal oxide nanoparticles in the base fluid increases the density of the overall nanofluid and has a temperature dependency. Pastoriza-Gallego [45] further suggested that nanofluid density is inversely proportional to nanoparticle size, nonlinear with increasing concentrations, and highly dependent on temperature.

1.4 Phenomenological Models of Thermophysical Properties

To explain some of the conflicting results seen in the experimentally obtained thermal conductivity values for nanofluids, many models have been presented that are based on one of two general effective medium theories: 1) low volume concentration, non-interacting nanoparticles, and 2) mean-field interacting nanoparticles. Maxwell [50] was the first to present a model that attempted to describe the effect of randomly distributed, non-interacting (low volume fraction) homogeneous solid spheres on a homogeneous fluid medium. Modifications and generalizations of Maxwell's work followed, investigating the impact of particle suspension shape [51], liquid nanolayer surrounding the nanoparticle [52, 53], Brownian motion [20], microconvection [54], and temperature dependence [55]. While these models have been shown to mirror experimental results in specific cases, the Maxwell-based models break down when applied to high volume-fraction nanofluid systems. Bruggeman [56], on the other hand, was able to develop a model that would incorporate the effect of high volume fractions, as well as the long-range interactions of particle suspensions. Later modifications to this model were also used to analyze the independent and combined effects of interfacial shells [52, 53, 57, 58], aggregation [58, 59], and percolation [60, 61]. A brief summary of the Maxwell and Bruggeman-based models for thermal conductivity enhancement previously mentioned is presented in table 1.2 and compared with experimental values presented in figure 1.1.

While there have been claims that the controversy surrounding thermal conductivity enhancement is finished as a result of the use of these models [62], both effective medium theories are dependent on the nanoparticle maintaining a thermal

conductivity significantly higher (greater than 100 times [18, 58]) than the bulk fluid. This requirement allows the bulk fluid thermal conductivity to be neglected in model calculations. However, numerical simulations and experimental analyses of nanoscale metallic nanolayers show that both electronic [63] and phonon [64-66] contributions to

Table 1.2 Various analytical models used to describe thermal conductivity of nanofluids.

Investigator	***Model***	***Comments***
[50]	$k_{eff} = \frac{k_{np} + 2k_{bf} - 2\left(k_{bf} - k_{np}\right)\phi}{k_{np} + 2k_{bf} + \left(k_{bf} - k_{np}\right)\phi} k_{bf}$	Maxwell Model: Non-interacting, low volume fraction solid spheres
[52]	$k_{eff} = \frac{k_{pe} + 2k_{bf} - 2\left(k_{pe} - k_{np}\right)(1-\beta)^3\phi}{k_{pe} + 2k_{bf} - \left(k_{pe} - k_{bf}\right)(1-\beta)^3\phi} k_{bf}$	Same as Maxwell [50], but taking into account a liquid nanolayer
[55]	$k_{eff} = k_{eff,Maxwell} + 5\times10^4 \beta\phi\rho_p c_p \sqrt{\frac{k_B T}{\rho_p D}} f(T,\phi)$	Maxwell [50] based model taking into account particle size, particle volume fraction, temperature dependence and Brownian motion
[56]	$\phi\left(\frac{k_{np} - k_{eff}}{k_{np} + 2k_{eff}}\right) + (1-\phi)\left(\frac{k_{bf} - k_{eff}}{k_{bf} + 2k_{eff}}\right) = 0$	Bruggeman Model: High volume fraction, long-range interacting spherical suspensions
[57]	$\left(1 - \frac{\phi}{\alpha}\right)\frac{k_{eff} - k_b}{2k_{eff} + k_b} + \frac{\phi}{\alpha}\frac{\left(k_{eff} - k_2\right)\left(2k_2 - k_1\right) - \alpha\left(k_1 - k_2\right)\left(2k_2 + k_{eff}\right)}{\left(2k_{eff} + k_2\right)\left(2k_2 + k_1\right) + 2\alpha\left(k_1 - k_2\right)\left(k_2 - k_{eff}\right)}$	Same as Bruggeman [56], but taking into account interfacial shells
[67]	$k_{eff} = k_b + c\frac{2k_b T}{\pi\nu d_p^2}\frac{\phi r_b}{k_b(1-\phi)r_p} k_b$	Stokes-Einstein based model taking into account temperature dependency
[68]	$k_{eff} = k_b(1-\phi) + k_p\phi + 3C\frac{d_b}{d_p} k_b Re_{d_p}^2 Pr\phi$	Model based on four modes of energy transfer

thermal transport decreases significantly, thereby reducing the thermal conductivity value of the nanoparticle by as much as 50% [69]. Additionally, Brownian motion of the nanoparticles [68], microconvection of the surrounding base fluid [70], and ordered liquid nanolayers [71] theories used in the previously mentioned models to describe thermal conductivity enhancement have either been disproven or shown to be negligible.

As with thermal conductivity analysis, modeling the viscosity of nanofluids began with macroscopic theories. First, Einstein [72, 73] presented a Taylor series approximation for the relative viscosity of a fluid with large (millimeter/micrometer), non-interacting spherical suspensions. Later models built on Einstein's theory by taking into account hydrodynamic interactions of individual particles [74], small colloidal interactions (Krieger-Dougherty model) [74], and large aggregates [75]. A different approach to modeling nanofluid viscosity was presented by Masoumi [76], where an "apparent viscosity", caused by the Brownian motion of individual nanoparticles, was calculated and added to the base fluid viscosity. While all the previously described models presented in table 1.3 do predict an increase in viscosity with low volume fractions, experimental results have shown that in some cases these macroscopic and microscopic theories miss actual effective nanofluid viscosity values by as much as 50% [77, 78]. This can also be seen in figure 1.3. These theoretical models also do not capture the non-Newtonian behavior of nanofluids, and do not take into account other critical factors such as particle size, mass, and temperature.

In many nanofluid heat transfer analyses, it has been assumed that both density and specific heat properties can be determined solely by using linear mixing models. However, it has been observed that the density of nanofluids is also size dependent, with

Table 1.3 Various analytical models used to describe viscosity of nanofluids.

Investigator	***Analytical Model***	***Comments***
[72, 73]	$\eta_{eff} = \eta_f \left(1 + [\eta]\phi + O\left(\phi^2\right)\right)$	Einstein model: Spherical particles and dilute non-interacting suspensions where$[\eta]$ is the intrinsic viscosity with a typical value of 2.5
[74]	$\eta_{eff} = \eta_f \left(1 + [\eta]\phi + k_H \left([\eta]\phi\right)^2 + O\left(\phi^3\right)\right)$	Einstein model: Spherical particles and semi-dilute suspensions, interaction of pair-particles are considered, k_H, the Huggin's coefficient, is interaction parameter characterizing the colloidal interactions between particles as opposed to the purely hydrodynamic effect
[75]	$\eta_{eff} = \left(1 - \frac{\phi}{\phi_m}\right)^{-2.5\phi_m}$	Krieger-Dougherty model: Packing fraction of spherical particle suspensions (ϕ_m) imposes limit on increases in effective viscosity
[76]	$\mu_{eff} = \mu_{bf} + \frac{\rho_P V_B d_P^2}{72 C \delta}$	Masoumi model: Effects of Brownian motion included in overall viscosity calculation

smaller nanoparticles leading to larger nanofluid densities perhaps due to interface effects on bulk fluid properties by the nanoparticle surface or interactions among the nanoparticles themselves [45, 79]. Other investigations have shown that nanofluid density is also dependent on temperature, decreasing with increasing temperature values [48, 49]. In addition to these observations, there have yet to be attempts to determine if aggregation or Brownian motion play a significant role in the determination of these properties as has been seen for thermal conductivity and viscosity.

1.5 Molecular Dynamics Modeling of Thermophysical Properties

In addition to the many macroscopic models proposed to describe nanofluid static and dynamic thermophysical property modification, both equilibrium and nonequilibrium molecular dynamics simulations have been useful observation tools to provide insight into the underlying physical mechanisms that govern molecular interactions at the nanoscale. Keblinski et al. [80] was the first to use molecular dynamics simulations to analyze the effect of nanoparticles on the thermal conductivity of a nanofluid system. While no actual values of thermal conductivity were calculated for the theoretical solid argon/liquid argon nanofluid system analyzed, it was shown that Brownian motion played an insignificant role in both thermal conductivity calculations and microscopic heat transport. This observation was later supported by Evans et al. and Vladkov et al. [70, 81] along with the suggestion that other phenomena, such as agglomeration are responsible for the large thermal conductivity increases seen in previously discussed experimental results. Other investigators [82-88] also used molecular dynamics simulations to support experimental results that indicated that volume concentration, nanoparticle size and temperature are significant contributors to the enhancement of thermal conductivity and shear viscosity of nanofluids. An overview of these results can be seen in figure 1.4. It is important to note that contrary results were obtained where the effect of Brownian motion is shown to have a significant role in enhanced heat transfer [68] and liquid layering of a simulated "real" nanofluid contributes more to thermal conductivity than is suggested by Keblinski [88].

In spite of the conflicting data obtained earlier, subsequent molecular dynamic investigations focused on understanding how nanoparticles affected thermal conductivity

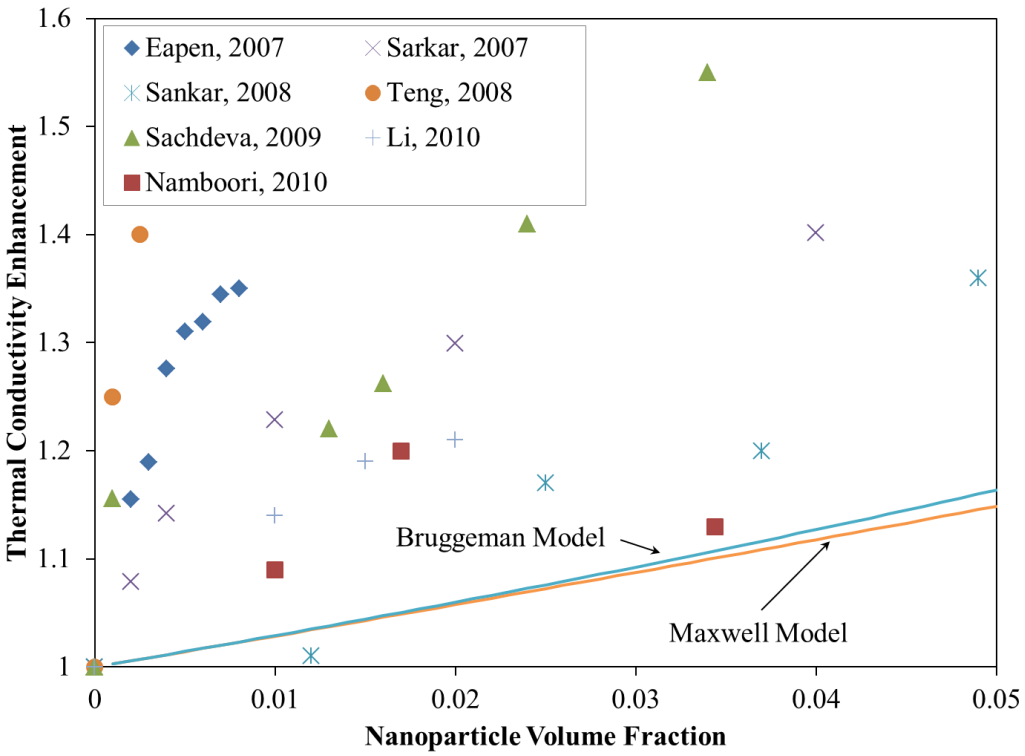

Figure 1.4 Molecular dynamics simulation calculations of thermal conductivity enhancements of various types of nanofluids at different nanoparticle volume fractions.

enhancement in nanofluids. For example, it was suggested that the particle/liquid interface played a key role in translating the high thermal transport properties of the suspended nanoparticle to the overall thermal conductivity enhancement of the nanofluid. This latter point was investigated by Xue et al. [89] where it was determined that there were two (wetted and non-wetted) regimes of the Kapitza thermal resistance at the liquid/solid interface. While further liquid/solid interface investigations [81, 90] have found that liquid near the surface had higher values of thermal conductivity compared to the bulk fluid and that the ratio of the thickness of the Kapitza resistance to the nanoparticle diameter was significant, Xue et al. [71] ruled out the possible beneficial effects of liquid layering. The conclusion was made based on the width of the ordered layer region (several atomic distances), which would introduce finite size scattering

effects, and the surface of the solid nanoparticle serving as a scattering site for collected motion of these ordered liquid atoms. Sankar et al. [85] used the mean squared displacement results of molecular dynamics simulations to suggest that the nanoparticle enhanced microconvection in the surrounding liquid atoms and that this was the mechanism for enhanced heat transfer in nanofluids.

A more in-depth analysis of the physical mechanisms that govern thermal conductivity in nanofluids began with Eapen et al. in 2007 [82]. In this work, the heat current vector used to determine thermal conductivity was decomposed into three modes of energy transfer (kinetic, potential, and collision) between the constitutive components of the nanofluid (xenon and platinum). It was through pair and cross correlations between these modes that it was determined the Xe-Pt potential-potential correlation function was the significant contributor to nanofluid thermal conductivity enhancement. As a result, it was suggested that a dynamic layer formed around the surface of the nanoparticle where potential energies between the solid and the liquid is exchanged. It was through this dynamic layer that a percolating network developed in the nanofluid system where potential energy exchange was maximized [82].

Although drawing similar conclusions using methodologies resembling that mentioned above, Sachdeva et al. [84] and Teng et al. [87] provided differing rationalizations for thermal conductivity enhancement. Sachdeva et al. stated that it was the *collision-collision* pair correlation function of the liquid molecules near the nanoparticle surface (hydration layer) that dominated the thermal conductivity enhancement in a theoretical nanoparticle/water system. Teng et al. found that the combined potential-kinetic pair correlation ("convection" term) dominated the calculation

of thermal conductivity, which is similar to the conclusion drawn by Eapen et al. However, Teng stated that it was the copper-copper (*solid-solid*) "convection" pair correlation term that was the influencing factor compared to the xenon-platinum (*solid-liquid*) potential-potential pair correlation results presented by Eapen et al.

Investigation into the effect nanoparticles have on the shear viscosity of fluid using molecular dynamics simulations has not been as extensive as has been done for thermal conductivity. However, Lu et al. [91, 92] demonstrated that shear viscosity is both dependent on nanoparticle concentration and diameter. McPhie et al. [93] also was able to determine that the nanofluid exhibits strong shear thinning behavior when a) the nanoparticle size and mass ratio relative to the fluid is greater than one, and b) when volume fraction increases with size and mass ratios of greater than one. Rudyak et al. [94, 95] also showed a shear viscosity dependence on the mass of the nanoparticle and further adding that influence of the nanoparticle extended up to half of its diameter away from its surface. It was then suggested that the coupling of the Brownian motion of the nanoparticle and its strong influence on a large volume of the surrounding fluid is what leads to a significant increase in the shear viscosity of the nanofluid system.

Various investigators have used density analyses using molecular dynamics simulations as reasoning for increases in thermal conductivity and shear viscosity of nanofluids compared to base fluids. While several different investigations comment on the highly ordered layering that occurs near the nanoparticle surface [84, 87, 95], Eapen et al. [82] suggested that the liquid atoms near the nanoparticle surface may, in fact, create an amorphous-like fluid structure that eventually networks with liquid layers of other nanoparticles and through which potential energy exchange is favored. Li et al. [88]

also suggested that the local density near the nanoparticle surface may also be time-dependent.

1.6 Statement of Objective and Scope of Dissertation

The objective of this investigation is to identify key fundamental theoretical concepts that govern the unique characteristics observed in the thermophysical properties of simple fluids with low volume fractions of nanoparticles suspensions. Thermal conductivity, shear viscosity, and density were the thermophysical properties selected for this investigation due to their significance in determining the heat transfer coefficient for a variety of heat transfer problems described by empirical correlations. Therefore, this dissertation is organized to allow for an in-depth analysis of each of these thermophysical properties based on the results of molecular dynamics simulations.

In chapter 2, a basic theoretical framework is laid for the calculation of the transport properties and an introduction to the methodology for data calculation is presented. A brief overview of the relevant aspects of nonequilibrium thermodynamics to the equilibrium molecular dynamics simulations performed in this investigation is performed. The reader is also introduced to the molecular dynamics model used to describe the nanoparticle and its interactions with the base fluid. This model was uniquely different from other nanoparticle models used in simulations discussed in section 1.5 in that the constitutive property of the nanoparticle does not contribute to the overall thermal conductivity calculations of the nanofluid. A consideration was further taken to address the lognormal size distribution observed in commercially available nanoparticles [96] by selecting a range of diameters to model with a corresponding interatomic potential for comparison. Finally, the nanofluid systems and their interaction

parameters are developed in a way to address the effects of nanoparticle size and interaction energy on the thermophysical properties discussed in later chapters.

In chapter 3, an understanding of the effect nanoparticles have on both the local structure and density is developed. The radial distribution functions for the two nanoparticle interactions presented in chapter 2 are presented to address local static structure characteristics of the liquid near the nanoparticle surface. Dynamic structural characteristics of the local fluid surrounding the nanoparticle were analyzed using a local density covariance matrix that identified the least correlated regions over a specified period.

In chapter 4, an understanding of the effect nanoparticle size and interaction energy on the calculated thermal conductivity of the fluid is developed. Molecular hydrodynamic theory is then used to determine the collective modes that characterize thermal diffusion within the nanofluid and isolate the physical mechanisms that enhance thermal transport. An analysis of the original equations developed from nonequilibrium thermodynamics is performed to integrate the results regarding molecular diffusion and its characteristics into relationship that predicts thermal conductivity enhancement in a nanofluid from macroscopic parameters.

In chapter 5, an understanding of the effect nanoparticle size and interaction energy on the calculated shear viscosity of the fluid is developed. Molecular hydrodynamic theory is once again used to determine the collective modes that characterize momentum transport within the nanofluid and isolate the physical mechanisms that are enhanced by nanoparticle suspensions. The behavior of the nanofluid under an applied shear stress of the form $\delta(t)$ is also approximated by a

calculation of the relaxation time using a calculated infinite frequency shear modulus value (G_∞) obtained from the radial distribution functions generated in chapter 2.

In chapter 6, the important results of this work is summarized and presented, and paths for future work in this area are suggested.

Chapter 2 – Theoretical Framework and Methodology

Thermal conductivity and shear viscosity are thermophysical properties that characterize material response due to the presence of nonequilibrium conditions taking the form of either a temperature or momentum gradient, respectively. While molecular dynamics simulations can replicate the nonequilibrium conditions required to determine these properties [60, 70, 81, 90, 97-102], critical information containing the physical mechanisms of thermal and momentum transport is lost. With this information, the underlying physics that drives the increases in both thermal conductivity and shear viscosity seen in fluids with nanoparticle suspensions can be isolated. Therefore, in order to obtain this information from the nanofluids investigated, the thermal conductivity and shear viscosity are instead calculated from molecular dynamics simulations that describe an equilibrium state.

To obtain dynamic properties from a system at equilibrium, the field of nonequilibrium thermodynamics has to be employed. Within this subject area, the principles of equilibrium thermodynamics are applied to an open system where potentially interacting irreversible processes (i.e., heat, mass, and momentum fluxes) are present. With this theoretical framework in place, macroscopic dynamic properties can be calculated from microscopic quantities of the equilibrium system through a systematic application of the first and second laws of thermodynamics supplemented by an

additional set of equations based on phenomenological relationships. Based on this nonequilibrium theory, the thermal conductivity can be shown to be

$$\lambda = \frac{1}{Vk_B T^2}\int_0^\infty \left\langle J_q(0) J_q(\tau)\right\rangle d\tau \tag{2.1}$$

where

$$J = \sum_{k=\alpha}^{\beta}\sum_{i=1}^{N_k}\frac{1}{2}m_l^k\left(\upsilon_l^k\right)^2\mathbf{v}_i^k + \sum_{k=\alpha}^{\beta}\sum_{l=\alpha}^{\beta}\sum_{i=1}^{N_k}\sum_{j>i}^{N_l}\left[\mathbf{I}U\left(r_{ij}^{kl}\right)\otimes\mathbf{F}\left(r_{ij}\right)\right]\cdot v_i^k - \sum_{k=\alpha}^{\beta}h^k\sum_{i=1}^{N_k}v_i^k \tag{2.2}$$

and m, v, h are the mass, velocity, and partial enthalpy of a particle, and U, $\mathbf{F}$, and r are the potential function, force vector, and distance between two particles, respectively. The shear viscosity can be shown to be

$$\eta = \frac{V}{k_B T}\int_0^\infty \left\langle P_{xy}(0) P_{xy}(\tau)\right\rangle d\tau \tag{2.3}$$

where

$$P_{xy}(t) = \sum_i \frac{\mathbf{p}_x^i \mathbf{p}_y^i}{m^i} - \frac{1}{2}\sum_i \mathbf{r}_x^{ij}\mathbf{F}_y^{ij} \tag{2.4}$$

and m and $\mathbf{p}$ are the mass and momentum of a particle, and $\mathbf{r}$ and $\mathbf{F}$ are the distance and force vectors between two particles, respectively.

While the origins of nonequilibrium thermodynamics have traditionally been associated with both the analysis of the thermo-electric phenomena performed by Thomson in 1854 [103] and the reciprocal relations of the rate of entropy production developed by Onsager in 1931 [104, 105], its usage to calculate the dynamic properties of nanofluids has seen significant interest in recent years. This can be clearly seen in works described in chapter 1 [82-86, 88, 91-93]. Other critical phenomenological properties can

be determined with this methodology as well, including the cross-coefficients of thermophoresis and thermodiffusion that arise as a result of the presence of coupled irreversible processes of heat and mass fluxes in a multicomponent system [61, 106-108].

A rigorous theoretical development of equations 2.1–2.4 from nonequilibrium thermodynamics is not presented here, and the reader is encouraged to review the works of Hanley, De Groot and Mazur, and Fitts [109-111]. However, key theoretical constructs of nonequilibrium thermodynamics that relate directly to the methodology employed during the molecular dynamics simulations and calculations performed in this work will be discussed at length here. First, a more detailed discussion of the theoretical concepts that allow for the calculation of dynamics properties from a system fluctuating about an equilibrium state will be presented. Then, the correlation function formalism that permits a relationship to be made between the macroscopic and averaged microscopic fluxes in a small element of volume in a system at equilibrium is developed.

2.1 Local Equilibrium Assumption

Equilibrium molecular dynamics simulations were performed in all the investigations of thermal conductivity and shear viscosity of the nanofluids selected in this work. While the term “equilibrium” here does refer to the thermodynamic state of the system being simulated, using these simulations to calculate transport properties requires that this designation receive further clarification.

A liquid at an equilibrium state is defined as having intensive properties that are not time dependent. A graphical representation of the process that follows can be found in figure 2.1. However, applying an external thermodynamic driving force (such as a heat flux or shear rate) will perturb the system to a nonequilibrium state, such that the

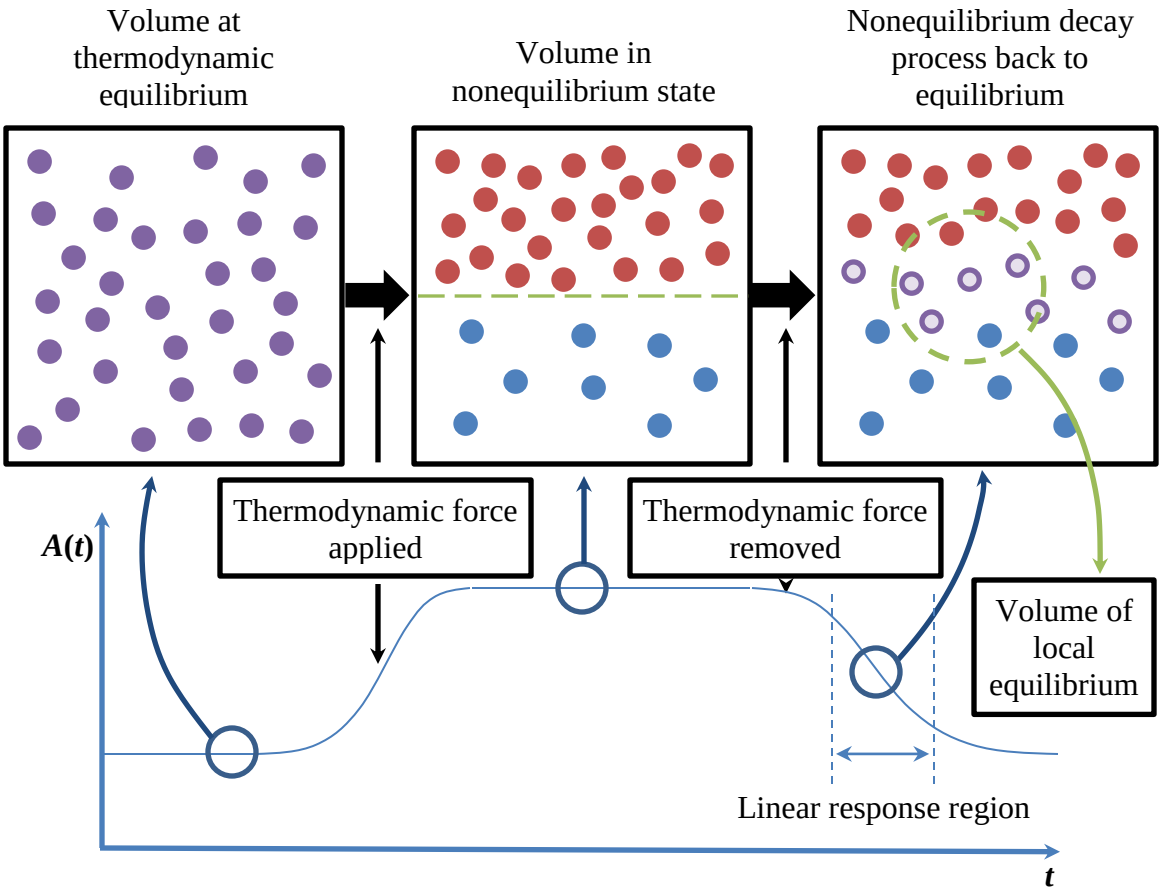

Figure 2.1 Graphical description of development of nonequilibrium state of volume at thermodynamic equilibrium.

observable thermodynamic parameters of the system (A) are now both a function of space and time. When the external driving force is removed, thermodynamic parameter gradients will be present in the system and an irreversible process to return to thermodynamic equilibrium will begin. If the assumption is made where the path to equilibrium is through a series of states that are themselves at equilibrium locally, then each of the independent gradients (X_k) can be related to the corresponding nonequilibrium

decay processes back to equilibrium (J_i) through a matrix of phenomenological coefficients, L_{ik}, and can be expressed as

$$J_i = \sum_{k=1}^{n} L_{ik} X_k \tag{2.5}$$

This is postulated as the *local equilibrium assumption* and is central to the concept of calculating linear transport properties from an equilibrium system using nonequilibrium thermodynamics.

The definition of locality in the physical system is arbitrary as long as variation of the state variables within the selected volume is negligible while remaining larger than the longest mean free path of each the constituent particles. It is within these volumes of local equilibrium that the molecular dynamics simulations are performed. Defining the thermodynamic state of these local volumes in molecular dynamics simulations cannot be expressed explicitly and has to be determined from a statistical average of an ensemble of possible microstates of the system. Several types of ensembles are used in molecular dynamics simulations [112], and within this investigation the canonical version was chosen. Here, the number of particles (N), volume (V), and temperature (T) are fixed values that specify the thermodynamic state and are obtained from values calculated from experimentally observed data.

The thermodynamic state selected for the local volume of simulated liquid argon at equilibrium was determined in a way that both the density and temperature were close to its triple point, which have been determined to be ρ_{TP} = 1.435 kg/m^3 and T_{TP} = 86.5 K [113, 114]. The values selected were T = 87.057 K and ρ = 1.418 kg/m^3, which are similar to the values other molecular dynamics simulations investigating the

Table 2.1 Thermodynamic states of liquid argon simulated in this investigation.

Nanoparticle Diameter (nm)	***Total number of particles***	***Volume (nm^3)***	***Temperature (K)***
0.4	864	40,424	87.057
0.5	2,048	95,820	
0.6	2,916	136,432	
0.7	4,000	187,149	
0.8	6,912	323,394	
1.0	13,500	5,050,446	

thermophysical properties of liquid argon and argon-based nanofluids [85, 114, 115]. From this density, initial FCC lattice configurations with a lattice constant of 5.72 Å were used to determine the values of *N* and *V* at the specified temperature *T*. All resulting values are recorded in table 2.1 and a plot of the temperature and total energy during the

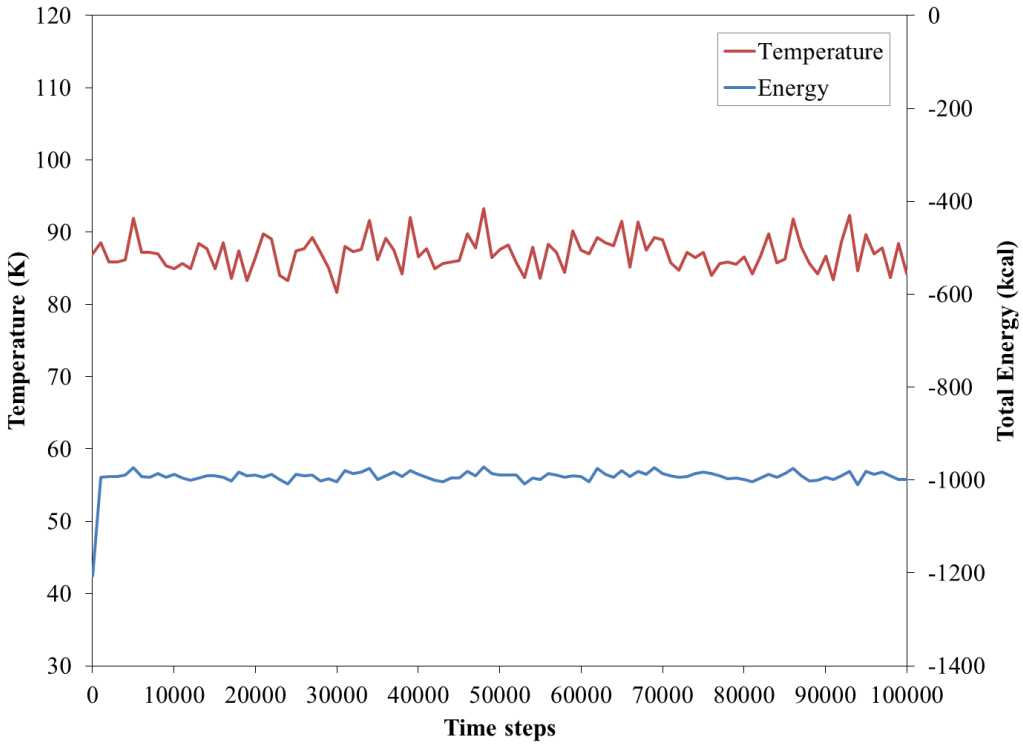

Figure 2.2 Temperature and total energy quantities for equilibration period of argon fluid molecular dynamics simulations.

equilibration period of a molecular dynamics simulation of pure argon fluid can be seen in figure 2.2. It can be seen that the temperature does fluctuate about the specified temperature of 87.057 K and that the total energy is conserved, even though it was not a defining parameter for the thermodynamic state of the system.

The volume fractions used in this investigation were based off the calculation of the volume occupied by the nanoparticle and the liquid and not the total volume of the simulation box, using the equation

$$\phi = \frac{N_{np}\left(\frac{4}{3}\pi r^3\right)}{\nu V - N_{np}\left(\frac{\nu V}{N_f}\right) + N_{np}\left(\frac{4}{3}\pi r^3\right)} \tag{2.6}$$

Here, ν is the atomic packing factor (0.74 for fcc structures), N_{np} is the number of nanoparticle suspensions, and r is the radius of the nanoparticle. In order to take into account for the increasing diameter of larger nanoparticles while still maintaining low nanoparticle concentrations, the corresponding volumes (V) and number of argon atoms (N) had to be increased accordingly.

2.2 Green-Kubo Relations

The next objective is to express the thermophysical coefficients obtained from well-established empirical laws, in terms of the microscopic quantities obtained from molecular dynamics simulations. While the thermophysical coefficients are directly

related to the main diagonal of the phenomenological coefficient matrix (L_{ik}) found in equation 2.5 and can be expressed as

$$\lambda = \frac{L_{qq}}{T^2} \tag{2.7}$$

$$\eta = \frac{L}{2T} \tag{2.8}$$

the calculation of the phenomenological coefficients themselves requires significant mathematical formulation derived from the theoretical concepts found in nonequilibrium thermodynamics.

With the local equilibrium assumption being used to analyze a system undergoing a nonequilibrium decay process, another methodology for determining the phenomenological coefficients matrix in equation 2.5 has to be employed since the temperature/momentum gradients are now equal to zero. Green [116], and later Kubo [117, 118], provided the theoretical mechanisms for this calculation with the relations

$$L_{ik} = \frac{V}{k_B T}\int_0^\infty \left\langle J_i(0) J_i(\tau)\right\rangle d\tau \tag{2.9}$$

which now express the phenomenological coefficients solely in terms of their conjugate fluxes (J_i). The integrand indicates an ensemble average of the autocorrelation of these fluxes as they undergo the nonequilibrium decay process to equilibrium. Onsager's regression hypothesis provides for this calculation in an equilibrium system by relating macroscopic nonequilibrium decay processes of thermodynamic parameters to thermal

fluctuations of these same parameters in an equilibrium system. So, the easily obtainable thermal fluctuations of the thermodynamic parameter

$$\delta A(t) = A(t) - \langle A(t) \rangle \tag{2.10}$$

can be used instead to determine the macroscopic decay of the parameter, since both become uncorrelated in a similar fashion over long periods of time

$$\frac{\langle \delta A(t) \delta A(0) \rangle}{\langle \delta A(0) \delta A(0) \rangle} = \frac{\langle A(t) A(0) \rangle}{\langle A(0) A(0) \rangle} \tag{2.11}$$

In the molecular dynamics simulations, the thermodynamic parameters are the microscopic positions and momenta of each particle in the *N*-body system, which are used to calculate the macroscopic heat (J_q), or momentum (P_{xy}) fluxes found in equations 2.1 and 2.3. After an equilibration of the system of 100,000 timesteps in the LAMMPS molecular dynamics [119], the microscopic positions and momenta were internally obtained every 4 fs. These were then used to calculate per-atom quantities of kinetic and potential energies, and the per-atom stress that are used to calculate the heat and momentum fluxes in equations 2.2 and 2.4. A sample LAMMPS code used to perform these calculations can be found in Appendix A.

The actual calculations of the thermophysical properties performed in this investigation did not include ensemble averaging, but rather were based on the assumption of ergodicity. This establishes that the ensemble average of a phase variable

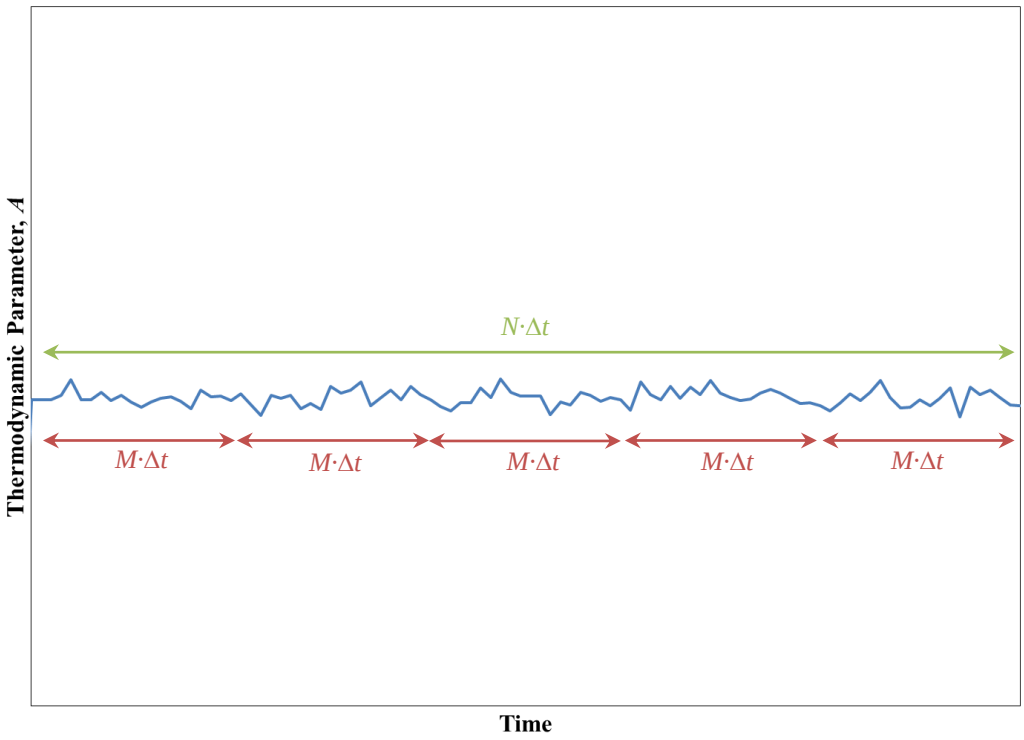

Figure 2.3 Visualization of integration steps, *M*, and the total number of steps, *N*, in a molecular dynamics simulations.

(in this case the calculated heat and momentum fluxes) is equivalent to the time average of the same phase variable

$$\langle A(t)A(0)\rangle = \lim \frac{1}{\tau}\int_0^{\tau} A(t+\tau)A(\tau)d\tau \tag{2.12}$$

The ergodic assumption now allows for direct calculation of the phenomenological coefficients over simulated time, during molecular dynamics simulations and now equation 2.9 can be rewritten into the form

$$L_{ik} = \frac{V\Delta t}{k_B T}\sum_{m=1}^{M}(M-n)^{-1}\sum_{n=1}^{N-m} J_i(m+n)J_i(n) \tag{2.13}$$

where *M* is the number of time steps for integration and *N* is the total number of time steps in the molecular dynamics simulation. A visualization of *M* and *N* relative to the

molecular dynamics results of thermodynamic parameter, $A(t)$, is shown in figure 2.3. The value M has to be long enough for the thermodynamic parameter to be completely uncorrelated and satisfy the conditions of ergodicity specified in equation 2.12. It was found through trial-and-error that the value of M did not need to be extremely large and a value of 1,000 was an adequate number of timesteps for $\langle A(t)A(0)\rangle$ to decay to zero. An additional specification of ergodicity includes ensuring that there is a large value of N so that there is a sufficient amount of M are present to adequately replicate an ensemble average of the system. The value of N chosen for a simulation run was 500,000 steps, which allowed for 500 autocorrelation calculations of the fluctuations in the thermodynamic parameter, $A(t)$, over M timesteps. Additionally, to increase phase space sampling to 4,000, each simulation run was performed eight times with varying starting parameters.

2.3 Colloid Interaction Model

Up until this point, all molecular dynamics simulations where nanofluids were modelled, the Lennard Jones potential is used to characterize nanoparticle-fluid interactions. A separate study (see Appendix B) showed that using the Lennard Jones potential provided highly inaccurate predictions for thermal conductivities in nanofluids at low concentrations. Therefore, application of a model developed by in t' Veld [120] is proposed for used to perform thermophysical calculations of nanofluids. A comparison between this colloid model and a corresponding Lennard Jones based model can also be found in Appendix B.

In the colloid model, the nanoparticle is described as a solid hard sphere that has a diameter larger than the fluid particles. The nanoparticle/fluid interactions are governed

by a variation of the Gay-Berne potential for two colloidal particles by letting one of the particle sizes go to zero [121] and is of the form

$$U = \frac{2a^3\sigma^3 A_{cs}}{9\left(a^2 - r^2\right)^3}\left[1 - \frac{\left(5a^6 + 45a^4r^2 + 63a^2r^4 + 15r^6\right)\sigma^6}{15\left(a - r\right)^6\left(a + r\right)^6}\right] \tag{2.14}$$

where σ is the size of the Lennard Jones solvent particle, a is the radius of the colloid particle, and A_{cs} is the Hamaker constant. For the simulations where there is more than one nanoparticle in the system, the colloid-colloid interactions are described by

$$U_A = -\frac{A_{CC}}{6}\left[\frac{2a^2}{r^2 - (2a)^2} + \frac{2a^2}{r^2} + \ln\left(\frac{r^2 - (2a)^2}{r^2}\right)\right] \tag{2.15}$$

$$U_R = \frac{A_{CC}}{37800}\frac{\sigma^6}{r}\cdot \left[\frac{r^2 - 14ar + 54a^2}{(r - 2a)^7} + \frac{r^2 + 14ar + 54a^2}{(r + 2a)^7} - \frac{r^2 - 30a^2}{r^7} + \frac{r^2 - 30a^2}{r^7}\right] \tag{2.16}$$

$$U = U_A + U_R \tag{2.17}$$

where a is the radius of the colloidal particle, σ is the size of the Lennard Jones solvent particle and A_{cc} is the value describing the interaction energy between constituent particles in the fluid known as the Hamaker constant. The Hamaker constants for the various nanoparticle-nanoparticle and nanoparticle-fluid interactions are provided in table 2.2 and were generated from using the equation [121]

$$A_{xx} = 4\pi^2\varepsilon_{LJ}\left(\rho\sigma^3\right)^2 \tag{2.18}$$

where the values for ε_{LJ} and σ were acquired from references found for copper [85] and platinum [122, 123]. A visualization of these interaction potentials for both copper-argon and platinum-argon potentials at different diameters can be seen in figures 2.4 and 2.5.

Table 2.2 Hamaker constants for interactions between the colloid and argon fluid.

N	A_{ArAr}	$A_{n,Ar}$	A_{nn}
Cu	34.2864	63.546	436.812
Pt	34.2864	18.8626	730.356

The interaction energy between the platinum nanoparticle and the fluid was approximately three times less than that of the copper nanoparticle/fluid interaction. The effects of this reduction on the calculated local density, thermal conductivity and shear viscosity will be discussed in subsequent chapters. Although not specifically investigated, the interaction energy between nanoparticles themselves also played a part on the calculations, especially for thermal conductivity and will be discussed in more detail in chapter 4.

In order to develop simulations that were similar to the experimental setups discussed in chapter 1, the diameters and the interaction energies ratios between the nanoparticle suspensions and the liquid argon atoms were calculated and compared to values found for common nanofluids. The results are presented in table 2.3. The values of the diameter (d_f) and mass (m_f) of the argon atom were selected to be 0.142 nm and 39.948 g/mol, respectively [124]. The interaction energy (ε_f) between the fluid argon atoms was calculated to be 34.2864 kcal/mol based on the depth of the potential well for the Lennard Jones potential (ε) for argon, which is valued at 0.2381 kcal/mol for the thermodynamic state selected [124]. The resulting ratios compare nicely with those calculated for common nanofluids, such as aluminum oxide/water [125] and copper oxide/water [126] (see table 2.4) and provided for the range of possible experimental conditions for which thermal conductivity and shear viscosity values would be obtained.

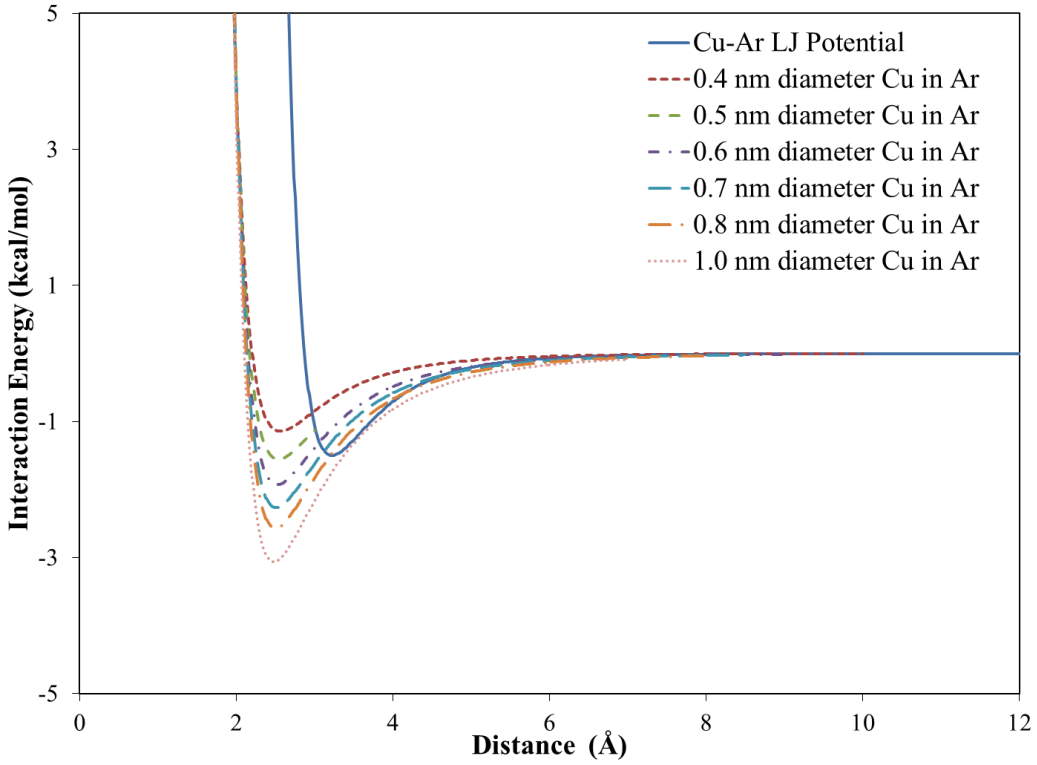

Figure 2.4 Interaction energies between varying diameter copper colloid suspensions and an argon fluid.

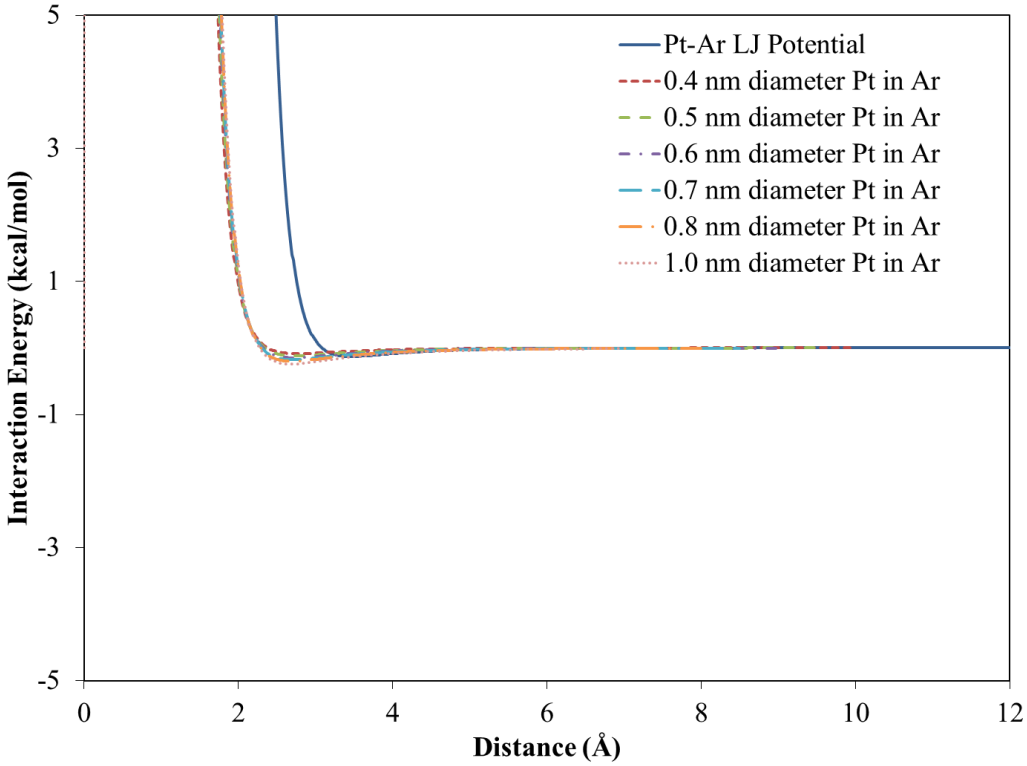

Figure 2.5 Interaction energies between varying diameter platinum colloid suspensions and an argon fluid.

Table 2.3 Colloid-nanoparticle comparison where $d_f = 0.142$, $m_f = 39.948$ g/mol and $\varepsilon_{f-f} = 34.2864$ kcal/mol.

Colloid Diameter (nm)	d_{np}/d_f	m_{np}/m_f		$\varepsilon_{np-f}/\varepsilon_{f-f}$	
		Copper	***Platinum***	***Copper***	***Platinum***
0.4	2.817	3.181	9.767	0.7639	0.6641
0.5	3.521	6.363	19.53	1.038	0.9172
0.6	4.225	7.954	24.42	1.288	1.152
0.7	4.930	9.544	29.30	1.512	1.364
0.8	5.634	15.91	48.83	1.710	1.555
1.0	7.042	34.99	107.4	2.042	1.877

Table 2.4 Nanofluid comparison to colloid-nanoparticle data in table 2.3.

Nanofluid	d_{np}/d_f	m_{np}/m_f	$\varepsilon_{np-f}/\varepsilon_{f-f}$
CuO (d=2 nm) /H_2O	3.636	110.498	$(H_2O)\leftrightarrow Cu(CuO)/O(H_2O)$ $\leftrightarrow O(H_2O)$: 65.270
Al_2O_3 (d=10 nm) /H_2O	36.36	69171.08	$O(H_2O)\leftrightarrow Al(Al_2O_3)/O(H_2O)$ $\leftrightarrow O(H_2O)$: 1.807 $H(H_2O)\leftrightarrow Al(Al_2O_3)/O(H_2O)$ $\leftrightarrow O(H_2O)$: 0.962

2.4 Summary

In order to develop an accurate representation of the nanofluid system, physical parameters needed to be defined. The thermodynamic properties that were chosen for argon allowed values to be easily compared and verified by experimental results. The parameters used in the molecular dynamics simulations performed in this analysis also required definitions that were based on the principles of nonequilibrium thermodynamics. It was through these definitions that the simulation and integration time used to determine the dynamic properties were obtained. Finally, the model used for describing the

nanoparticle and its interactions with the fluid allowed for analysis of the thermophysical properties to be obtained without the need for knowledge of its properties.

Chapter 3 – Distribution Functions and Local Density

As discussed in chapter 1, the density of nanofluids at the macroscopic level has been described as varying possibly either linearly [48, 49, 79] or nonlinearly [45] with increasing nanoparticle concentration. However, the effect on the local density due to the presence of nanoparticle suspensions at the nanoscale level has yet to be determined. While molecular dynamics simulations have already been used to suggest highly ordered liquid structure near the nanoparticle surface [71, 127], a potential energy formulation has been developed recently for molecular dynamics simulations which better describe nanoparticle-fluid interactions. In this chapter, a description of the local liquid structure is presented based on analyses using this recently developed interaction energy potential. First, the local density as a function of radial distance from the centrally located nanoparticle suspension is determined as a function of both volume fraction and nanoparticle diameter. Then, the radial fluctuations in the local density is both presented and compared among increasing diameter nanoparticles.

3.1 Radial Distribution Functions

In an ideal homogeneous fluid at a given thermodynamic state, the constituent particles are uniformly distributed throughout the entire system and each of their

positions relative to one another can be described mathematically by what is commonly referred to as the radial distribution function and is of the form

$$g^{(n)}(\mathbf{r}_1,\ldots,\mathbf{r}_N) = \frac{V^n N!}{N^n (N-n)!} \frac{\int \cdots \int e^{-\beta U_N} d\mathbf{r}_{n+1} \cdots d\mathbf{r}_N}{Z_N} \tag{3.1}$$

where Z_n is the configuration integral (average over all the relative locations of the particles in the system), $\beta = 1/k_b T$, and U_N is the total potential energy of the system of N particles in the volume V. From the radial distribution function described above, insight can be gained regarding the local fluid structure and density surrounding a given particle. For example, the local density of argon surrounding an arbitrary argon atom within the specified volume can be calculated using the radial distribution function in the form

$$\rho_{local} = \frac{1 + \int_0^{R_c} \rho g(r) 4\pi r^2 dr}{\frac{4}{3}\pi R_c^3} \tag{3.2}$$

With this information, the effect of the presence of the nanoparticle on the local density as a function of radial distance can be determined.

In a pure liquid argon fluid governed by Lennard Jones parameters (solid blue line in figures 3.1 and 3.3), the radial distribution function suggests that there are three shells of argon atoms that are influenced by the arbitrary central argon atom. At approximately r = 0.366 nm away from the center of the argon atom, the local density is calculated to be nearly three times higher than that of the bulk density, which at the 87.057 K specified in the molecular dynamics simulations performed in the investigation is approximately 1,423.8 kg/m^3 [128], corresponding to an average number density of 21.463 atoms/nm^3. This location of increased local density correlates to the location along the Lennard Jones potential found in figures 2.4 and 2.5 where the interaction energy is at its minimum

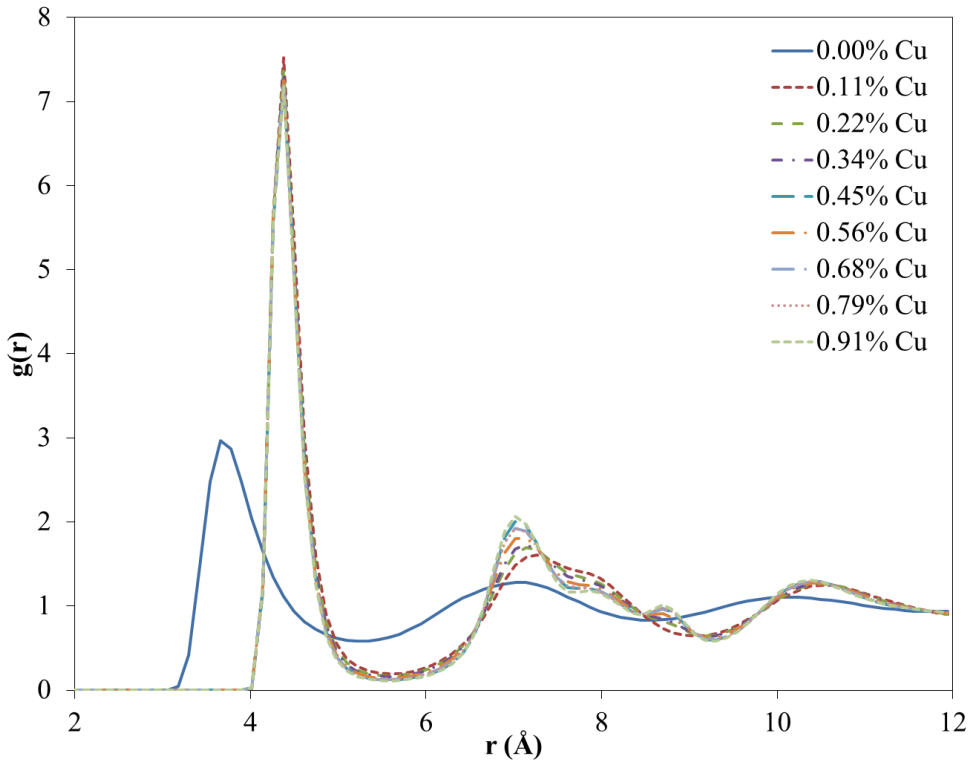

Figure 3.1 Radial distribution function for 0.4 nm copper nanoparticles suspended in argon at various concentrations.

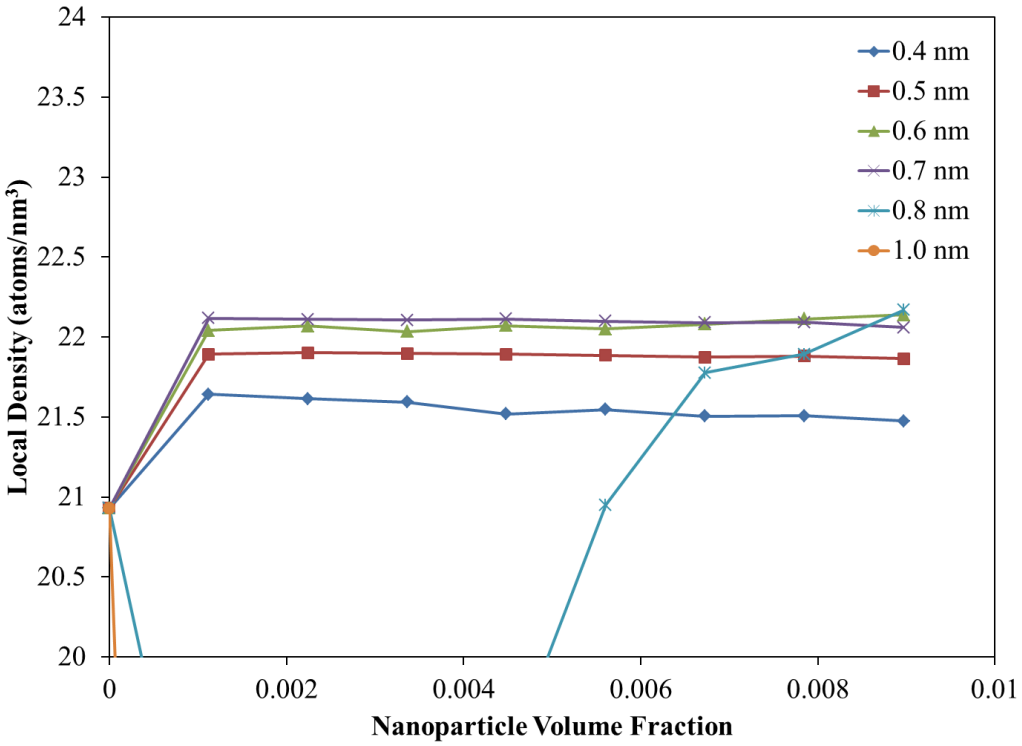

Figure 3.2 Local density of argon surrounding varying diameter copper nanoparticles at increasing volume fractions.

value. As $r \rightarrow \infty$ though, the local density decreases and approaches the bulk density value of the fluid.

When 0.4 nm diameter copper nanoparticles are suspended in the fluid (figures 3.1), there is a noticeable change in the radial distribution function that reflects its influence on the local structure and density of the surrounding argon. It can be seen that at approximately r = 0.438 nm away from the center of the 0.4 nm diameter copper nanoparticle, the local density is over seven times that of the bulk density of liquid argon. (See appendix C for radial distribution functions for 0.5 nm, 0.6 nm, and 0.7 nm diameter copper nanoparticles). While there generally is still three shells of argon atoms surrounding a 0.4 nm copper nanoparticle, the overall total density increases and remains generally constant over the volume fractions investigated here (figure 3.2). For volumes containing increasingly larger diameter copper nanoparticles, the local density is shown to increase by as much as 3.4% for 0.4 nm diameter copper nanoparticle and up to 5.7% with a 0.7 nm diameter nanoparticle. These increases in the local density that are a result of the increased interaction energy between the copper nanoparticle and the fluid is often referenced as the method for enhanced thermal energy transfer between the liquid and nanoparticle and thus the overall thermal conductivity of the nanofluid, although this is later disproven [71]. Another interesting observation that can be made is that the radial distribution function manifests a non-liquid, amorphous-like structure, and is comparable in form to the simulation results of Cui [129].

The radial distribution function for argon in the presence of a 0.4 nm diameter platinum nanoparticle presented in figure 3.3 did not reflect the same change in form as was seen for a 0.4 nm diameter copper nanoparticle. (See appendix C for the radial

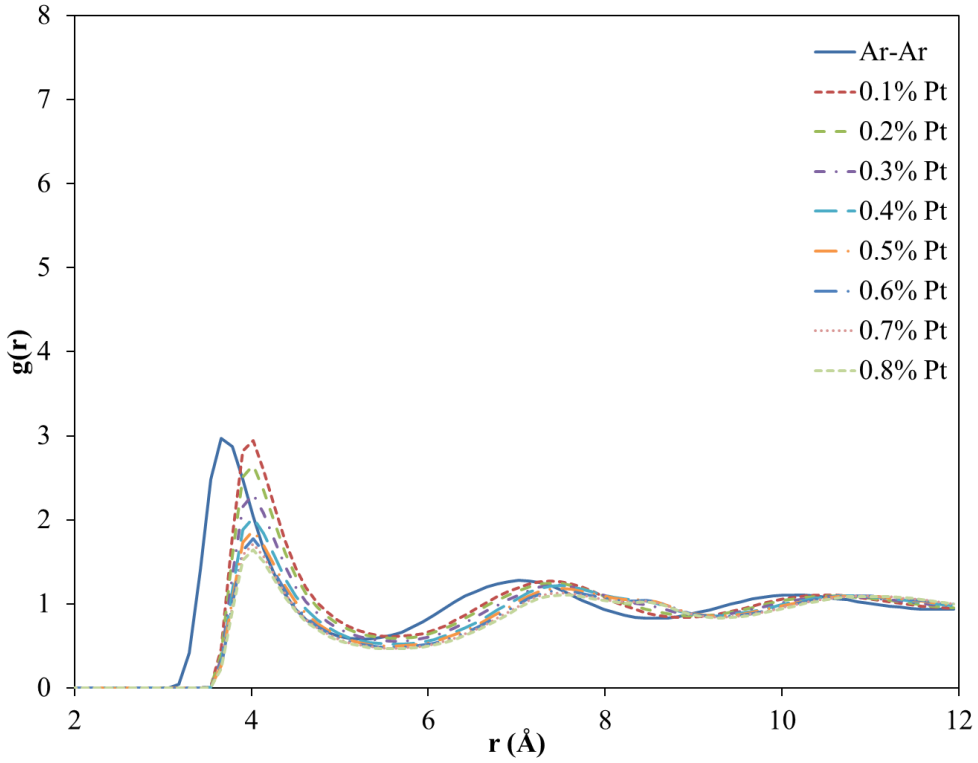

Figure 3.3 Radial distribution function for 0.4 nm platinum nanoparticles suspended in argon at various concentrations.

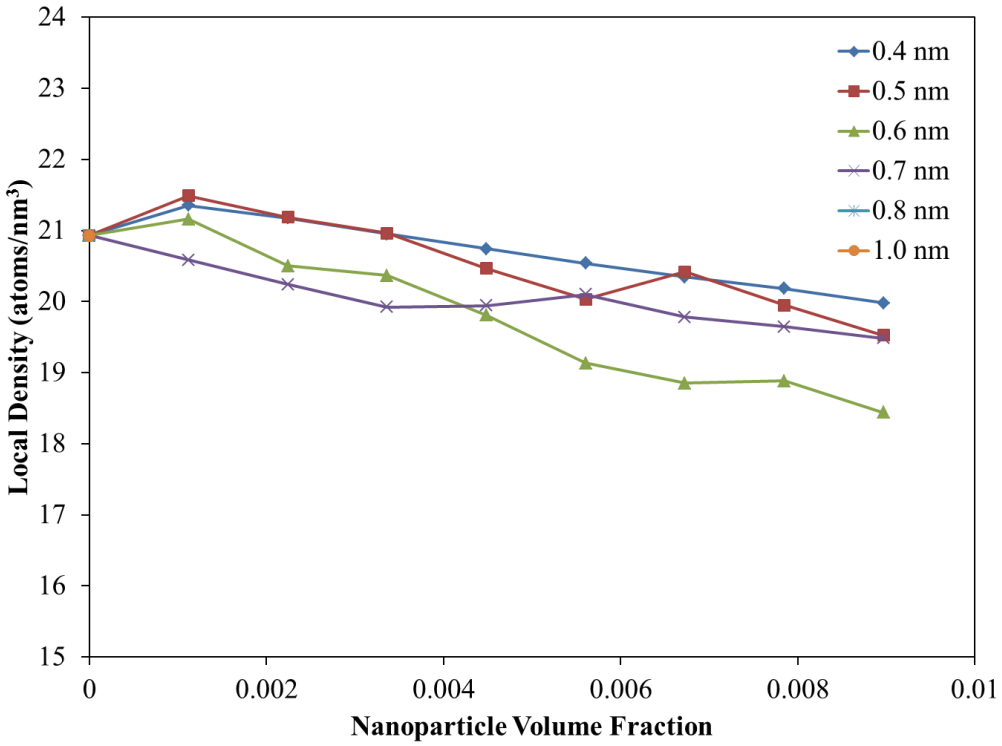

Figure 3.4 Local density of argon surrounding varying diameter platinum nanoparticles at increasing volume fractions.

distribution functions for 0.5 nm, 0.6 nm, and 0.7 nm diameter platinum nanoparticle diameters in argon). The maximum local density of argon at r = 0.402 nm of a 0.4 nm platinum nanoparticle is approximately three times higher than that of the bulk density of the liquid, which is similar to the increase seen if the central particle was an argon atom. In fact, the radial distribution function did not deviate at all from the form that is normally associated with a pure argon fluid. Another interesting observation that could be made about platinum nanoparticles in argon is that increasing volume fractions decreased local density (figure 3.4). This phenomenon appears to be the result of the decreased interaction energy between the platinum and argon when compared to the Lennard Jones potential (see figure 2.7); thereby making the platinum nanoparticles serve as non-interacting spacers within the fluid. Since the interaction between the platinum and liquid argon decreased with nanoparticle diameter, the liquid-liquid interactions became the dominant physical mechanism in the fluid, drawing liquid away from near the surface of the nanoparticle. This could explain the decrease in the overall local density with increasing volume fractions for increasing platinum nanoparticle diameters (0.5 nm, 0.6 nm, and 0.7 nm). There also does not appear to be a correlation between nanoparticle diameter and the local density as there was for a copper nanoparticle.

3.2 Local Density Fluctuations

In addition to the local static structure of the argon liquid in the presence of copper and platinum nanoparticles, information regarding the dynamic behavior of the local fluid structure is equally as important, especially when investigating the transport processes within a fluid and their relaxation mechanisms. In order to quantify this local dynamic behavior in the surrounding fluid of a nanoparticle, a principal component

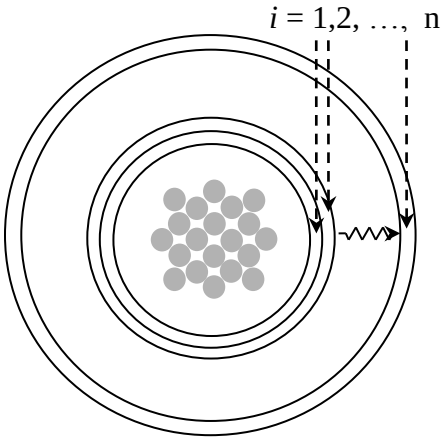

Figure 3.5 Surrounding fluid separated into *n* spherical concentric layers.

analysis technique that has been adapted by D'Abramo [130] to characterize local liquid density is used. In this analysis, the fluid surrounding the nanoparticle is separated into *n* spherical concentric layers (figure 3.5) where their respective densities are described by distribution functions presented in the previous section. The time-averaged density in each layer surrounding the respective nanoparticle is shown in figure 3.6 – 3.13. Although these graphs appear to be similar in form to the radial distribution functions of the previous section, the values obtained here represent densities of equal volumes and not equal bin sizes. These figures still do reflect the same general behavior as the radial distribution functions, where densities increased near the nanoparticle surface for copper and decreasing for platinum.

To determine how the local density at each layer fluctuates relative to the time-averaged local density, a local density covariance matrix, $\tilde{C}$, is formed by

$$\tilde{C} = \left\langle \left(\rho - \langle \rho \rangle\right)\left(\rho - \langle \rho \rangle\right)^{T} \right\rangle \tag{3.3}$$

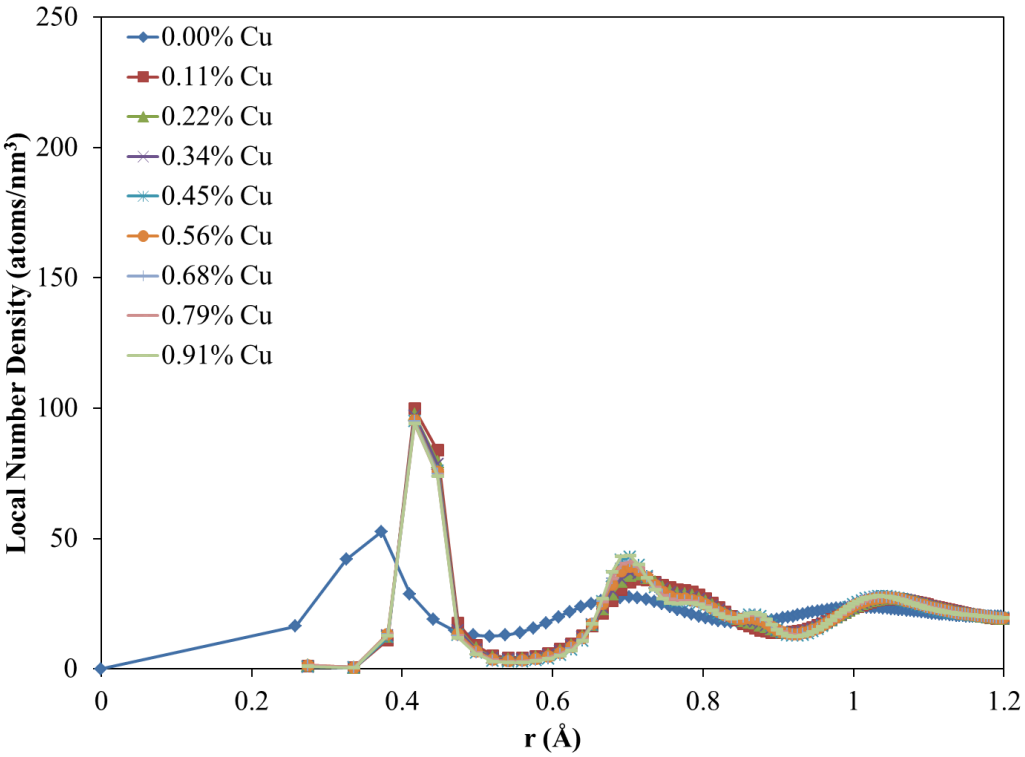

Figure 3.6 Average density pattern in the argon fluid due to the presence of a centrally located 0.4 nm diameter copper nanoparticle.

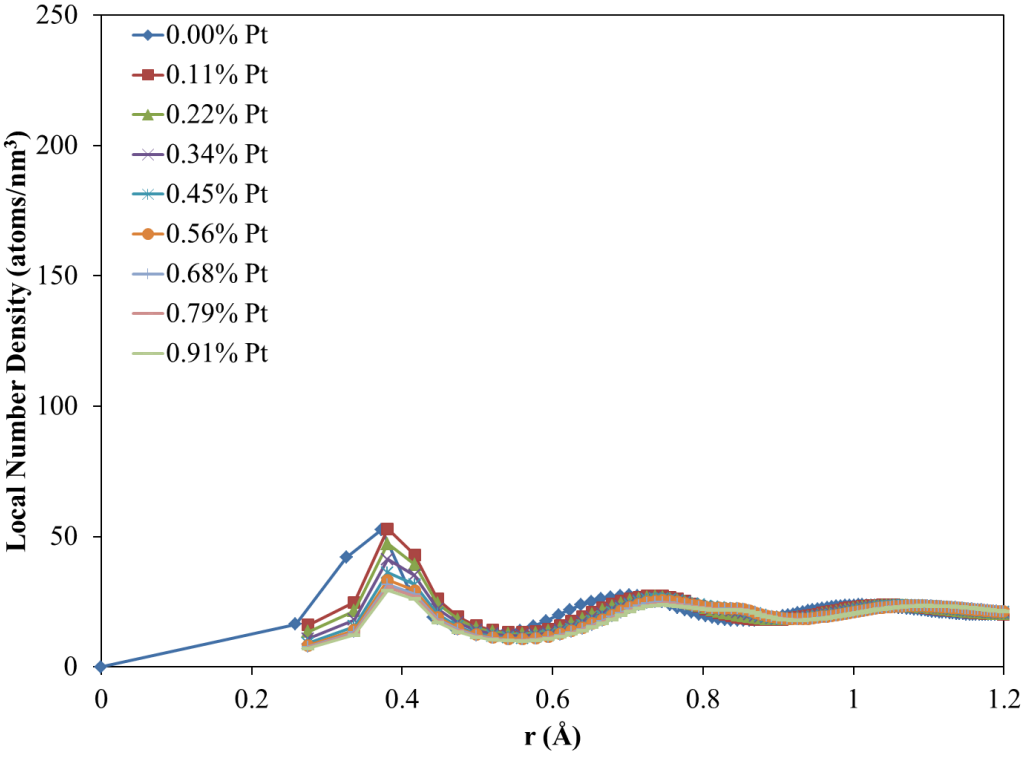

Figure 3.7 Average density pattern in the argon fluid due to the presence of a centrally located 0.4 nm diameter platinum nanoparticle.

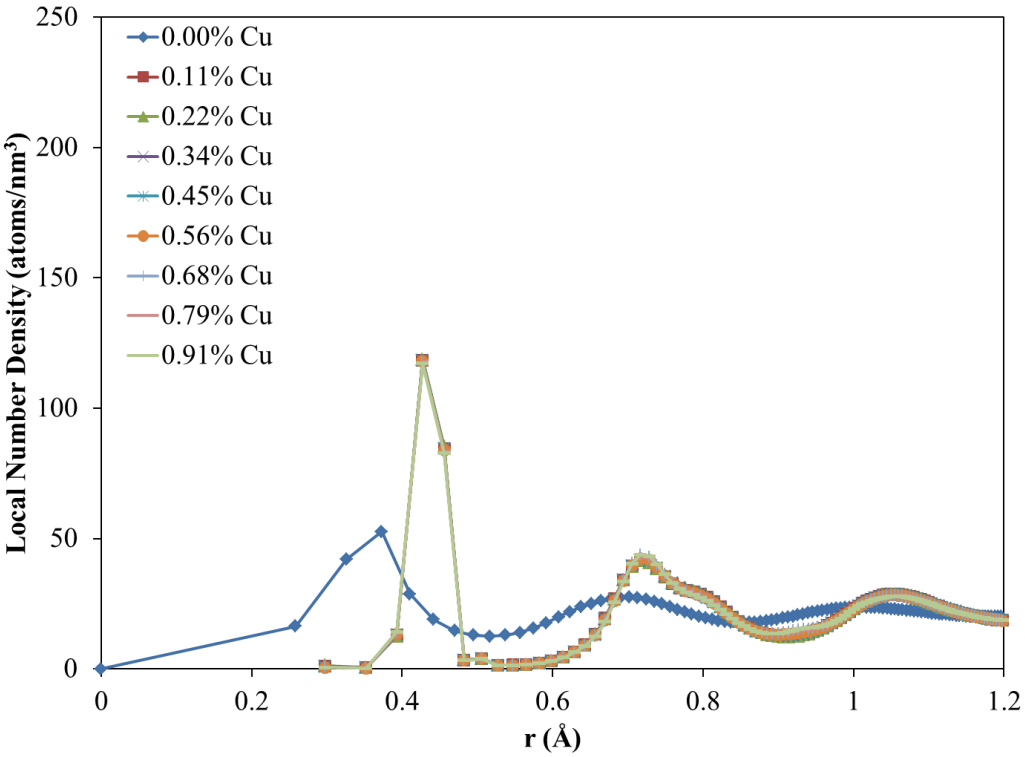

Figure 3.8 Average density pattern in the argon fluid due to the presence of a centrally located 0.5 nm diameter copper nanoparticle.

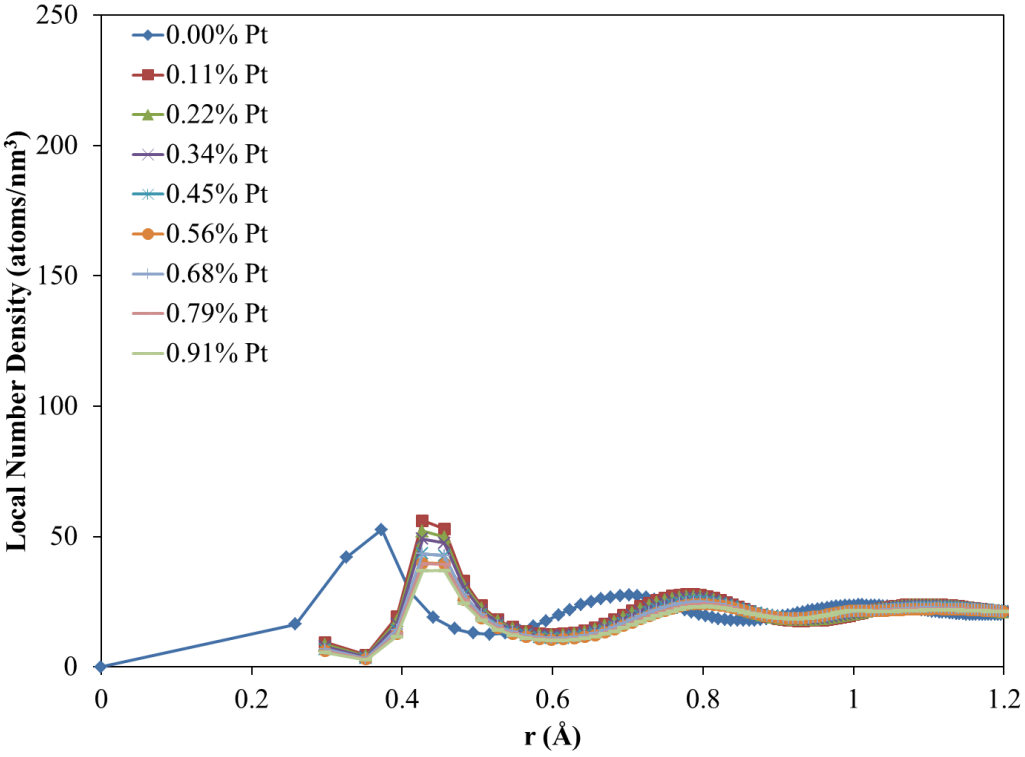

Figure 3.9 Average density pattern in the argon fluid due to the presence of a centrally located 0.5 nm diameter platinum nanoparticle.

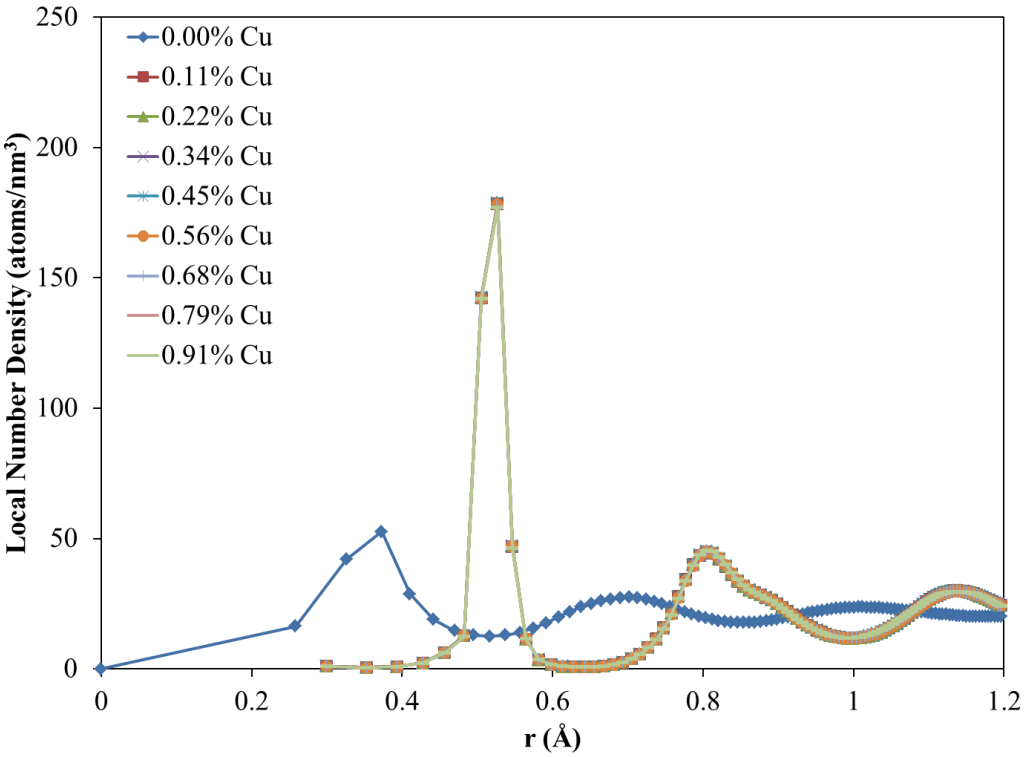

Figure 3.10 Average density pattern in the argon fluid due to the presence of a centrally located 0.6 nm diameter copper nanoparticle.

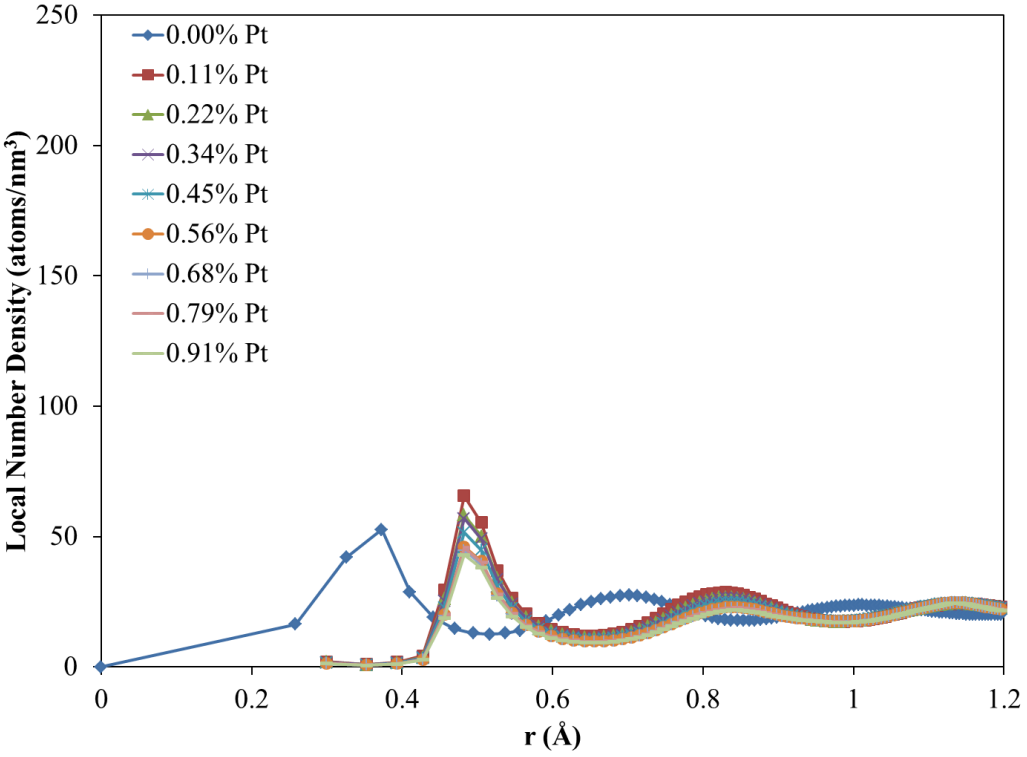

Figure 3.11 Average density pattern in the argon fluid due to the presence of a centrally located 0.6 nm diameter platinum nanoparticle.

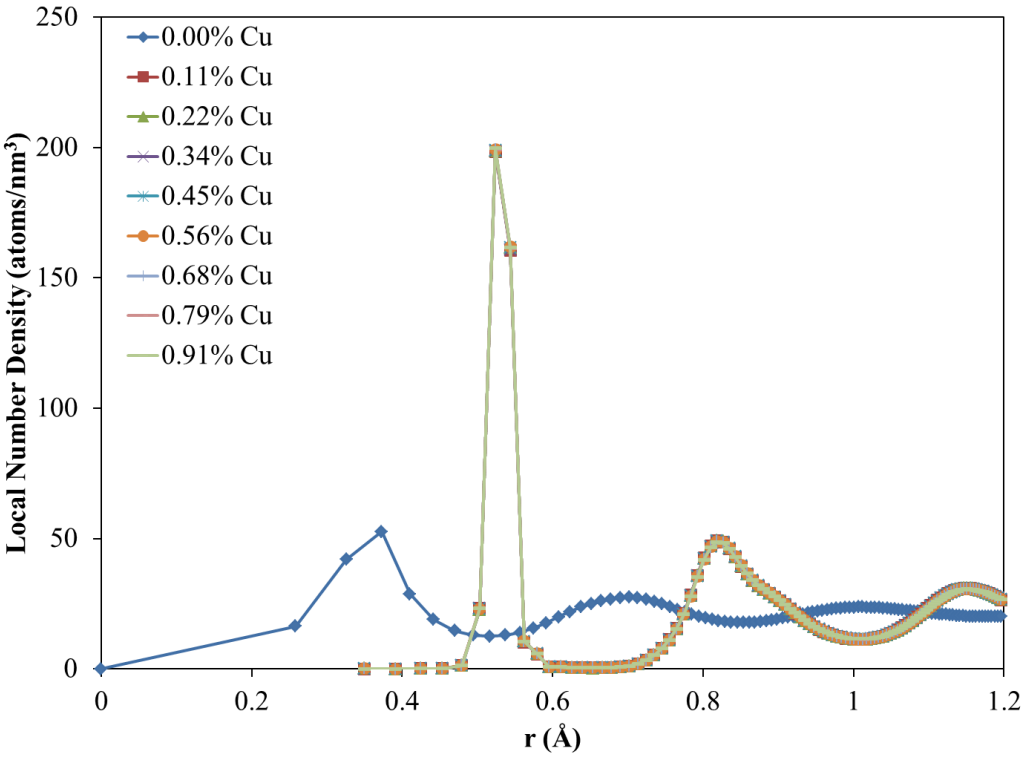

Figure 3.12 Average density pattern in the argon fluid due to the presence of a centrally located 0.7 nm diameter copper nanoparticle.

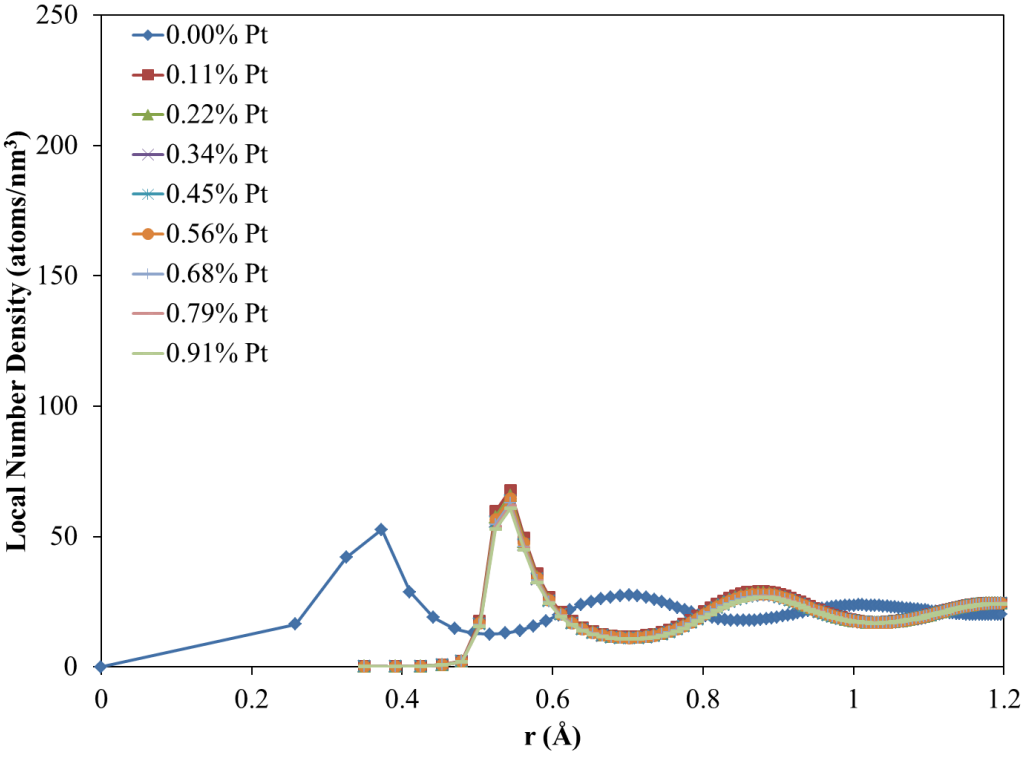

Figure 3.13 Average density pattern in the argon fluid due to the presence of a centrally located 0.7 nm diameter platinum nanoparticle.

This symmetric matrix, $\tilde{C}$ is an $m \times n$ matrix of m observations of n volume slices surrounding the nanoparticle describing the radial density distribution within the system, and $\langle\ \rangle$ denotes time average. Next, the rotational matrix $\tilde{O}$ composed of the eigenvectors of $\tilde{C}$ is found such that it transforms into the diagonal matrix of eigenvalues

$$\tilde{O}^T \tilde{C} \tilde{O} = \tilde{\Lambda} \tag{3.4}$$

These eigenvectors in $\tilde{O}$ are the principal components of $\tilde{C}$ and have been shown to describe the structural configuration in multidimensional space that maximize/minimize fluctuations in density. In general, the highest concentrations of fluctuations occur in the first three eigenvectors of $\tilde{O}$, which may account for as much as 95% of the variation. Using these eigenvectors, the configuration of density within the system can then be reconstructed to visualize these variations. The calculations used to determine this eigenvectors and eigenvalues were performed using Matlab. (See Appendix B for Matlab code).

The eigenvalues of the local density covariance matrix characterize the fluctuation frequency of the local fluid surrounding the nanoparticle having a structure of the form of the corresponding eigenvector. As is discussed by D'Abramo, similar eigenvalues implies that there are many correlated density fluxes of similar amplitude and free energy variation [130]. As can be seen in figures 3.14-3.21, there were very few correlated density fluxes near the nanoparticle, which indicates high fluctuations in the local density of the nanoparticle. Li, et al. arrived at a similar conclusion by determining that the width of the distribution of densities of liquid at a distance r away from the nanoparticle surface decreased with increasing r [131].

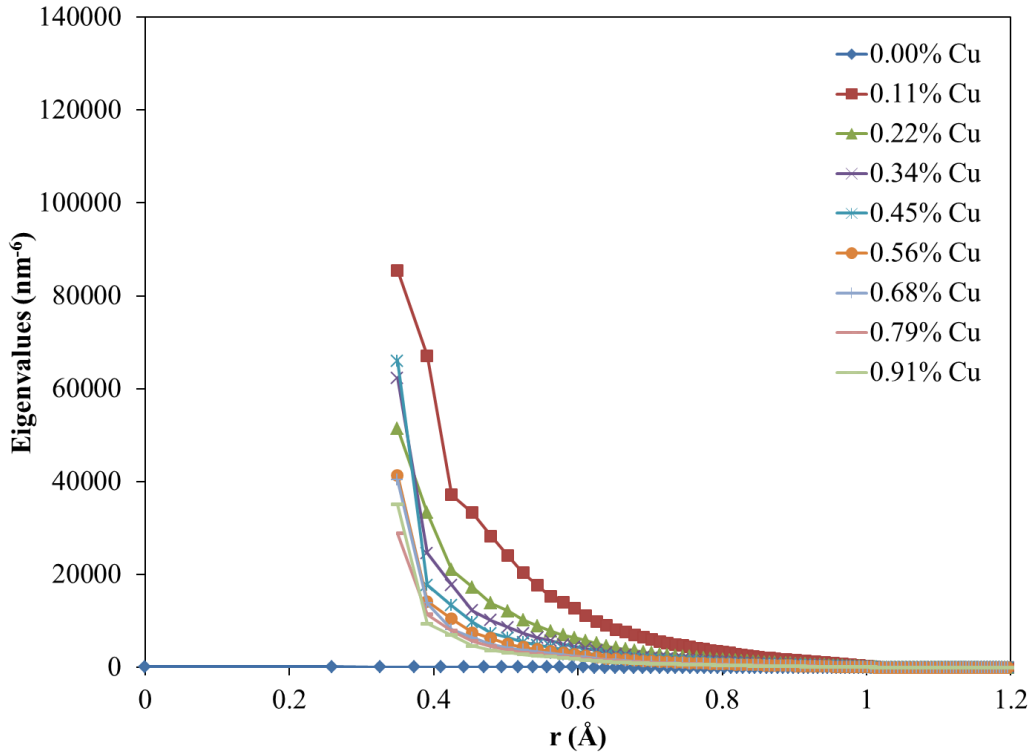

Figure 3.14 Eigenvalues of the local density correlation matrix for fluid surrounding a copper nanoparticle of diameter 0.4 nm.

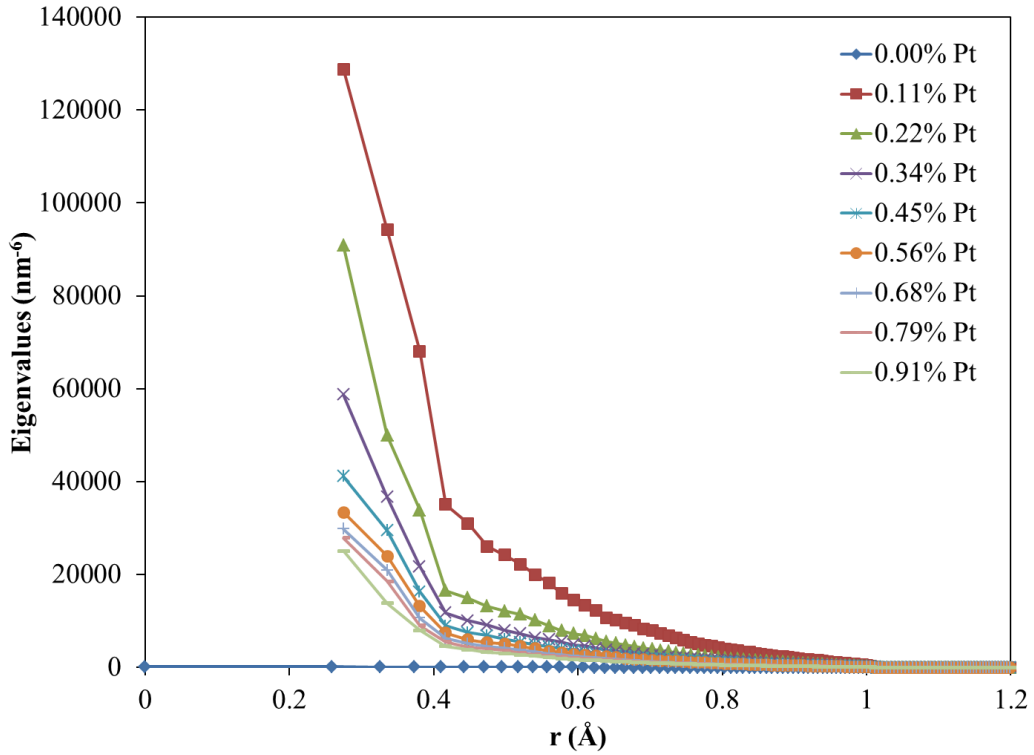

Figure 3.15 Eigenvalues of the local density correlation matrix for fluid surrounding a platinum nanoparticle of diameter 0.4 nm.

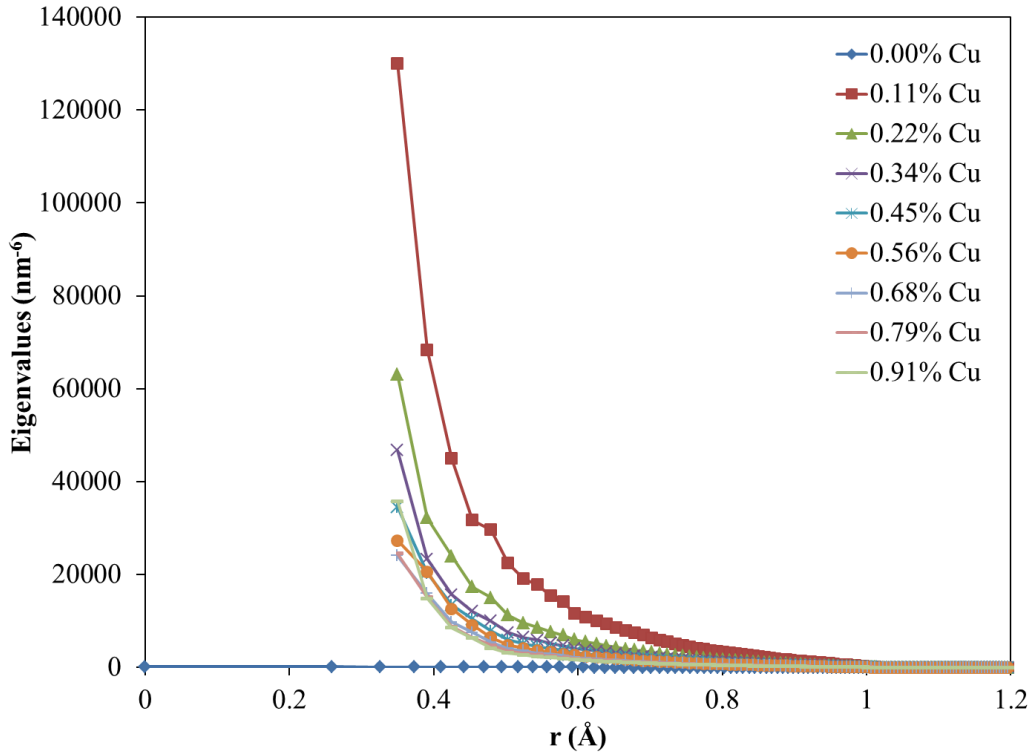

Figure 3.16 Eigenvalues of the local density correlation matrix for fluid surrounding a copper nanoparticle of diameter 0.5 nm.

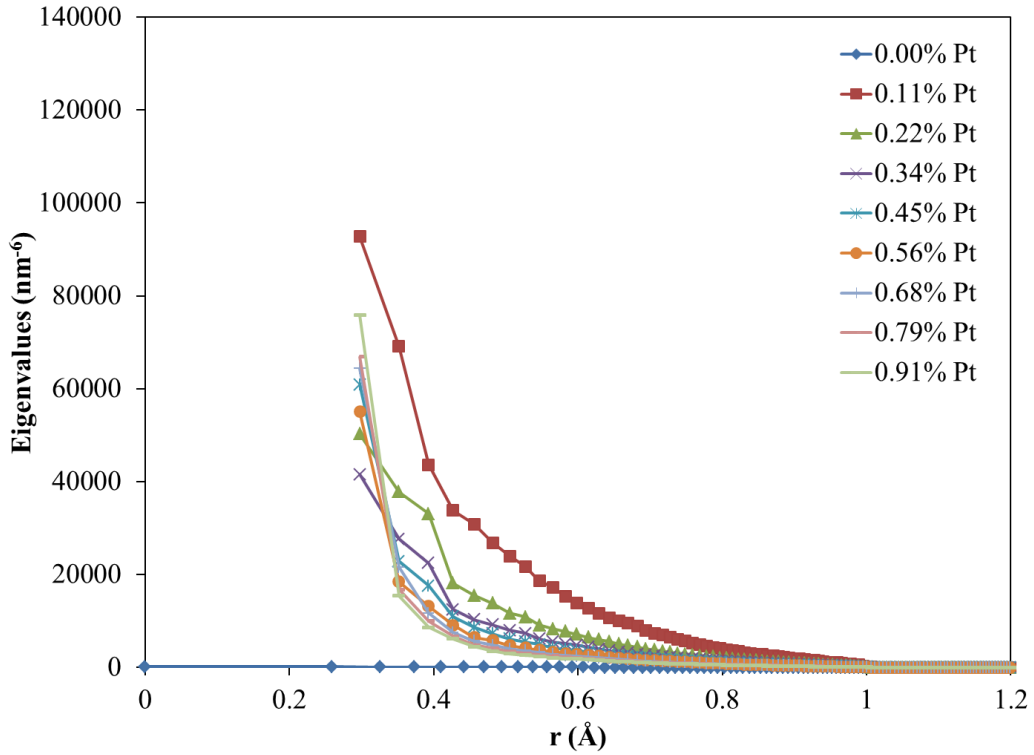

Figure 3.17 Eigenvalues of the local density correlation matrix for fluid surrounding a platinum nanoparticle of diameter 0.5 nm.

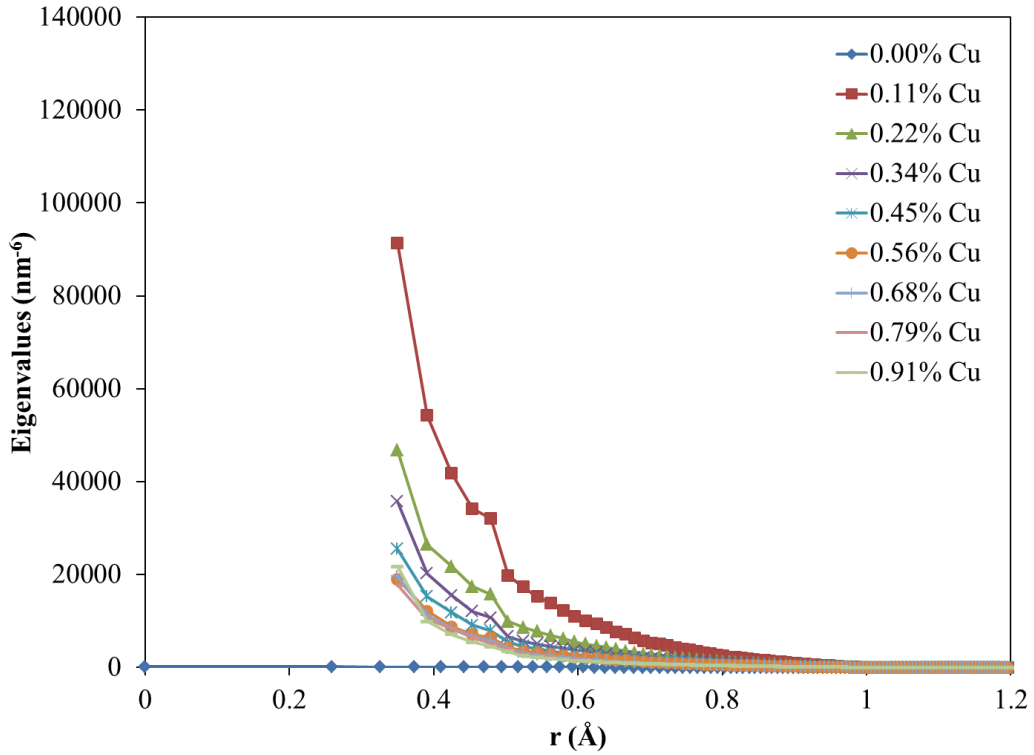

Figure 3.18 Eigenvalues of the local density correlation matrix for fluid surrounding a copper nanoparticle of diameter 0.6 nm.

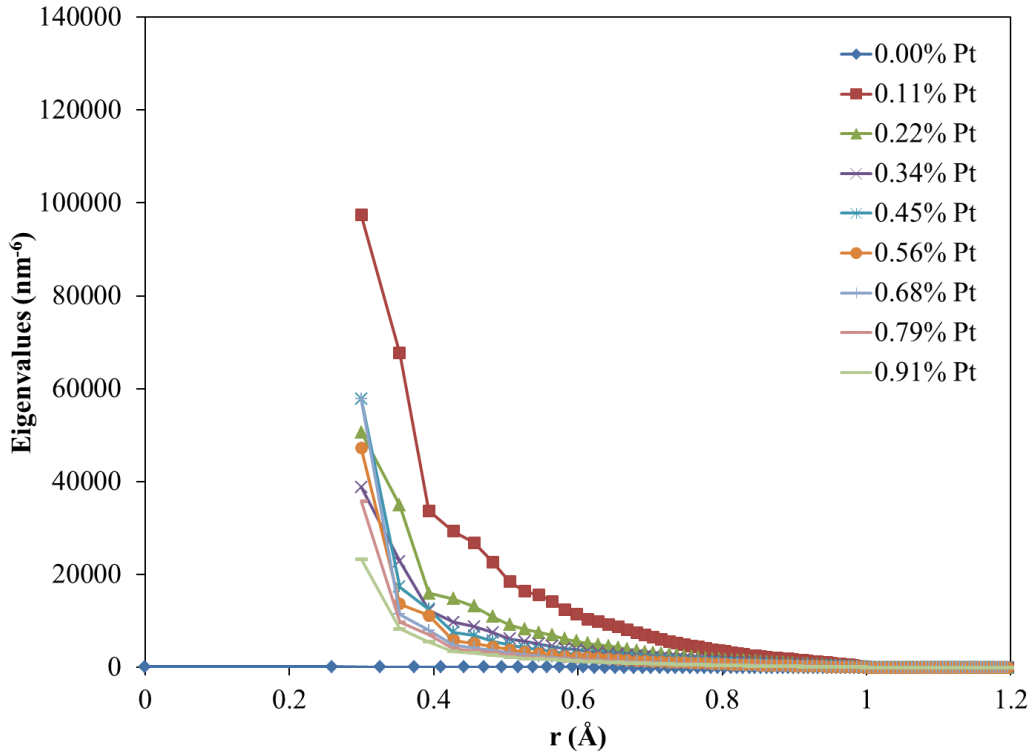

Figure 3.19 Eigenvalues of the local density correlation matrix for fluid surrounding a platinum nanoparticle of diameter 0.6 nm.

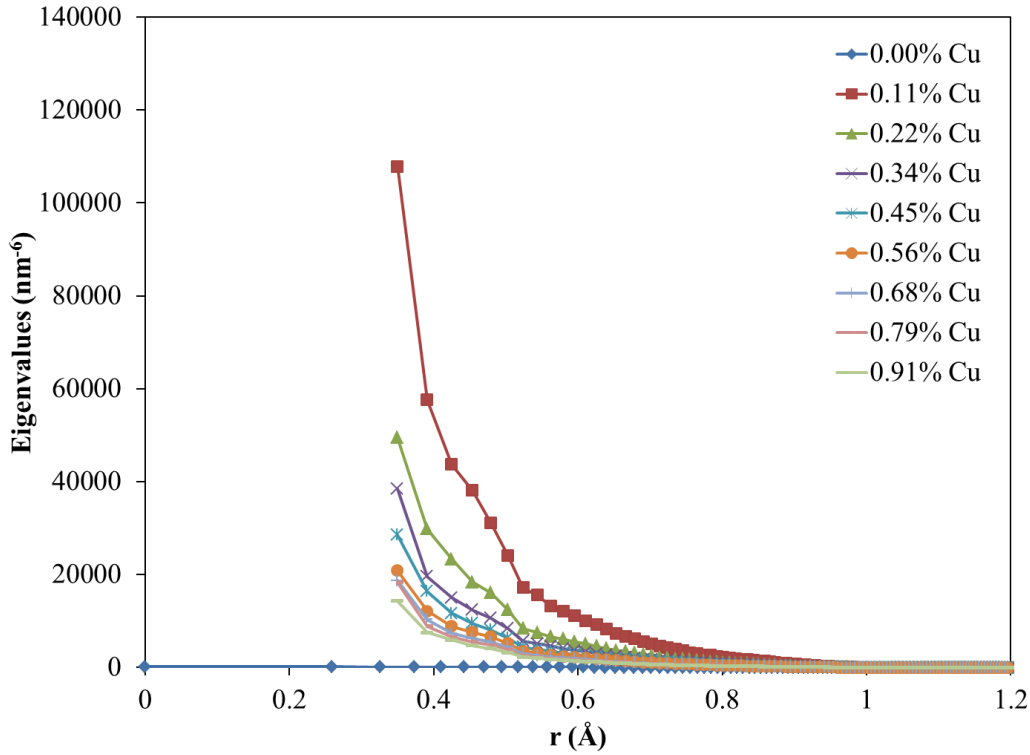

Figure 3.20 Eigenvalues of the local density correlation matrix for fluid surrounding a copper nanoparticle of diameter 0.7 nm.

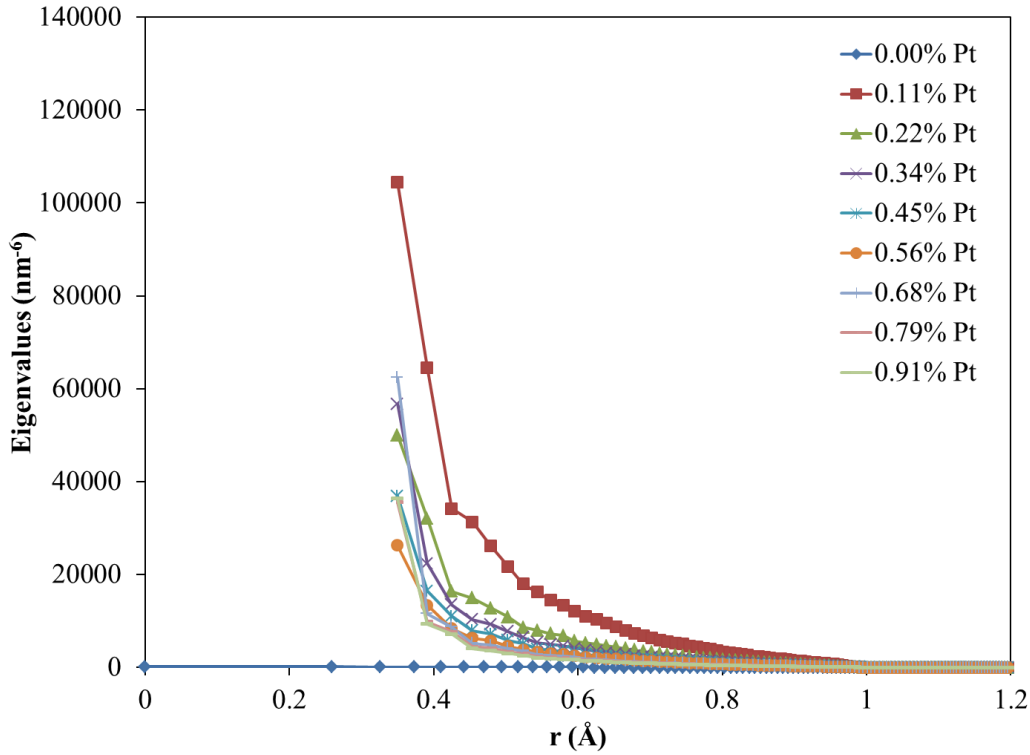

Figure 3.21 Eigenvalues of the local density correlation matrix for fluid surrounding a platinum nanoparticle of diameter 0.7 nm.

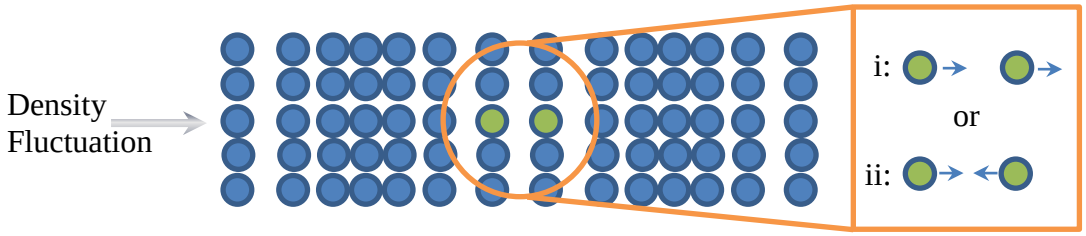

Figure 3.22 Longitudinal acoustic mode for density fluctuations in a simple fluid.

3.3 Physical Mechanisms of Local Density Dissipation

Due to the thermal fluctuations occurring in a fluid at equilibrium (figure 2.2), the system undergoes a constant process of relaxation through a set of possible dissipation modes [132]. In this section, a discussion of the dissipation mode associated with density fluctuations will be performed. In chapters 4 and 5, the remaining dissipation modes associated with thermal and momentum transport will be discussed.

The process by which density fluctuations of the constituent particles within the control volume of a fluid become uncorrelated involves the combination of fluctuation decay without propagation characterized by the thermal diffusivity and fluctuation propagation at the speed of sound of long-wavelength longitudinal acoustic waves (see figure 3.22) that decays through thermal conduction and viscosity through the medium [133]. These modes of fluctuation decay are determined from the Fourier-Laplace transformation of the conservation laws for the local densities used to develop equations 2.1 – 2.4. The solution of the resulting hydrodynamic matrix yields a set of three coupled solutions (one imaginary and two complex roots) that correspond to the each of the decay modes.

In a homogeneous Lennard-Jones fluid, the hydrodynamic collective mode for the decay of density fluctuations was determined to be without propagation and associated with the diffusion of thermal energy in the system [134]. An analysis of the eigenvalues

of the local density covariance matrix indicates that this is also the dissipation mode within a nanofluid due to the lack of correlated density fluxes over the volume surrounding the nanoparticle. A Fourier transform of the density autocorrelation function should be performed though to verify these results.

3.4 Summary

Through use of the colloid potential, a size dependent radial distribution function was obtained that provided insight into the local density characteristics of the surrounding fluid. With this information, it was seen that there was an increasing local density of liquid argon near the copper nanoparticle surface and that the overall density of the system remained constant at increasing nanoparticle volume fraction. This was in direct contrast to the local density of liquid argon near the surface of platinum nanoparticles, which had decreasing local density with increasing nanoparticle volume fraction. This counterintuitive result can be explained with the weak interactions between the nanoparticle and the fluid. Since the overall fluid density has to remains constant for the system to remain at equilibrium, the liquid at a distance beyond the influence of the nanoparticle will increase in density.

In addition, the local density fluxes near the nanoparticle surface quickly became uncorrelated over the short distance 2-3 atom diameters. This decay in the density flux corresponds to the short-range diffusion characteristics of simple fluids and indicates that fluid density characteristics are not significantly different from that of a homogeneous fluid.

Chapter 4 – Thermal Conductivity and Physical Mechanisms of Thermal Transport

By using molecular dynamics simulations, several works have demonstrated that by increasing the concentration of nanoparticle suspensions there is a corresponding increase in the thermal conductivity of the base fluid that can also be modeled using basic theoretical models. However, there has not been a systematic study on the effects of nanoparticle size and interaction energy between the suspension and the fluid on this enhancement. Also, affected by these parameters are the mechanisms of thermal energy transport within the nanofluid. In this chapter, the results of molecular dynamics simulations will be used to address both topics and draw conclusions regarding their effects.

4.1 Verification of Equilibrium Molecular Dynamics Method

As was described in chapter 2, the concept of acquiring transport coefficients from a system at thermodynamic equilibrium requires thermal fluctuations of the constituent particles to be uncorrelated over a specified period. Therefore, it was first important to verify that the heat current autocorrelation function in the Green-Kubo relations for the thermal conductivity of copper/argon and platinum/argon nanofluids decay to zero over the M =1,000 integration steps specified in chapter 2. As can be seen in figures 4.1–4.8, over the designated $M\Delta t$ = 4 ps integration period, all heat current autocorrelation functions for each nanoparticle type varying in diameter do decay to zero, which validates further calculations discussed in this chapter based on this data.

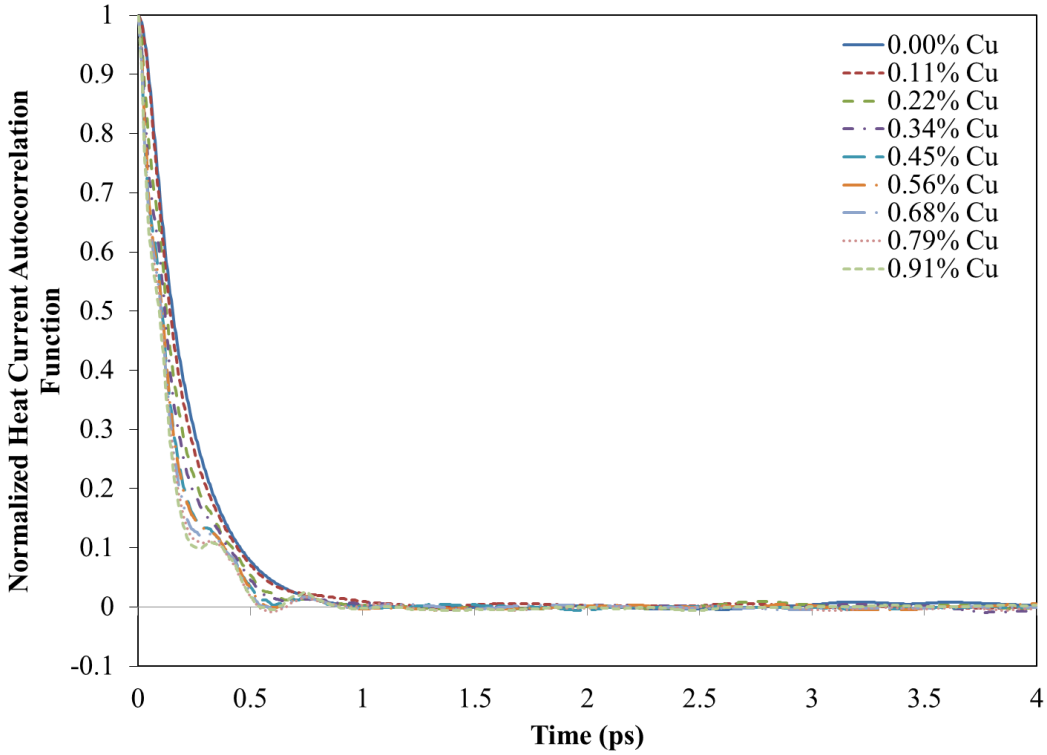

Figure 4.1 Normalized heat current autocorrelation function for 0.4 nm diameter copper in argon.

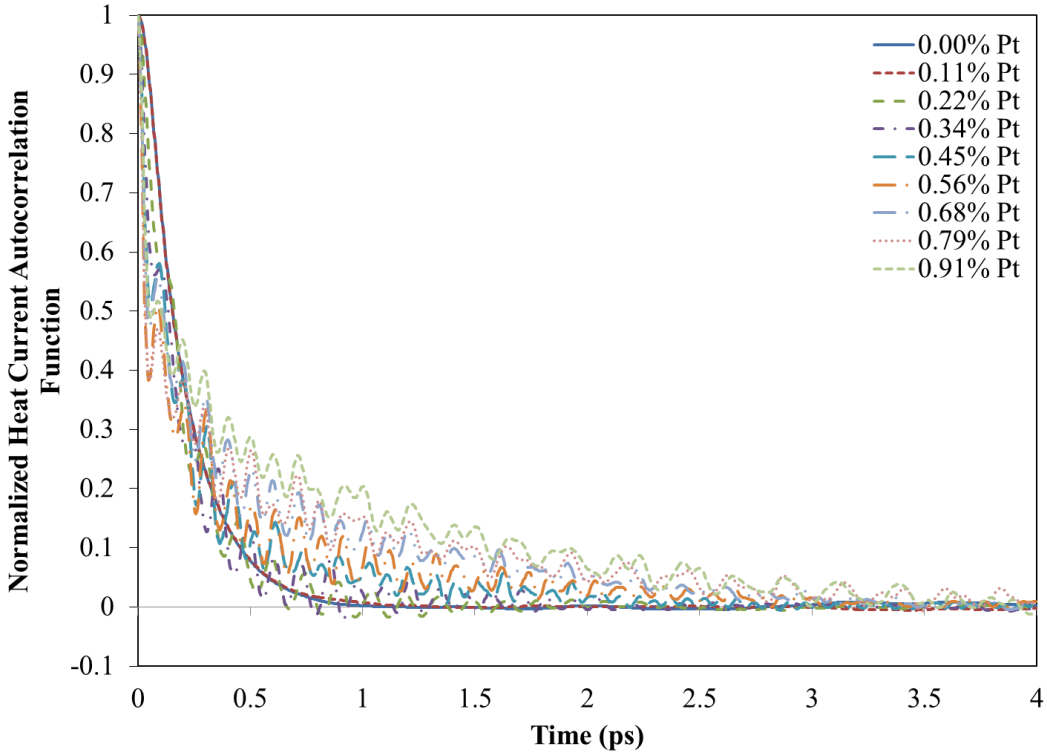

Figure 4.2 Normalized heat current autocorrelation function for 0.4 nm diameter platinum in argon.

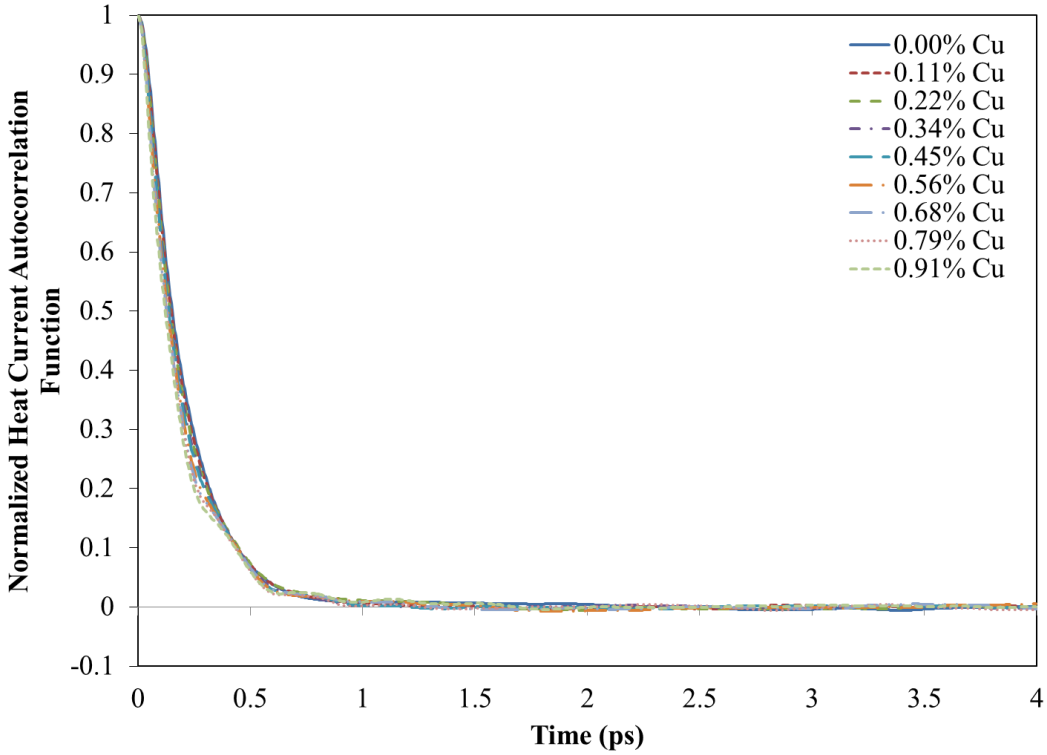

Figure 4.3 Normalized heat current autocorrelation function for 0.5 nm diameter copper in argon.

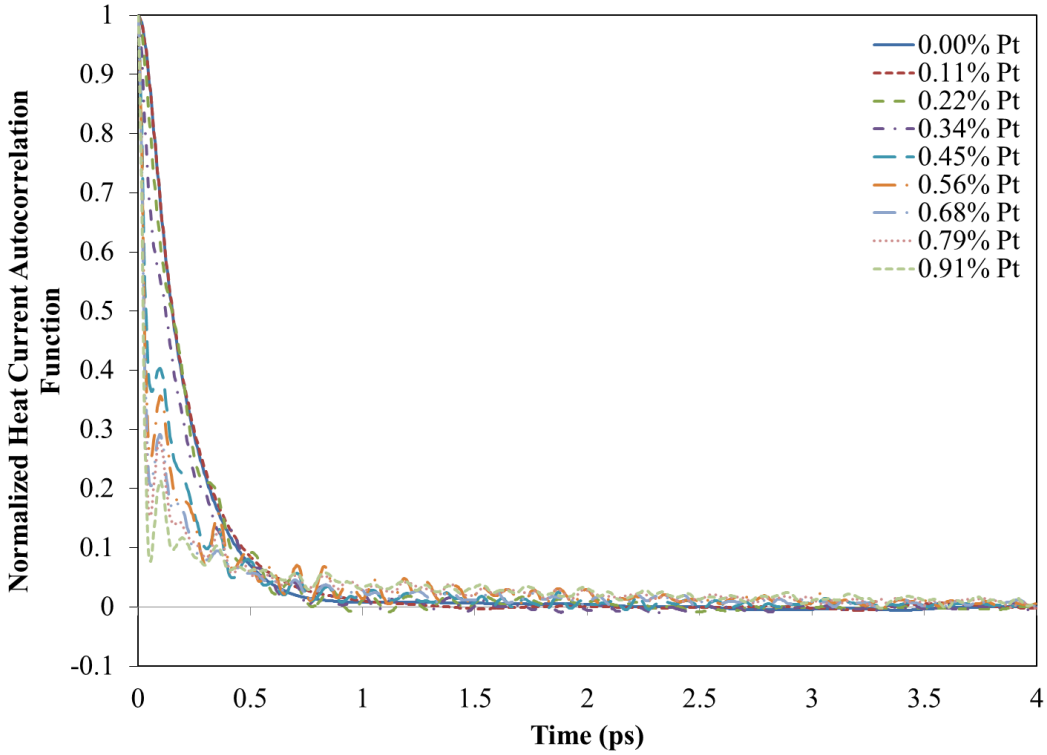

Figure 4.4 Normalized heat current autocorrelation function for 0.5 nm diameter platinum in argon.

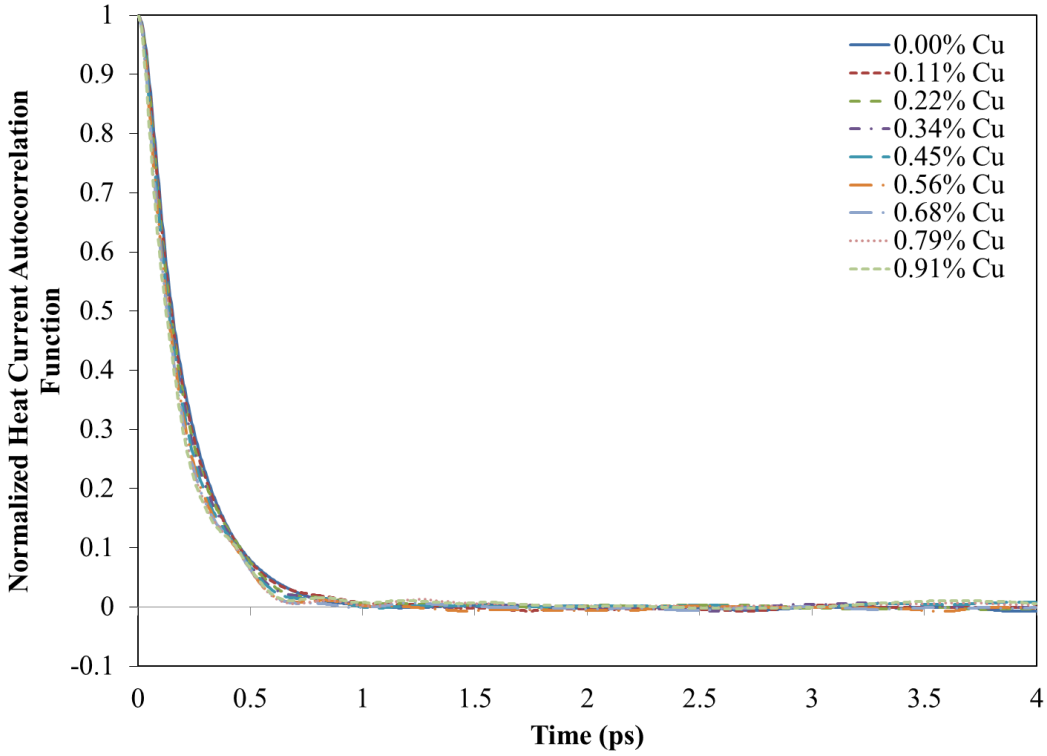

Figure 4.5 Normalized heat current autocorrelation function for 0.6 nm diameter copper in argon.

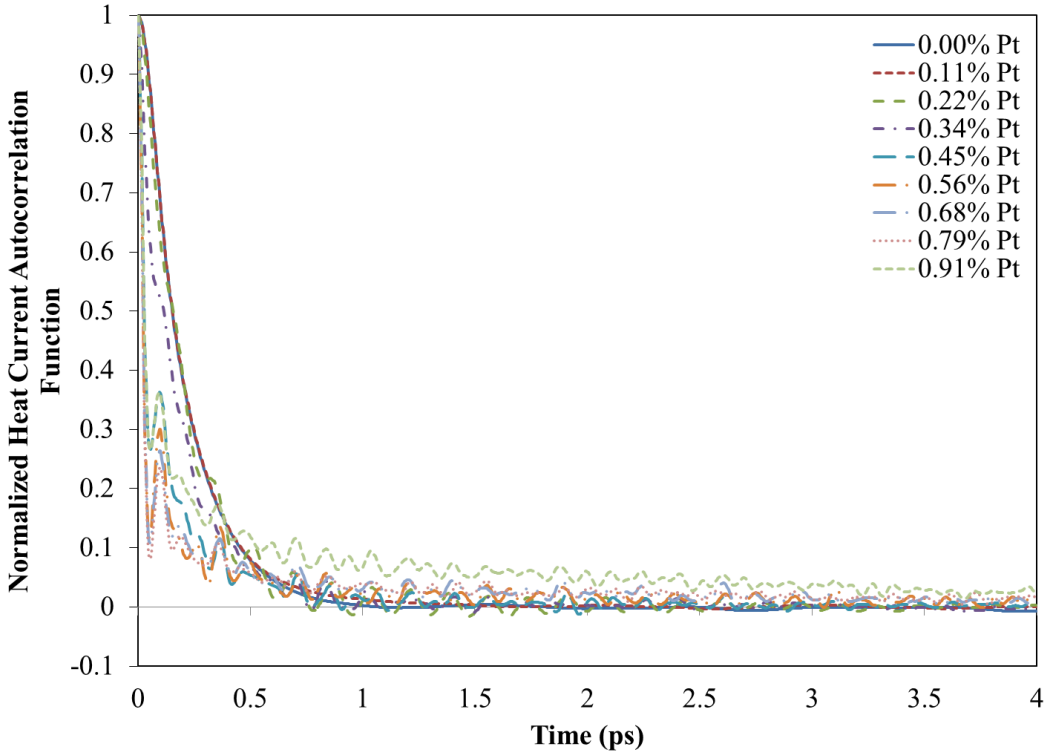

Figure 4.6 Normalized heat current autocorrelation function for 0.6 nm diameter platinum in argon.

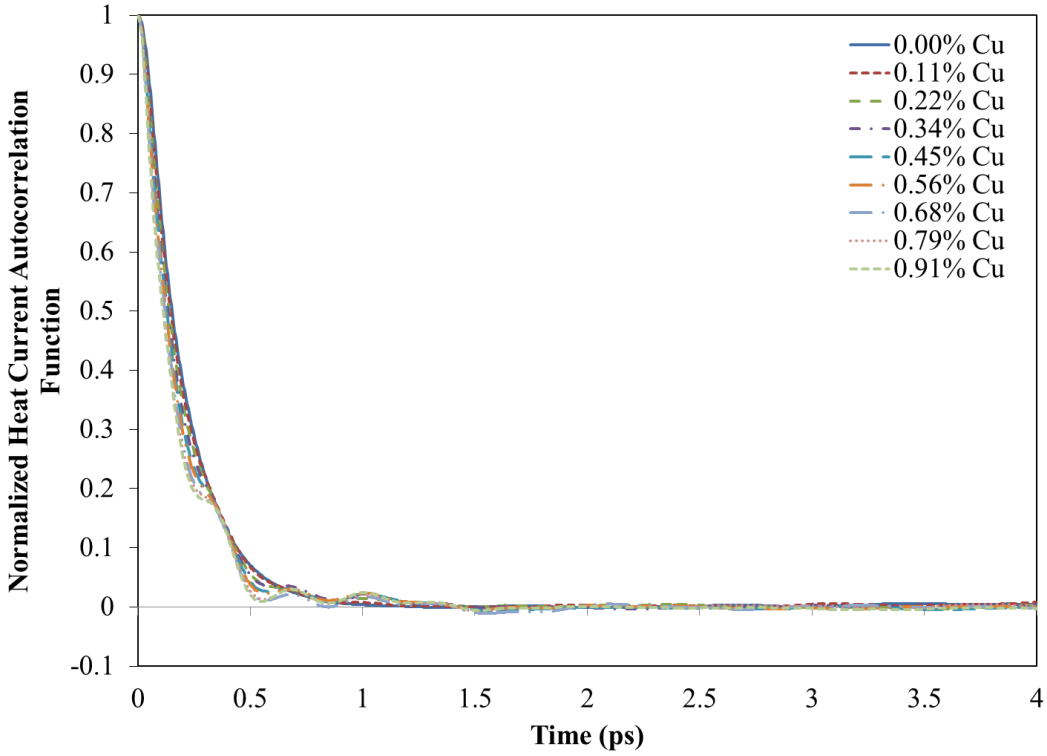

Figure 4.7 Normalized heat current autocorrelation function for 0.7 nm diameter copper in argon.

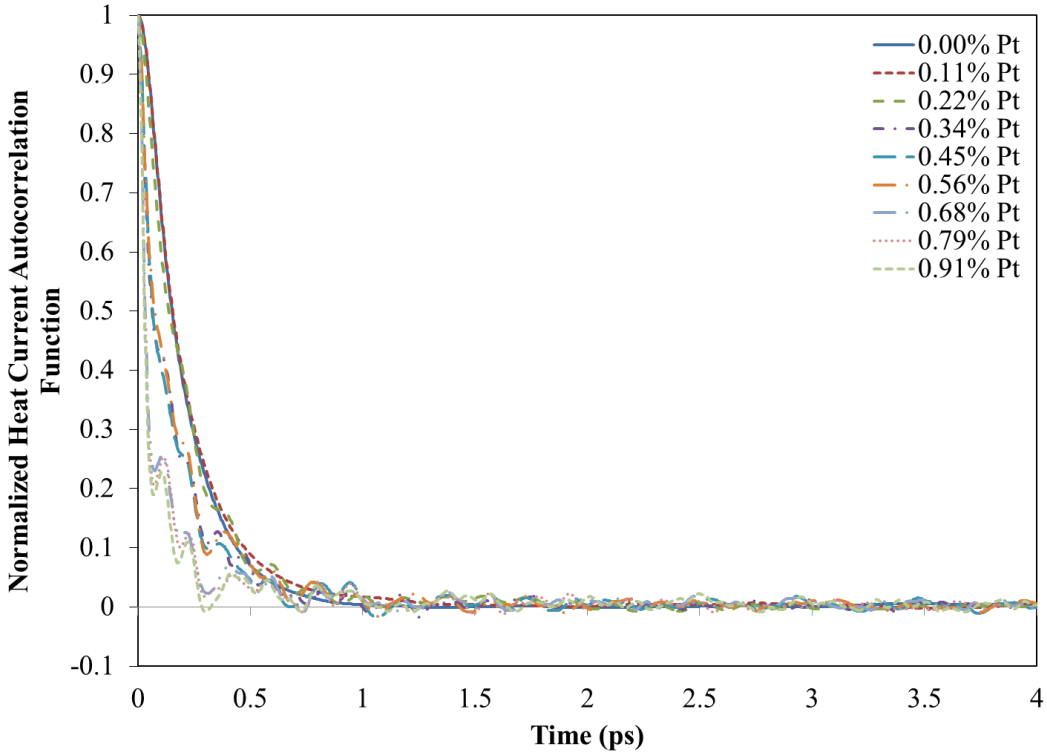

Figure 4.8 Normalized heat current autocorrelation function for 0.7 nm diameter platinum in argon.

An interesting observation can be noted regarding the decay of the heat current autocorrelation functions for the each of the nanofluids compared to the pure homogeneous argon fluid. In a homogeneous material, like pure argon, a normal heat current autocorrelation function will decay monotonically, meaning that over the time interval $t > 0$, the function preserves order and the value of $f(b) > f(a)$ for $b > a$. Within this monotonically decreasing function of pure argon fluid, it is suggested that there are two regions of decay: 1) a region of rapid decay at the beginning of the function which is due to purely atomistic interactions, and 2) a subsequent larger region of slower decay that results from phonon energy transfer [135].

However, the insertion of either platinum or copper nanoparticles changes the decay into a non-monotonic form and in some cases displays an oscillatory behavior. The effect that appears to be more prominent in the platinum/argon nanofluid has been normally associated with the "caging" that is seen in molecular dynamics simulations of water [136-138]. A further investigation of the physical mechanisms of thermal energy discussed in section 4.3 will shed more light on this topic.

4.2 Size and Interaction Energy Effects on Thermal Conductivity

In order to capture the size and interaction energy effects of the nanoparticle on the thermal conductivity of the overall nanofluid, molecular dynamics simulations utilizing the colloid model described in chapter 2 were used with the parameters found in tables 2.1 and 2.2. Keeping in mind that the volume changed with increasing nanoparticle diameter, the thermal conductivity of pure argon for each volume was first calculated and analyzed to ensure consistency. The average value for the volumes corresponding to nanoparticle diameters ranging from 0.4 nm to 1.0 nm was found to be

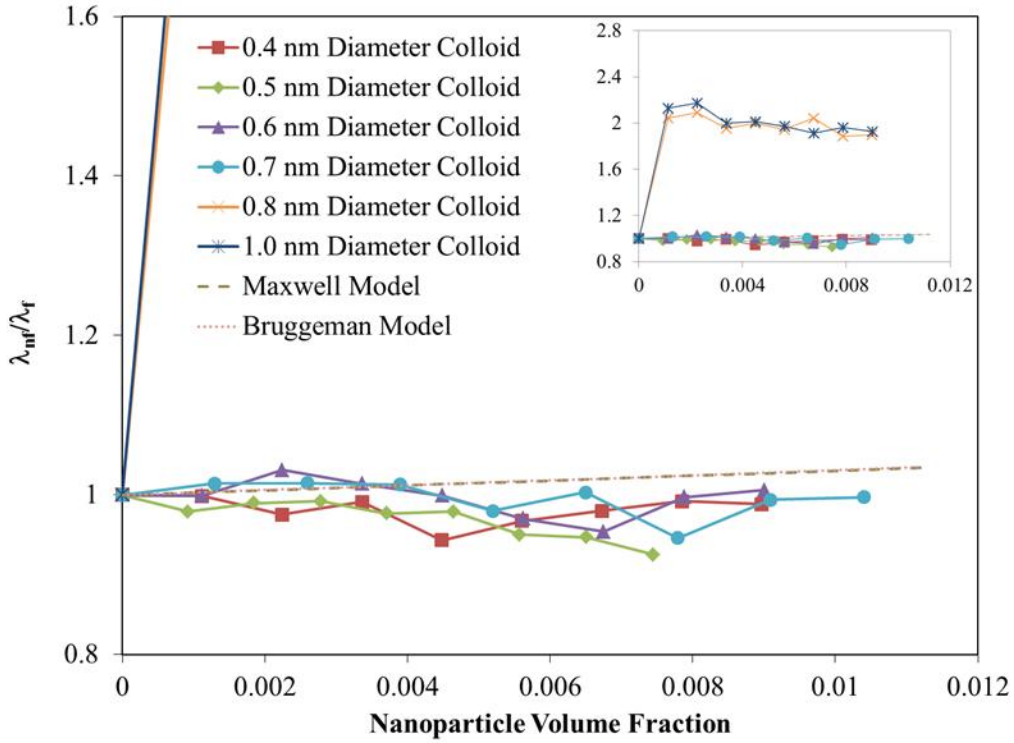

Figure 4.9 Thermal conductivity enhancement of argon fluid with increasing copper nanoparticle diameter compared to theoretical models.

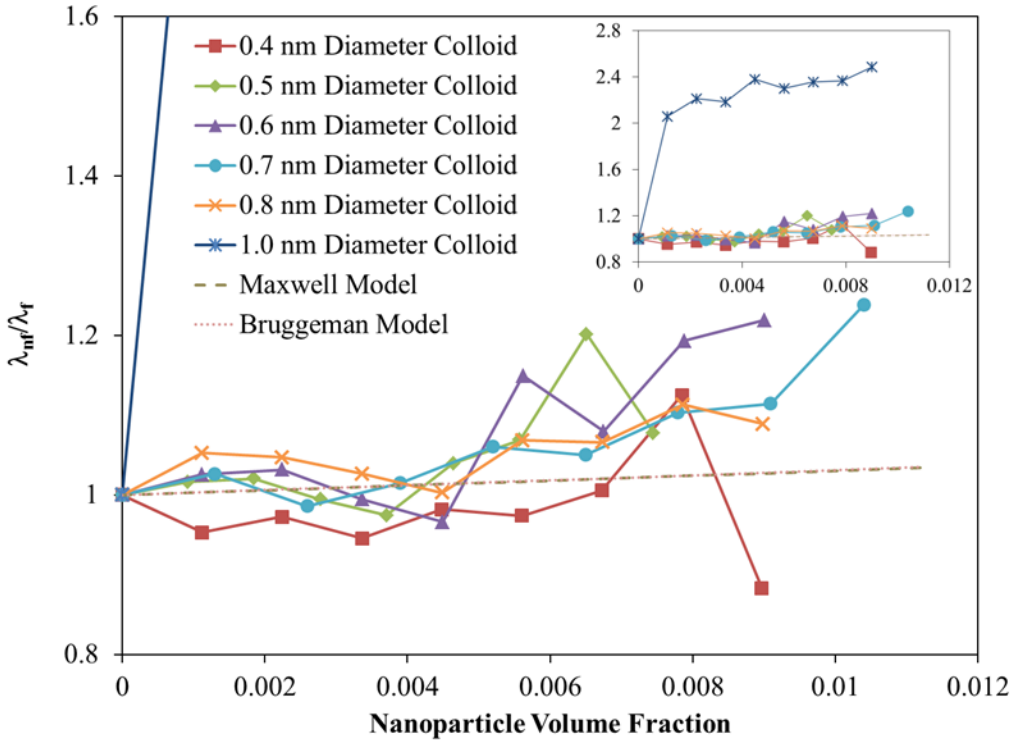

Figure 4.10 Thermal conductivity enhancement of argon fluid with increasing platinum nanoparticle diameter compared to theoretical models.

0.1297±0.001897 W/m·K, which is consistent with the value of 0.13326 W/m·K provided by the National Institute of Standards and Technology [128].

Next, a quick overview of figure 4.9 shows that as the copper nanoparticle diameter increased, the thermal conductivity of the overall nanofluid did not increase over the volume fractions investigated and were below the theoretical approximations of thermal conductivity enhancements predicted by Maxwell and Bruggeman. In contrast with this result, increasing the diameter of a platinum nanoparticle (figure 4.10) did affect thermal conductivity enhancement over the volume fractions investigated and demonstrated similar behavior to the theoretical predictions of Maxwell and Bruggeman. From an analysis of the results from figures 4.9 and 4.10, it can be concluded that the sole factor of nanoparticle size does not directly affect thermal conductivity increases seen in previous studies.

A few comments will now be made about the thermal conductivity values of the nanofluids that contained copper nanoparticles of 0.8 nm and 1.0 nm diameters and the platinum nanoparticles of 1.0 nm diameter. For a pure substance, the maximum thermal conductivity value would normally occur when the substance is in its solid-state crystalline form, where phonon (and in the case of metals, electron) transfer dominate heat conductance. In the case of fcc crystalline argon near the triple point, the thermal conductivity has been shown both experimentally [139] and through molecular dynamics simulations [140-142] to be between 1.5 and 1.7 times higher than that of liquid argon at a similar thermodynamic state. Therefore, the thermal conductivity enhancements of greater than 1.9 seen for the copper and platinum nanofluids described at the outset should not be attainable. These unrealistic results can be explained by the colloid

potential used in these molecular dynamics simulations, which determines the interaction energy of the nanoparticle with the fluid from an integration of the interatomic potentials between each of the uniformly distributed set of atoms within the nanoparticle to the fluid. As the nanoparticle diameter increases, the minimized interaction between atoms at the center and opposite end of the nanoparticle and the fluid continues to factor into the calculation for interaction energy. This results in Lennard Jones well depth values greater than 1.5 times that of the corresponding purely interatomic potential well depth between platinum/copper and argon. Therefore, like the corresponding liquid particles near the nanoparticle surface, only the first few sublayers of the constituent nanoparticle atoms should contribute to the calculation of interaction energy of the overall nanoparticle with the fluid.

An analysis of the effect that the nanoparticle/fluid interaction energy has on thermal conductivity calculations for fluids with nanoparticle suspensions of the same diameter is shown in figures 4.11-4.14. As the nanoparticle/fluid-to-fluid/fluid interaction energy ratio increased for the same sized nanoparticle suspended in fluid, the correlation between nanoparticle volume fraction and thermal conductivity enhancement was lost and failed to follow the behavior of the theoretical model predictions of Maxwell and Bruggeman. Although higher interaction energies correspond to larger local fluid densities surrounding the nanoparticle (as is discussed in section 3.1) and would suggest a more effective thermal energy transport within this interfacial region, the results obtained here show that interaction energies have minimal to negative effect on the enhancement of thermal conductivity of the base fluid. These results support the findings of the works of Xue [71] and

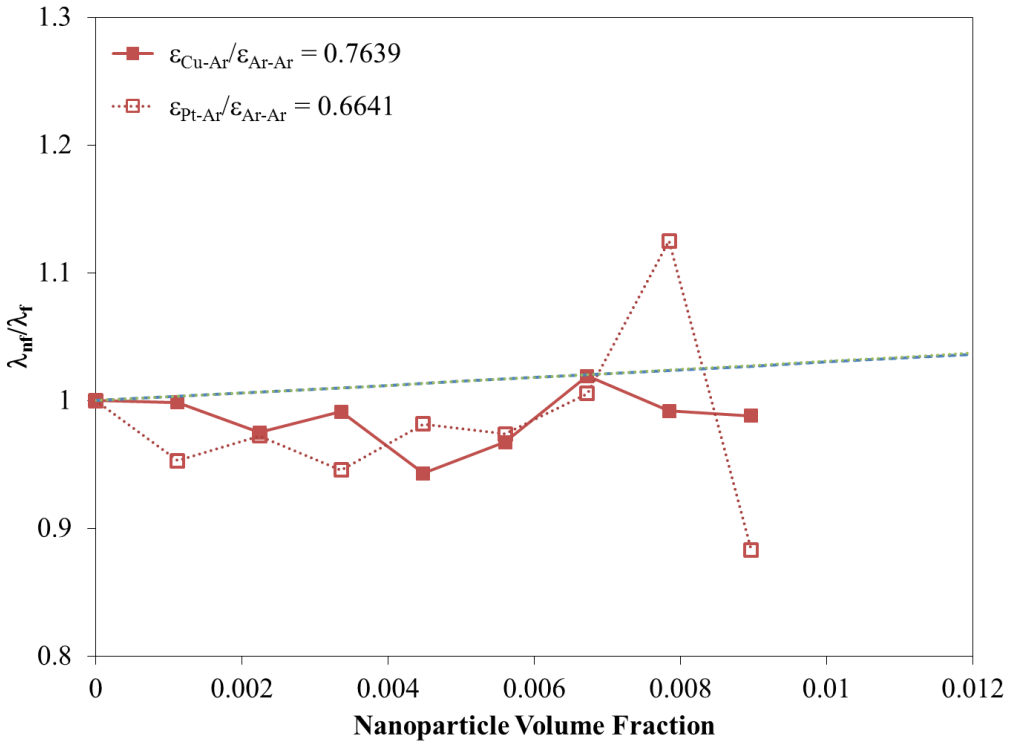

Figure 4.11 Effects of interaction energy on thermal conductivity calculation results of copper and platinum nanoparticles with a diameter of 0.4 nm.

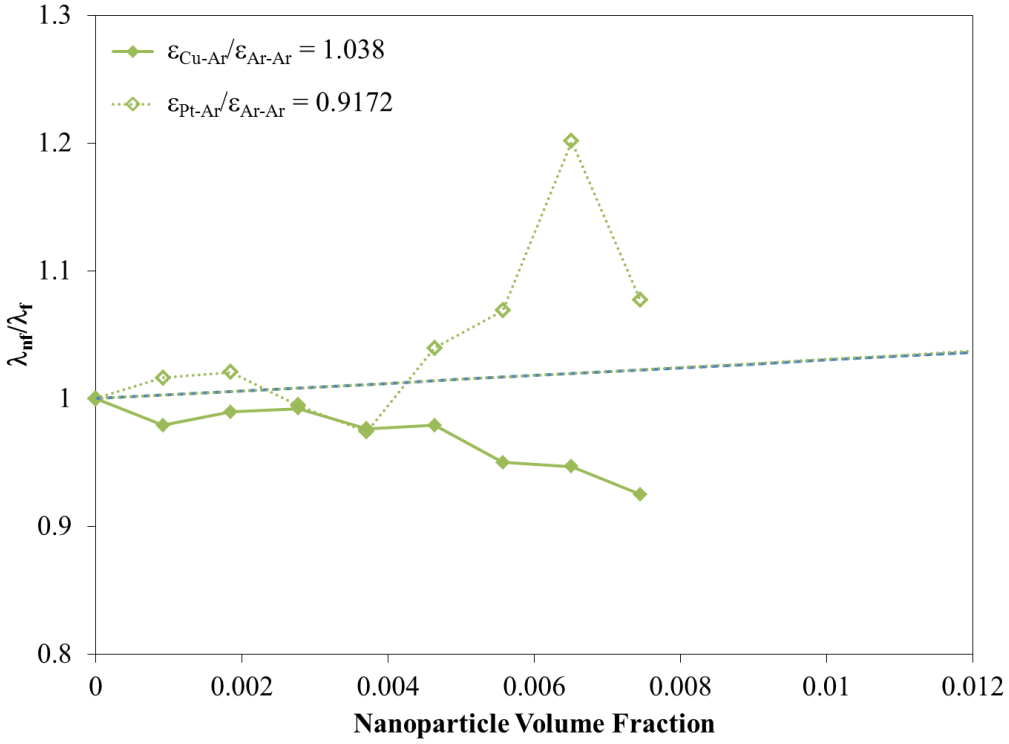

Figure 4.12 Effects of interaction energy on thermal conductivity calculation results of copper and platinum nanoparticles with a diameter of 0.5 nm.

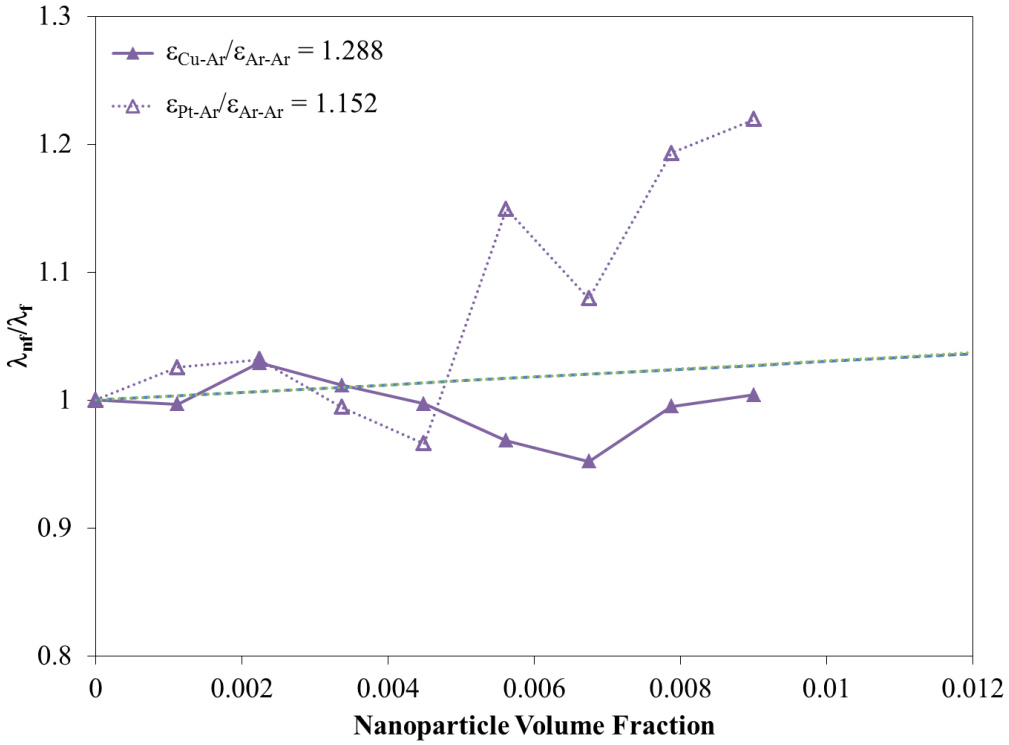

Figure 4.13 Effects of interaction energy on thermal conductivity calculation results of copper and platinum nanoparticles with a diameter of 0.6 nm.

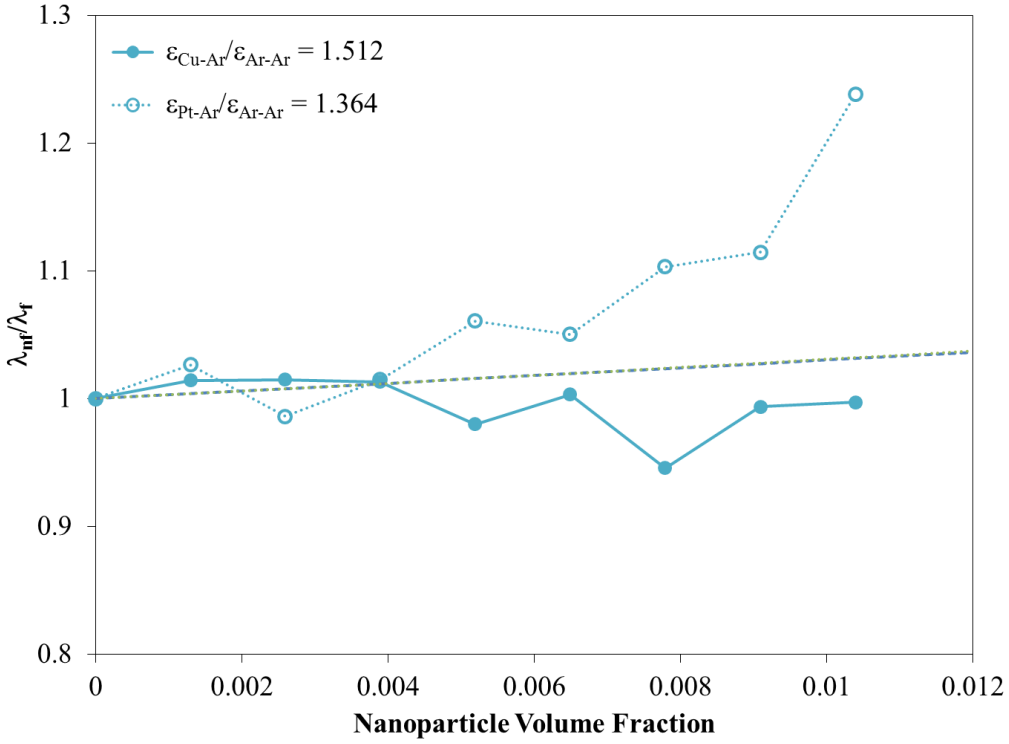

Figure 4.14 Effects of interaction energy on thermal conductivity calculation results of copper and platinum nanoparticles with a diameter of 0.7 nm.

Eapen [61], who both proposed that the interfacial region between the nanoparticle and the fluid was too small and the Kapitza resistance was too large to have a significant impact on thermal conductivity enhancement. However, the results obtained here prove to be contrary to work of Eapen [60], who advanced the idea that strong nanoparticle-fluid interactions would also create a percolating amorphous-like liquid structure in the base fluid that would more effectively transport thermal energy. Although the molecular dynamics model used in this investigation was similarly configured to the work of Eapen, the monoatomic base fluid modeled did not create a percolating liquid structure, but rather followed classical uniform radial distributions. Therefore, it can be concluded that when the interatomic potentials that govern nanoparticle/fluid interactions are uniform in the spherical coordinate system and the nanoparticle volume fraction is in the low concentration limit, the percolating liquid structure proposed by Eapen to facilitate thermal transport within the fluid will not develop regardless of the strength of the interaction energy in the interfacial region. Further investigation is required to determine the results persist for volume fractions.

Finally, unlike the other molecular dynamics investigations described in chapter 1, the colloid model used in this study did not include the constituent atoms of the nanoparticle in the thermal conductivity calculations for the nanofluids while still obtaining similar enhancements. These results suggest that the intrinsic thermophysical properties of the nanoparticle are not contributing factors to the enhancements seen in experimental observations. Also, although the theoretical models discussed in chapter 1 are used for comparison in this section have been useful in the prediction of thermal conductivity enhancements of nanofluids, they are dependent on the thermal conductivity

of the nanoparticle being significantly larger than that of the base fluid. Therefore, in the next section, a novel alternative reason for the increase in the thermal conductivity of nanofluids will be suggested that will deviate from theories previously proposed.

4.3 Mechanisms of Thermal Transport and their Characteristics

The process by which thermal fluctuations of the constituent particles within the control volume of a fluid become uncorrelated involves the combination of fluctuation decay without propagation characterized by the thermal diffusivity and fluctuation propagation at the speed of sound of long-wavelength longitudinal acoustic waves (see figure 4.15) that decays through thermal conduction and viscosity through the medium [133]. These modes of fluctuation decay are determined from the Fourier-Laplace transformation of the conservation laws for the local densities used to develop equations 2.1 – 2.4. The solution of the resulting hydrodynamic matrix yields a set of three coupled solutions (one imaginary and two complex roots) that correspond to the decay modes that will be discussed next.

An analysis of equations 2.1 and 2.2 show that thermal energy can be propagated a longitudinal wave through a liquid in three distinct ways: 1) kinetically, 2) potentially, and 3) through collisions. A graphical representation of these modes can be found in figure 4.16. The transport of thermal energy through kinetic motion, *K*, (figure 4.16-a) is defined by the velocity of each individual particle in the overall system. The contribution

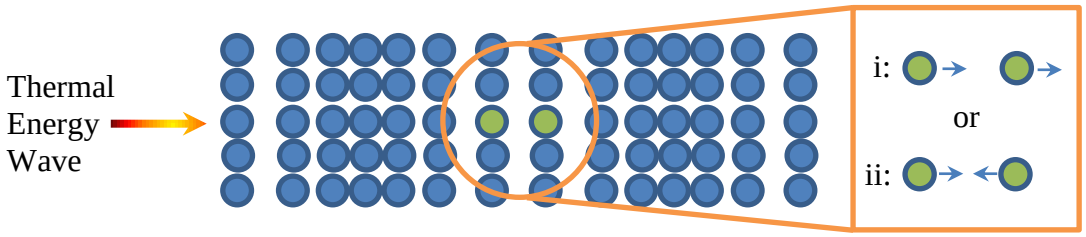

Figure 4.15 Hydrodynamic collective modes for heat fluxes in a fluid and the corresponding particle motion characteristics.

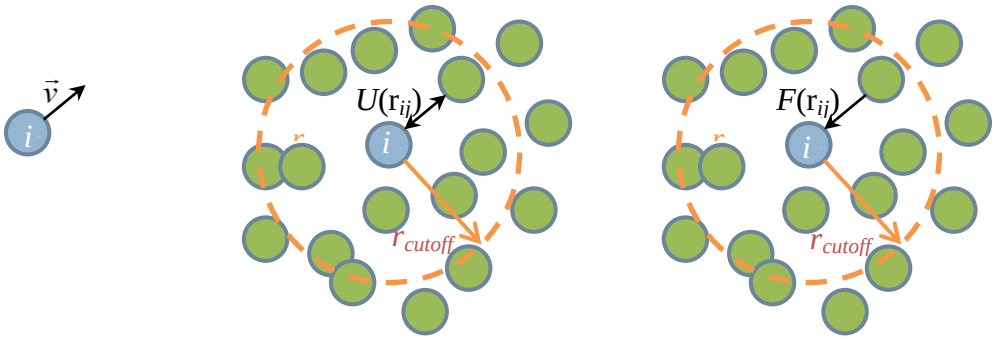

(a) (b) (c)

Figure 4.16 Modes of thermal energy conduction in a fluid where (a) is kinetic energy transport, (b) is potential energy transport, and (c) is collision energy transport.

towards the transport of thermal energy from non-contact interactions of atom pairs, *P*, (figure 4.16-b) is calculated from the position of particles *j* less than some distance r_{cutoff} to particle *i* at a specific time. The final form of thermal transport is through particle collisions, *C*, (figure 4.16-c) that arises from normal forces applied to particle *i* from the sum total of particles *j* less than some distance r_{cutoff} away. This term is often called a virial term since it is associated with the pressure on the system due to movement of particle *i*. To determine the contribution of these modes of thermal transport and their frequency characteristics, the thermal conductivity calculations were decomposed into self- and cross-correlation functions of each mode of energy conduction. Plots of these functions are shown in figures 4.17–4.24. Three key observations can be made from these plots regarding the effect nanoparticle suspensions on the modes of energy transfer in the fluid.

Firstly, since the system is at equilibrium with no velocity gradients, there is very little to no velocity change for each of the constituent particles in the system and the contribution to thermal energy transport from the self-correlation of the kinetic portion

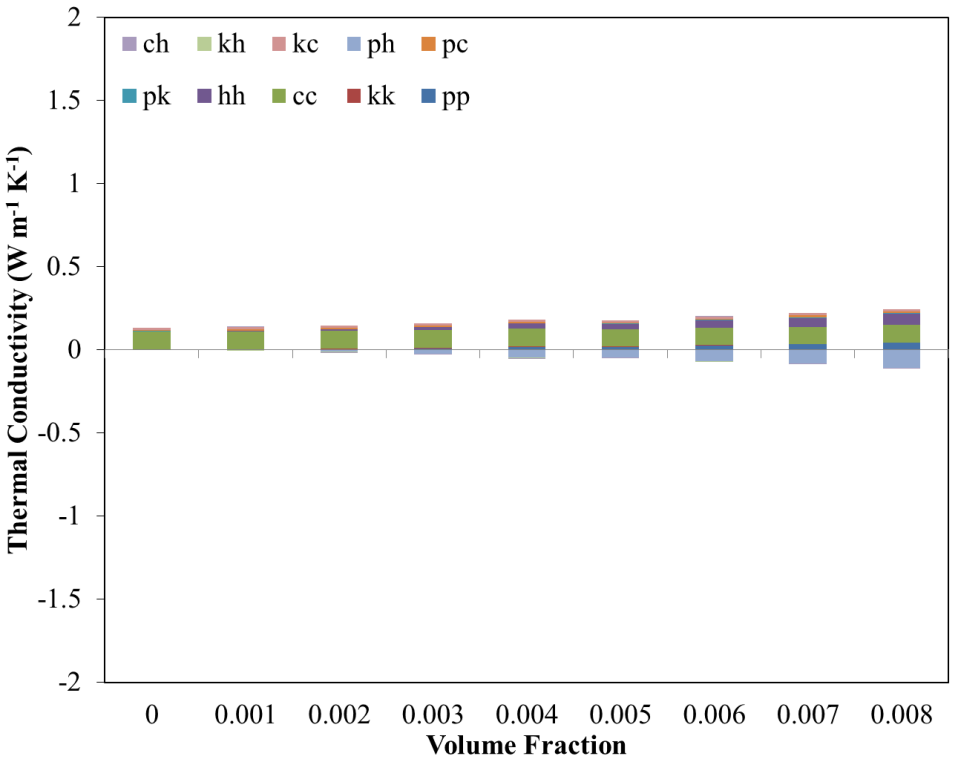

Figure 4.17 Components of energy transfer within argon fluid with 0.4 nm copper suspensions.

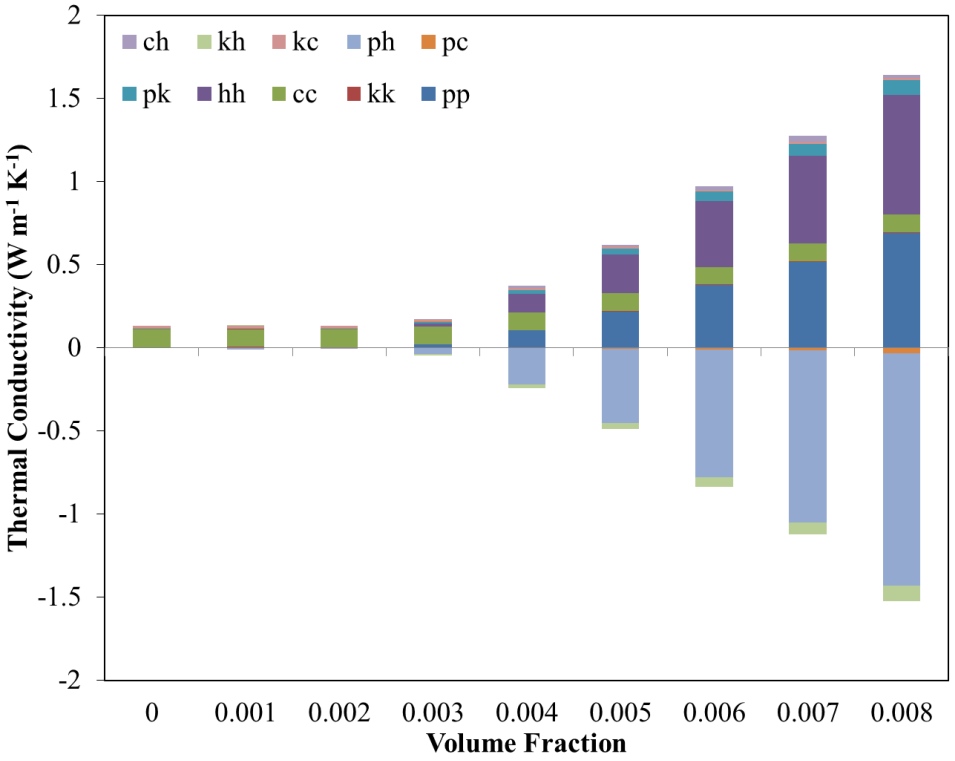

Figure 4.18 Components of energy transfer within argon fluid with 0.4 nm platinum suspensions.

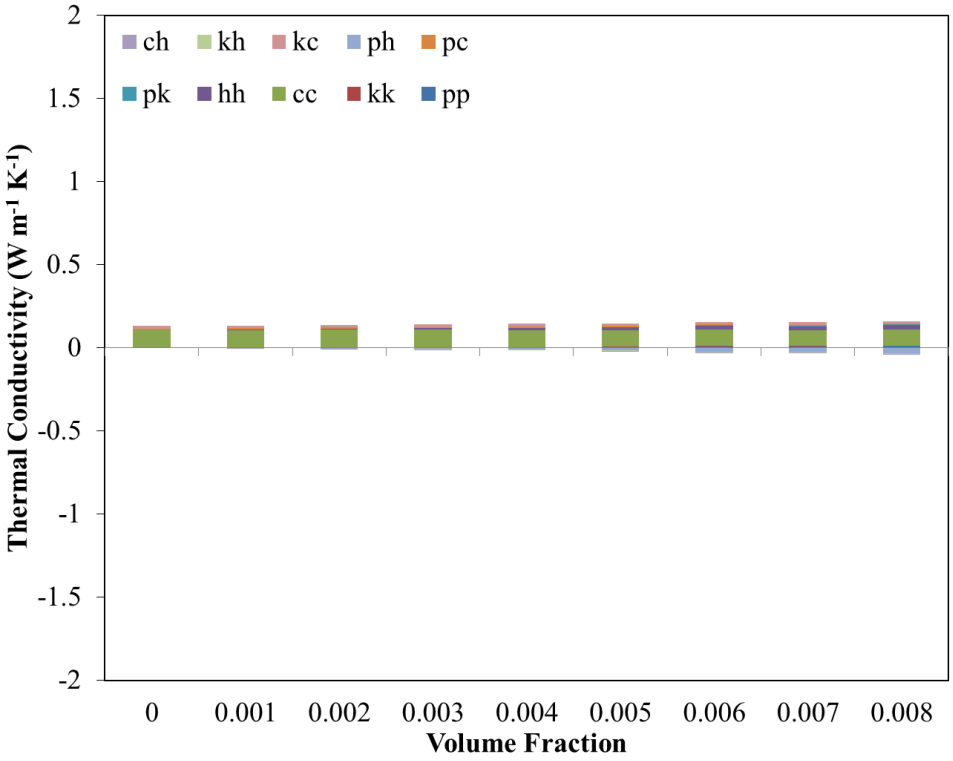

Figure 4.19 Components of energy transfer within argon fluid with 0.5 nm copper suspensions.

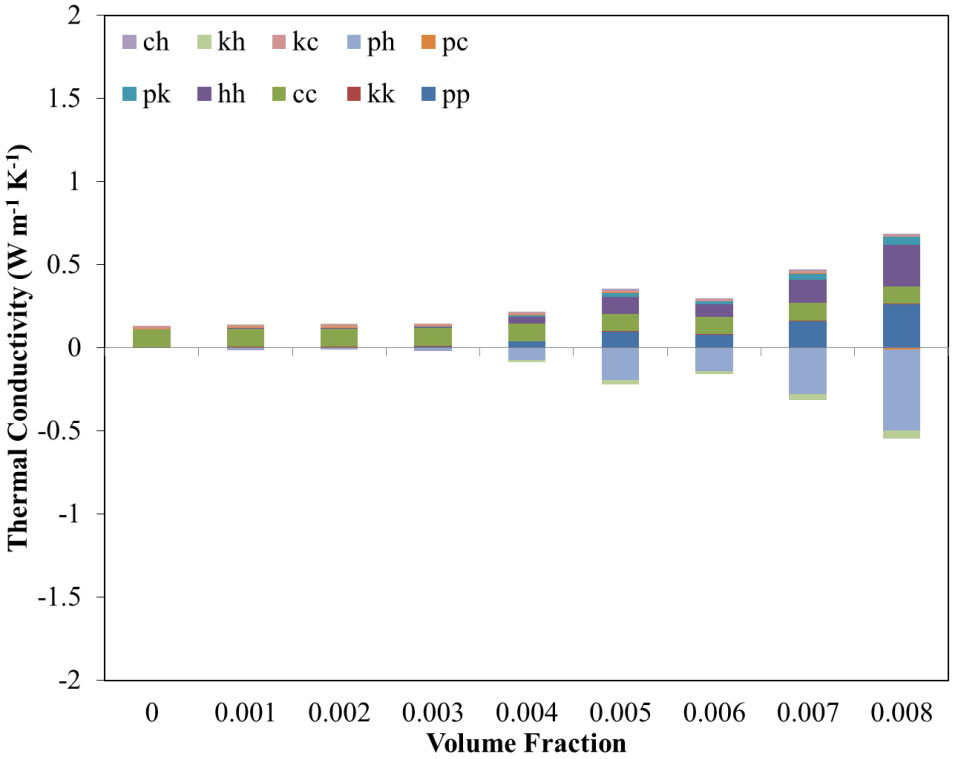

Figure 4.20 Components of energy transfer within argon fluid with 0.5 nm platinum suspensions.

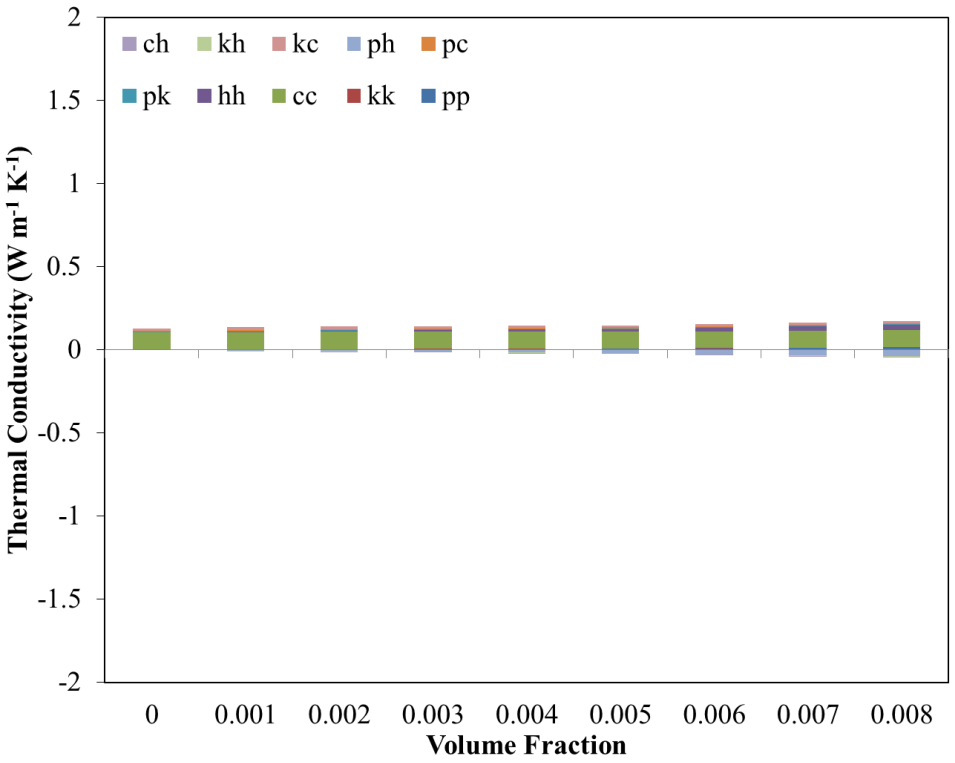

Figure 4.21 Components of energy transfer within argon fluid with 0.6 nm copper suspensions.

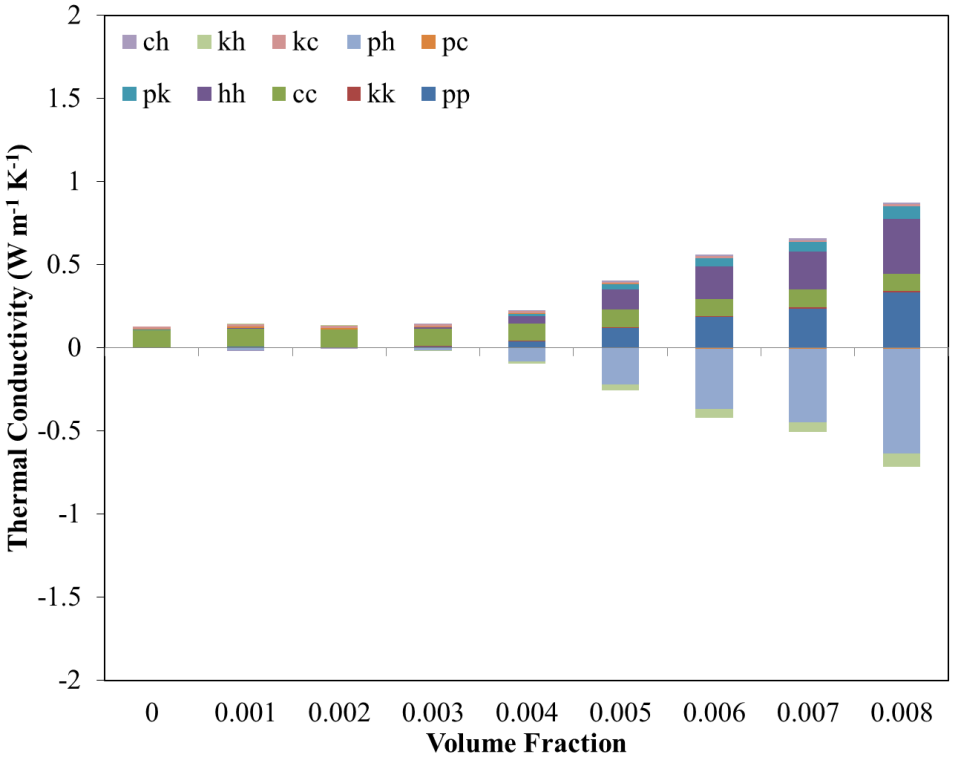

Figure 4.22 Components of energy transfer within argon fluid with 0.6 nm platinum suspensions.

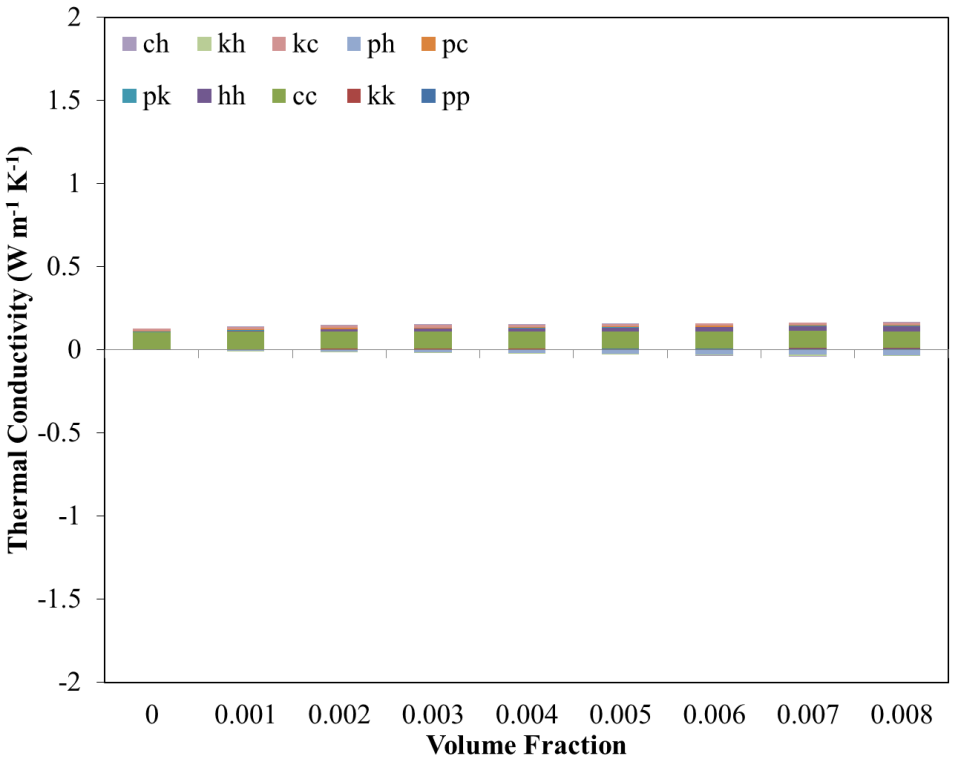

Figure 4.23 Components of energy transfer within argon fluid with 0.7 nm copper suspensions.

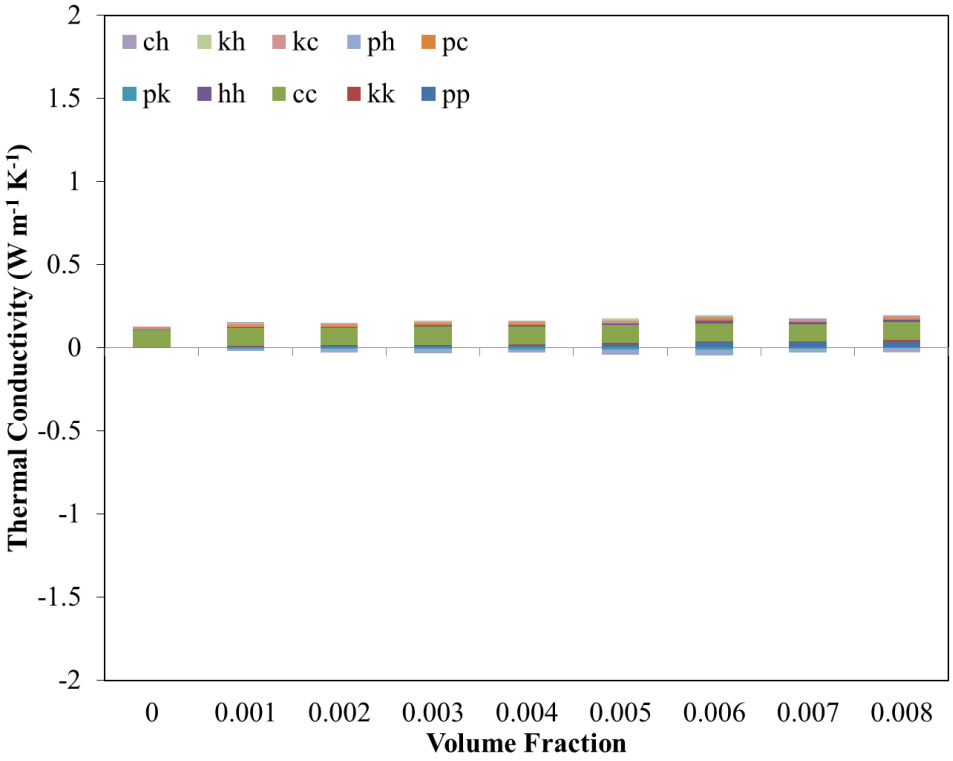

Figure 4.24 Components of energy transfer within argon fluid with 0.7 nm platinum suspensions.

(KK) is negligible. The contribution to thermal energy transport is also minimal for those cross-correlations that contain the kinetic energy component (PK, KC).

Secondly, as is discussed in chapter 2, there is little long-range order between the nanoparticle and the fluid, with only 2-3 atomic diameters directly contributing to the calculation of the local potential energy. Fluctuations in the local density results from chapter 3 also show that positions of fluid particles near the surface of the nanoparticle are not permanently fixed and lead to a rotation of fluid particles near the surface over the specified integration period. Both of the preceding factors lead to a quick decay of the potential-potential (PP) correlation function in the calculation of the thermal conductivity of the copper-argon and platinum-argon nanofluids. However, figures 4.18, 4.20, and 4.22 show that at increasing volume fractions of platinum nanoparticles the contribution toward the calculated thermal conductivity by the potential-potential (PP) correlation function also increases. A comparison of the *xyz* positions obtained from the molecular dynamics simulations (at 0.4, 1.2, and 2.0 ps) for the 0.6 nm and 0.7 nm diameter platinum nanoparticles in the argon fluid (see figure 4.25) shows this increase in the potential-potential (PP) correlation function is due to the agglomeration of platinum nanoparticles and the increase in potential energy due the strong interactions between them. Agglomeration appears to be an arbitrary event, as can be seen in the same figure 4.25, where 0.7 nm diameter nanoparticles did not clump, resulting in a considerably smaller potential-potential correlation contribution. Agglomeration also did not appear to occur in the simulations containing copper nanoparticles because of the comparatively weak interaction energy between nanoparticles. Therefore, while many investigators have suggested that the thermal conductivity enhancement seen in nanofluids can be attributed

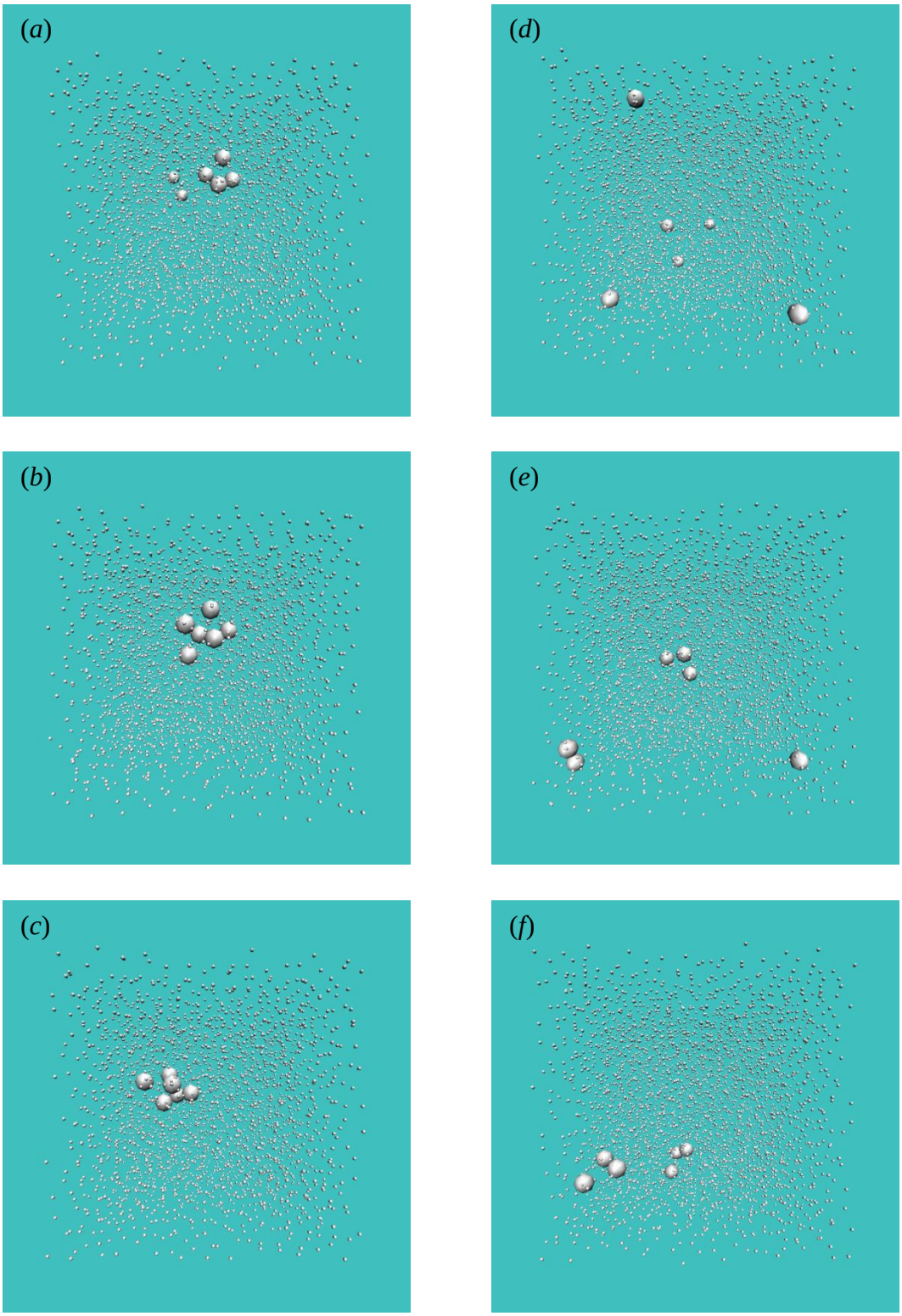

Figure 4.25 The *xyz* positions of nanoparticles (large spheres) and fluids (small spheres) for 0.6 nm (*a-c*) and 0.7 nm (*d-f*) platinum/argon nanofluids, where the first row corresponds to snapshots of the positions at 0.4 ps, the second row at 1.2 ps, and the third row at 2.0 ps.

to agglomeration, the data suggests that its affect is not as significant as other contributing factors.

Lastly, the consistently significant contribution to the thermal conductivity calculation was the self-correlation of the collision (CC) component of equation 2.2. This intuitive conclusion can be drawn considering that thermal fluctuations in the volume induce collisions between particles. The energy dissipated through these collisions gradually becomes uncorrelated which is the reason for the long tail behavior of the heat flux autocorrelation function seen in figures 4.1–4.8. This result compares relatively well with the work presented by Eapen, et al., Teng, et al. and Sachdeva, et al., which all suggested that interaction between the nanoparticle and the fluid factored significantly into the thermal conductivity of the overall nanofluid. However, by using the colloid model in the molecular dynamics simulations, the results obtained focus solely on the nanoparticle-fluid interactions.

In addition, it is noteworthy to mention that for the self- and cross-correlation of the kinetic, potential, and collision components, there is a noticeable lack of dependency on the volume fraction of nanoparticle suspension over the values selected. However, there is an indication that agglomeration is a significant factor in the calculation of the potential energy component of thermal energy transport. Therefore, it is suggested that at larger concentrations, where the likelihood of nanoparticle interactions increase, the effect on thermal conductivity values will continue to be significant.

Now, remembering that thermal energy transport can be characterized by thermal diffusion or longitudinal wave propagation, the next step is to quantify the effect of the presence of a nanoparticle suspension on the collective dynamics of the fluid system.

This was done by performing a Fourier transform on the dominant mode of thermal energy transport (self-correlation of the collision term in the heat flux autocorrelation function) and analyzing its frequency characteristics.

In the case of a single-component and isotropic fluid, molecular dynamics simulations have shown that the dominant mode of fluctuation decay is without propagation characterized by the thermal diffusivity [114, 133]. Therefore, it is reasonable to see no frequency information in the Fourier transforms of the self-correlation of the collision term (CC) for pure argon (see figures 4.26–4.33). Thermal diffusion is an inefficient mode of thermal transport when compared to the longitudinal acoustic modes associated with solids and so it is no surprise that the thermal conductivity in pure liquids is low. However, the insertion of platinum nanoparticles (see figures 4.27, 4.29, 4.31, 4.33) appears to have enhanced thermal diffusion in the nanofluid by coupling it with longitudinal acoustic waves that have frequencies between 1–10 THz. There also appears to be a dependency on the size of the nanoparticle diameter, with a clear dominant frequency of approximately 4.0 THz developing with a platinum nanoparticle of 0.7 nm. The noticeable absence of these frequency characteristics with the insertion of copper nanoparticles in the argon fluid (see figures 4.26, 4.28, 4.30, 4.32) leads to the focal point of this discussion.

4.4 Thermal Transport in a Multicomponent System and the Dufour Coefficient

Until this point, the last term in equation 2.2 has been deliberately omitted from this discussion. This enthalpy term (H) arises in multi-component fluid system where energy transfer occurs by both conduction *and* thermal diffusion. While it would be ideal to separate the total energy flux in the system into two distinct energy transfer

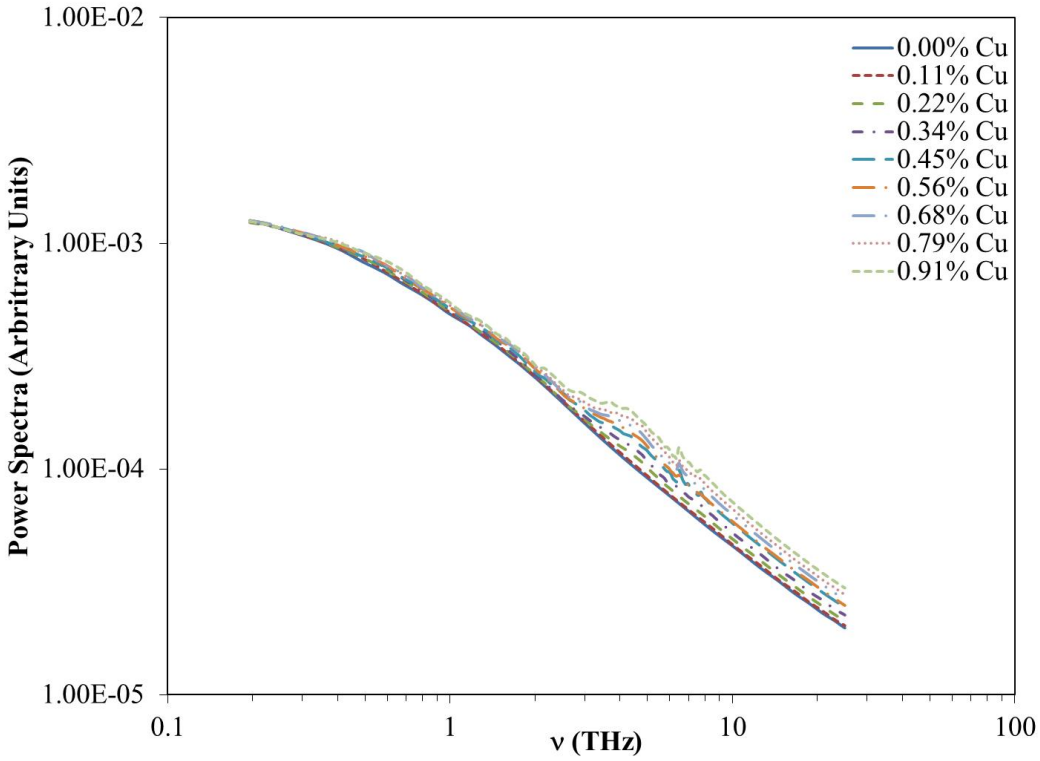

Figure 4.26 Power spectra for CC self-correlation function of argon fluid with varying concentrations of 0.4 nm diameter copper suspensions.

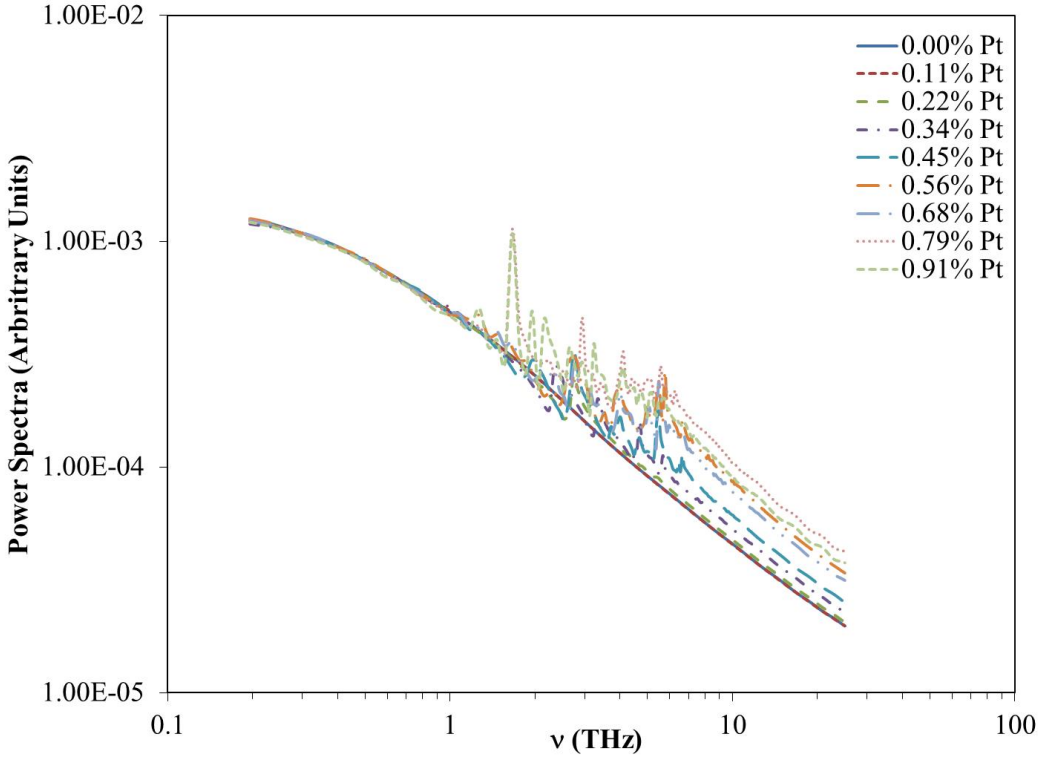

Figure 4.27 Power spectra for CC self-correlation function of argon fluid with varying concentrations of 0.4 nm diameter platinum suspensions.

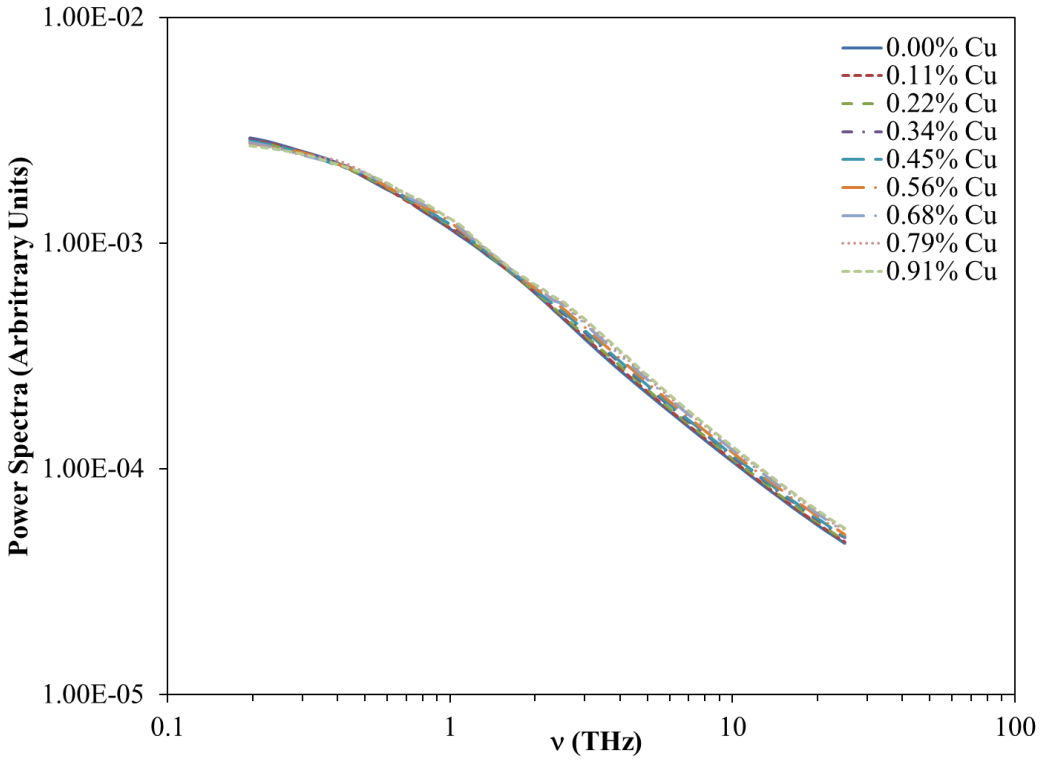

Figure 4.28 Power spectra for CC self-correlation function of argon fluid with varying concentrations of 0.5 nm diameter copper suspensions.

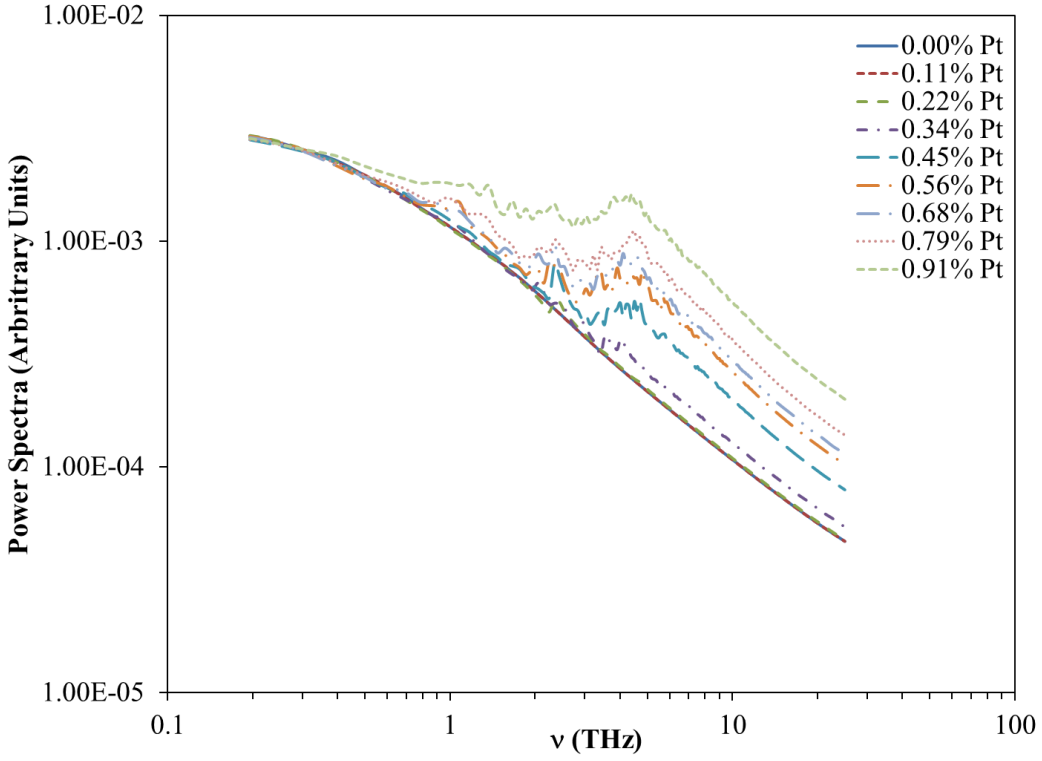

Figure 4.29 Power spectra of CC self-correlation function of argon fluid with varying concentrations of 0.5 nm diameter platinum suspensions.

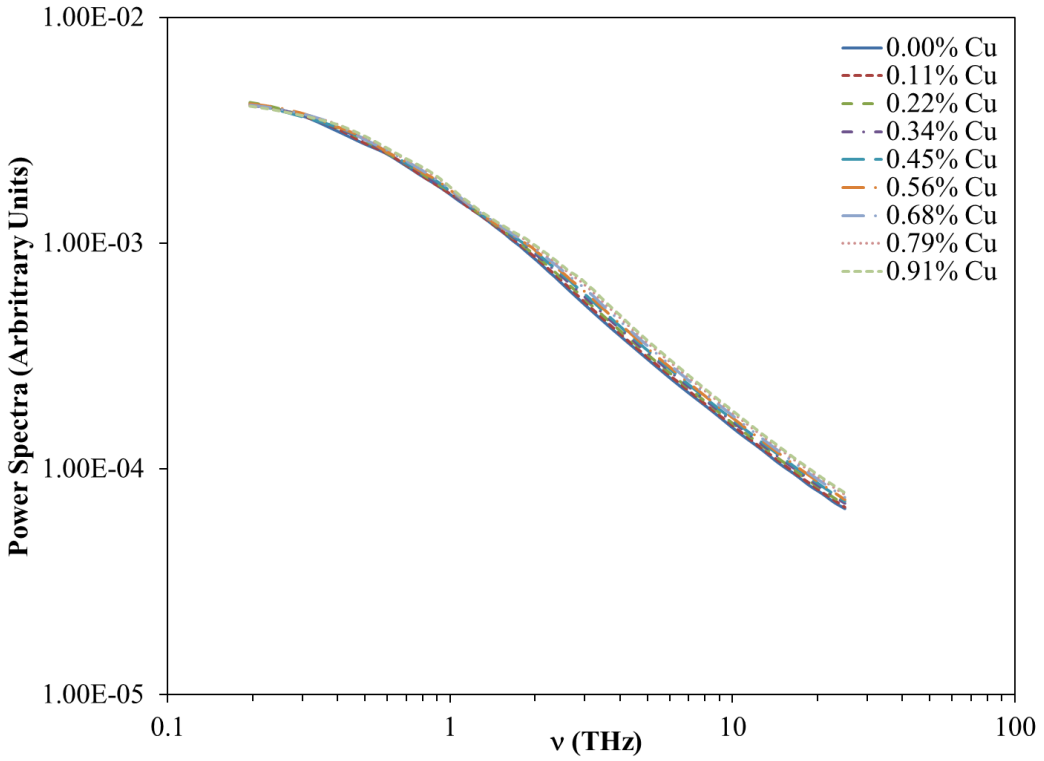

Figure 4.30 Power spectra of CC self-correlation function of argon fluid with varying concentrations of 0.6 nm diameter copper suspensions.

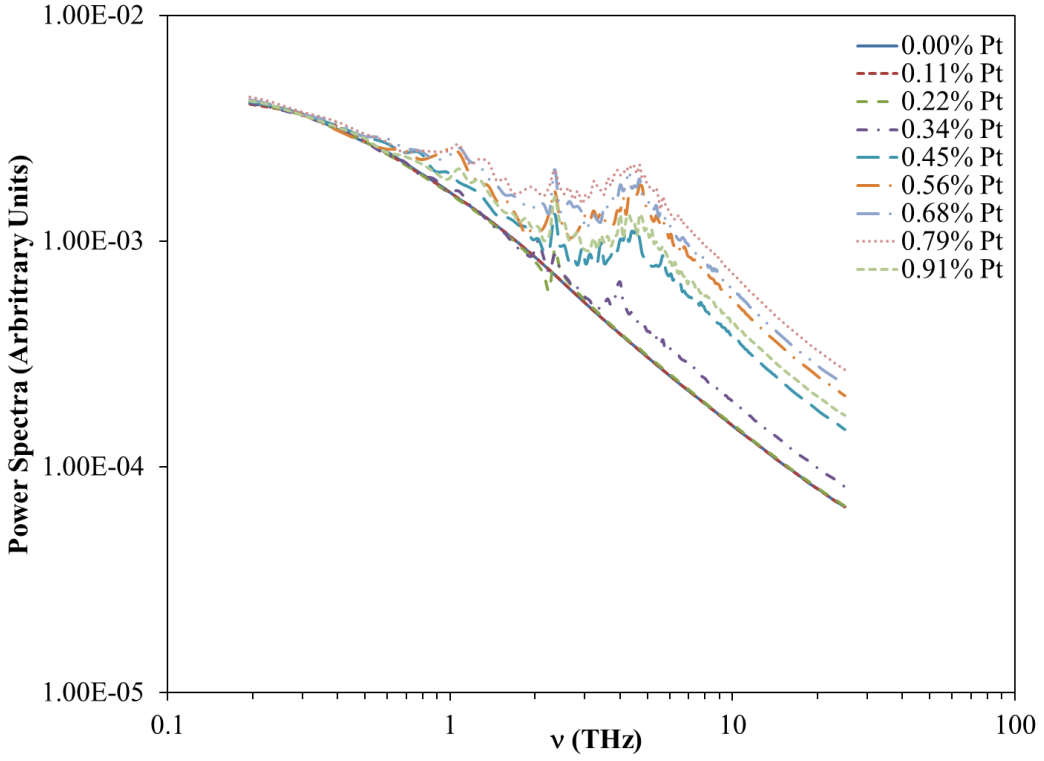

Figure 4.31 Power spectra of CC self-correlation function of argon fluid with varying concentrations of 0.6 nm diameter platinum suspensions.

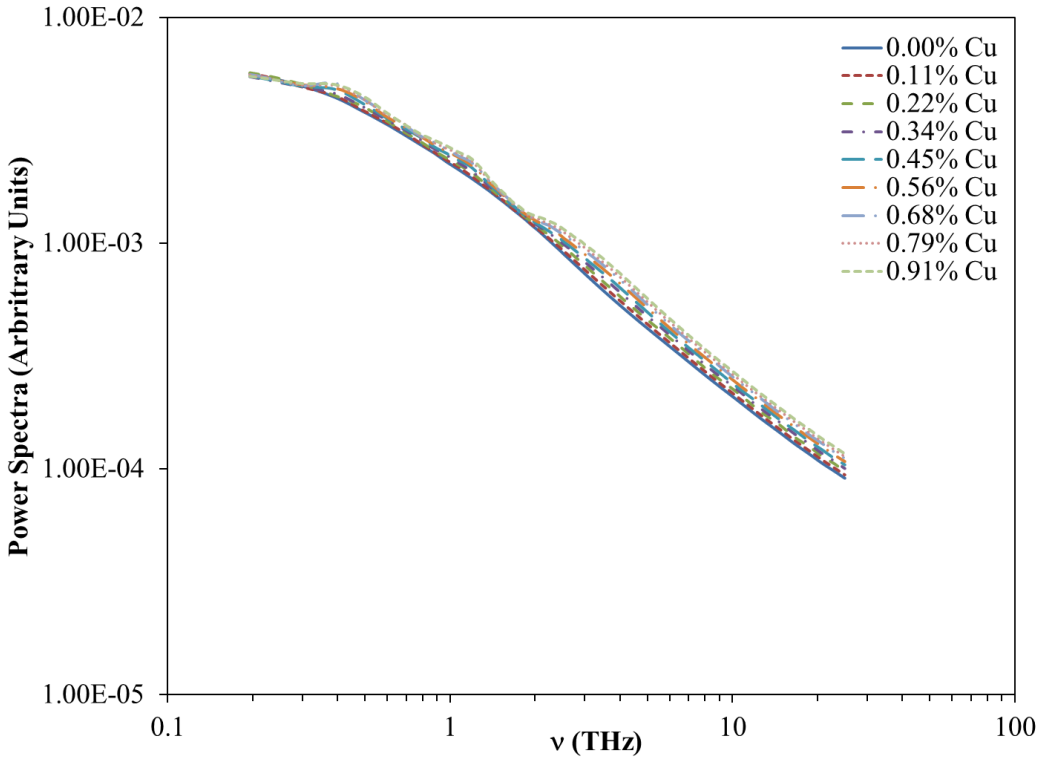

Figure 4.32 Power spectra of CC self-correlation function of argon fluid with varying concentrations of 0.7 nm diameter copper suspensions.

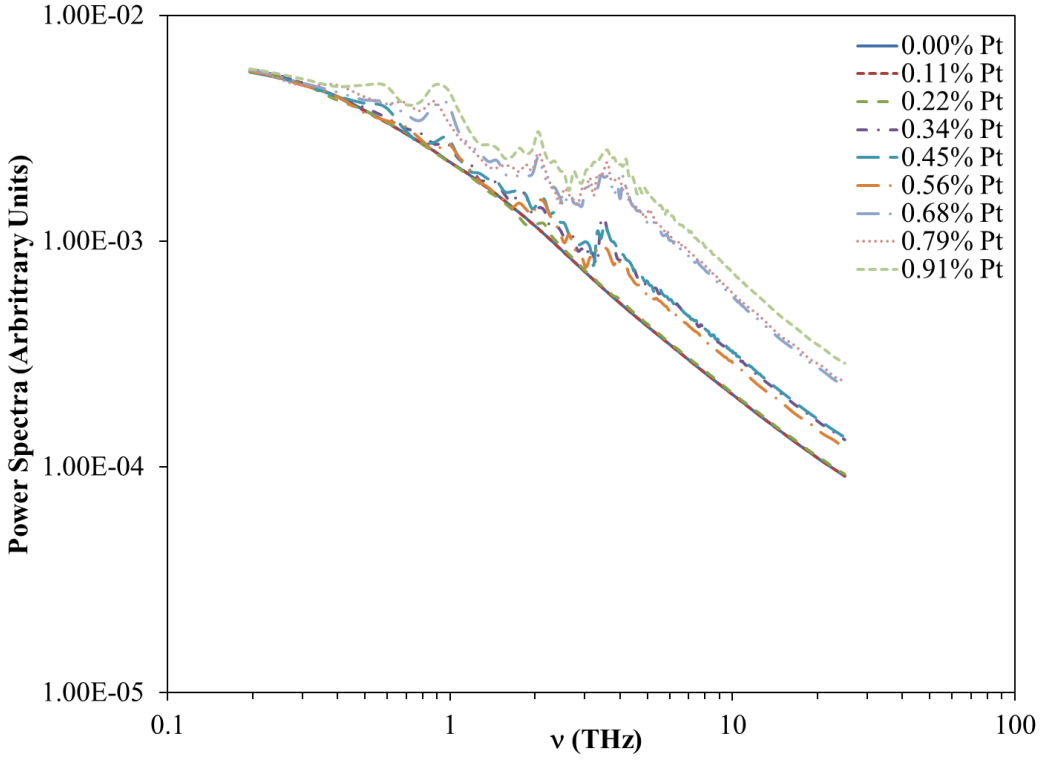

Figure 4.33 Power spectra of CC self-correlation function of argon fluid with varying concentrations of 0.7 nm diameter platinum suspensions.

modes to specifically analyze the heat flux due to conduction, this is impossible to perform due to their coupled nature [111]. A common way to circumvent this problem is subtract a partial enthalpy term from the total energy flux vector to account for the energy transfer due to thermal diffusion [78,100,101]

$$\mathbf{J}'_q = \mathbf{J}_q - \sum_{k=1}^{n} h_k \mathbf{J}_k \tag{4.1}$$

which leads to the final form found in equation 2.2. The calculation of this partial enthalpy term, h_k, is a complicated procedure, which either involves the addition/subtraction of particles from the system or the substitution of particle *a*/*b* with particle *b*/*a*, with the subsequent calculation of the change in chemical potential [143-146]. In this investigation, the method for calculating the partial enthalpy was based on a simplified procedure introduced by Vogelsang [147] and adopted by several authors [82, 84, 85] for simulations of nanofluids. In this calculation, the partial enthalpy is defined as

$$h^{\alpha} = \left\langle \sum_{k=1}^{N_\alpha} \frac{p_k^2}{2m_k} \mathbf{v}_k \right\rangle + \left\langle \frac{1}{2} \sum_{j \neq k}^{N_\alpha} \mathbf{I} U\left(r_{jk}\right) \cdot \mathbf{v}_k \right\rangle + \left\langle \frac{1}{2} \sum_{j \neq k}^{N_\alpha} \left[\mathbf{r}_{jk} \otimes \mathbf{F}\left(r_{jk}\right)\right] \cdot \mathbf{v}_k \right\rangle \tag{4.2}$$

where the total kinetic, potential, and collision energies are calculated and ensemble averaged for each species α.

Reanalyzing figures 4.17 – 4.24 highlights the effect this enthalpy term has on the calculation of the thermal conductivity of the copper/argon and platinum/argon nanofluids. Once again, the platinum nanoparticle suspensions had a greater contribution on the thermal conductivity of the argon fluid from the components that contained the enthalpy terms (KH, PH, CH, HH) than was seen in fluid containing copper nanoparticle suspensions. The reason for this can now be explained by the frequency characteristics of

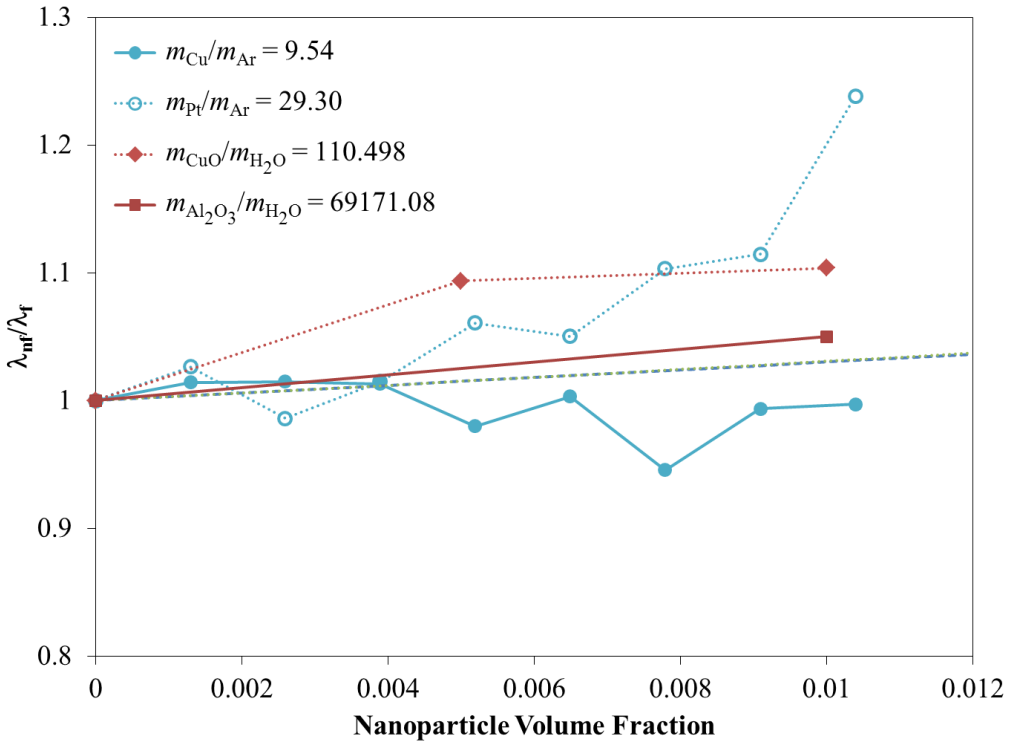

Figure 4.34 Comparison of thermal conductivity enhancement between molecular dynamics simulations of 0.7 nm nanoparticle suspensions with both aluminum oxide and copper oxide nanofluids.

the observed enhanced thermal diffusivity. The increased mass ratio of the platinum and argon seen in table 2.3 allowed more energy dissipation to occur via diffusion of the nanoparticle that propagated at the speed of sound within the fluid by longitudinal acoustic waves. When the mass ratio is reduced (as is the case for the copper/argon nanofluid), the copper nanoparticles almost act as the fluid particles and the nanofluid retained the thermal diffusion characteristics of the homogeneous, isotropic base fluid. The negative values observed for the cross-correlation of the enthalpy term with the potential and the kinetic terms (PH and KH) are possibly the "caging" mechanisms that dissipate the longitudinal acoustic waves in a similar fashion as is seen for water

simulations [136-138]. A comparison can now also be made with experimental results using the mass ratios presented in table 2.4 and is presented in figure 4.34. The thermal conductivity enhancement observed using the more massive aluminum oxide nanoparticle suspensions [15] was greater that seen for the copper oxide suspension under similar testing conditions [35].

Recognizing the significant role diffusion plays in thermal energy dissipation within a nanofluid now justifies reanalysis of the phenomenological relations that has been the motivation for the proposed use of nanofluids for heat transfer applications. Originally, the phenomenological relationship between the heat flux applied to the nanofluid system ($\mathbf{J}_q$) and the system temperature response ($\mathbf{X}_q$) was of the form set forth by equation 2.5, and was expressed as

$$\mathbf{J}_q = L_{qq}\mathbf{X}_q \tag{4.3}$$

where L_{qq} is used by equation 2.6 to define the thermal conductivity and the heat flux was further modified by equation 4.1 to focus solely on the transport of thermal energy due to conduction. Now, considering that the enhancement in thermal energy transport seen in

nanofluids is mainly due the effects of thermal diffusion and not conduction, equation 4.3 can now be rewritten as

$$\mathbf{J}_q = L_{qq}\mathbf{X}_q + \sum_{k=1}^{2} L_{qk}\mathbf{X}_k \tag{4.4}$$

where L_{qk} is the phenomenological coefficient is used to define the Dufour coefficient

$$D_D = \frac{L_{qk}}{T^2 x_1 x_2} \tag{4.5}$$

This Dufour coefficient describes thermal energy transport through a multicomponent fluid by means of the resulting concentration gradient. As is suggested by equation 4.5, the Dufour coefficient is dependent on the concentration of the nanoparticle, x_i. However, because of the work discussed above, this value should also be dependent on the mass ratio of the nanoparticle to the base fluid. A defined relationship between the mass ratio and the Dufour coefficient is not proposed here and is left as the source for future work.

Bastea [148] also performed an analysis of the dependency of the thermal conductivity on the mass and diameter ratio. In one portion of the results, a similar conclusion was drawn where higher mass ratios yielded better agreement with effective medium theory models, like Maxwell and Bruggeman. However, another portion of the results suggested that larger (yet still with a small mass ratio = 1) suspensions yielded significantly higher (~50%) thermal conductivities than even the high mass ratio simulations. The results of which are direct contrast with the large copper nanoparticle/argon nanofluid results obtained in this investigation. The discrepancy in results may have resulted from one of many sources, including:

1) the use of a soft sphere potential that fails to include a long range attraction component to describe nanoparticle/fluid interactions,
2) the use of a potential that does not increase with larger diameter nanoparticle suspensions, and
3) not including the partial enthalpy term into the heat flux calculations.

4.5 Summary

The enhanced thermal conductivities obtained through experimentation discussed in chapter 1 are now theoretically verified using molecular dynamics simulations based on the theories of nonequilibrium thermodynamics. Using a size-dependent colloid potential to describe nanoparticle interactions in a fluid, it was determined that the presence of a nanoparticle that strongly interacts with the base fluid creating locally high fluid density does not correlate to increases in the thermal conductivity of the overall fluid. The platinum/argon nanofluid had a relatively weak nanoparticle/fluid interaction and decreased with increasing diameter. This led to decreasing local densities and even to values below the bulk density of the argon fluid. However, the platinum/argon nanofluid had consistent increases in thermal conductivity over the volume fractions investigated. Analysis of the components of thermal energy transfer suggests that the mass of the nanoparticle suspensions enhanced particle diffusion within the fluid by amplifying the propagating longitudinal wave characteristics. Considering that the thermophysical properties of the nanoparticle were not involved in the thermal conductivity calculations, it is concluded that this nanoparticle mass relative to the base fluid is a physical characteristic that is critical to the conduction of thermal energy within a fluid.

Chapter 5 – Shear Viscosity and Physical Mechanisms of Momentum Transport

While several works have demonstrated using molecular dynamics simulations that the base fluid experiences increases in shear viscosity with increasing concentrations of nanoparticle suspensions of up to 2%, there has not been a systematic study on the effects of nanoparticle size and interaction energy between the suspension and the fluid on these increases. Also affected by these parameters are the mechanisms of momentum transport within the nanofluid and nonlinear increase in shear viscosity due to the infinite modulus of rigidity. In this chapter, the results of molecular dynamics simulations will be used to address both topics and draw conclusions regarding their effects.

5.1 Verification of Equilibrium Molecular Dynamics Method

As was described in chapter 2, the concept of acquiring transport coefficients from a system at thermodynamic equilibrium requires that fluctuations in the momentum flux of the system to be uncorrelated over a specified period. Therefore, it was first important to verify that the stress autocorrelation function in the Green-Kubo relations for the shear viscosity of copper/argon and platinum/argon nanofluids decay to zero over the M =1,000 integration steps specified in chapter 2. Unlike the heat flux autocorrelation functions in chapter 3 for copper and platinum, only the fluids that contained copper nanoparticle suspensions decayed to zero over the integration period (figures 5.1, 5.3, 5.5, and 5.7). The argon fluid that suspended platinum nanoparticles did not adequately decay

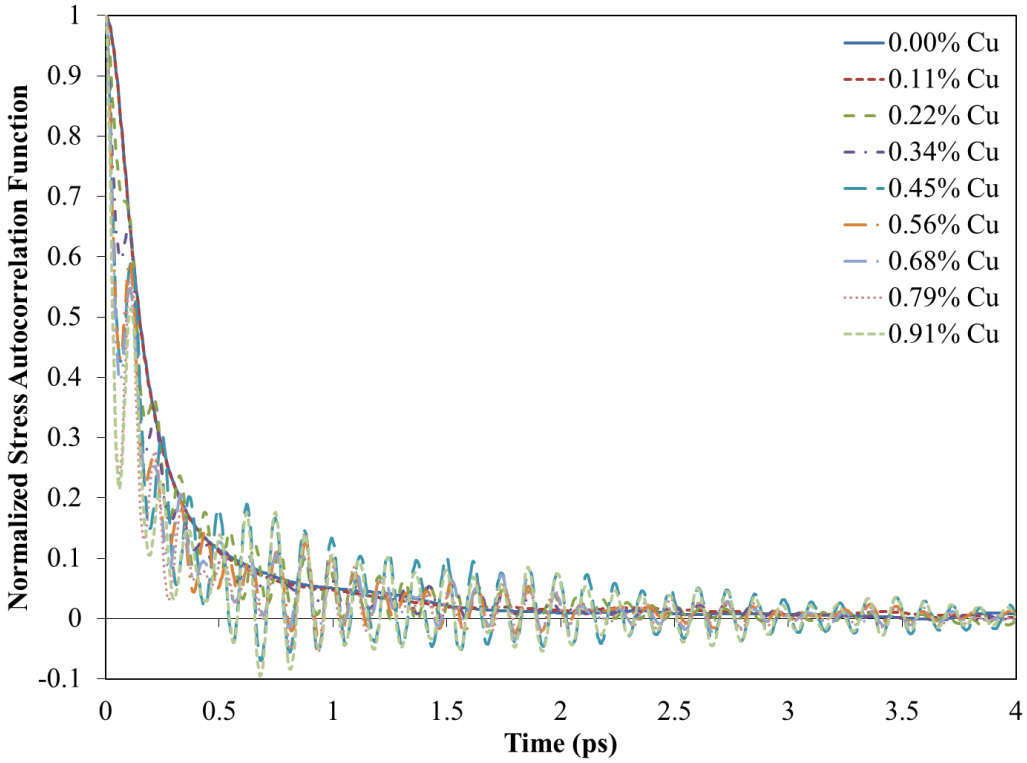

Figure 5.1 Normalized stress autocorrelation function for 0.4 nm diameter copper in argon.

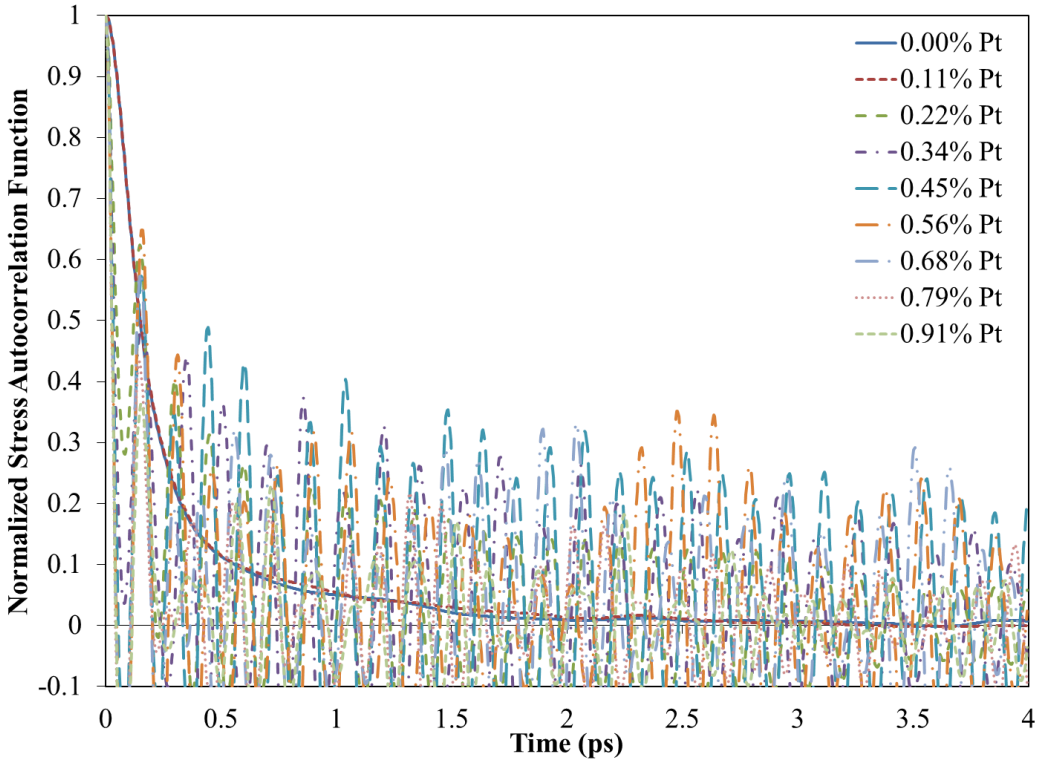

Figure 5.2 Normalized stress autocorrelation function for 0.4 nm diameter platinum in argon.

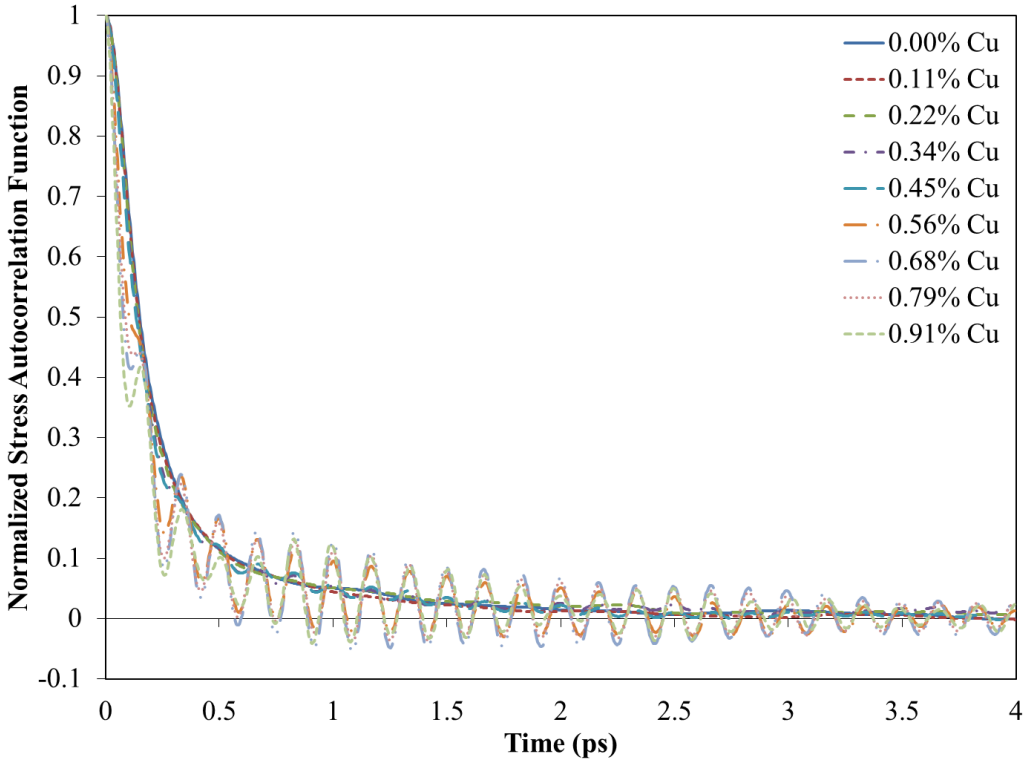

Figure 5.3 Normalized stress autocorrelation function for 0.5 nm diameter copper in argon.

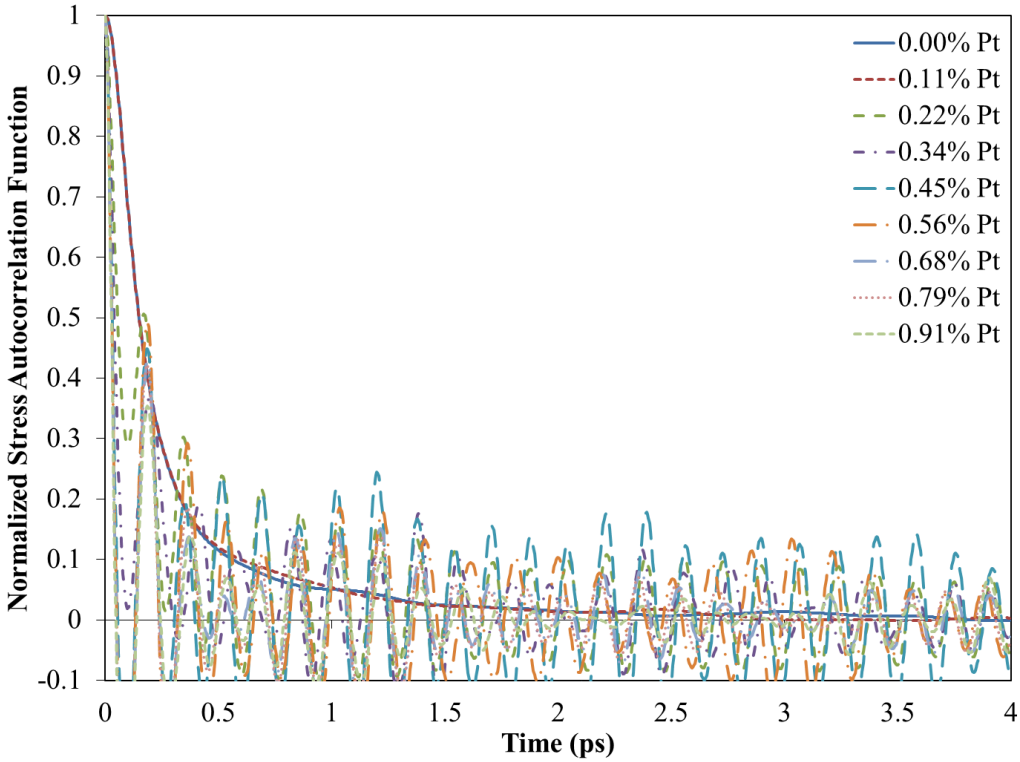

Figure 5.4 Normalized stress autocorrelation function for 0.5 nm diameter platinum in argon.

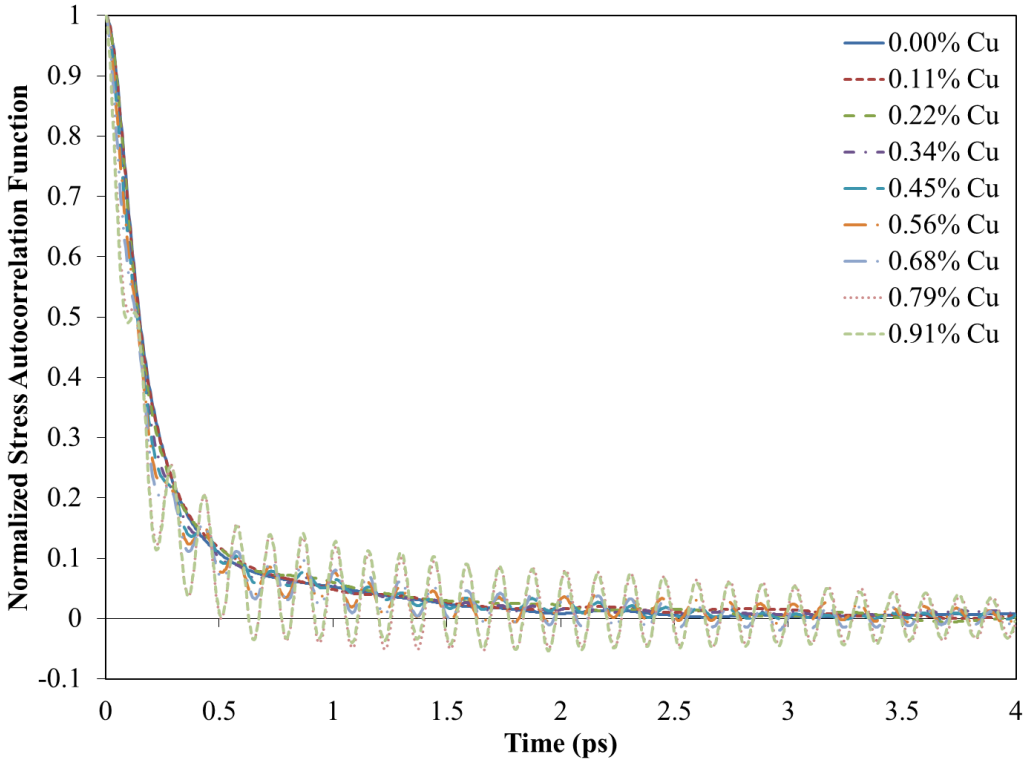

Figure 5.5 Normalized stress autocorrelation function for 0.6 nm diameter copper in argon.

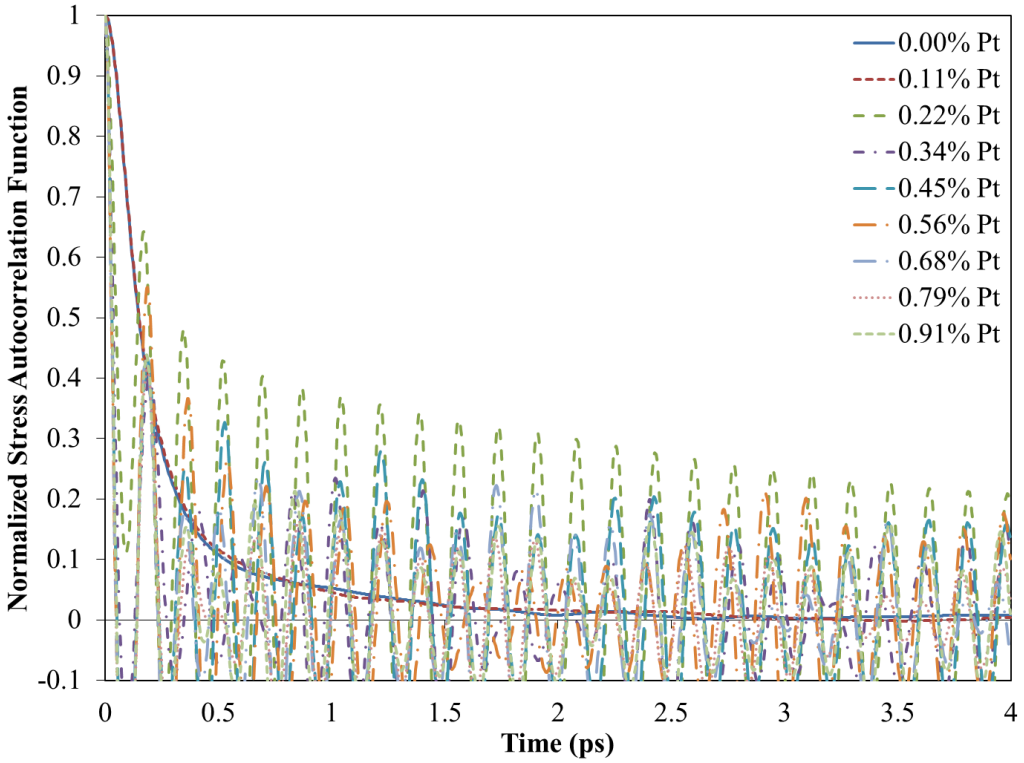

Figure 5.6 Normalized stress autocorrelation function for 0.6 nm diameter platinum in argon.

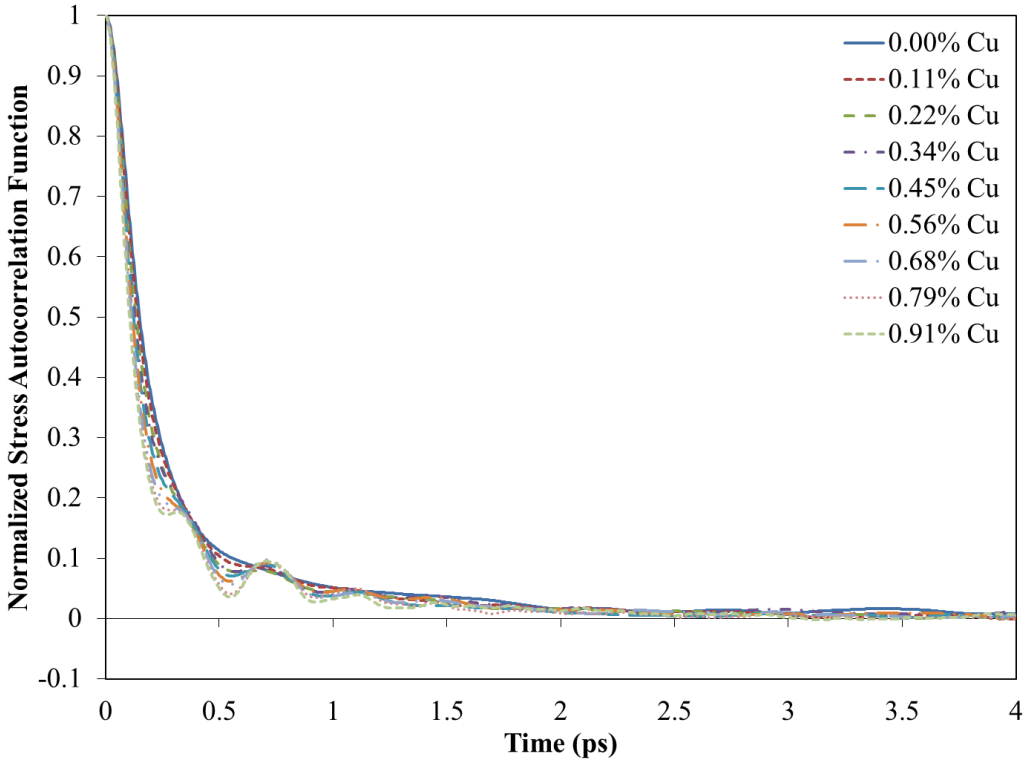

Figure 5.7 Normalized stress autocorrelation function for 0.7 nm diameter copper in argon.

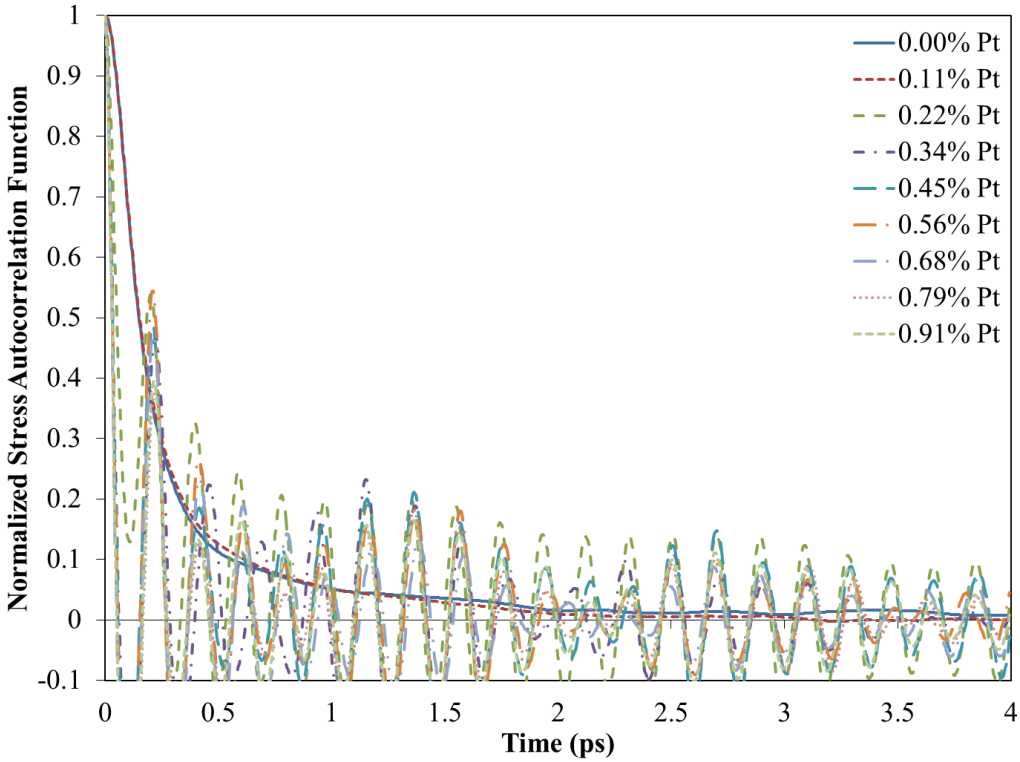

Figure 5.8 Normalized stress autocorrelation function for 0.7 nm diameter platinum in argon.

to zero over the $M\Delta t$ = 4 ps integration period (figures 5.2, 5.4, 5.6, and 5.8) and had increasingly larger amplitude oscillatory behavior. While this invalidates the shear viscosity data obtained from these results, insights can still be obtained regarding shear viscosity characteristics of fluids with nanoparticle suspensions that have relatively larger masses than the base fluid. This will be addressed further in section three of this chapter.

An interesting observation can be noted regarding the decay of the stress autocorrelation functions for the each of the nanofluids compared to the pure homogeneous argon fluid. In a homogeneous material like pure argon, it has been shown that the normal stress autocorrelation function for pure argon will decay monotonically, as was the case for heat flux autocorrelation function [149]. Within this monotonically decreasing function of pure argon fluid, there are also two regions of decay: 1) a region of rapid decay at the beginning of the function which is due to purely atomistic interactions, and 2) a subsequent larger region of slower decay that results from the exchange of momentum during a collision [150].

However, the insertion of either platinum or copper nanoparticles changes the decay into a non-monotonic, oscillatory form. Once again, this effect is similar to what is seen in the molecular dynamics simulations of water, where this behavior was explained as possibly originating from the librational motion of bounded water molecules generating a strong coupling between the rotational and translational degrees of freedom [151]. Since the system modeled in this investigation consists of spherical molecules where rotational and translational degrees of freedom are not a factor, another suggestion for this behavior is proposed and will be discussed further in section 3 of this chapter.

5.2 Size and Interaction Energy Effects on Shear Viscosity

In order to capture the size and interaction energy effects on the shear viscosity of the nanofluid, molecular dynamics simulations utilizing the colloid model described in chapter 2 were used with the parameters found in tables 2.1 and 2.2. Keeping in mind that the volume changed with increasing nanoparticle diameter, the shear viscosity of pure argon for each volume was first calculated and analyzed to ensure consistency. The average value for the volumes corresponding to nanoparticle diameters ranging from 0.4 nm to 1.0 nm was found to be 265.83 ± 9.72 μPa·s, which is consistent with the value of 299.37 μPa·s provided by the National Institute of Standards and Technology [128].

A quick overview of figure 5.9 shows that the increase in shear viscosity may be directly proportional to the concentration of copper nanoparticles suspended in the argon fluid with the proportionality constant being a function of the nanoparticle diameter. The larger nanoparticle diameters caused the proportionality to approach the increments predicted by the theoretical models of Krieger and Einstein. In contrast with this result, increasing the diameter of a platinum nanoparticle (figure 5.10) did not proportionally affect the correlation between shear viscosity increment and nanoparticle concentration. A comparison between these results and those of thermal conductivity enhancement (figures 4.9 and 4.10) leads to a similar conclusion drawn in section 5.3; the sole factor of nanoparticle size does not directly affect shear viscosity increases seen in previous theoretical and experimental studies.

Unlike thermal conductivity seen in chapter 4 that had certain thermal conductivity enhancements invalidated by the theoretical limit imposed by the most

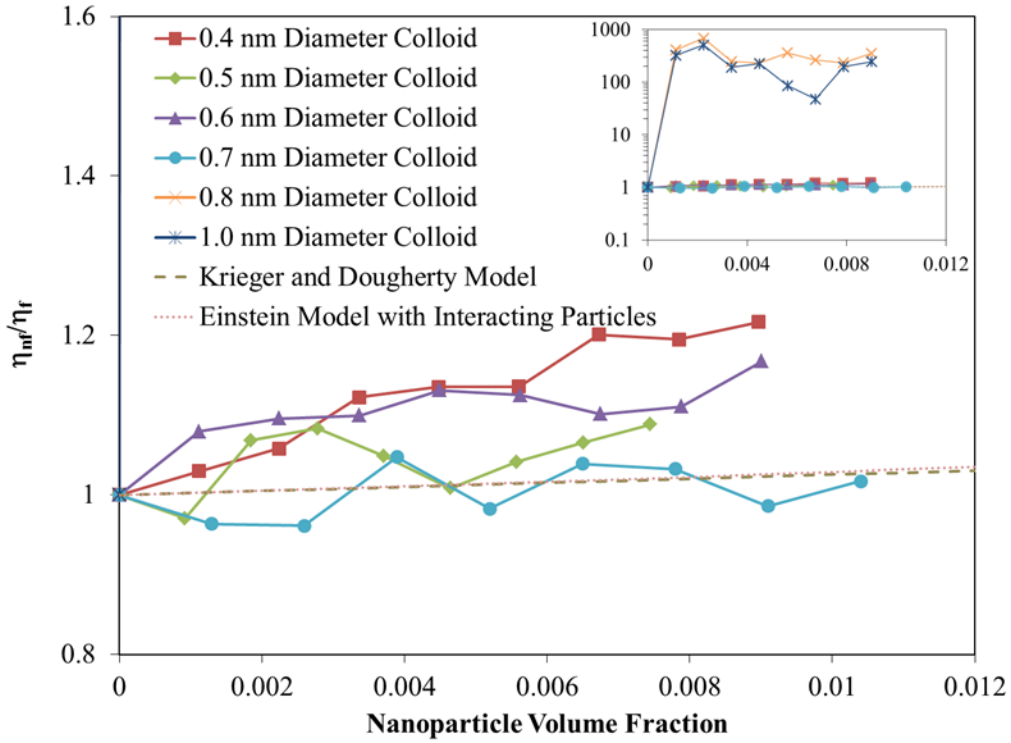

Figure 5.9 Increases of shear viscosity in argon fluid with increasing copper nanoparticle diameter compared to theoretical models.

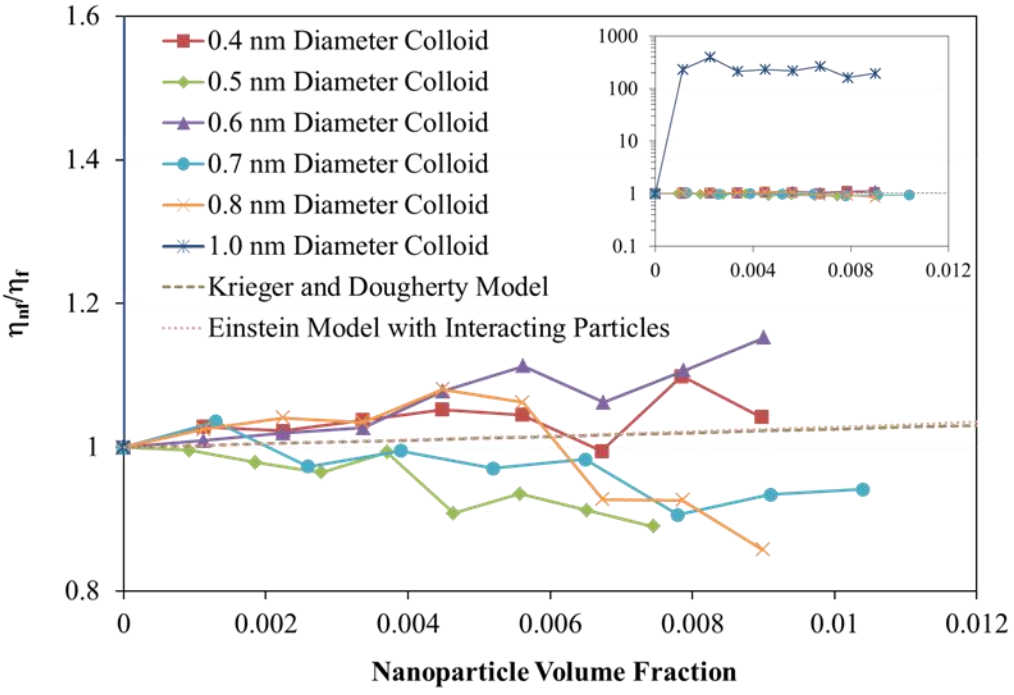

Figure 5.10 Increases of shear viscosity in argon fluid with increasing platinum nanoparticle diameter compared to theoretical models.

efficient methods of heat conductance the solid phase of pure argon, it is possible for shear viscosities to reach the high values obtained by the molecular dynamics simulations in this investigation. As discussed in chapter 1, fluids with particle suspensions can exhibit non-Newtonian characteristics that are dependent on the applied shear stresses. At high shear stresses, shear thickening could occur and lead to increases in the shear viscosity of as much as 200%, even at low particle concentrations. However, since this analysis assumes that the shear stress applied is such that the response remains in the linear regime, these increases would not be applicable. An analysis of the effect that the nanoparticle/fluid interaction energy has on shear viscosity calculations for fluids with nanoparticle suspensions of the same diameter is shown in figures 5.11–5.14. As the nanoparticle/fluid-to-fluid/fluid interaction energy ratio increased for the same sized nanoparticle suspended in fluid, there appeared to be correlation between nanoparticle volume fraction and shear viscosity increase and more closely followed the behavior of the theoretical model predictions of finely dispersed particles (Krieger and Dougherty) and the interacting particles (modified Einstein model). Although the higher interaction energies that corresponded to larger local fluid densities surrounding the nanoparticle (as is discussed in section 3.1) failed to predict enhancements in thermal energy transport, the increased interaction at the interfacial region appears to have a significant effect on the increase in shear viscosity of the base fluid. While the increase in shear viscosity does not appear to correlate with stronger interactions of the same nanoparticle type, the more strongly interacting copper had higher shear viscosities that the platinum nanoparticles. Since the difference in interaction energies between copper and platinum to the argon

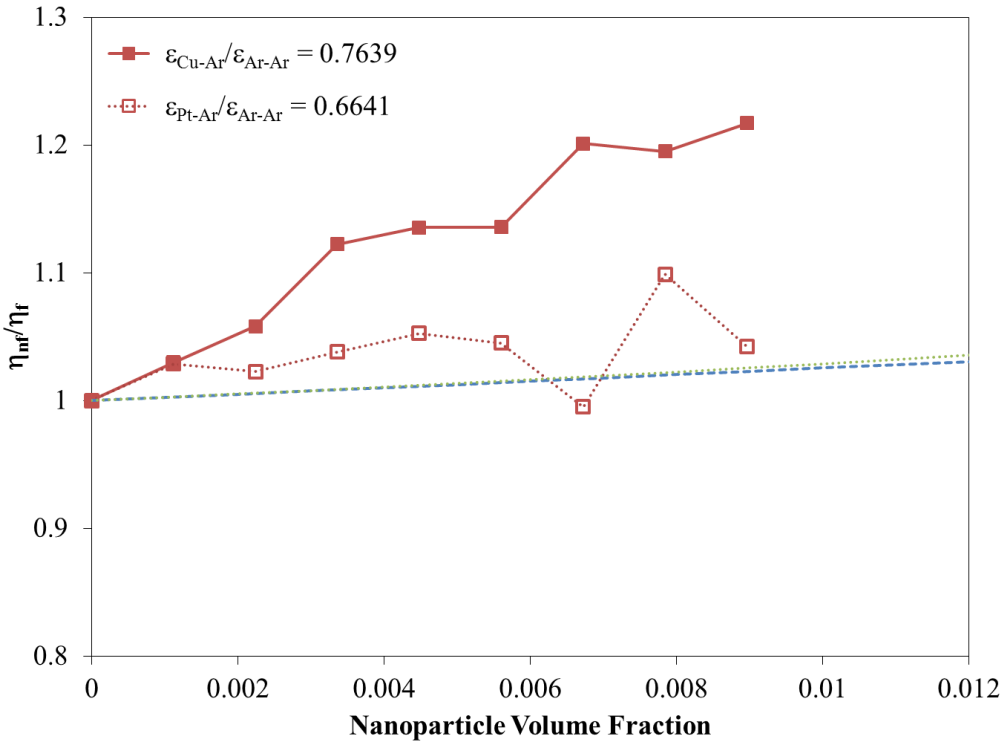

Figure 5.11 Effects of interaction energy on shear viscosity calculation results of copper and platinum nanoparticles with a diameter of 0.4 nm.

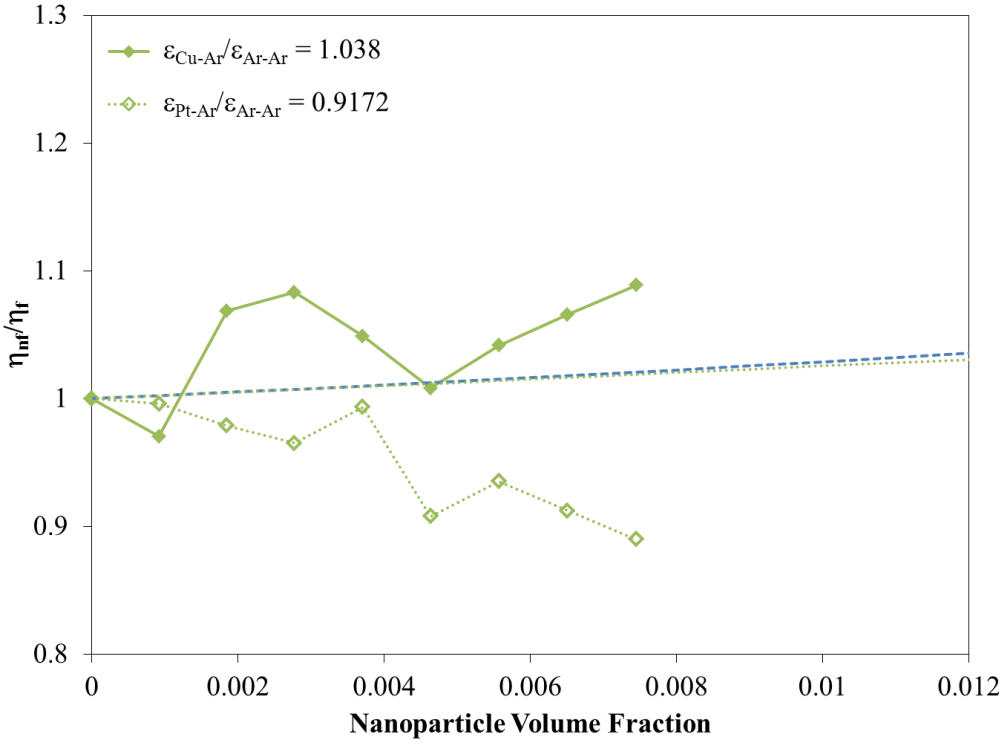

Figure 5.12 Effects of interaction energy on shear viscosity calculation results of copper and platinum nanoparticles with a diameter of 0.5 nm.

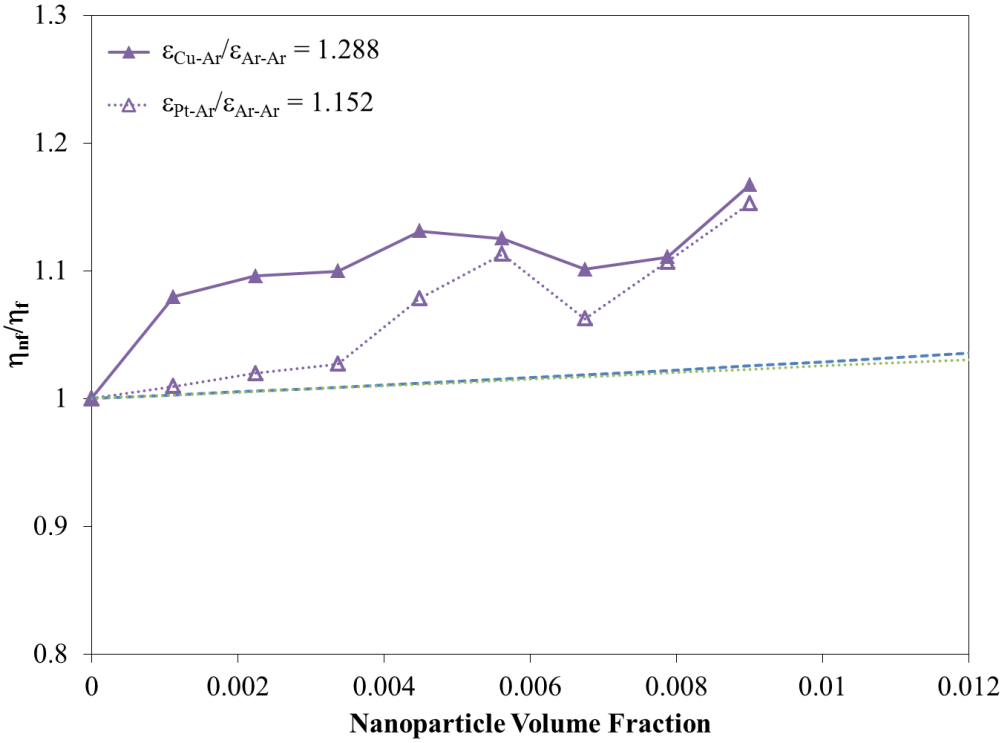

Figure 5.13 Effects of interaction energy on shear viscosity calculation results of copper and platinum nanoparticles with a diameter of 0.6 nm.

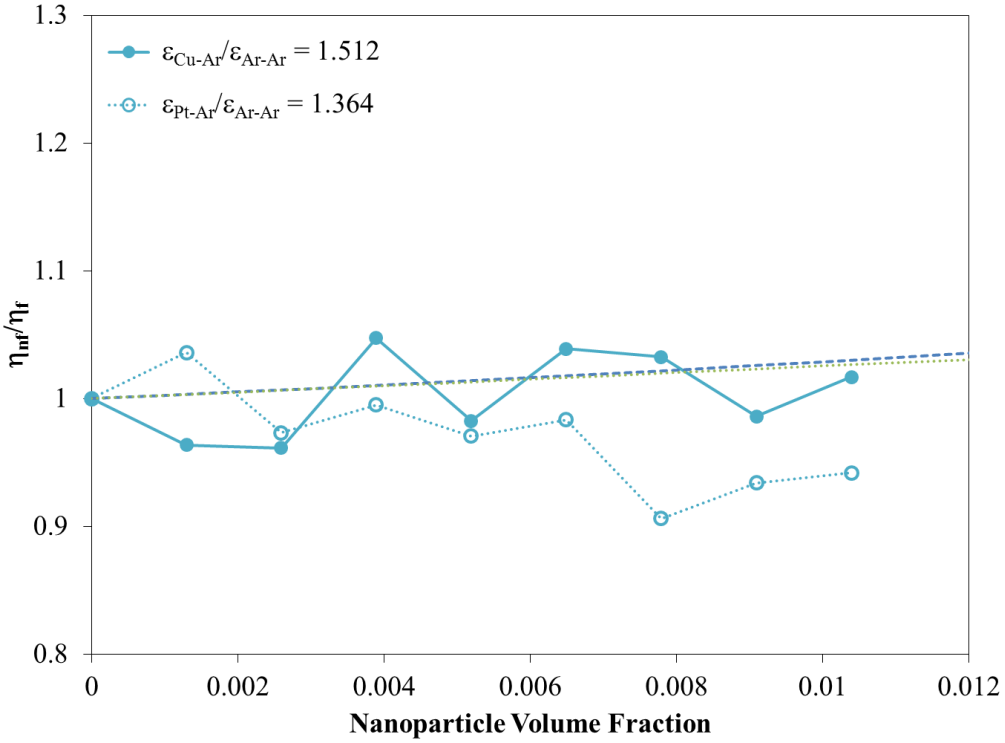

Figure 5.14 Effects of interaction energy on shear viscosity calculation results of copper and platinum nanoparticles with a diameter of 0.7 nm.

fluid was minimal, this factor could be a significant factor to how the shear viscosity increases in nanofluids.

5.3 Mechanisms of Momentum Transport and their Characteristics

The process by which the thermal fluctuations of the constituent particles within the control volume of a fluid become uncorrelated also involves the propagation of long-wavelength transverse acoustic waves through the medium [133]. (See figure 5.15) These modes of fluctuation decay are determined from the Fourier-Laplace transform of the conservation laws for the local densities used to develop equations 2.1 – 2.4. The solution of the resulting hydrodynamic matrix yields a solution that has a set of imaginary double roots that correspond to the decay modes that will be discussed next.

An analysis of equations 2.3 and 2.4 shows that momentum can be transferred within a liquid in two distinct ways: 1) kinetically and 2) through collisions. Figure 5.16 can be used as a graphical representation of these modes. Like thermal transport, the transport of momentum through kinetic motion, *K*, (figure 5.16-a) is defined by the velocity of each individual particle in the overall system. Particle collisions, *C*, (figure 5.16-b) that arises from shear forces applied to particle *i* from the sum total of particles *j* less than some distance r_{cutoff} away also play a role in momentum transport. Unlike the heat flux autocorrelation function that is calculated from vectors that express the flow of

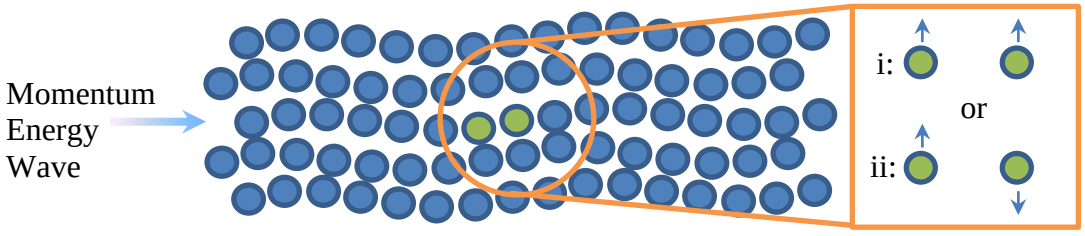

Figure 5.15 Hydrodynamic collective modes for heat and momentum fluxes in a fluid and the corresponding particle motion characteristics.

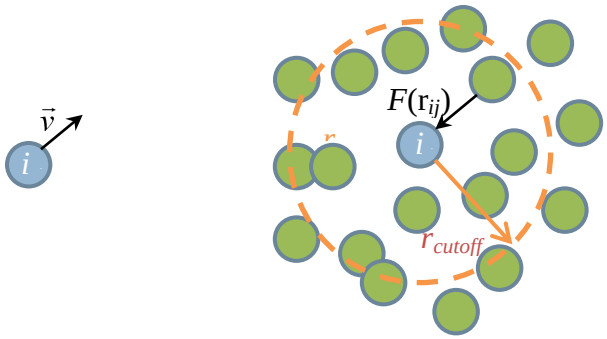

(a) (b)

Figure 5.16 Modes of momentum transfer in a fluid.

heat through the system, the stress autocorrelation function is calculated from the scalar off-diagonal components of the stress tensor experiences in the volume investigated. This means that the calculated shear viscosity is just a component of the total shear stress seen in the volume and that isotropicity cannot be assumed. In this work, the shear viscosity calculated is in the *xy* direction.

Each of these momentum transport modes can be characterized as thermal fluctuations propagating at the speed of sound through the fluid as longitudinal transverse waves, as depicted in figure 5.15. To determine the contribution of these modes of momentum transport and their frequency characteristics, the shear viscosity calculations were decomposed into self- and cross-correlations of the components of momentum transfer, with the resulting data presented in figures 5.14–5.22. Three key observations can be made from these plots regarding the effect nanoparticle suspensions on the modes of energy transfer in the fluid.

Firstly, as was determined to be the case for the thermal conductivity calculations, since the system is at equilibrium with no velocity gradients, there is very little to no velocity change for each of the constituent particles in the system and the contribution to

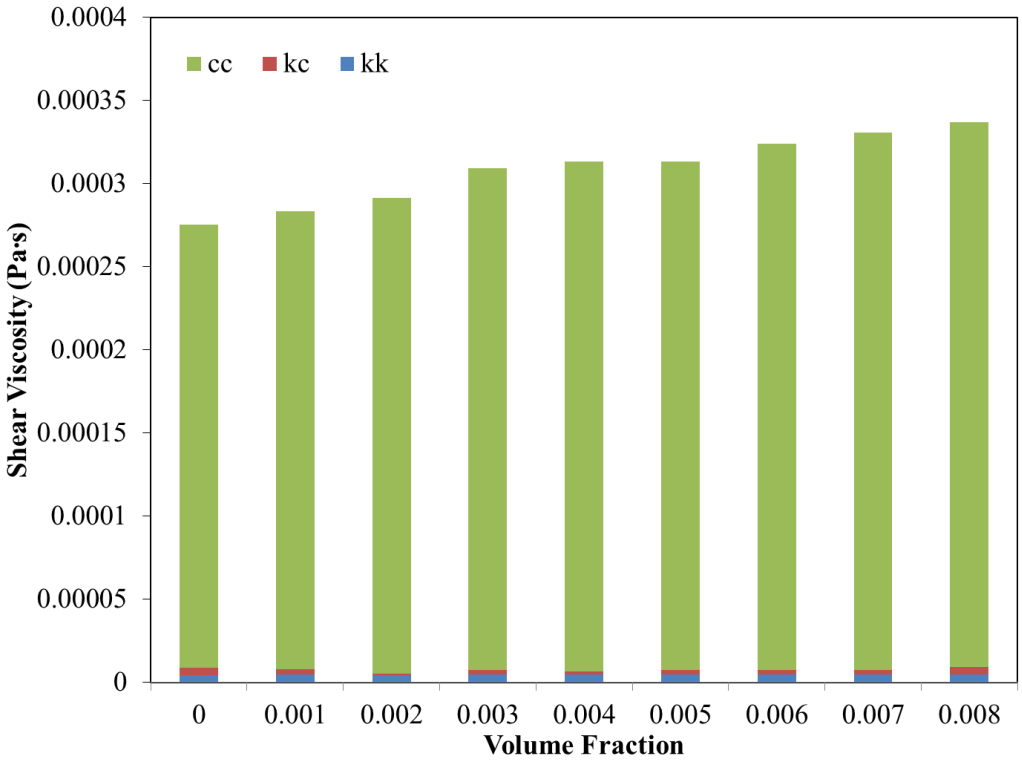

Figure 5.17 Components of momentum transfer within argon fluid with 0.4 nm copper suspensions.

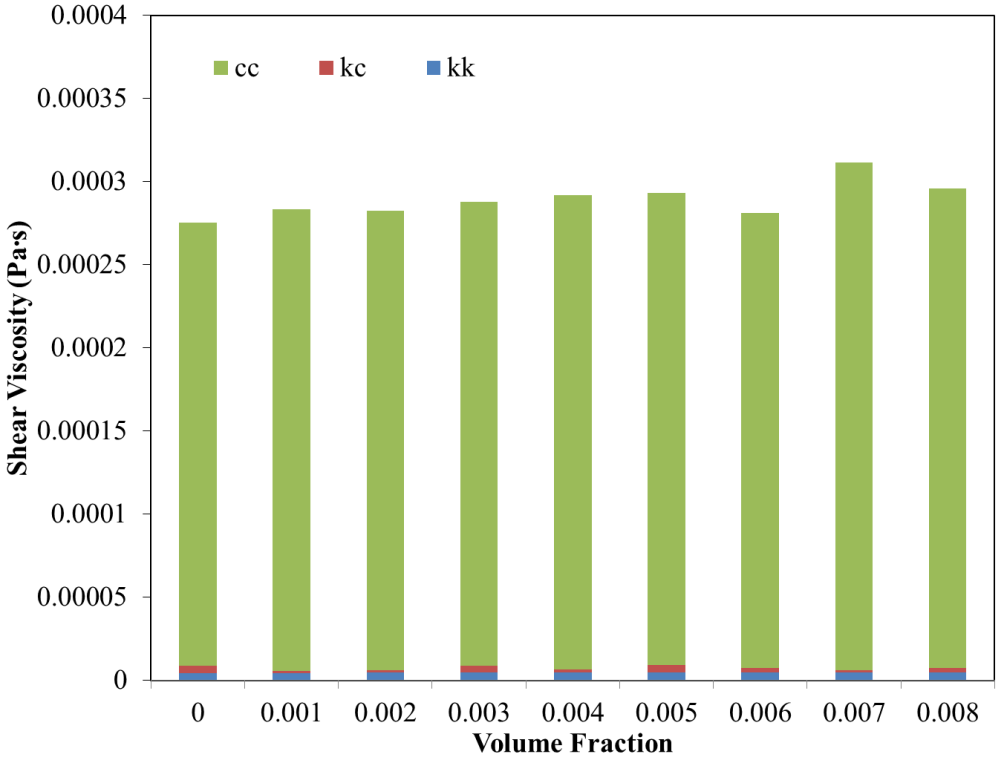

Figure 5.18 Components of momentum transfer within argon fluid with 0.4 nm platinum suspensions.

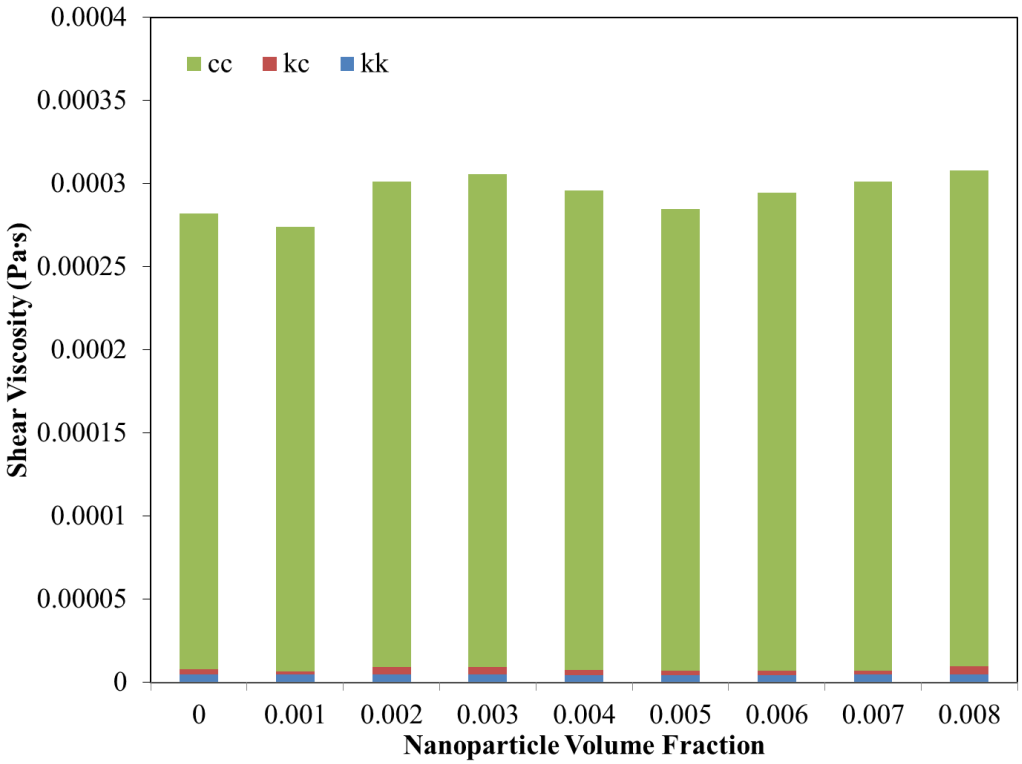

Figure 5.19 Components of momentum transfer within argon fluid with 0.5 nm copper suspensions.

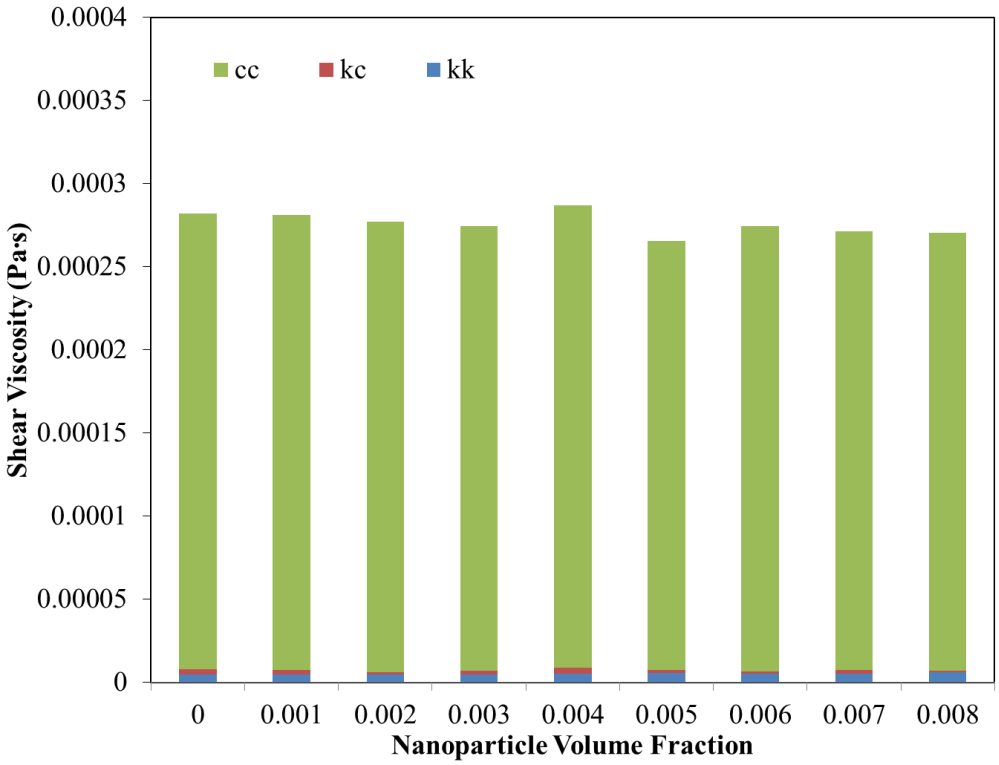

Figure 5.20 Components of momentum transfer within argon fluid with 0.5 nm platinum suspensions.

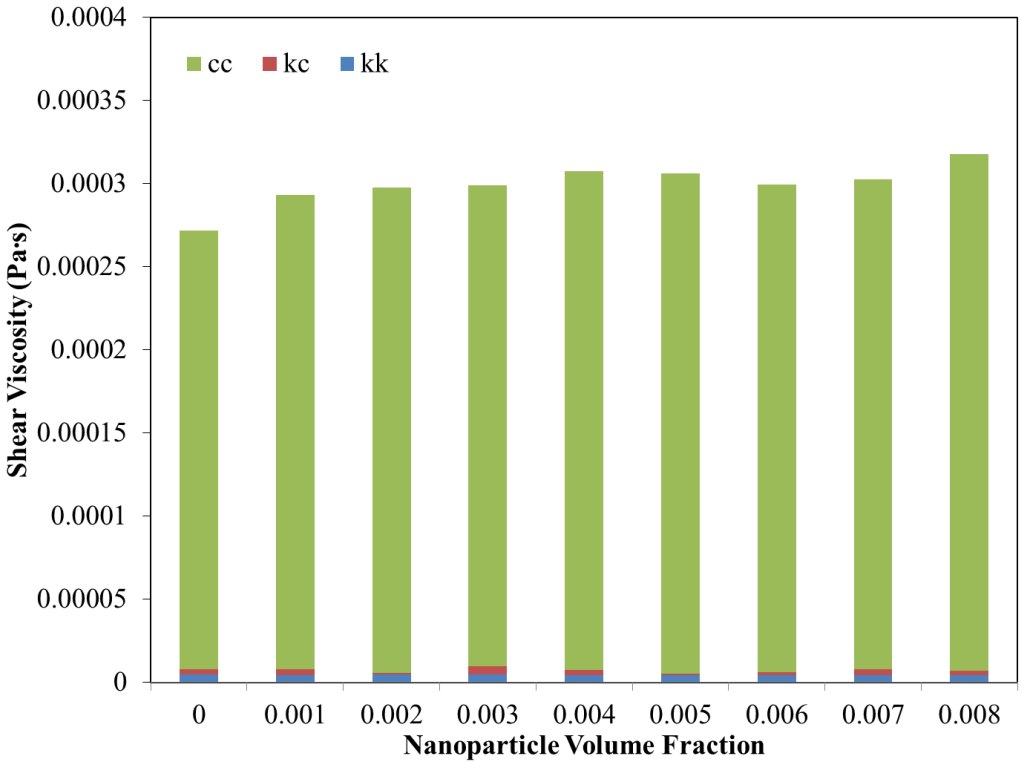

Figure 5.21 Components of momentum transfer within argon fluid with 0.6 nm copper suspensions.

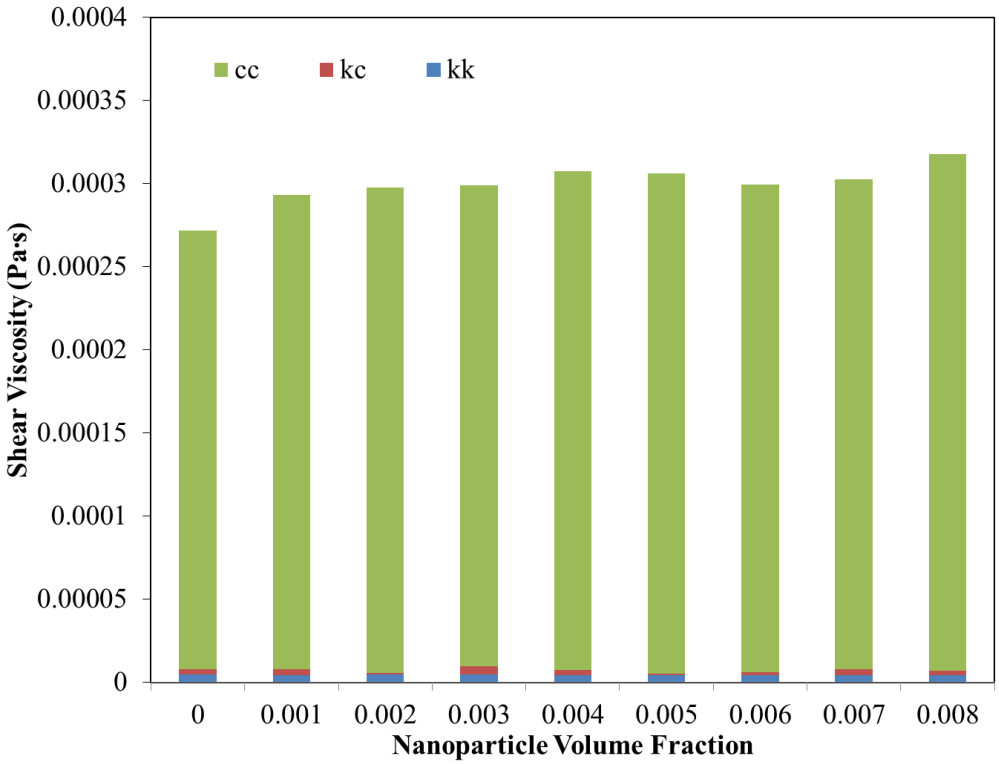

Figure 5.22 Components of momentum transfer within argon fluid with 0.6 nm platinum suspensions.

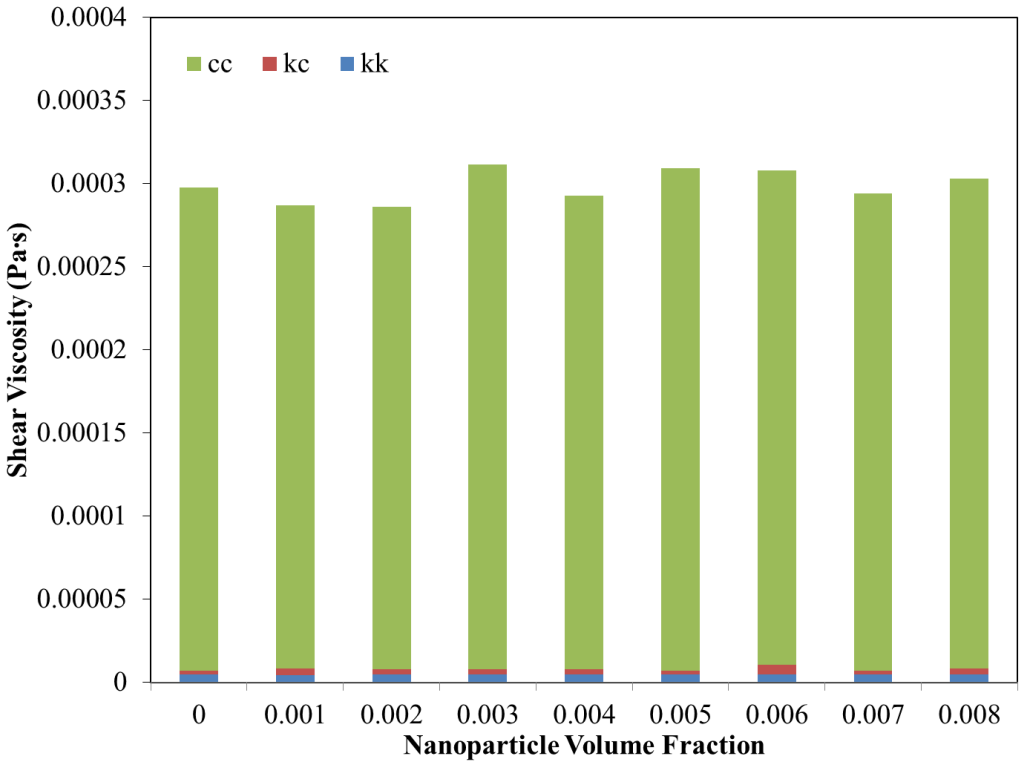

Figure 5.23 Components of momentum transfer within argon fluid with 0.7 nm copper suspensions.

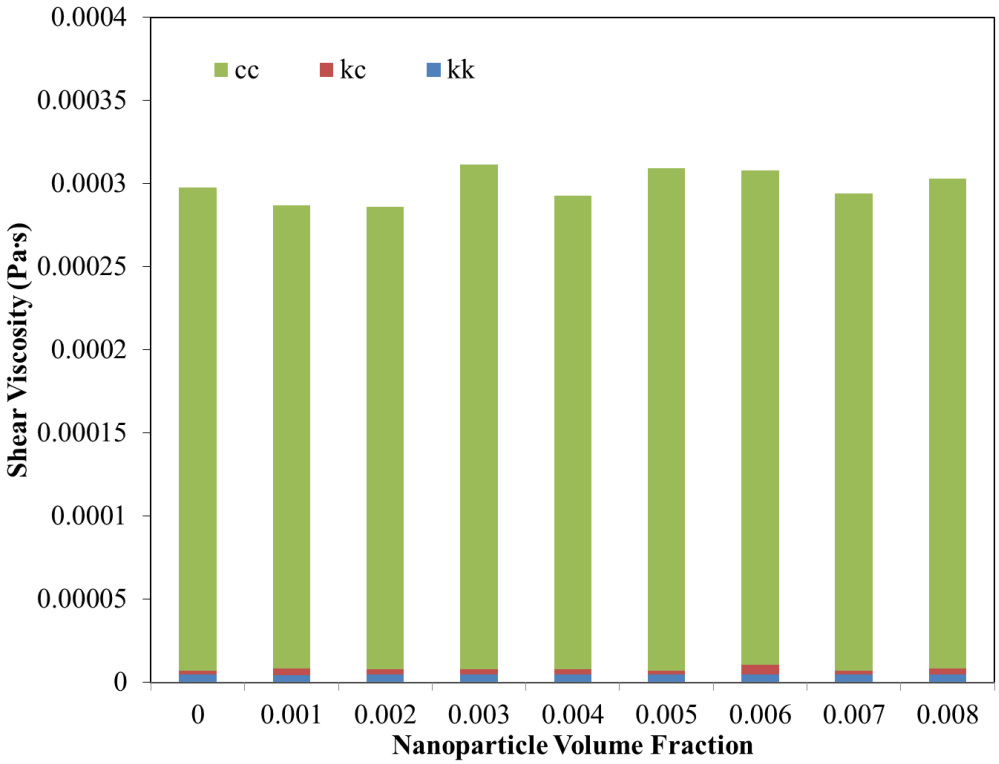

Figure 5.24 Components of momentum transfer within argon fluid with 0.7 nm platinum suspensions.

momentum transport from the self-correlation of the kinetic portion (KK) is negligible. The contribution to momentum transport is also minimal for the cross-correlation of the kinetic and collision energy components (KC).

Lastly, the consistently significant contribution to shear viscosity was the self-correlation of the collision component (CC) of equation 2.4. This intuitive conclusion can easily be drawn considering that thermal fluctuations in the volume induce collisions between particles. The thermal fluctuations dissipated through these collisions gradually become uncorrelated which is the reason for the long tail behavior of the stress autocorrelation function seen in figures 5.1–5.8. This result relatively compares with other work, which has suggested that interactions between the nanoparticle and the fluid factored significantly into the shear viscosity of the overall nanofluid. However, by using the colloid model in the molecular dynamics simulations, the results obtained focuses solely on the nanoparticle-fluid interactions.

In addition, it is noteworthy to mention that for the self- and cross-correlation of the kinetic and collision components, there is a noticeable lack of dependency on the volume fraction of nanoparticle suspension over the values selected. However, there is no indication that agglomeration is a significant factor in the calculation of momentum energy transport as was found to be the case for thermal conductivity. However, additional work needs to be performed to determine if larger concentrations of nanoparticle interactions would affect shear viscosity as was suggested for thermal conductivity values.

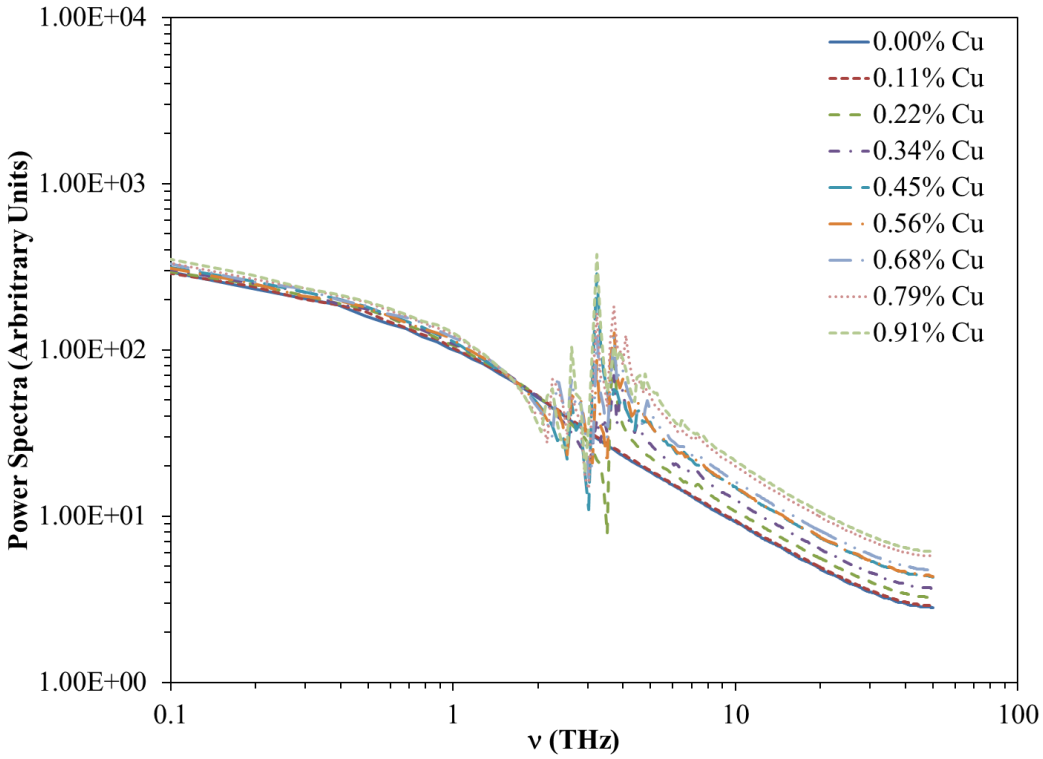

Figure 5.25 Power spectra for CC self-correlation function of argon fluid with varying concentrations of 0.4 nm diameter copper suspensions.

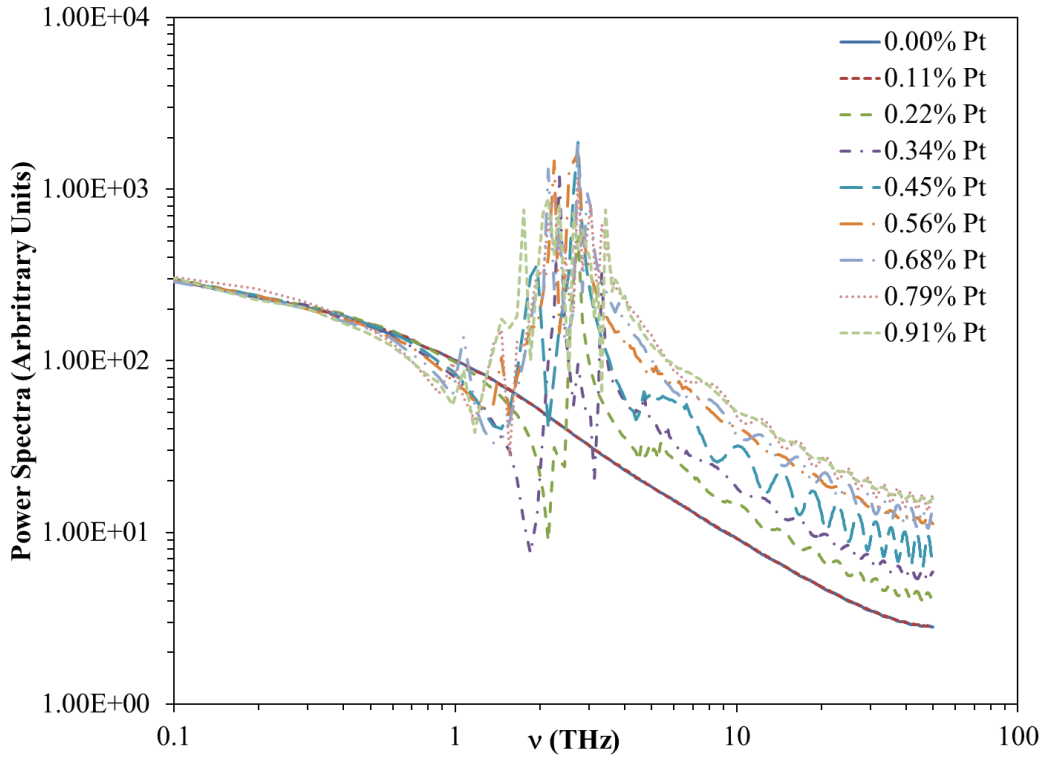

Figure 5.26 Power spectra for CC self-correlation function of argon fluid with varying concentrations of 0.4 nm diameter platinum suspensions.

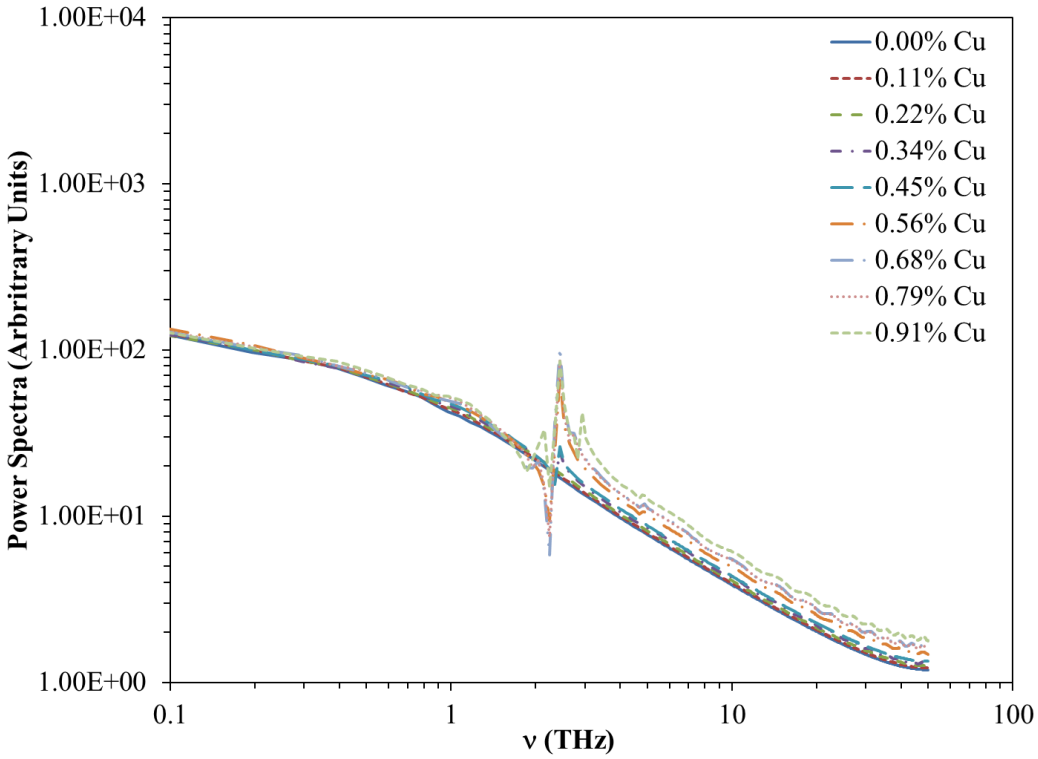

Figure 5.27 Power spectra for CC self-correlation function of argon fluid with varying concentrations of 0.5 nm diameter copper suspensions.

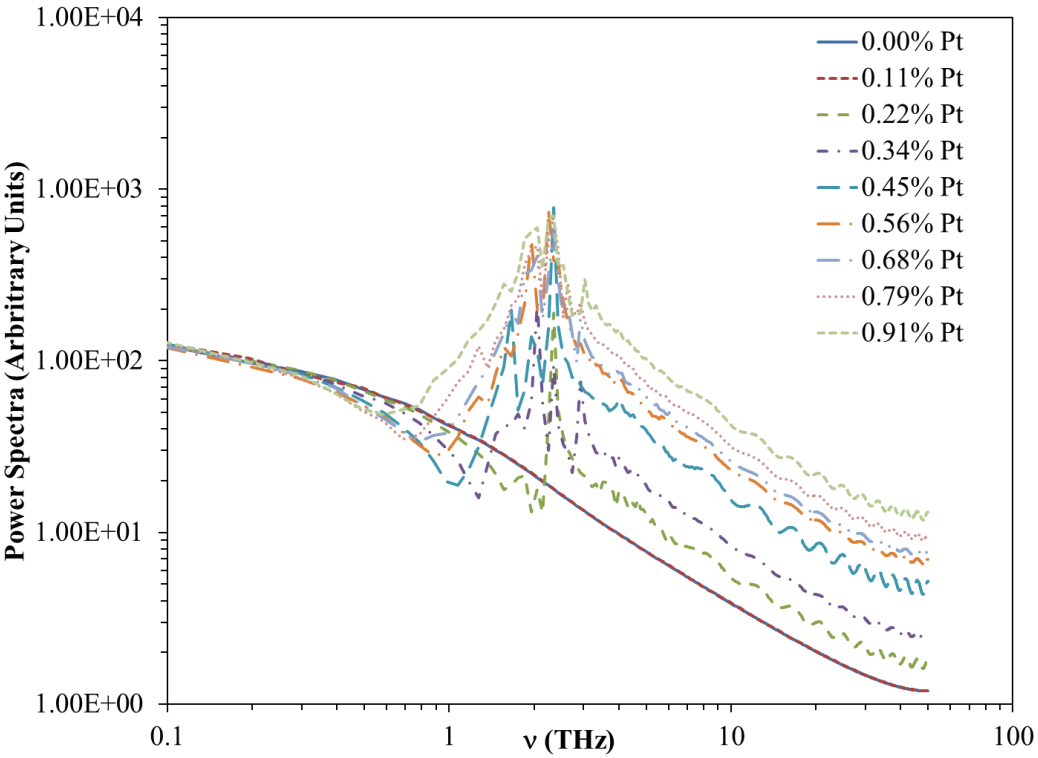

Figure 5.28 Power spectra for CC self-correlation function of argon fluid with varying concentrations of 0.5 nm diameter platinum suspensions.

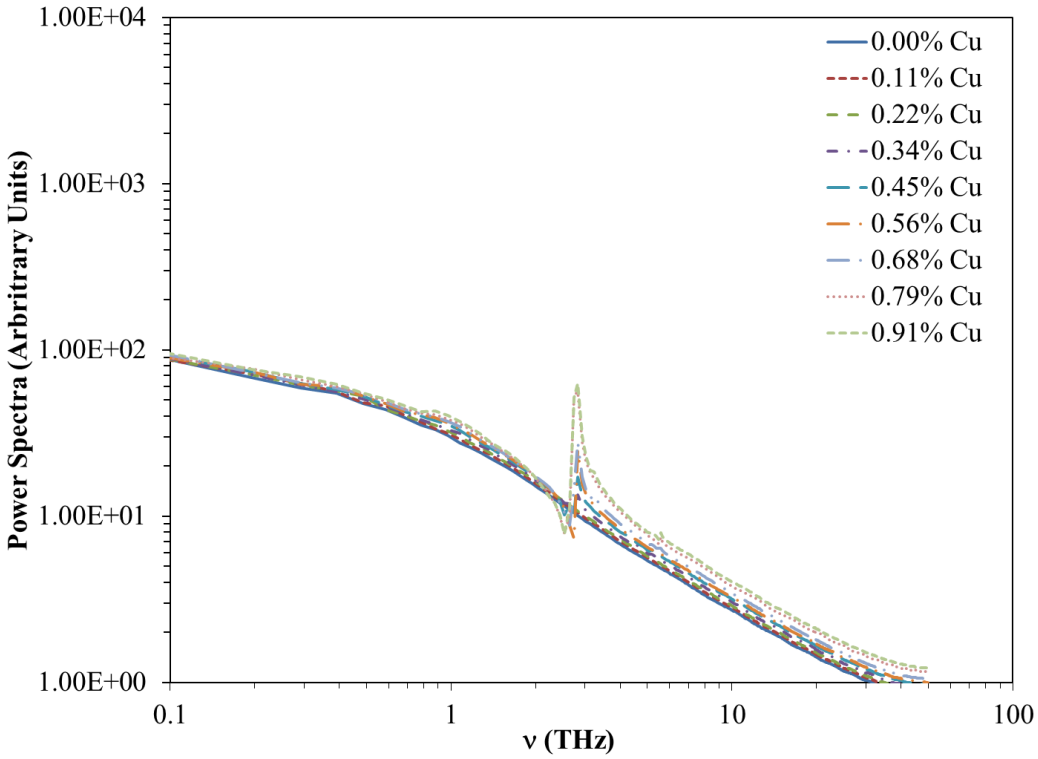

Figure 5.29 Power spectra for CC self-correlation function of argon fluid with varying concentrations of 0.6 nm diameter copper suspensions.

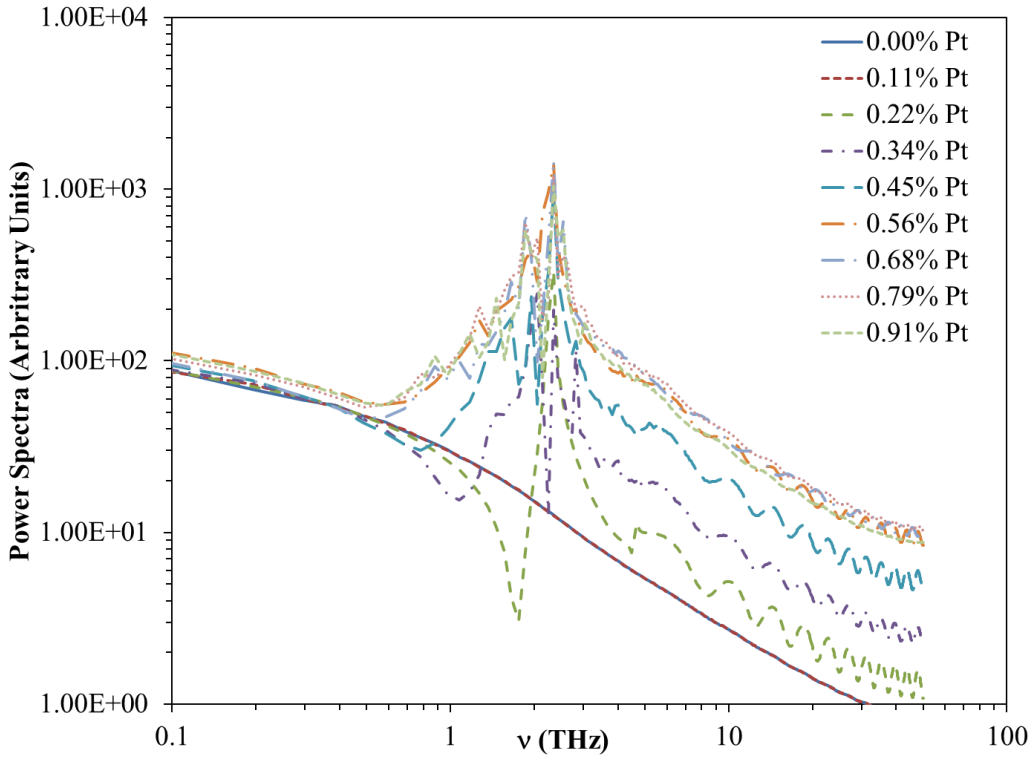

Figure 5.30 Power spectra for CC self-correlation function of argon fluid with varying concentrations of 0.6 nm diameter platinum suspensions.

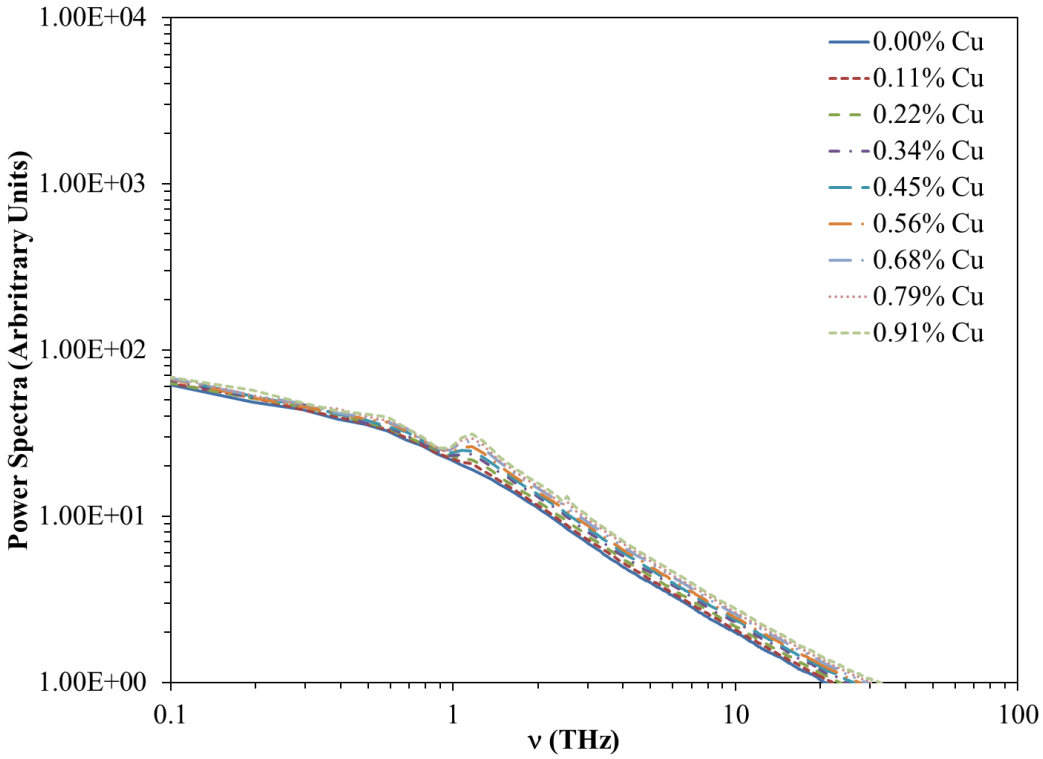

Figure 5.31 Power spectra for CC self-correlation function of argon fluid with varying concentrations of 0.7 nm diameter copper suspensions.

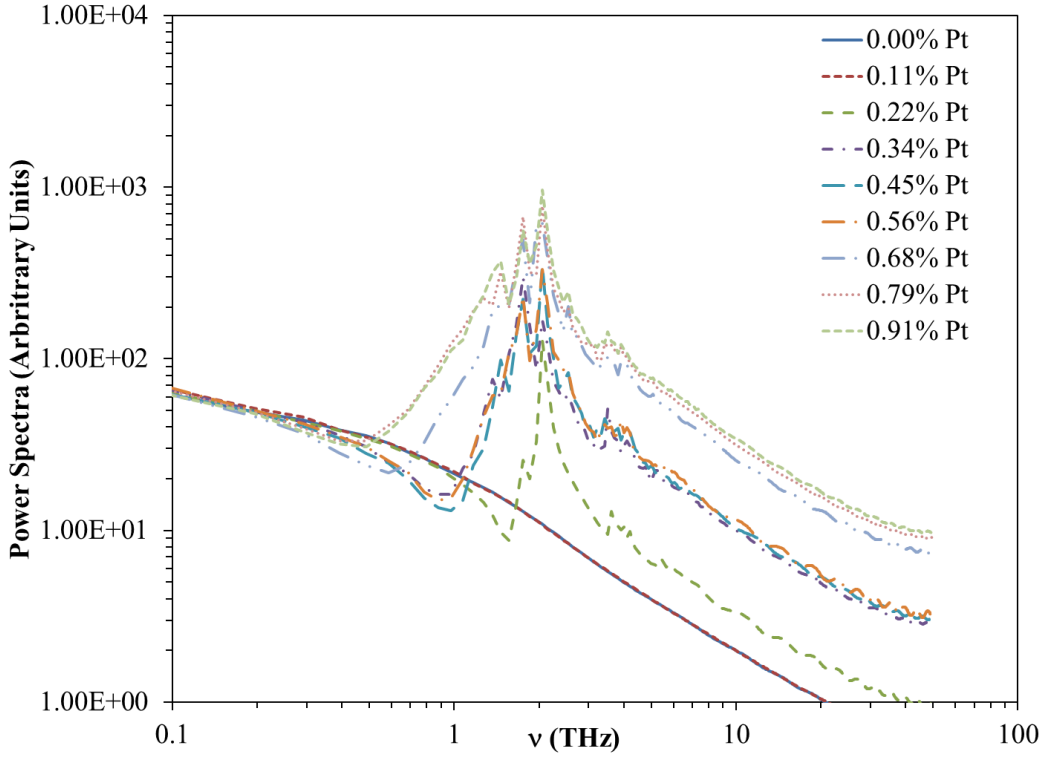

Figure 5.32 Power spectra for CC self-correlation function of argon fluid with varying concentrations of 0.7 nm diameter platinum suspensions.

Now, remembering that momentum transport can be characterized by transverse wave propagation, the next step is to quantify the effect of the presence of a nanoparticle suspension on the collective dynamics of the fluid system. This was done by performing a Fourier transform on the dominant mode of momentum transport (self-correlation of the collision term in the stress autocorrelation function) and analyzing its frequency characteristics.

In the case of a single-component, isotropic fluid, molecular dynamics simulations have shown that the dominant mode of fluctuation decay is without propagation characterized once again by diffusive process [114, 133]. Therefore, it is reasonable to see no frequency information in the Fourier transforms of the self-correlation of the collision term (CC) for pure argon (see figures 4.24–4.31). The long tails seen in figure 5.1-5.8 for the pure argon stress autocorrelation function support this idea of a slowly decaying diffusive process. However, the insertion of both copper and platinum nanoparticles (see figures 5.25-5.32) appears to have enhanced transport of transverse momentum within the nanofluid through an amplification of the transverse acoustic waves that have frequencies between 1–10 THz. There also appears to be a dependency on the size of the nanoparticle diameter, with a clear dominant frequency of approximately 2.0 THz developing with a platinum nanoparticle of 0.7 nm. The broad range of frequencies seen in the Fourier transform of the platinum nanoparticle may have attenuated the key frequency for shear viscosity increase that is seen for the copper nanoparticle.

5.4 Infinite Frequency Shear Modulus and Maxwell Relaxation Time

In field of solid mechanics, the resistance of a bulk material to an applied shear force is called the shear modulus (G) and is defined by the ratio of the shear force to the shear strain. This material property is independent of the shear force applied and defines the deformation characteristics of the solid. However, within the field of fluid mechanics, meaningful information regarding the shear modulus can only be obtained when the shear force is applied as a waveform with some frequency, ω. In the case where the shear force is instantaneous ($\omega \to \infty$), a fluid at the length scales being used in this investigation has an infinite frequency shear modulus governed by the atomic interactions and local densities discussed earlier in chapters 2 and 3 and can be written as

$$G_\infty = \rho kT + \frac{2\pi}{15}\rho^2 \int_0^\infty g(r) \frac{d}{dr}\left[r^4 \frac{dU}{dr} \right] dr \tag{5.1}$$

At the thermodynamic state defined in chapter 2 for pure argon, the infinite frequency shear modulus has been determined to be 1,003.25 MPa, which is similar to the calculated value of 955.06 MPa found by Schoen [152].

As can be noted in figure 5.33, the infinite frequency shear modulus is highly dependent on the size of the copper nanoparticle suspension, but not over the volume fractions investigated. Therefore, when these values are used to calculate the shear relaxation time based on the zero-frequency shear values determined in section 5.2 (figure 5.34)

$$\tau = \frac{\eta_o}{G_\infty} \tag{5.2}$$

it can be seen that the values only decreased with the presence of nanoparticle suspensions, regardless of size and volume fraction. These decreased relaxation times

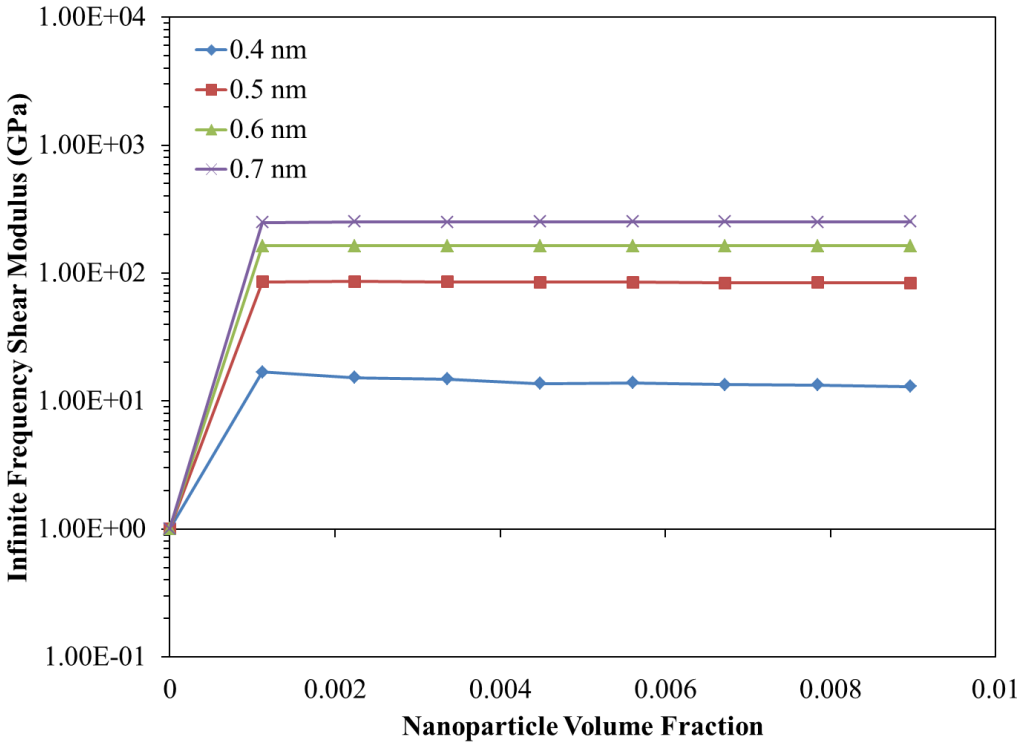

Figure 5.33 Shear modulus of argon with copper nanoparticles of increasing diameter.

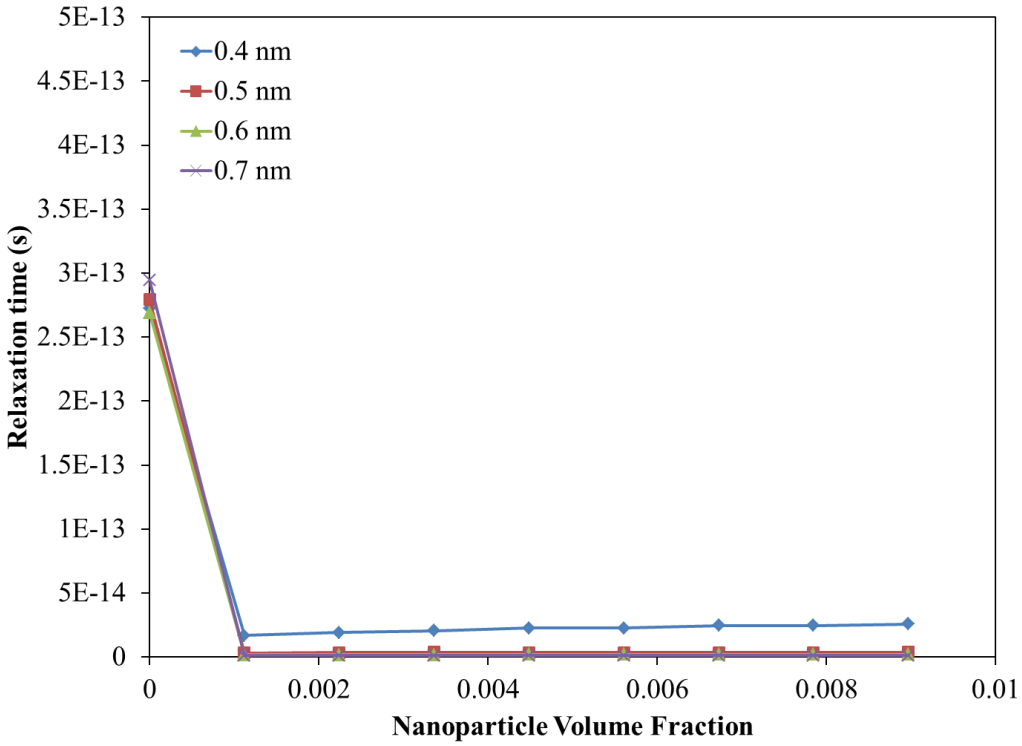

Figure 5.34 Relaxation times for argon fluid with copper nanoparticle suspensions of varying volume fractions.

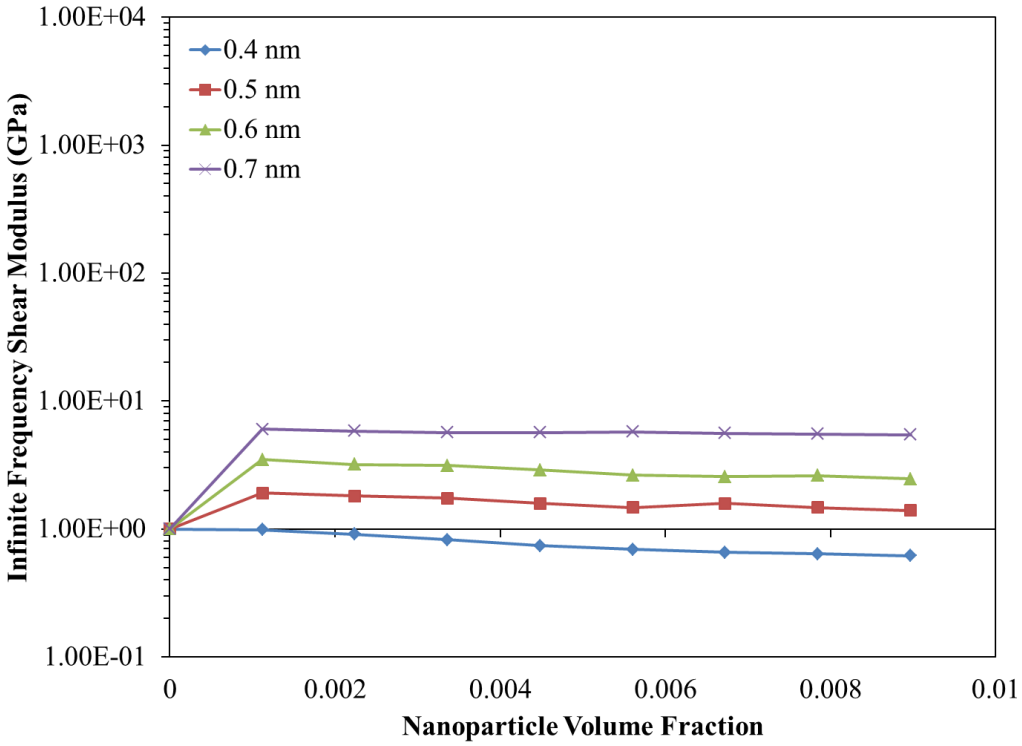

Figure 5.35 Shear modulus of argon with platinum nanoparticles of increasing diameter.

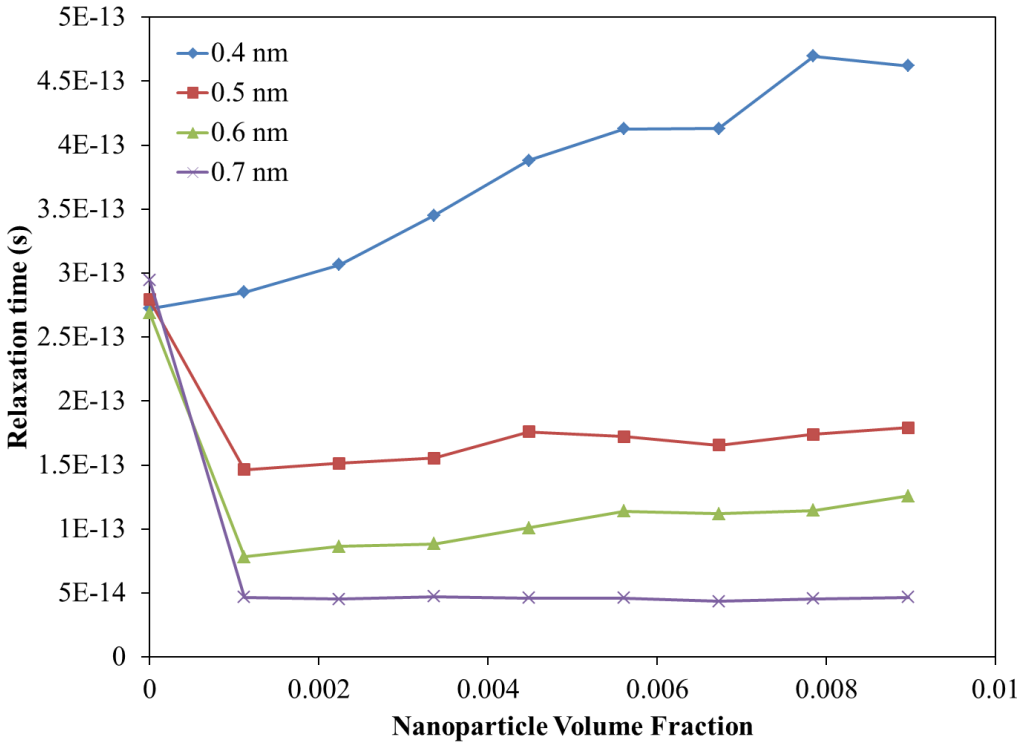

Figure 5.36 Relaxation times for argon fluid with platinum nanoparticle suspensions of varying volume fractions.

support the experimental results that suggest that the shear characteristics of nanofluids are Newtonian and do not deviate from bulk fluid properties.

Figure 5.35 shows that the infinite frequency shear modulus is not only highly dependent on the size of platinum nanoparticle suspensions, but also over volume fraction. This is directly related to the decrease in local density surrounding platinum nanoparticles discussed in chapter 2. Therefore, when the shear relaxation time is calculated as presented in figure 5.36, the reduced infinite-frequency shear modulus for 0.4 nm platinum nanoparticle suspensions increased the shear relaxation time with increasing nanoparticle concentration. This increase corresponds to a shift in the shear response of the nanofluid to a viscoelastic region similarly discussed in table 1.1. The characteristic viscoelastic response found in ultra-low volume fraction nanofluids may be the source of high shear viscosities seen in some experimental results.

5.5 Summary

Molecular dynamics simulation results indicate that the calculated shear viscosity of the nanofluids investigated depend on the interaction between the particle and the fluid. However, this dependency was not significant compared to the volume fraction dependent theoretical models. Therefore, it can be concluded once again that the nanoparticle fluid interaction models used in molecular dynamics simulations is a less than significant factor in the determination of the shear viscosity of the overall nanofluid. It does appear that the insertion of nanoparticle suspensions does enhance the transverse acoustic wave propagation characteristics of the overall fluid by extending the momentum relaxation mode beyond the diffusive behavior seen in pure fluids. The calculated shear viscosity of the nanofluids investigated showed a dependency on the

interaction between the particle and the fluid. However, this dependency was not significant compared to the volume fraction dependent theoretical models. Therefore, it can be concluded once again that the nanoparticle fluid interaction models used in molecular dynamics simulations is a less than significant factor in the determination of the shear viscosity of the overall nanofluid. It does appear that the insertion of nanoparticle suspensions does enhance the transverse acoustic wave propagation characteristics of the overall fluid by extending the momentum relaxation mode beyond the diffusive behavior seen in pure fluids.

Chapter 6 – Conclusion

Due to the lack of consensus amongst experimental results, characterization of the thermophysical properties that most influence heat transfer were investigated using molecular dynamics simulations. Within these simulations, different nanoparticle types, ranges of nanoparticle diameters, and a simple base fluid were used to best approximate macroscale characteristics seen in experimental investigations. It is through this bottom-up approach that a set of possible underlying static and dynamic characteristics that increase these properties due to the presence of nanoparticle suspensions were identified and isolated.

Using a size-dependent colloid potential to describe nanoparticle interactions in a fluid, it was determined that the presence of a nanoparticle that strongly interacts with the base fluid creating locally high fluid density does not correlate to increases in the thermal conductivity of the overall fluid. The platinum/argon nanofluid had a relatively weak nanoparticle/fluid interaction and decreased with increasing diameter. This led to decreasing local densities and even to values below the bulk density of the argon fluid. However, the platinum/argon nanofluid had consistent increases in thermal conductivity over the volume fractions investigated. Analysis of the components of thermal energy transfer suggests that the mass of the nanoparticle suspensions enhanced particle diffusion within the fluid by amplifying the propagating longitudinal wave characteristics. Considering that the thermophysical properties of the nanoparticle were

not involved in the thermal conductivity calculations, it is concluded that this nanoparticle mass relative to the base fluid is a physical characteristic that is critical to the conduction of thermal energy within a fluid.

On the other hand, the calculated shear viscosity of the nanofluids investigated showed a dependency on the interaction between the particle and the fluid. However, this dependency was not significant compared to the volume fraction dependent theoretical models. Therefore, it can be concluded once again that the nanoparticle fluid interaction models used in molecular dynamics simulations is a less than significant factor in the determination of the shear viscosity of the overall nanofluid. It does appear that the insertion of nanoparticle suspensions does enhance the transverse acoustic wave propagation characteristics of the overall fluid by extending the momentum relaxation mode beyond the diffusive behavior seen in pure fluids.

Finally, even though there are local static structural characteristics near the nanoparticle surface that are of a higher magnitude than for a pure argon fluid, this does not appear to change the linear shear response of the base fluid. The shear response time also remained small and was on the other order of 10^{-13} s. These results do not appear to hold true for the case of a small, strongly interacting nanoparticle like the copper nanoparticle in argon fluid. In this case, the shear relaxation time increased with increasing nanoparticle volume fraction indicating a possible viscoelastic response at volume fractions less than 0.001. While the increase in the relaxation time was not large, this was the only set of conditions that indicated that there was a dependency of the shear response time on the nanoparticle volume fraction.

6.1 Theory and Experiments

Even though, there have been hundreds of experiments conducted investigating the thermal conductivity, shear viscosity, and density of nanofluids, it is not entirely possible to test some of the parameters and conditions investigated here. This would be the ideal method for verification of the data generated, validate the conclusions drawn in this investigation, and allow for a proper correlation to experimental results. In addition, the nanoparticle/fluid interactions used here do not completely describe the long-range interactions seen in water-based nanofluids or the molecular chain networks developed in oil-based nanofluids. The computation costs for simulating these conditions are high and in some cases impractical. However, with the information gathered here a more focused experimental setup could be performed to yield possible correlations with the theoretical investigations.

6.2 Contribution

The most important contribution of the work presented here may be the theoretical framework developed to support two key characteristics of nanofluids in regards to thermal conductivity enhancement:

1) There is lack of dependency on high thermal conductivity materials to obtain increases in the thermal conductivity of the overall nanofluid. Popular relationships between nanoparticle concentration and thermal conductivity enhancement, such as Maxwell's model and Bruggeman's model, are dependent on large nanoparticle thermal conductivities. If the nanoparticle thermal conductivity is not a factor, then these models break down and no thermal conductivity enhancement should be present. However, this investigation was

able to show that thermal conductivity enhancement is obtained without the use of the material properties of the nanoparticle.

2) The mass ratio of the nanoparticle to the base fluid appears to be a significant contributor to enhanced thermal diffusion within the base fluid, even at nanoparticle fractions < 0.001.

6.3 Future Work

There are three possible extensions of this investigation that should be pursued:

1) Recent experimental work has suggested that the shape of the nanoparticle plays a significant role in thermal conductivity enhancement. Therefore, modification of the colloid model used in this investigation should be performed to allow for colloids of a variety of shapes, especially those that have high aspect ratios.

2) There is a significant lack of molecular dynamics simulations of nanofluids where the base fluid is of molecular form, especially long chain molecules. These more realistic models will provide additional insight into the mechanisms of thermal transport that may not be evident when modeling atomic fluids, as was performed here.

3) Carbon nanotubes have been experimentally shown to make the nanofluid with the highest enhancement in thermal conductivity. Carbon nanotubes have high thermal conductivity values, but their value is one-dimensional. Therefore, a molecular dynamics study to determine the mechanisms of thermal transport within carbon nanotube-based nanofluids would be especially useful.

6.4 Outlook

While the interest in nanoparticles as a viable mechanism for thermal conductivity enhancement in fluids has waned in recent years, the methodologies developed are beneficial for use in other technologies, especially at the nanoscale. As the development and design of materials and devices continue to be performed using the "bottom-up" approach, an understanding of the properties and physical conditions at the nanoscale become increasing more important. In addition to this, the link from the nanoscale to the macroscale has to be strengthened for engineering of the future to progress. It is at this link, that the future in modeling will grow and be the source of new research in the near future.

References

1. Arpaci, V. and P. Larsen, *Convection Heat Transfer*. 1984, Englewoods Cliff, NJ 07632: Prentice-Hall, Inc. 512.

2. Arden, W., et al., *International Technology Roadmap for Semiconductors 2006 Update: Overview and Working Group Summaries*. 2006. p. 15,16.

3. Lorenzen, D., et al., *Micro thermal management of high-power diode laser bars.* Industrial Electronics, IEEE Transactions on, 2001. 48; 48(2): p. 286-297.

4. Choi, S.U.S., *Nanofluids for Improved Efficiency in Cooling Systems*. 2006.

5. Wambsganss, M.W. *Thermal Management in Heavy Vehicles: A Review Identifying Issues and Research Requirements*. in *Vehicle Thermal Management Systems 4 Conference*.

6. Choi, S.U.S. *Enhancing thermal conductivity of fluids with nanoparticles*. in *Proceedings of the 1995 ASME International Mechanical Engineering Congress and Exposition, November 12, 1995 - November 17*. San Francisco, CA, USA: ASME.

7. Lee, S., et al., *Measuring thermal conductivities of fluids containing oxide nanoparticles.* Journal of Heat Transfer, 1999. 121(Journal Article): p. 280-281,282,283,284,285,286,287,288,289.

8. Kim, S.J., et al., *Study of pool boiling and critical heat flux enhancement in nanofluids.* Bulletin of the Polish Academy of Sciences Technical Sciences, 2007. 55(2): p. 211-216.

9. Lee, J. and I. Mudawar, *Assessment of the effectiveness of nanofluids for single-phase and two-phase heat transfer in micro-channels.* International Journal of Heat and Mass Transfer, 2007. 50(3-4): p. 452-463.

10. Wen, D. and Y. Ding, *Experimental investigation into convective heat transfer of nanofluids at the entrance region under laminar flow conditions.* International Journal of Heat and Mass Transfer, 2004. 47(24): p. 5181-5188.

11. Xue, H.S., et al., *Characteristic boiling curve of carbon nanotube nanofluid as determined by the transient calorimeter technique.* Applied Physics Letters, 2007. 90(18): p. 184107.

12. Xie, H., W. Yu, and Y. Li, *Thermal performance enhancement in nanofluids containing diamond nanoparticles.* Journal of Physics D: Applied Physics, 2009. 42(9): p. 095413.

13. Chen, L. and H. Xie, *Silicon oil based multiwalled carbon nanotubes nanofluid with optimized thermal conductivity enhancement.* Colloids and Surfaces A: Physicochemical and Engineering Aspects, 2009. 352(1-3): p. 136-140.

14. Buongiorno, J., et al., *A benchmark study on the thermal conductivity of nanofluids.* Journal of Applied Physics, 2009. 106(9): p. 094312.

15. Patel, H.E., T. Sundararajan, and S.K. Das, *An experimental investigation into the thermal conductivity enhancement in oxide and metallic nanofluids.* Journal of Nanoparticle Research, 2009. 12(3): p. 1015-1031.

16. Timofeeva, E.V., J.L. Routbort, and D. Singh, *Particle shape effects on thermophysical properties of alumina nanofluids.* Journal of Applied Physics, 2009. 106(1): p. 014304.

17. Patel, H.E., et al., *Thermal conductivities of naked and monolayer protected metal nanoparticle based nanofluids: Manifestation of anomalous enhancement and chemical effects.* Applied Physics Letters, 2003. 83(14): p. 2931-2933.

18. Wang, X.-Q. and A.S. Mujumdar, *Heat transfer characteristics of nanofluids: a review.* International Journal of Thermal Sciences, 2007. 46(1): p. 1-19.

19. Wen, D. and Y. Ding, *Effective Thermal Conductivity of Aqueous Suspensions of Carbon Nanotubes (Carbon Nanotube Nanofluids).* Journal of Thermophysics and Heat Transfer, 2004. 18(4): p. 481-485.

20. Xuan, Y., Q. Li, and W. Hu, *Aggregation structure and thermal conductivity of nanofluids.* AIChE Journal, 2003. 49(4): p. 1038-1043.

21. Witharana, S., *Boiling of refrigerants on enhanced surfaces and boiling of nanofluids*. 2003, The Royal Institute of Technology: Stockholm, Sweden.

22. In, C.B. and H.C. Soon, *Boiling heat transfer performance and phenomena of Al2O3-water nano-fluids from a plain surface in a pool.* International Journal of Heat and Mass Transfer, 2005. 48(12): p. 2407-19.

23. Xuan, Y. and Q. Li, *Investigation on Convective Heat Transfer and Flow Features of Nanofluids.* Journal of Heat Transfer, 2003. 125(1): p. 151.

24. Buongiorno, J., *Convective Transport in Nanofluids.* Journal of Heat Transfer, 2006. 128(3): p. 240.

25. Eastman, J.A., et al. *Enhanced thermal conductivity through the development of nanofluids*. in *Proceedings of the 1996 MRS Fall Symposium, December 2, 1996 - December 5*. Boston, MA, USA: Materials Research Society.

26. Jang, S., et al. *Effective Thermal Conductivities and Viscosities of Water-based Nanofluids Containing Al2O3 with Low Concentration*. in *International Conference on Nanotechnology*. 2007. Hong Kong: IEEE.

27. Wong, K.-F.V. and T. Kurma, *Transport properties of alumina nanofluids.* Nanotechnology, 2008. 19(34): p. 345702.

28. Beck, M.P., et al., *The effect of particle size on the thermal conductivity of alumina nanofluids.* Journal of Nanoparticle Research, 2008. 11(5): p. 1129-1136.

29. Teng, T.-P., et al., *The effect of alumina/water nanofluid particle size on thermal conductivity.* Applied Thermal Engineering, 2010. 30(14-15): p. 2213-2218.

30. Yu, W., et al., *Investigation of thermal conductivity and viscosity of ethylene glycol based ZnO nanofluid.* Thermochimica Acta, 2009. 491(1-2): p. 92-96.

31. Gao, J.W., et al., *Experimental investigation of heat conduction mechanisms in nanofluids. Clue on clustering.* Nano Letters, 2009. 9(12): p. 4128-4132.

32. Choi, C., H. Yoo, and J. Oh, *Preparation and heat transfer properties of nanoparticle-in-transformer oil dispersions as advanced energy-efficient coolants.* Current Applied Physics, 2008. 8(6): p. 710-712.

33. Tsai, T.-H., et al., *Effect of viscosity of base fluid on thermal conductivity of nanofluids.* Applied Physics Letters, 2008. 93(23): p. 233121.

34. Li, D., et al., *Preparation of Well-Dispersed Silver Nanoparticles for Oil-Based Nanofluids.* Industrial & Engineering Chemistry Research, 2010. 49(4): p. 1697-1702.

35. Hwang, Y., et al., *Stability and thermal conductivity characteristics of nanofluids.* Thermochimica Acta, 2007. 455(1-2): p. 70-74.

36. Shaikh, S., K. Lafdi, and R. Ponnappan, *Thermal conductivity improvement in carbon nanoparticle doped PAO oil: An experimental study.* Journal of Applied Physics, 2007. 101(6): p. 064302.

37. Hong, T.K., H.S. Yang, and C.J. Choi, *Study of the enhanced thermal conductivity of Fe nanofluids.* Journal of Applied Physics, 2005. 97(6): p. 064311-064314.

38. Eastman, J.A., et al., *Anomalously increased effective thermal conductivities of ethylene glycol-based nanofluids containing copper nanoparticles.* Applied Physics Letters, 2001. 78(6): p. 718.

39. Anoop, K.B., et al., *Rheological and flow characteristics of nanofluids: Influence of electroviscous effects and particle agglomeration.* Journal of Applied Physics, 2009. 106(3): p. 034909.

40. Egan, V.M., P.A. Walsh, and E.J. Walsh, *On viscosity measurements of nanofluids in micro and mini tube flow.* Journal of Physics D: Applied Physics, 2009. 42(16): p. 165502.

41. Nguyen, C., et al., *Temperature and particle-size dependent viscosity data for water-based nanofluids – Hysteresis phenomenon.* International Journal of Heat and Fluid Flow, 2007. 28(6): p. 1492-1506.

42. Wang, X.-J. and X.-F. Li, *Influence of pH on nanofluids' viscosity and thermal conductivity.* Chinese Physics Letters, 2009. 26(5): p. 056601 (4 pp.).

43. Chen, H., Y. Ding, and C. Tan, *Rheological behaviour of nanofluids.* New Journal of Physics, 2007. 9(10): p. 367-367.

44. Kwak, K. and C. Kim, *Viscosity and thermal conductivity of copper oxide nanofluid dispersed in ethylene glycol* Korea-Austrailia Rheology Journal, 2005. 17(2): p. 35-40.

45. Pastoriza-Gallego, M.J., et al., *A study on stability and thermophysical properties (density and viscosity) of Al[sub 2]O[sub 3] in water nanofluid.* Journal of Applied Physics, 2009. 106(6): p. 064301.

46. Li, X., D. Zhu, and X. Wang, *Experimental investigation on viscosity of Cu-H2O nanofluids.* Journal of Wuhan University of Technology-Mater. Sci. Ed., 2009. 24(1): p. 48-52.

47. Jia-Fei, Z., et al., *Dependence of Nanofluid Viscosity on Particle Size and pH Value.* Chinese Physics Letters, 2009. 26(6): p. 066202.

48. Vajjha, R.S. and D.K. Das. *Measurements of Specific Heat and Density of AI2O3 Nanofluid*. in *International Workshop on Mesoscopic, Nanoscopic and Macroscopic Materials (IWMNMM-2008)*. 2008. Bhubaneswar, India: American Institute of Physics.

49. Vajjha, R.S., D.K. Das, and B.M. Mahagaonkar, *Density Measurement of Different Nanofluids and Their Comparison With Theory.* Petroleum Science and Technology, 2009. 27(6): p. 612-624.

50. Maxwell, J.C., *A treatise on Electricity and Magnetism*. Vol. 1. 1881, London: Oxford University Press. 435.

51. Hamilton, R.L. and O.K. Crosser, *Thermal Conductivity of Heterogeneous Two-Component Systems.* Industrial & Engineering Chemistry Fundamentals, 1962. 1(3): p. 187-191.

52. Yu, W. and S.U.S. Choi, *The role of interfacial layers in the enhanced thermal conductivity of nanofluids: A renovated Maxwell model.* Journal of Nanoparticle Research, 2003. 5: p. 167-171.

53. Yu, W. and S.U.S. Choi, *The role of interfacial layers in the enhanced thermal conductivity of nanofluids: A renovated Hamilton-Crosser model.* Journal of Nanoparticle Research, 2004. 6(355-361): p. 355.

54. Prasher, R., P. Bhattacharya, and P. Phelan, *Thermal Conductivity of Nanoscale Colloidal Solutions (Nanofluids).* Physical Review Letters, 2005. 94(2).

55. Koo, J. and C. Kleinstreuer, *A new thermal conductivity model for nanofluids.* Journal of Nanoparticle Research, 2005. 6(6): p. 577-588.

56. Bruggeman, D.A.G., *Calculation of various physical constants of heterogeneous substances. I. Dielectric constant and conductivity of mixtures of isotropic substances.* Annalen der Physik, 1935. 24(7): p. 636-664.

57. Xue, Q. and W.-M. Xu, *A model of thermal conductivity of nanofluids with interfacial shells.* Materials Chemistry and Physics, 2005. 90(2-3): p. 298-301.

58. Evans, W., et al., *Effect of aggregation and interfacial thermal resistance on thermal conductivity of nanocomposites and colloidal nanofluids.* International Journal of Heat and Mass Transfer, 2008. 51(5-6): p. 1431-1438.

59. Prasher, R., et al., *Effect of aggregation on thermal conduction in colloidal nanofluids.* Applied Physics Letters, 2006. 89(14): p. 143119.

60. Eapen, J., J. Li, and S. Yip, *Beyond the Maxwell limit: Thermal conduction in nanofluids with percolating fluid structures.* Physical Review E, 2007. 76(6).

61. Eapen, J., et al., *The Classical Nature of Thermal Conduction in Nanofluids.* Journal of Heat Transfer, 2010. 132(10): p. 102402.

62. Keblinski, P., R. Prasher, and J. Eapen, *Thermal conductance of nanofluids: is the controversy over?* Journal of Nanoparticle Research, 2008. 10(7): p. 1089-1097.

63. Kumar, S. and G.C. Vradis, *Thermal Conductivity of Thin Metallic Films.* Transactions of the ASME, 1994. 116: p. 28-34.

64. Chantrenne, Raynaud, and Barrat, *Study of Phonon Heat Transfer in Metallic Solids from Molecular Dynamic Simulations.* Nanoscale and Microscale Thermophysical Engineering, 2003. 7(2): p. 117-136.

65. Heino, P. and E. Ristolainen, *Nanoscale Thermal Conductivity: Size Dependence by Molecular Dynamics.* Physica Scripta, 2004. T114: p. 171-174.

66. Heino, P. and E. Ristolainen, *Thermal conduction at the nanoscale in some metals by MD.* Microelectronics Journal, 2003. 34(9): p. 773-777.

67. Kumar, D., et al., *Model for Heat Conduction in Nanofluids.* Physical Review Letters, 2004. 93(14).

68. Jang, S.P. and S.U.S. Choi, *Role of Brownian motion in the enhanced thermal conductivity of nanofluids.* Applied Physics Letters, 2004. 84(21): p. 4316.

69. Yuan, S.P. and P.X. Jiang, *Thermal Conductivity of Small Nickel Particles.* International Journal of Thermophysics, 2006. 27(2): p. 581-595.

70. Evans, W., J. Fish, and P. Keblinski, *Role of Brownian motion hydrodynamics on nanofluid thermal conductivity.* Applied Physics Letters, 2006. 88(9): p. 093116.

71. Xue, L., *Effect of liquid layering at the liquid?solid interface on thermal transport.* International Journal of Heat and Mass Transfer, 2004. 47(19-20): p. 4277-4284.

72. Einstein, A., *A new determination of the molecular dimensions (vol 19, pg 289, 1906).* Annalen der Physik, 1911. 34(3): p. 591.

73. Einstein, A., *New determination of molecular dimensions.* Annalen der Physik, 1906. 19(2): p. 289-306.

74. Batchelor, G.K., *EFFECT OF BROWNIAN MOTION ON THE BULK STRESS IN A SUSPENSION OF SPHERICAL PARTICLES.* Journal of Fluid Mechanics, 1977. 83(Journal Article): p. 97-117.

75. Krieger, I.M. and T.J. Dougherty, *A Mechanism for Non-Newtonian Flow in Suspensions of Rigid Spheres.* Journal of Rheology, 1959. 3(1): p. 137-152.

76. Masoumi, N., N. Sohrabi, and A. Behzadmehr, *A new model for calculating the effective viscosity of nanofluids.* Journal of Physics D: Applied Physics, 2009. 42(5): p. 055501.

77. Murshed, S., K. Leong, and C. Yang, *Investigations of thermal conductivity and viscosity of nanofluids.* International Journal of Thermal Sciences, 2008. 47(5): p. 560-568.

78. Turgut, A., et al., *Thermal Conductivity and Viscosity Measurements of Water-Based TiO2 Nanofluids.* International Journal of Thermophysics, 2009. 30(4): p. 1213-1226.

79. Kulkarni, D.P., D.K. Das, and R.S. Vajjha, *Application of nanofluids in heating buildings and reducing pollution.* Applied Energy, 2009. 86(12): p. 2566-2573.

80. Keblinski, P., *Mechanisms of heat flow in suspensions of nano-sized particles (nanofluids).* International Journal of Heat and Mass Transfer, 2002. 45(4): p. 855-863.

81. Vladkov, M. and J.-L. Barrat, *Modeling Transient Absorption and Thermal Conductivity in a Simple Nanofluid.* Nano Letters, 2006. 6(6): p. 1224-1228.

82. Eapen, J., J. Li, and S. Yip, *Mechanism of Thermal Transport in Dilute Nanocolloids.* Physical Review Letters, 2007. 98(2).

83. Namboori, P.K.K., et al., *Thermal Analysis of Nanofluids Using Modeling and Molecular Dynamics Simulation.* AIP Conference Proceedings, 2010. 1276(1): p. 407-412.

84. Sachdeva, P. and R. Kumar, *Effect of hydration layer and surface wettability in enhancing thermal conductivity of nanofluids.* Applied Physics Letters, 2009. 95(22): p. 223105.

85. Sarkar, S. and R.P. Selvam, *Molecular dynamics simulation of effective thermal conductivity and study of enhanced thermal transport mechanism in nanofluids.* Journal of Applied Physics, 2007. 102(7): p. 074302.

86. Sankar, N., N. Mathew, and C. Sobhan, *Molecular dynamics modeling of thermal conductivity enhancement in metal nanoparticle suspensions*. International Communications in Heat and Mass Transfer, 2008. 35(7): p. 867-872.

87. Teng, K.-L., et al. *Enhanced thermal conductivity of nanofluids diagnosis by molecular dynamics simulations*. 2008. 25650 North Lewis Way, Stevenson Ranch, CA 9138-1439, United States: American Scientific Publishers.

88. Li, L., et al., *Molecular dynamics simulation of effect of liquid layering around the nanoparticle on the enhanced thermal conductivity of nanofluids.* Journal of Nanoparticle Research, 2009. 12(3): p. 811-821.

89. Xue, Q., *Model for effective thermal conductivity of nanofluids.* Physics Letters A, 2003. 307(5-6): p. 313-317.

90. Shukla, R.K. and V.K. Dhir. *Numerical study of the effective thermal conductivity of nanofluids*. in *ASME Summer Heat Transfer Conference*. 2005. San Franscisco, CA.

91. Lu, W. and Q. Fan, *Study for the particle's scale effect on some thermophysical properties of nanofluids by a simplified molecular dynamics method.* Engineering Analysis with Boundary Elements, 2008. 32(4): p. 282-289.

92. Lu, W.Q. and Q.M. Fan. *Molecular Dynamical Study on the Nanoscale Effect of Particles on the Thermal Conductivity and Viscosity in Nanofluids*. in *International Conference on Integration and Commercialization of Micro and Nanosystems*. 2007. Sanya, Hainan, China.

93. McPhie, M., P. Daivis, and I. Snook, *Viscosity of a binary mixture: Approach to the hydrodynamic limit.* Physical Review E, 2006. 74(3).

94. Rudyak, V.Y., A.A. Belkin, and V.V. Egorov. *Effective Viscosity Coefficient of Nanosuspensions*. in *Rarefied Gas Dynamics: 26th International Symposium*. 2009.

95. Rudyak, V.Y., et al., *Nanoparticle Friction Force and Effective Viscosity of Nanosuspensions.* Defect and Diffusion Forum, 2008. 273-276: p. 566-571.

96. Kiss, L.B., et al. *The real origin of lognormal size distributions of nanoparticles in vapor growth processes*. in *Fourth International Conference on Nanostructured Materials (NANO'98), 14-19 June 1998*. 1999. USA: Elsevier.

97. Vladkov, M. and J.-L. Barrat, *Modeling thermal conductivity and collective effects in a simple nanofluid.* Journal of Computational and Theoretical Nanoscience, 2008. 5(2): p. 187-193.

98. Le Goff, C., et al., *Enhanced thermal conductivity in nanofluids under the action of oscillating force fields.* Journal of Nanoparticle Research, 2008. 10(7): p. 1115-1120.

99. Ryckaert, J.P., et al., *Evaluation of transport coefficients of simple fluids by molecular dynamics: Comparison of Green-Kubo and nonequilibrium approaches for shear viscosity.* Physical Review A, 1989. 39(1): p. 259.

100. Ryckaert, J.P., et al., *Shear-Rate Dependence of the Viscosity of Simple Fluids by Nonequilibrium Molecular Dynamics.* Physical Review Letters, 1988. 60(2): p. 128.

101. Muller-Plathe, F., *A simple nonequilibrium molecular dynamics method for calculating the thermal conductivity.* Journal of Chemical Physics, 1997. 106(Copyright 1997, IEE): p. 6082-5.

102. Yukawa, S., et al., *Nonequilibrium Microscopic Distribution of Thermal Current in Particle Systems.* Journal of the Physical Society of Japan, 2009. 78(2): p. 023002.

103. Kelvin), W.T.L., *On the Dynamical Theory of Heat.* Proceedings of the Royal Society of Edinburgh, 1851. 1(3).

104. Onsager, L., *Reciprocal relations in irreversible processes, I.* Physical Review, 1931. 37: p. 405-426.

105. Onsager, L., *Reciprocal relations in irreversible processes, II.* Physical Review, 1931. 38: p. 2265-2279.

106. Galliero, G. and S. Volz, *Thermodiffusion in model nanofluids by molecular dynamics simulations.* The Journal of Chemical Physics, 2008. 128(6): p. 064505.

107. Zhang, Y., et al., *Effect of Brownian and Thermophoretic Diffusions of Nanoparticles on Nonequilibrium Heat Conduction in a Nanofluid Layer with Periodic Heat Flux.* Numerical Heat Transfer, Part A: Applications, 2009. 56(4): p. 325-341.

108. Pozhar, L.A. and K.E. Gubbins, *Transport Properties of Inhomogeneous Fluid Mixtures.* International Journal of Thermophysics, 1999. 20(3): p. 805-813.

109. Groot, S.R.d. and P. Mazur, *Non-equilibrium thermodynamics*. 1962, Amsterdam: North-Holland Pub. Co.; New York, Interscience Publishers. 510.

110. Fitts, D.D., *Nonequilibrium thermodynamics; a phenomenological theory of irreversible processes in fluid systems*. McGraw-Hill series in advanced chemistry. 1962, New York: McGraw-Hill. 173.

111. Hanley, H.J.M.e., *Transport phenomena in fluids*. 1969, New York, M: Dekker. 509.

112. McQuarrie, D.A., *Statistical mechanics*. 2000, Sausalito, Calif.: University Science Books. 641.

113. Hansen, J.P. and L. Verlet, *Phase Transisitions of the Lennard-Jones System.* Physics Reviews, 1969. 184(Compendex): p. 151-161.

114. Levesque, D., L. Verlet, and J. Kurkijarvi, *Computer `experiments' on classical fluids. IV. Transport properties and time-correlation functions of the Lennard-Jones liquid near its triple point.* Physical Review A (General Physics), 1973. 7(Copyright 1973, IEE): p. 1690-700.

115. Vogelsang, R., C. Hoheisel, and G. Ciccotti, *Thermal conductivity of the Lennard-Jones liquid by molecular dynamics calculations.* Journal of Chemical Physics, 1987. 86(Copyright 1987, IEE): p. 6371-5.

116. Green, M.S., *Markoff random processes and the statistical mechanics of time-dependent phenomena. II. Irreversible processes in fluids.* Journal of Chemical Physics, 1954. 22: p. 398-413.

117. Kubo, R., *Statistical-mechanical theory of irreversible processes. I. General theory and simple applications to magnetic and conduction problems.* Journal of the Physical Society of Japan, 1957. 12(6): p. 570-586.

118. Kubo, R., M. Yokota, and S. Nakajima, *Statistical-mechanical theory of irreversible processes. II. Responses to thermal disturbance.* Journal of the Physical Society of Japan, 1957. 12(11): p. 1203-1211.

119. Plimpton, S., *Fast parallel algorithms for short-range molecular dynamics.* Journal of Computational Physics, 1995. 117(Copyright 1995, IEE): p. 1-19.

120. in 't Veld, P., M. Petersen, and G. Grest, *Shear thinning of nanoparticle suspensions.* Physical Review E, 2009. 79(2).

121. Everaers, R. and M. Ejtehadi, *Interaction potentials for soft and hard ellipsoids.* Physical Review E, 2003. 67(4).

122. Maroo, S.C. and J.N. Chung, *Molecular dynamic simulation of platinum heater and associated nano-scale liquid argon film evaporation and colloidal adsorption characteristics.* Journal of Colloid and Interface Science, 2008. 328(1): p. 134-146.

123. Pan, Y., et al., *Molecular dynamics simulation of vaporization of an ultra-thin liquid argon layer on a surface.* International Journal of Heat and Mass Transfer, 2002. 45(10): p. 2087-100.

124. Rahman, A., *Correlations in the motion of atoms in liquid argon.* Physical Review, 1964. 136(2A): p. A405-A411.

125. de, S.C.P., et al., *Simulations of hydrocarbon adsorption and subsequent water penetration on an aluminum oxide surface.* Journal of Chemical Physics, 1997. 106(Compendex): p. 7331-7331.

126. Parsonage, N.G. and D. Nicholson, *Computer simulation of water between metal walls.* Journal of the Chemical Society, Faraday Transactions 2, 1986. 82(9): p. 1521.

127. Xue, L., et al., *Two regimes of thermal resistance at a liquid–solid interface.* The Journal of Chemical Physics, 2003. 118(1): p. 337.

128. Lemmon, E.W., M.O. McLinden, and D.G. Friend, *Thermophysical Properties of Fluid Systems*. NIST Chemistry WebBook, ed. P.J. Linstrom and W.G. Mallard. Vol. NIST Standard Reference Database Number 69, Gaithersburg MD, 20899: National Institute of Standards and Technology.

129. Cui, S.T., P.T. Cummings, and R.E. Johnson, *Classical dynamics description of low energy cascades in solids: atomic ejection from amorphous argon.* Surface Science, 1989. 222(Copyright 1990, IEE): p. 491-8.

130. Dabramo, M., et al., *Characterization of liquid behaviour by means of local density fluctuations.* Journal of Molecular Liquids, 2005. 117(1-3): p. 17-21.

131. Li, L., et al., *An Investigation of Molecular Layering at the Liquid-Solid Interface in Nanofluids by Molecular Dynamics Simulation.* Physics Letters A, 2008. 372: p. 4541-4544.

132. Yip, S. and J.P. Boon, *Molecular Hydrodynamics*. 1980: McGraw-Hill.

133. Hansen, J.P. and I.R. McDonald, *Theory of simple liquids*. Vol. 2. 1986, London: Academic. 556.

134. Schepper, I.M., E.G.D. Cohen, and C. Bruin, *Hydrodynamic time correlation functions for a Lennard-Jones fluid.* Physical Review A, 1988. 38(1): p. 271-287.

135. Kaburaki, H., *Thermal Transport Process by the Molecular Dynamics Method*, in *Handbook of Materials Modeling* S. Yip, Editor. 2005, Springer. p. 763-771.

136. Kataoka, Y., *Studies of Liquid Water by Computer Simulations. VI. Transport Properties of Carravetta-Clementi Water.* Bulletin of the Chemical Society of Japan, 1989. 62: p. 1421-1431.

137. Bertolini, D. and A. Tani, *Thermal Conductivity of Water: Molecular dynamics and generalized hydrodynamics results.* Physical Review E, 1997. 56(4): p. 4135-4151.

138. Bertolini, D. and A. Tani, *Generalized hydrodynamics and the acoustic modes of water: Theory and simulation results.* Physical Review E, 1995. 51(2): p. 1091-1118.

139. Christen, D. and G. Pollack, *Thermal conductivity of solid argon.* Physical Review B, 1975. 12(8): p. 3380-3391.

140. Tretiakov, K.V. and S. Scandolo, *Thermal conductivity of solid argon from molecular dynamics simulations.* The Journal of Chemical Physics, 2004. 120(8): p. 3765.

141. Kaburaki, H., J. Li, and S. Yip, *Thermal Conductivity of Solid Argon by Classical Molecular Dynamics* Materials Research Society Symposium - Proceedings, 1999. 538: p. 503-508.

142. McGaughey, A., *Thermal conductivity decomposition and analysis using molecular dynamics simulations. Part I. Lennard-Jones argon.* International Journal of Heat and Mass Transfer, 2004. 47(8-9): p. 1783-1798.

143. Sindzingre, P., et al., *Calculation of partial enthalpies of an argon-krypton mixture by NPT molecular dynamics.* Chemical Physics, 1989. 129(Copyright 1989, IEE): p. 213-24.

144. Heyes, D.M., *Chemical potential, partial enthalpy and partial volume of mixtures by NPT molecular dynamics.* Chemical Physics, 1992. 159(Copyright 1992, IEE): p. 149-67.

145. Fixman, M., *Direct simulation of the chemical potential.* Journal of Chemical Physics, 1983. 78(Copyright 1983, IEE): p. 4223-6.

146. Romano, S. and K. Singer, *Calculation of the entropy of liquid chlorine and bromine by computer simulation.* Molecular Physics, 1979. 37(Copyright 1979, IEE): p. 1765-72.

147. Vogelsang, R. and C. Hoheisel, *Thermal conductivity of a binary-liquid mixture studied by molecular dynamics with use of Lennard-Jones potentials.* Physical Review A (General Physics), 1987. 35(Copyright 1987, IEE): p. 3487-91.

148. Bastea, S., *Transport in a highly asymmetric binary fluid mixture.* Physical Review E, 2007. 75(3).

149. Fernandez, G., *A molecular simulation study of shear and bulk viscosity and thermal conductivity of simple real fluids*1.* Fluid Phase Equilibria, 2004. 221(1-2): p. 157-163.

150. Alder, B.J., D.M. Gass, and T.E. Wainwright, *Studies in Molecular Dynamics. VIII. The Transport Coefficients for a Hard-Sphere Fluid.* Journal of Chemical Physics, 1970. 53(10): p. 3813-3826.

151. Heyes, D.M., *Physical properties of liquid water by molecular dynamics simulations.* Journal of the Chemical Society, Faraday Transactions, 1994. 90(20): p. 3039.

152. Schoen, M. and C. Hoheisel, *The shear viscosity of a Lennard-Jones fluid calculated by equilibrium molecular dynamics.* Molecular Physics, 1985. 56(Copyright 1986, IEE): p. 653-72.

Appendices

Appendix A: Computer Code

A.1 LAMMPS Input Code: "in_cu_colloid.tc_sv"

```
atom_style        atomic
units             real

variable          T equal 87.057
variable          V equal vol
variable          dt equal 4.0
variable          p equal 1000 # correlation length
variable          s equal 1  # sample interval
variable          d equal $p*$s # dump interval

variable          kB equal 1.3806504e-23 # [J/K] Boltzmann

variable          kCal2J equal 4186.0/6.02214e23

variable          atm2Pa equal 101325.0
variable          A2m equal 1.0e-10
variable          fs2s equal 1.0e-15
variable          convert equal
                  ${atm2Pa}*${atm2Pa}*${fs2s}*${A2m}*${A2m}*${A2m}

# ---------------------------------------------------------

dimension         3
boundary          p p p
lattice           fcc 5.72 orient x 1 0 0 orient y 0 1 0 orient z 0 0 1
region            box block 0 6 0 6 0 6
create_box        2 box
create_atoms      1 box
region            sph1 sphere 2.0 2.0 2.0 0.7 units lattice
delete_atoms      region sph1
create_atoms      2 single 2.0 2.0 2.0 units lattice
group             ar type 1
group             cu type 2

mass              1 39.948
mass              2 127.092

pair_style        colloid 17.78
pair_coeff        1 1 34.2864 3.405 0 0 10.215
pair_coeff        1 2 226.775 2.645 0 4.00 12.000
pair_coeff        2 2 436.812 1.215 4.00 4.00 12.000

# ------------- equilibration and thermalization ----------------

velocity          all create $T 939349 mom yes rot yes dist gaussian
fix               NVT all nvt temp $T $T 80

# multi neighbor and comm for efficiency

neighbor          2.0 multi
neigh_modify      delay 0
```

Appendix A (Continued)

```
communicate       multi

timestep          ${dt}
thermo            $d
run               100000

# -------------- flux calculation ---------------

reset_timestep    0
dump              1 all xyz 1000 arcu_colloid.xyz
compute           myKE all ke/atom
compute           myPE all pe/atom pair
compute           myStress all stress/atom pair
compute           flux all heat/flux myKE myPE myStress
fix               JJ all ave/correlate $s $p $d &
                  c_flux[4] c_flux[5] c_flux[6] &
                  c_flux[7] c_flux[8] c_flux[9] &
                  c_flux[10] c_flux[11] c_flux[12] &
                  c_flux[13] c_flux[14] c_flux[15] &
                  type auto/upper file J0Jt.dat ave running
variable          scale equal
                  ${kCal2J}*${kCal2J}/${kB}/$T/$T/$V*$s*${dt}*1.0e25
variable          kppx equal trap(f_JJ[3])*${scale}
variable          kppy equal trap(f_JJ[15])*${scale}
variable          kppz equal trap(f_JJ[26])*${scale}
variable          kpkx equal trap(f_JJ[6])*${scale}
variable          kpky equal trap(f_JJ[18])*${scale}
variable          kpkz equal trap(f_JJ[29])*${scale}
variable          kpcx equal trap(f_JJ[9])*${scale}
variable          kpcy equal trap(f_JJ[21])*${scale}
variable          kpcz equal trap(f_JJ[32])*${scale}
variable          kphx equal trap(f_JJ[12])*${scale}
variable          kphy equal trap(f_JJ[24])*${scale}
variable          kphz equal trap(f_JJ[35])*${scale}
variable          kkkx equal trap(f_JJ[36])*${scale}
variable          kkky equal trap(f_JJ[45])*${scale}
variable          kkkz equal trap(f_JJ[53])*${scale}
variable          kkcx equal trap(f_JJ[39])*${scale}
variable          kkcy equal trap(f_JJ[48])*${scale}
variable          kkcz equal trap(f_JJ[56])*${scale}
variable          kkhx equal trap(f_JJ[42])*${scale}
variable          kkhy equal trap(f_JJ[51])*${scale}
variable          kkhz equal trap(f_JJ[59])*${scale}
variable          kccx equal trap(f_JJ[60])*${scale}
variable          kccy equal trap(f_JJ[66])*${scale}
variable          kccz equal trap(f_JJ[71])*${scale}
variable          kchx equal trap(f_JJ[63])*${scale}
variable          kchy equal trap(f_JJ[69])*${scale}
variable          kchz equal trap(f_JJ[74])*${scale}
variable          khhz equal trap(f_JJ[75])*${scale}
variable          khhx equal trap(f_JJ[78])*${scale}
variable          khhy equal trap(f_JJ[80])*${scale}
```

Appendix A (Continued)

```
variable          kpp equal (v_kppx+v_kppy+v_kppz)/3.0
variable          kpk equal (v_kpkx+v_kpky+v_kpkz)/3.0
variable          kpc equal (v_kpcx+v_kpcy+v_kpcz)/3.0
variable          kph equal (v_kphx+v_kphy+v_kphz)/3.0
variable          kkk equal (v_kkkx+v_kkky+v_kkkz)/3.0
variable          kkc equal (v_kkcx+v_kkcy+v_kkcz)/3.0
variable          kkh equal (v_kkhx+v_kkhy+v_kkhz)/3.0
variable          kcc equal (v_kccx+v_kccy+v_kccz)/3.0
variable          kch equal (v_kchx+v_kchy+v_kchz)/3.0
variable          khh equal (v_khhx+v_khhy+v_khhz)/3.0

compute           ke all pressure thermo_temp ke
compute           virial all pressure thermo_temp virial
fix               SS all ave/correlate $s $p $d &
                  c_ke[4] c_virial[4] &
                  type auto/upper file S0St.dat ave running
variable          scale_sv equal ${convert}/(${kB}*$T)*$V*$s*${dt}
variable          kkxy equal trap(f_SS[3])*${scale_sv}
variable          kcxy equal trap(f_SS[4])*${scale_sv}
variable          ccxy equal trap(f_SS[5])*${scale_sv}

compute           rdf all rdf 100 1 1 2 2 2 1
variable          rhoss equal (sum(c_rdf[1])/62)*(count(all)/vol)
variable          rhonn equal (sum(c_rdf[3])/62)*(count(all)/vol)
variable          rhons equal (sum(c_rdf[5])/56)*(count(all)/vol)
variable          rho0 equal count(all)/vol
variable          dross equal v_rhoss-v_rho0
variable          dronn equal v_rhonn-v_rho0
variable          drons equal v_rhons-v_rho0
fix               RR all ave/correlate $s $p $d &
                  v_dross v_dronn v_drons &
                  type auto file R0Rt.dat ave running
fix               gofr all ave/time $s $p $d c_rdf file
                  gofr_arcu_colloid.rdf mode vector

thermo_style      custom step temp

run               500000

variable          k equal "v_kpp + v_kkk + v_kcc + v_khh + v_kpk +
                  v_kpk + v_kpc + v_kpc + v_kph + v_kph + v_kkc + v_kkc
                  + v_kkh + v_kkh + v_kch + v_kch"
variable          v equal (v_kkxy+v_kcxy+v_ccxy)
variable          ndens equal count(all)/vol

print             "average thermal conductivity: ${k} [W/mK]"
print             "average shear viscosity: $v [Pa.s] @ $T K, ${ndens}
                  /A^3]"
```

Appendix A (Continued)

A.2 Modified LAMMPS Kernel: "compute_heat_flux.cpp"

```
/* ----------------------------------------------------------------------
--
   LAMMPS - Large-scale Atomic/Molecular Massively Parallel Simulator
   http://lammps.sandia.gov, Sandia National Laboratories
   Steve Plimpton, sjplimp@sandia.gov

   Copyright (2003) Sandia Corporation.  Under the terms of Contract
   DE-AC04-94AL85000 with Sandia Corporation, the U.S. Government
   retains
   certain rights in this software.  This software is distributed under
   the GNU General Public License.

   See the README file in the top-level LAMMPS directory.
-------------------------------------------------------------------------
-- */

/* ----------------------------------------------------------------------
--
   Contributing authors: German Samolyuk (ORNL) and
                         Mario Pinto (Computational Research Lab, Pune,
India)
-------------------------------------------------------------------------
-- */

#include "math.h"
#include "string.h"
#include "compute_heat_flux.h"
#include "atom.h"
#include "update.h"
#include "modify.h"
#include "force.h"
#include "group.h"
#include "error.h"

using namespace LAMMPS_NS;

#define INVOKED_PERATOM 8

/* ----------------------------------------------------------------------
-- */

ComputeHeatFlux::ComputeHeatFlux(LAMMPS *lmp, int narg, char **arg) :
  Compute(lmp, narg, arg)
{
  if (narg != 6) error->all("Illegal compute heat/flux command");

  vector_flag = 1;
  size_vector = 12;
  extvector = 1;
```

Appendix A (Continued)

```
// store ke/atom, pe/atom, stress/atom IDs used by heat flux
computation
  // insure they are valid for these computations

  int n = strlen(arg[3]) + 1;
  id_ke = new char[n];
  strcpy(id_ke,arg[3]);

  n = strlen(arg[4]) + 1;
  id_pe = new char[n];
  strcpy(id_pe,arg[4]);

  n = strlen(arg[5]) + 1;
  id_stress = new char[n];
  strcpy(id_stress,arg[5]);

  int ike = modify->find_compute(id_ke);
  int ipe = modify->find_compute(id_pe);
  int istress = modify->find_compute(id_stress);
  if (ike < 0 || ipe < 0 || istress < 0)
    error->all("Could not find compute heat/flux compute ID");
  if (strcmp(modify->compute[ike]->style,"ke/atom") != 0)
    error->all("Compute heat/flux compute ID does not compute
      ke/atom");
  if (modify->compute[ipe]->peatomflag == 0)
    error->all("Compute heat/flux compute ID does not compute
      pe/atom");
  if (modify->compute[istress]->pressatomflag == 0)
    error->all("Compute heat/flux compute ID does not compute
      stress/atom");

  vector = new double[12];
}

/* ----------------------------------------------------------------------
-- */

ComputeHeatFlux::~ComputeHeatFlux()
{
  delete [] id_ke;
  delete [] id_pe;
  delete [] id_stress;
  delete [] vector;
}

/* ----------------------------------------------------------------------
-- */

void ComputeHeatFlux::init()
{
  // error checks

  int ike = modify->find_compute(id_ke);
  int ipe = modify->find_compute(id_pe);
```

Appendix A (Continued)

```
  int istress = modify->find_compute(id_stress);
  if (ike < 0 || ipe < 0 || istress < 0)
    error->all("Could not find compute heat/flux compute ID");

  c_ke = modify->compute[ike];
  c_pe = modify->compute[ipe];
  c_stress = modify->compute[istress];
}

/* ----------------------------------------------------------------------
-- */

void ComputeHeatFlux::compute_vector()
{
  invoked_vector = update->ntimestep;

  // invoke 3 computes if they haven't been already

  if (!(c_ke->invoked_flag & INVOKED_PERATOM)) {
    c_ke->compute_peratom();
    c_ke->invoked_flag |= INVOKED_PERATOM;
  }
  if (!(c_pe->invoked_flag & INVOKED_PERATOM)) {
    c_pe->compute_peratom();
    c_pe->invoked_flag |= INVOKED_PERATOM;
  }
  if (!(c_stress->invoked_flag & INVOKED_PERATOM)) {
    c_stress->compute_peratom();
    c_stress->invoked_flag |= INVOKED_PERATOM;
  }

  // heat flux vector = jc[3] + jv[3]
  // jc[3] = convective portion of heat flux = sum_i (ke_i + pe_i)
      v_i[3]
  // jv[3] = virial portion of heat flux = sum_i (stress_tensor_i .
      v_i[3])
  // normalization by volume is not included

  double *ke = c_ke->vector_atom;
  double *pe = c_pe->vector_atom;
  double **stress = c_stress->array_atom;

  double **v = atom->v;
  int *mask = atom->mask;
  int nlocal = atom->nlocal;
  int *type = atom->type;
  int itype;

  double jp[3] = {0.0,0.0,0.0};
  double jk[3] = {0.0,0.0,0.0};
  double jc[3] = {0.0,0.0,0.0};
  for (int i = 0; i < nlocal; i++) {
    if (mask[i] & groupbit) {
```

Appendix A (Continued)

```
        jp[0] += pe[i]*v[i][0];
        jp[1] += pe[i]*v[i][1];
        jp[2] += pe[i]*v[i][2];
        jk[0] += ke[i]*v[i][0];
        jk[1] += ke[i]*v[i][1];
        jk[2] += ke[i]*v[i][2];
        jc[0] -= stress[i][0]*v[i][0] + stress[i][3]*v[i][1] +
          stress[i][4]*v[i][2];
        jc[1] -= stress[i][3]*v[i][0] + stress[i][1]*v[i][1] +
          stress[i][5]*v[i][2];
        jc[2] -= stress[i][4]*v[i][0] + stress[i][5]*v[i][1] +
          stress[i][2]*v[i][2];
    }
  }

  // convert jv from stress*volume to energy units via nktv2p factor

  double nktv2p = force->nktv2p;
  jc[0] /= nktv2p;
  jc[1] /= nktv2p;
  jc[2] /= nktv2p;

  // sum across all procs
  // 1st 3 terms are total heat flux
  // 2nd 3 terms are just conductive portion

  double data[12] =
{jp[0]+jk[0]+jc[0],jp[1]+jk[1]+jc[1],jp[2]+jk[2]+jc[2],jp[0],jp[1],jp[2
],jk[0],jk[1],jk[2],jc[0],jc[1],jc[2]};
  MPI_Allreduce(data,vector,12,MPI_DOUBLE,MPI_SUM,world);
```

Appendix A (Continued)

A.3 MATLAB Code

A.3.1 "hc_plots.m"

```
clear all;

clc;

kB=1.3806504e-23;
kCal2J = 4186.0/6.02214e23;
T = 87.057;
dt = 4.0;
V = (6*5.72)^3;
s = 1;
scale = kCal2J*kCal2J/kB/T/T/V*s*dt*1.0e25;

Fs = 1e15;

nps = 9;
datasets = 8;

for k = 1:nps

    cd(strcat(num2str(k-1),'np'));

    if k == 1

        for i = 1:datasets

            cd(num2str(i))

            hc_data = load(strcat('hc_data'));

            hcacf_temp(:,i) = sum(hc_data(:,4:48),2);

            pp_temp(:,i) = hc_data(:,4) + hc_data(:,13) +
                  hc_data(:,21);
            kk_temp(:,i) = hc_data(:,28) + hc_data(:,34) +
                  hc_data(:,39);
            cc_temp(:,i) = hc_data(:,43) + hc_data(:,46) +
                  hc_data(:,48);

            % P-P

            Jppx = scale*trapz(hc_data(:,4));
            Jppy = scale*trapz(hc_data(:,13));
            Jppz = scale*trapz(hc_data(:,21));

            Jppxy = scale*trapz(hc_data(:,5));
            Jppxz = scale*trapz(hc_data(:,6));
            Jppyz = scale*trapz(hc_data(:,14));

            % P-K
```

Appendix A (Continued)

```
Jpkx = scale*trapz(hc_data(:,7));
Jpky = scale*trapz(hc_data(:,16));
Jpkz = scale*trapz(hc_data(:,24));

Jpkxy = scale*trapz(hc_data(:,8));
Jpkxz = scale*trapz(hc_data(:,9));
Jpkyz = scale*trapz(hc_data(:,17));

% P-C

Jpcx = scale*trapz(hc_data(:,10));
Jpcy = scale*trapz(hc_data(:,19));
Jpcz = scale*trapz(hc_data(:,27));

Jpcxy = scale*trapz(hc_data(:,11));
Jpcxz = scale*trapz(hc_data(:,12));
Jpcyz = scale*trapz(hc_data(:,20));

% K-K

Jkkx = scale*trapz(hc_data(:,28));
Jkky = scale*trapz(hc_data(:,34));
Jkkz = scale*trapz(hc_data(:,39));

Jkkxy = scale*trapz(hc_data(:,29));
Jkkxz = scale*trapz(hc_data(:,30));
Jkkyz = scale*trapz(hc_data(:,35));

% K-C

Jkcx = scale*trapz(hc_data(:,31));
Jkcy = scale*trapz(hc_data(:,37));
Jkcz = scale*trapz(hc_data(:,42));

Jkcxy = scale*trapz(hc_data(:,32));
Jkcxz = scale*trapz(hc_data(:,33));
Jkcyz = scale*trapz(hc_data(:,38));

% C-C

Jccx = scale*trapz(hc_data(:,43));
Jccy = scale*trapz(hc_data(:,46));
Jccz = scale*trapz(hc_data(:,48));

Jccxy = scale*trapz(hc_data(:,44));
Jccxz = scale*trapz(hc_data(:,45));
Jccyz = scale*trapz(hc_data(:,47));

Jpp = (Jppx + Jppy + Jppz)/3;
Jpk = (Jpkx + Jpky + Jpkz)/3;
Jpc = (Jpcx + Jpcy + Jpcz)/3;
```

Appendix A (Continued)

```
            Jkk = (Jkkx + Jkky + Jkkz)/3;
            Jkc = (Jkcx + Jkcy + Jkcz)/3;

            Jcc = (Jccx + Jccy + Jccz)/3;

            k_temp(:,i) = [Jpp Jkk Jcc 0 (2 * Jpk) (2 * Jpc) 0 (2 *
                  Jkc) 0 0]';

            clear hc_data

            cd ..

        end

        k_comps(:,k) = mean(k_temp,2);

        hcacf(:,k) = mean(hcacf_temp,2);

        pp(:,k) = mean(pp_temp,2);

        pp_L = size(pp(:,k),1);
        pp_NFFT = 2^nextpow2(pp_L);
        pp_Y = fft(pp(:,k),pp_NFFT)/pp_L;
        pp_f = Fs/2*linspace(0,1,pp_NFFT/2+1);

        ps_pp_x(:,k) = pp_f';
        ps_pp_y(:,k) = 2*abs(pp_Y(1:pp_NFFT/2+1));

        kk(:,k) = mean(kk_temp,2);

        kk_L = size(kk(:,k),1);
        kk_NFFT = 2^nextpow2(kk_L);
        kk_Y = fft(kk(:,k),kk_NFFT)/kk_L;
        kk_f = Fs/2*linspace(0,1,kk_NFFT/2+1);

        ps_kk_x(:,k) = kk_f';
        ps_kk_y(:,k) = 2*abs(kk_Y(1:kk_NFFT/2+1));

        cc(:,k) = mean(cc_temp,2);

        cc_L = size(cc(:,k),1);
        cc_NFFT = 2^nextpow2(cc_L);
        cc_Y = fft(cc(:,k),cc_NFFT)/cc_L;
        cc_f = Fs/2*linspace(0,1,cc_NFFT/2+1);

        ps_cc_x(:,k) = cc_f';
        ps_cc_y(:,k) = 2*abs(cc_Y(1:cc_NFFT/2+1));

    else

        for i = 1:datasets

            cd(num2str(i));
```

Appendix A (Continued)

```
hc_data = load(strcat('hc_data'));

hcacf_temp(:,i) = sum(hc_data(:,4:81),2);

pp_temp(:,i) = hc_data(:,4) + hc_data(:,16) +
      hc_data(:,27);
kk_temp(:,i) = hc_data(:,37) + hc_data(:,46) +
      hc_data(:,54);
cc_temp(:,i) = hc_data(:,61) + hc_data(:,67) +
      hc_data(:,72);

% P-P

Jppx = scale*trapz(hc_data(:,4));
Jppy = scale*trapz(hc_data(:,16));
Jppz = scale*trapz(hc_data(:,27));

Jppxy = scale*trapz(hc_data(:,5));
Jppxz = scale*trapz(hc_data(:,6));
Jppyz = scale*trapz(hc_data(:,17));

% P-K

Jpkx = scale*trapz(hc_data(:,7));
Jpky = scale*trapz(hc_data(:,19));
Jpkz = scale*trapz(hc_data(:,30));

Jpkxy = scale*trapz(hc_data(:,8));
Jpkxz = scale*trapz(hc_data(:,9));
Jpkyz = scale*trapz(hc_data(:,20));

% P-C

Jpcx = scale*trapz(hc_data(:,10));
Jpcy = scale*trapz(hc_data(:,22));
Jpcz = scale*trapz(hc_data(:,33));

Jpcxy = scale*trapz(hc_data(:,11));
Jpcxz = scale*trapz(hc_data(:,12));
Jpcyz = scale*trapz(hc_data(:,23));

% P-H

Jphx = scale*trapz(hc_data(:,13));
Jphy = scale*trapz(hc_data(:,25));
Jphz = scale*trapz(hc_data(:,36));

Jphxy = scale*trapz(hc_data(:,14));
Jphxz = scale*trapz(hc_data(:,15));
Jphyz = scale*trapz(hc_data(:,26));

% K-K
```

Appendix A (Continued)

```
Jkkx = scale*trapz(hc_data(:,37));
Jkky = scale*trapz(hc_data(:,46));
Jkkz = scale*trapz(hc_data(:,54));

Jkkxy = scale*trapz(hc_data(:,38));
Jkkxz = scale*trapz(hc_data(:,39));
Jkkyz = scale*trapz(hc_data(:,47));

% K-C

Jkcx = scale*trapz(hc_data(:,40));
Jkcy = scale*trapz(hc_data(:,49));
Jkcz = scale*trapz(hc_data(:,57));

Jkcxy = scale*trapz(hc_data(:,41));
Jkcxz = scale*trapz(hc_data(:,42));
Jkcyz = scale*trapz(hc_data(:,50));

% K-H

Jkhx = scale*trapz(hc_data(:,43));
Jkhy = scale*trapz(hc_data(:,52));
Jkhz = scale*trapz(hc_data(:,60));

Jkhxy = scale*trapz(hc_data(:,44));
Jkhxz = scale*trapz(hc_data(:,45));
Jkhyz = scale*trapz(hc_data(:,53));

% C-C

Jccx = scale*trapz(hc_data(:,61));
Jccy = scale*trapz(hc_data(:,67));
Jccz = scale*trapz(hc_data(:,72));

Jccxy = scale*trapz(hc_data(:,62));
Jccxz = scale*trapz(hc_data(:,63));
Jccyz = scale*trapz(hc_data(:,68));

% C-H

Jchx = scale*trapz(hc_data(:,64));
Jchy = scale*trapz(hc_data(:,70));
Jchz = scale*trapz(hc_data(:,75));

Jchxy = scale*trapz(hc_data(:,65));
Jchxz = scale*trapz(hc_data(:,66));
Jchyz = scale*trapz(hc_data(:,71));

% H-H

Jhhx = scale*trapz(hc_data(:,76));
Jhhy = scale*trapz(hc_data(:,79));
Jhhz = scale*trapz(hc_data(:,81));
```

Appendix A (Continued)

```
        Jhhxy = scale*trapz(hc_data(:,77));
        Jhhxz = scale*trapz(hc_data(:,78));
        Jhhyz = scale*trapz(hc_data(:,80));

        % Vector sums

        Jpp = (Jppx(1) + Jppy(1) + Jppz(1))/3;
        Jpk = (Jpkx(1) + Jpky(1) + Jpkz(1))/3;
        Jpc = (Jpcx(1) + Jpcy(1) + Jpcz(1))/3;
        Jph = (Jphx(1) + Jphy(1) + Jphz(1))/3;

        Jkk = (Jkkx(1) + Jkky(1) + Jkkz(1))/3;
        Jkc = (Jkcx(1) + Jkcy(1) + Jkcz(1))/3;
        Jkh = (Jkhx(1) + Jkhy(1) + Jkhz(1))/3;

        Jcc = (Jccx(1) + Jccy(1) + Jccz(1))/3;
        Jch = (Jchx(1) + Jchy(1) + Jchz(1))/3;

        Jhh = (Jhhx(1) + Jhhy(1) + Jhhz(1))/3;

        JJ = Jpp + Jkk + Jcc + Jhh + (2 * Jpk) + (2 * Jpc) + (2 *
              Jph) + (2 * Jkc) + (2 * Jkh) + (2 * Jch);

        k_temp(:,i) = [Jpp Jkk Jcc Jhh (2 * Jpk) (2 * Jpc) (2 *
              Jph) (2 * Jkc) (2 * Jkh) (2 * Jch)]';

        clear hc_data

        cd ..
    end

    k_comps(:,k) = mean(k_temp,2);

    hcacf(:,k) = mean(hcacf_temp,2);

    pp(:,k) = mean(pp_temp,2);

    pp_L = size(pp(:,k),1);
    pp_NFFT = 2^nextpow2(pp_L);
    pp_Y = fft(pp(:,k),pp_NFFT)/pp_L;
    pp_f = Fs/2*linspace(0,1,pp_NFFT/2+1);

    ps_pp_x(:,k) = pp_f';
    ps_pp_y(:,k) = 2*abs(pp_Y(1:pp_NFFT/2+1));

    kk(:,k) = mean(kk_temp,2);

    kk_L = size(kk(:,k),1);
    kk_NFFT = 2^nextpow2(kk_L);
    kk_Y = fft(kk(:,k),kk_NFFT)/kk_L;
    kk_f = Fs/2*linspace(0,1,kk_NFFT/2+1);

    ps_kk_x(:,k) = kk_f';
```

Appendix A (Continued)

```
        ps_kk_y(:,k) = 2*abs(kk_Y(1:kk_NFFT/2+1));

        cc(:,k) = mean(cc_temp,2);

        cc_L = size(cc(:,k),1);
        cc_NFFT = 2^nextpow2(cc_L);
        cc_Y = fft(cc(:,k),cc_NFFT)/cc_L;
        cc_f = Fs/2*linspace(0,1,cc_NFFT/2+1);

        ps_cc_x(:,k) = cc_f';
        ps_cc_y(:,k) = 2*abs(cc_Y(1:cc_NFFT/2+1));

    end
    cd ..
end

save('k_comps_hc.txt','k_comps','-ascii');
save('hcacf_hc.txt','hcacf','-ascii');
save('pp_hc.txt','pp','-ascii');
save('kk_hc.txt','kk','-ascii');
save('cc_hc.txt','cc','-ascii');
save('ps_xx_x_hc.txt','ps_pp_x','-ascii');
save('ps_pp_y_hc.txt','ps_pp_y','-ascii');
save('ps_kk_y_hc.txt','ps_kk_y','-ascii');
save('ps_cc_y_hc.txt','ps_cc_y','-ascii');

tar('hc_data.gz','*_hc.txt');

!echo | mutt -a hc_data.gz -s "data" jshelto3@mail.usf.edu

!rm *.txt
```

Appendix A (Continued)

A.3.2 "sv_plots.m"

```
clear all;

clc;

kB=1.3806504e-23;
atm2Pa = 101325.0;
A2m = 1.0e-10;
fs2s = 1.0e-15;
convert = atm2Pa*atm2Pa*fs2s*A2m*A2m*A2m;

T = 87.057;
dt = 4.0;
V = (6*5.72)^3;
s = 1;
scale = convert/(kB*T)*V*s*dt;

Fs = 1e15;

nps = 9;
datasets = 8;

for k = 1:nps

    cd(strcat(num2str(k-1),'np'));

    for i = 1:datasets

        cd(num2str(i))

        sv_data = load(strcat('sv_data'));

        sacf_temp(:,i) = sum(sv_data(:,4:6),2);

        kk_temp(:,i) = sv_data(:,4);
        cc_temp(:,i) = sv_data(:,6);

        % K-K

        Jkk = scale*trapz(sv_data(:,4));

        % K-C

        Jkc = scale*trapz(sv_data(:,5));

        % C-C

        Jcc = scale*trapz(sv_data(:,6));

        sv_temp(:,i) = [Jkk Jkc Jcc]';

        clear sv_data
```

Appendix A (Continued)

```
        cd ..

    end

    sv_comp(:,k) = mean(sv_temp,2);

    sacf(:,k) = mean(sacf_temp,2);

    kk(:,k) = mean(kk_temp,2);

    kk_L = size(kk(:,k),1);
    kk_NFFT = 2^nextpow2(kk_L);
    kk_Y = fft(kk(:,k),kk_NFFT)/kk_L;
    kk_f = Fs/2*linspace(0,1,kk_NFFT/2+1);

    ps_kk_x(:,k) = kk_f';
    ps_kk_y(:,k) = 2*abs(kk_Y(1:kk_NFFT/2+1));

    cc(:,k) = mean(cc_temp,2);

    cc_L = size(cc(:,k),1);
    cc_NFFT = 2^nextpow2(cc_L);
    cc_Y = fft(cc(:,k),cc_NFFT)/cc_L;
    cc_f = Fs/2*linspace(0,1,cc_NFFT/2+1);

    ps_cc_x(:,k) = cc_f';
    ps_cc_y(:,k) = 2*abs(cc_Y(1:cc_NFFT/2+1));

    cd ..
end

save('sv_comp_sv.txt','sv_comp','-ascii');
save('sacf_sv.txt','sacf','-ascii');
save('kk_sv.txt','kk','-ascii');
save('cc_sv.txt','cc','-ascii');
save('ps_xx_x_sv.txt','ps_kk_x','-ascii');
save('ps_kk_y_sv.txt','ps_kk_y','-ascii');
save('ps_cc_y_sv.txt','ps_cc_y','-ascii');

tar('sv_data.gz','*_sv.txt');

!echo | mutt -a sv_data.gz -s "data" jshelto3@mail.usf.edu

!rm *.txt
```

Appendix A (Continued)

A.3.3 "gofrplots.m"

```
clear all;

clc;

% Constants

kB=1.3806504e-23;     % Boltzmann constant
T = 87.057;           % Temperature in K
rho = 2.146371514e28; % Density of argon at 87.057 K in units of
atoms/m^3

nps = 9;              % Numper of nanoparticles
datasets = 8;         % Number of data sets for each nanoparticles

% Vector of 'r' values to make 100 concentric spheres with volume of
% 0.07238 nm^3 for pure argon

r(1) = 0;

for i = 2:101
    r(i) = ((3*0.07238/4/pi)+r(i-1)^3)^(1/3);
end

% Calculating principal spontaneous density fluctuations of pure argon
% using principal component analysis
%
% There are 4 steps:

gofr_data_argon =
load('/work/j/jshelto3/lammps_work/ar_cu/0.4nm/0np/9/gofr_data');

dens_coeff = 4*3.1416*rho/(10^9)^3;

% 1) Calculating instantaneous local density that has been broken into
100
%    concentric spheres of equal volume mentioned earlier

for j = 1:500
    gofr_argon_xx(:,j) = gofr_data_argon(1+(100*(j-1)):100+(100*(j-
      1)),2);
    gofr_argon_yy(:,j) = gofr_data_argon(1+(100*(j-1)):100+(100*(j-
      1)),3);

    gofr_instant_spline =
      spline(gofr_argon_xx(:,j)/10,gofr_argon_yy(:,j));
    new_gofr_instant = ppval(gofr_instant_spline,r);
    N_instant_int = new_gofr_instant.*(r).^2;
    N_instant_int_spline = spline(r,N_instant_int);
    int_N_instant_spline = fnint(N_instant_int_spline);
    int_N_instant_spline_val = ppval(int_N_instant_spline,r);
    N_count_instant = 1 + dens_coeff.*int_N_instant_spline_val; %1 +
```

Appendix A (Continued)

```
 (N-1)
    rho_instant(1,j) = 0;
    rho_instant(2:100,j) = abs(N_count_instant(3:101) -
N_count_instant(2:100)) ./ ((4/3 * 3.1416) .* (r(3:101).^3 -
r(2:100).^3));

end

% 2) Calculating averaged local density that has been broken into 100
%    concentric spheres of equal volume mentioned earlier

gofr_argon_x_avg = mean(gofr_argon_xx,2);
gofr_argon_y_avg = mean(gofr_argon_yy,2);

gofr_avg_spline = spline(gofr_argon_x_avg/10,gofr_argon_y_avg);
new_gofr_avg = ppval(gofr_avg_spline,r);
N_avg_int = new_gofr_avg.*(r).^2;
N_avg_int_spline = spline(r,N_avg_int);
int_N_avg_spline = fnint(N_avg_int_spline);
int_N_avg_spline_val = ppval(int_N_avg_spline,r);
N_count_avg = 1 + dens_coeff.*int_N_avg_spline_val; %1 + (N-1)
rho_avg(1,1) = 0;
rho_avg(2:100,1) = abs(N_count_avg(3:101) - N_count_avg(2:100)) ./
((4/3 * 3.1416) .* (r(3:101).^3 - r(2:100).^3));

% 3) Create the local density covariance matrix

ldcm_argon = (rho_instant -
repmat(rho_avg(:,1),1,size(rho_instant,2)))*(rho_instant -
repmat(rho_avg(:,1),1,size(rho_instant,2)))';

% 4) Use 'pcacov' to find the eigenvectors, eigenvalues, and their
%    percentage of the total variance

[coeff_aa,eigen_aa,per_var_aa] = pcacov(ldcm_argon);

eigen_vec_1(:,1) = coeff_aa(:,1);
eigen_vec_2(:,1) = coeff_aa(:,2);
eigen_vec_3(:,1) = coeff_aa(:,3);
eigen_val(:,1) = eigen_aa;
per_var(:,1) = per_var_aa;

% Vector of 'r' values to make 100 concentric spheres with volume of
% 0.0720 nm^3 for nanofluid with 0.7 nm diameter nanoparticle

r(1) = 0.275;

for i = 2:101
    r(i) = ((3*0.0720/4/pi)+r(i-1)^3)^(1/3);
end

% Calculating principal spontaneous density fluctuations of a nanofluid
% using principal component analysis for each of the 8 different volume
```

Appendix A (Continued)

```
% fractions

for k = 1:nps

    cd(strcat(num2str(k-1),'np'));

    for i = 1:datasets

        cd(num2str(i))

        gofr_data = load(strcat('gofr_data'));

        if k > 1
            for j = 1:500
                gofr_ba_xx(:,j) = gofr_data(1+(100*(j-1)):100+(100*(j-
                  1)),2);
                gofr_ba_yy(:,j) = gofr_data(1+(100*(j-1)):100+(100*(j-
                  1)),7);

                gofr_instant_spline =
                  spline(gofr_ba_xx(:,j)/10,gofr_ba_yy(:,j));
                new_gofr_instant = ppval(gofr_instant_spline,r);
                N_instant_int = new_gofr_instant.*(r).^2;
                N_instant_int_spline = spline(r,N_instant_int);
                int_N_instant_spline = fnint(N_instant_int_spline);
                int_N_instant_spline_val =
                  ppval(int_N_instant_spline,r);
                N_count_instant = 1 +
                  dens_coeff.*int_N_instant_spline_val; %1 + (N-1)
                rho_instant_temp(1,j) = 0;
                rho_instant_temp(2:100,j) = abs(N_count_instant(3:101)
                  - N_count_instant(2:100)) ./ ((4/3 * 3.1416) .*
                  (r(3:101).^3 - r(2:100).^3));
            end

            gofr_ba_avg_xx(:,i) = mean(gofr_ba_xx,2);
            gofr_ba_avg_yy(:,i) = mean(gofr_ba_yy,2);

            gofr_avg_spline =
                  spline(gofr_ba_avg_xx(:,i)/10,gofr_ba_avg_yy(:,i));
            new_gofr_avg = ppval(gofr_avg_spline,r);
            N_avg_int = new_gofr_avg.*(r).^2;
            N_avg_int_spline = spline(r,N_avg_int);
            int_N_avg_spline = fnint(N_avg_int_spline);
            int_N_avg_spline_val = ppval(int_N_avg_spline,r);
            N_count_avg = 1 + dens_coeff.*int_N_avg_spline_val; %1 +
            (N-1)
            rho_avg_temp(1:100,i) = abs(N_count_avg(2:101) -
            N_count_avg(1:100)) ./ ((4/3 * 3.1416) .* (r(2:101).^3 -
            r(1:100).^3));
            ldcm_ba = (rho_instant_temp -
            repmat(rho_avg_temp(:,i),1,size(rho_instant_temp,2)))*(rho_
            instant_temp -
```

Appendix A (Continued)

```
            repmat(rho_avg_temp(:,i),1,size(rho_instant_temp,2)))';

            [coeff_ba,eigen_ba,per_var_ba] = pcacov(ldcm_ba);

            eigen_vec_1_temp(:,i) = coeff_ba(:,1);
            eigen_vec_2_temp(:,i) = coeff_ba(:,2);
            eigen_vec_3_temp(:,i) = coeff_ba(:,3);
            eigen_val_temp(:,i) = eigen_ba;
            per_var_temp(:,i) = per_var_ba;

        end

        clear gofr_data

        cd ..

    end

    % Calculating shear modulus for...

    if k == 1
        % 1) Pure Argon (Lennard Jones Potential)

        sig_lj = 3.405e-10;
        eps_lj = 1.65424611e-21;

        xx_temp = [3.01:0.1:10.51]';

        lj_pot = 4*eps_lj*(((sig_lj./(xx_temp*1e-10)).^12) -
            ((sig_lj./(xx_temp*1e-10)).^6));

        lj_pot_spline = spline(xx_temp*1e-10,lj_pot);
        lj_pot_deriv_pp =fnder(lj_pot_spline);
        lj_pot_deriv = ppval(lj_pot_deriv_pp,xx_temp*1e-10);

        new_fun = (xx_temp*1e-10).^4 .* lj_pot_deriv;
        new_fun_spline = spline(xx_temp*1e-10,new_fun);
        new_fun_deriv_pp = fnder(new_fun_spline);
        new_fun_deriv = ppval(new_fun_deriv_pp,xx_temp*1e-10);

        load('gofr_argon.txt');

        int_fun = gofr_argon(25:100) .* new_fun_deriv;
        int_fun_spline = spline(xx_temp*1e-10,int_fun);
        int_int_fun_spline_pp = fnint(int_fun_spline);
        int_int_fun_spline = ppval(int_int_fun_spline_pp,xx_temp*1e-
            10);
        int_g = int_int_fun_spline(length(xx_temp));

        rho2 = rho^2;

        g_inf(:,k) = rho*kB*T + 2*pi/15*rho2*int_g;
```

Appendix A (Continued)

```
    elseif k > 1
        gofr_xx_avg(:,k) = mean(gofr_ba_avg_xx,2);
        gofr_ba_avg(:,k) = mean(gofr_ba_avg_yy,2);
        rho_avg(:,k) = mean(rho_avg_temp,2);
        eigen_vec_1(:,k) = mean(eigen_vec_1_temp,2);
        eigen_vec_2(:,k) = mean(eigen_vec_2_temp,2);
        eigen_vec_3(:,k) = mean(eigen_vec_3_temp,2);
        eigen_val(:,k) = mean(eigen_val_temp,2);
        per_var(:,k) = mean(per_var_temp,2);

        % 2) Copper nanoparticle in argon (Colloid Potential)
        coll_radius = 2.5e-10;
        sigma = 2.87135e-10;
        A_cs = 1.5755e-18;

        xx_temp = gofr_xx_avg(39:100,k)*1e-10;

        coll_pot(:,k) =
            ((2*(coll_radius^3)*(sigma^3)*A_cs)./(9*((coll_radius^2)-
            (xx_temp.^2)).^3)).*(1-
            ((((5*coll_radius^6)+(45*(coll_radius^4).*(xx_temp.^2))+(63
            *(coll_radius^2).*(xx_temp.^4))+(15.*xx_temp.^6))*sigma^6).
            /(15.*((coll_radius-
            xx_temp).^6).*((coll_radius+xx_temp).^6))));
        coll_pot_spline = spline(xx_temp,coll_pot(:,k));
        coll_pot_deriv_pp =fnder(coll_pot_spline);
        coll_pot_deriv = ppval(coll_pot_deriv_pp,(xx_temp));

        new_fun = (xx_temp.^4) .* coll_pot_deriv;
        new_fun_spline = spline(xx_temp,new_fun);
        new_fun_deriv_pp = fnder(new_fun_spline);
        new_fun_deriv = ppval(new_fun_deriv_pp,xx_temp);

        int_fun = gofr_ba_avg(39:100,k) .* new_fun_deriv;
        int_fun_spline = spline(xx_temp,int_fun);
        int_int_fun_spline_pp = fnint(int_fun_spline);
        int_int_fun_spline = ppval(int_int_fun_spline_pp,xx_temp);
        int_g = int_int_fun_spline(length(xx_temp));

        rho2 = rho^2;

        g_inf(:,k) = rho*kB*T + 2*pi/15*rho2*int_g;
    end

    cd ..
end

save('gofr_xx.txt','gofr_xx_avg','-ascii');
save('gofr_ba.txt','gofr_ba_avg','-ascii');

save('rho_avg.txt','rho_avg','-ascii');
save('rho_r.txt','r','-ascii');
```

Appendix A (Continued)

```
save('eigen_vec_1.txt','eigen_vec_1','-ascii');
save('eigen_vec_2.txt','eigen_vec_2','-ascii');
save('eigen_vec_3.txt','eigen_vec_3','-ascii');
save('eigen_val.txt','eigen_val','-ascii');
save('eigen_per_val.txt','per_var','-ascii');

save('g_infinity.txt','g_inf','-ascii');

tar('gofr_data.gz','gofr_*.txt');
tar('rho_avg.gz','rho_*.txt');
tar('eigen_data.gz','eigen_*.txt');
tar('g_infinity_data.gz','g_infinity.txt');

!echo | mutt -a gofr_data.gz -s "0.4nm gofr_data" jshelto3@mail.usf.edu
!echo | mutt -a rho_avg.gz -s "0.4nm local_density"
jshelto3@mail.usf.edu
!echo | mutt -a eigen_data.gz -s "0.4nm eigen_data"
jshelto3@mail.usf.edu
!echo | mutt -a g_infinity_data.gz -s "0.4nm g_inf_data"
jshelto3@mail.usf.edu

!rm *.txt
```

Appendix B: Journal Articles

B.1 Molecular Simulation (Accepted November 4, 2011)

Modelling Nanoparticles in Nanofluids for Thermal Transport Calculations

John Shelton
Department of Mechanical Engineering, University of South Florida, Tampa, USA
4202 E. Fowler Ave.
ENB 118
Tampa, FL 33620
813-974-2280 (Office)
813-974-3539 (Fax)
jshelto3@mail.usf.edu

Venkat Bhenthanabotla
Department of Chemical Engineering, University of South Florida, Tampa, USA
bhethana@usf.edu

Frank Pyrtle, III
Department of Mechanical Engineering, University of South Florida, Tampa, USA
pyrtle@usf.edu

Appendix B (Continued)

Modelling Nanoparticles in Nanofluids for Thermal Transport Calculations

Molecular dynamics simulations using a model that characterizes nanoparticle suspensions as a uniformly distributed collection of Lennard Jones particles is presented as an alternative for the calculation of thermal transport in nanofluids. With this model, the interactions of the atoms within the nanoparticle do not contribute to the thermal conductivity calculations, which have been shown to be an insignificant factor to enhancements at that length scale. By using this model, an analysis of the interactions between the particle and the fluid can now be properly performed. It is shown that the thermal conductivity enhancements achieved using this colloid model fall within the minimum theoretical value of a pure xenon fluid and the maximum theoretical value of an fcc xenon solid.

Keywords: nanofluids; nanoparticle; colloid; equilibrium molecular dynamics simulations

1. Introduction

The thermal conductivity of fluids with nanoparticle suspensions ("nanofluids") has seen extensive investigation in recent years due to its potential benefits as a working fluid in advanced heat transfer applications [1-10]. Some results obtained [3, 5] have shown that these fluids with nanoparticle suspensions exhibited significantly higher values (> 30%) of thermal conductivity when compared to its corresponding base fluid. There have been many proposed continuum-level theories to explain this thermophysical property enhancement, which has included: 1) microconvection induced by Brownian motion [11-14], 2) solid-like liquid layering [15-17], and 3) agglomeration [18-21]. However, experimental verification of these theories is difficult to quantify at the macroscale. Therefore, in recent years, molecular dynamics simulations and statistical mechanics have been used to characterize energy transfer within nanofluids at the nanoscale and use these results to gain insight as to the effects that the nanoparticle suspensions have on the thermal conductivity of the base fluid.

Eapen [22] was the first to propose application of the analysis method employed by Vogelsang [23] to nanofluids. Through an analysis of the self and cross correlations of the three

Appendix B (Continued)

modes of energy transfer that compose the heat flux vector: kinetic, (K), potential (P) , and collision (C),

$$\mathbf{J}_Q(t) = \sum_{k-\alpha}^{\beta}\sum_{i=1}^{N_k}\overbrace{\frac{1}{2}m_i^k\left(\upsilon_i^k\right)^2}^{K}\mathbf{v}_i^k + \sum_{k-\alpha}^{\beta}\sum_{j-\alpha}^{\beta}\sum_{i=1}^{N_k}\sum_{j>i}^{N_l}\left[\overbrace{\mathbf{I}U\left(r_{ij}^M\right)}^{P} - \overbrace{\mathbf{r}_{ij}^M \otimes \mathbf{F}\left(r_{ij}\right)}^{C}\right]\cdot\mathbf{v}_i^k - \sum_{k-\alpha}^{\beta}h^k\sum_{i=1}^{N_k}\mathbf{v}_i^k \qquad (1)$$

Eapen proposed that the thermal conductivity enhancement seen in nanofluids was due to strong nanoparticle-fluid interactions manifesting itself in the self-correlation of the potential energy transfer mode. Teng [24] and Sachdeva [25] have also both used this methodology, although Teng combined the kinetic and potential energy modes into a "convective term". Their results and conclusions, though, differed significantly from that of Eapen. Teng suggested that the self-correlation of the "convective term" corresponding to the nanoparticle atoms was the biggest contributor to thermal conductivity enhancement [24]. Meanwhile , Sachdeva proposed that it was in fact the self-correlation of the collision term that was responsible for the increase in the thermal conductivity of their model [25]. It is important to note that in all the previous investigations the nanoparticle is modelled as a spherical FCC lattice structure of Lennard Jones atoms when, in fact, this analysis was originally developed for use with a binary mixture of atoms with equal size and mass. While the characterization of thermal transport of binary systems has been examined quite thoroughly [26-34], this approach has only recently been used to describe the liquid structure of nanofluids, in which the nanoparticle suspensions are viewed as the dispersed phase of a colloidal system. In using this approach, Bastea [35] demonstrated that the thermal conductivity of the system is affected favorably by increases in the colloid diameter (σ_c/σ = 10, 15) but adversely by increases in colloidal mass (m_c/m = 1,1000). In comparison with the Lennard Jones interatomic potential used in the FCC model, Bastea used an

inverse-12, "soft sphere" to describe the nanoparticle-fluid interactions, which does not adequately describe the complex interactions seen in experimental results.

In this report, we review a simple approximation of the interaction potential to describe Hamaker theory for a sphere of arbitrary size suspended in a fluid. We use this model to calculate thermal conductivity values of fluids with nanoparticle suspensions of increasing size according to methodologies similar to earlier works. The validity of using an FCC model to describe nanoparticle suspensions in molecular dynamics simulations is presented alongside an analysis of the modes of energy transfer using this colloid model. These results are, to the best of our knowledge, the first study of the thermal conductivity of nanofluids as a colloidal system using a colloid-specific interaction model.

2. Model

In the colloid model, the nanoparticle is described as a solid hard sphere that has a diameter larger than the fluid particles. The nanoparticle/fluid interactions are governed by a variation of the Gay-Berne potential for two colloidal particles by letting one of the particle sizes go to zero [36] and is of the form

$$U(r) = \frac{2a^3\sigma^3 A_{cs}}{9\left(a^2 - r^2\right)^3}\left[1 - \frac{\left(5a^6 + 45a^4r^2 + 63a^2r^4 + 15r^6\right)\sigma^6}{15(a-r)^6(a+r)^6}\right] \quad (1)$$

where σ is the size of the Lennard Jones solvent particle, a is the radius of the colloid particle, and A_{cs} is the Hamaker constant for interactions between the colloid and liquid. The Hamaker constant value A_{cs} is given by $A_{cs} = 4\pi^2\varepsilon(\rho\sigma^3)^2$. The parameters used in equation 1 are listed in Table 1.

Appendix B (Continued)

3. Simulation details

The LAMMPS molecular dynamics software package was used to perform the simulations and analysis [37]. The initial positions of the fluid atoms were arranged in a regular fcc lattice structure and the volume fraction of the platinum suspensions in the xenon fluid (0%, 0.1%, 0.2%, 0.3%, 0.4%, 0.5%, 0.6%, 0.7%, 0.8%) was determined according to the methodology outlined by Eapen [11]. Each volume fraction simulation was performed eight times in the NVT ensemble over 300000 timesteps where the timestep used in each simulation was 4 fs. The heat current autocorrelation function used to determine the thermal conductivity was also calculated during each simulation and averaged over 500 sets. The temperature of the system was set at 200 K.

4. Results and discussion

4.1 Model comparison

A comparison between the Lennard Jones and the colloidal potential can be seen in figure 1. In the colloid model only the interaction between the nanoparticle and the fluid contributes to the calculation of thermal transport properties, unlike the Lennard Jones potential where the interaction energies of the constituent atoms of the nanoparticles are also included. With this colloid model, the larger nanoparticle size investigated (0.7 nm – green line) had more than 1.5 times the interaction energy within its interfacial region that for smaller diameter (0.4 nm – blue line) and for the Lennard Jones interactions (red dashed line). With these larger interaction energies specifically defining nanoparticle-fluid interactions, a clearer definition of the significance of the potential and collision components of the heat current autocorrelation function and their impact on the overall thermal conductivity enhancement is obtained.

4.2 Thermal conductivity calculations

A graphical comparison of the thermal conductivity calculations obtained from both the FCC and colloid models is shown in figure 2. As can clearly be seen, for larger concentrations of platinum nanoparticles formed by carving out atoms from an FCC lattice in the fluid, the interaction energies of the constituent atoms in the nanoparticles dominate thermal conductivity calculated values. Similar results were obtained from Teng *et al*. This highlights the fact that for only small nanoparticles of approximately 0.4 nm in diameter can properly be modelled using this technique, which was what was done by Eapen, *et al*.

However, the use of the colloid model allowed for larger nanoparticles to be simulated to approach a more realistic d_{np}/d_f ratio seen in experimental results. In part b of figure 2, the thermal conductivity values for larger concentrations of nanoparticles more closely translated to realistic values of thermal conductivity enhancements and staying below the maximum theoretical limit to thermal conduction within argon, which is at its solid state. A more significant result obtained from using the colloid model is the definition of mass of the nanoparticle and its contribution to the partial enthalpy term in equation 1. A direct relationship was developed that linked the mass of nanoparticles within the simulation to the increase in partial enthalpy and the overall contribution to the thermal transport due to diffusion. Figure 3 shows the contribution to thermal transport from thermal diffusion played a more significant role to thermal transport as the concentration increased.

4. Conclusions

The thermal conductivity calculations of nanofluids using a colloidal model in molecular dynamics simulations clarified some issues that arose when large nanoparticles represented by a FCC lattice were used. The colloidal model removed the calculations of interaction energies

between the constituent atoms in the nanoparticle from the calculated thermal conductivity values, leaving behind solely interactions of the nanoparticle and the fluid. With this model, a more refined description of the mechanisms of thermal transport can be obtained.

Acknowledgements

The authors would like to acknowledge the use of the services provided by Research Computing, University of South Florida, and the Florida Georgia LSAMP Bridge to the Doctorate program for their support of this research.

References

[1] H. Chen, et al., *Predicting thermal conductivity of liquid suspensions of nanoparticles (nanofluids) based on rheology*, in *Particuology*, 2009, pp. 151-157.
[2] L. Chen, and H. Xie, *Silicon oil based multiwalled carbon nanotubes nanofluid with optimized thermal conductivity enhancement*, in *Colloids and Surfaces A: Physicochemical and Engineering Aspects*, 2009, pp. 136-140.
[3] H.E. Patel, et al., *An experimental investigation into the thermal conductivity enhancement in oxide and metallic nanofluids*, in *Journal of Nanoparticle Research*, 2009, pp. 1015-1031.
[4] D. Singh, et al., *An investigation of silicon carbide-water nanofluid for heat transfer applications*, in *Journal of Applied Physics*, 2009, pp. 064306.
[5] E.V. Timofeeva, et al., *Particle shape effects on thermophysical properties of alumina nanofluids*, in *Journal of Applied Physics*, 2009, pp. 014304.
[6] A. Turgut, et al., *Thermal Conductivity and Viscosity Measurements of Water-Based TiO2 Nanofluids*, in *International Journal of Thermophysics*, 2009, pp. 1213-1226.
[7] H. Xie, et al., *Thermal performance enhancement in nanofluids containing diamond nanoparticles*, in *Journal of Physics D: Applied Physics*, 2009, pp. 095413.
[8] W. Yu, et al., *Investigation of thermal conductivity and viscosity of ethylene glycol based ZnO nanofluid*, in *Thermochimica Acta*, 2009, pp. 92-96.
[9] X.-Q. Wang, and A.S. Mujumdar, *Heat transfer characteristics of nanofluids: a review*, in *International Journal of Thermal Sciences*, 2007, pp. 1-19.
[10] J. Buongiorno, et al., *A benchmark study on the thermal conductivity of nanofluids*, in *Journal of Applied Physics*, 2009, pp. 094312.
[11] P.D. Shima, et al., *Role of microconvection induced by Brownian motion of nanoparticles in the enhanced thermal conductivity of stable nanofluids*, in *Applied Physics Letters*, 2009, pp. 223101.
[12] J. Eapen, et al., *The Classical Nature of Thermal Conduction in Nanofluids*, in *Journal of Heat Transfer*, 2010, pp. 102402.

Appendix B (Continued)

[13] R. Prasher, et al., *Thermal Conductivity of Nanoscale Colloidal Solutions (Nanofluids)*, in *Physical Review Letters*, 2005.

[14] R. Prasher, et al., *Brownian-Motion-Based Convective-Conductive Model for the Effective Thermal Conductivity of Nanofluids*, in *Journal of Heat Transfer*, 2006, pp. 588.

[15] Q. Xue, *Model for effective thermal conductivity of nanofluids*, in *Physics Letters A*, 2003, pp. 313-317.

[16] L. Xue, *Effect of liquid layering at the liquid?solid interface on thermal transport*, in *International Journal of Heat and Mass Transfer*, 2004, pp. 4277-4284.

[17] Q. Xue, and W.-M. Xu, *A model of thermal conductivity of nanofluids with interfacial shells*, in *Materials Chemistry and Physics*, 2005, pp. 298-301.

[18] R. Prasher, et al., *Effect of aggregation on thermal conduction in colloidal nanofluids*, in *Applied Physics Letters*, 2006, pp. 143119.

[19] J. Philip, et al., *Enhancement of thermal conductivity in magnetite based nanofluid due to chainlike structures*, in *Applied Physics Letters*, 2007, pp. 203108.

[20] J. Eapen, et al., *Beyond the Maxwell limit: Thermal conduction in nanofluids with percolating fluid structures*, in *Physical Review E*, 2007.

[21] J. Philip, et al., *Evidence for enhanced thermal conduction through percolating structures in nanofluids*, in *Nanotechnology*, 2008, pp. 305706.

[22] J. Eapen, et al., *Mechanism of Thermal Transport in Dilute Nanocolloids*, in *Physical Review Letters*, 2007.

[23] R. Vogelsang, et al., *Thermal conductivity of the Lennard-Jones liquid by molecular dynamics calculations*, in *Journal of Chemical Physics*, USA, 1987, pp. 6371-5.

[24] K.-L. Teng, et al., *Enhanced thermal conductivity of nanofluids diagnosis by molecular dynamics simulations*, American Scientific Publishers, 25650 North Lewis Way, Stevenson Ranch, CA 9138-1439, United States, 2008, pp. 3710-3718.

[25] P. Sachdeva, and R. Kumar, *Effect of hydration layer and surface wettability in enhancing thermal conductivity of nanofluids*, in *Applied Physics Letters*, 2009, pp. 223105.

[26] D. MacGowan, and D.J. Evans, *Heat and matter transport in binary liquid mixtures*, in *Physical Review A (General Physics)*, USA, 1986, pp. 2133-42.

[27] D. MacGowan, *Time correlation functions in a binary liquid mixture*, in *Physical Review A (General Physics)*, USA, 1987, pp. 1367-73.

[28] R. Vogelsang, and C. Hoheisel, *Thermal conductivity of a binary-liquid mixture studied by molecular dynamics with use of Lennard-Jones potentials*, in *Physical Review A (General Physics)*, USA, 1987, pp. 3487-91.

[29] R. Vogelsang, et al., *Soret coefficient of isotopic Lennard-Jones mixtures and the Ar-Kr system as determined by equilibrium molecular-dynamics calculations*, in *Physical Review A (General Physics)*, USA, 1987, pp. 3964-74.

[30] G.V. Paolini, and G. Ciccotti, *Cross thermotransport in liquid mixtures by nonequilibrium molecular dynamics*, in *Physical Review A (General Physics)*, USA, 1987, pp. 5156-66.

[31] G. Ciccotti, et al., *Dense-fluid transport coefficients via the constrained-subtraction technique*, in *Physical Review A (General Physics)*, USA, 1987, pp. 3471-3.

[32] J.J. Erpenbeck, *Transport coefficients of hard-sphere mixtures: theory and Monte Carlo molecular-dynamics calculations for an isotopic mixture*, in *Physical Review A (General Physics)*, USA, 1989, pp. 4718-31.

Appendix B (Continued)

[33] J.J. Erpenbeck, *Transport coefficients of hard-sphere mixtures. II. Diameter ratio 0.4 and mass ratio 0.03 at low density*, in *Physical Review A (Statistical Physics, Plasmas, Fluids, and Related Interdisciplinary Topics)*, USA, 1992, pp. 2298-307.

[34] A. Perronace, et al., *Soret coefficient for liquid argon-krypton mixtures via equilibrium and nonequilibrium molecular dynamics: A comparison with experiments*, in *Physical Review E*, 2002.

[35] S. Bastea, *Transport in a highly asymmetric binary fluid mixture*, in *Physical Review E*, 2007.

[36] R. Everaers, and M. Ejtehadi, *Interaction potentials for soft and hard ellipsoids*, in *Physical Review E*, 2003.

[37] S. Plimpton, *Fast parallel algorithms for short-range molecular dynamics*, in *Journal of Computational Physics*, USA, 1995, pp. 1-19.

Appendix B (Continued)

Table 1. Parameters for platinum-xenon nanofluid using colloid model.

n	A_{ArAr}	$A_{n,Ar}$	A_{nn}
Pt	34.2864	18.8626	730.356

Figure 1. Comparison of potentials for the platinum nanoparticle/xenon fluid interactions.

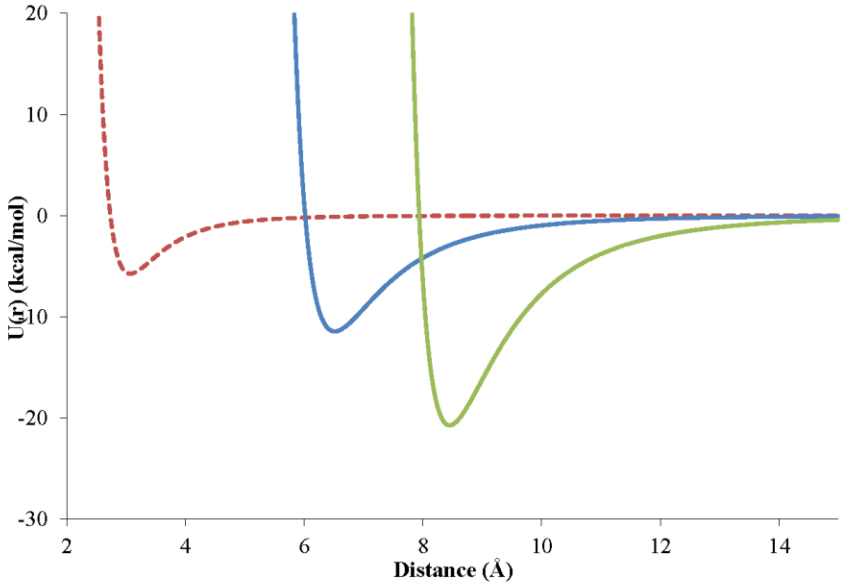

Appendix B (Continued)

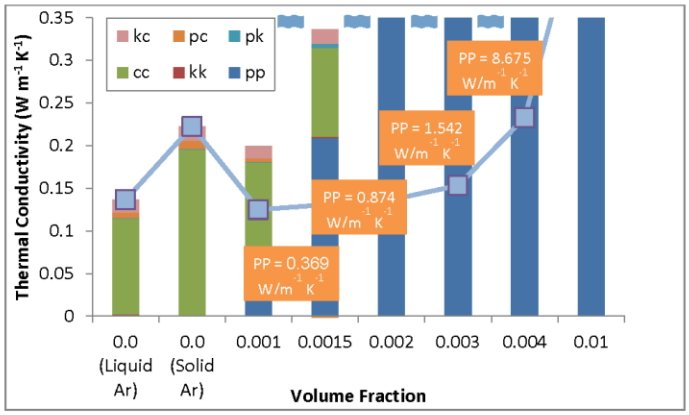

(a)

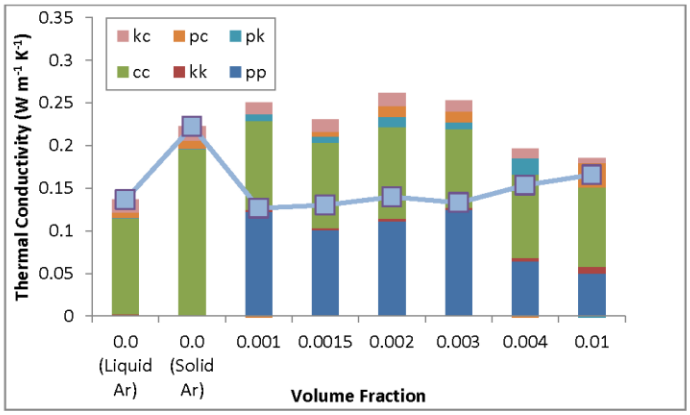

(b)

Figure 2. Contributions of the various components of energy transfer on thermal conductivity calculations in platinum nanoparticle/xenon fluid interactions using a) FCC model and b) colloid model.

Appendix B (Continued)

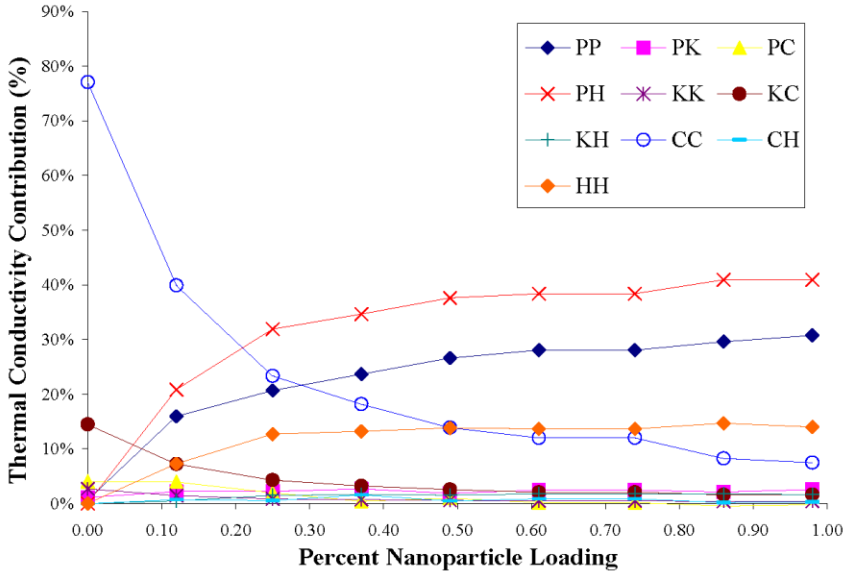

Figure 3. Contributions of the various components of energy transfer on thermal conductivity calculations in platinum nanoparticle/xenon fluid interactions at different concentrations using the colloid model.

Appendix C: Supplemental Data

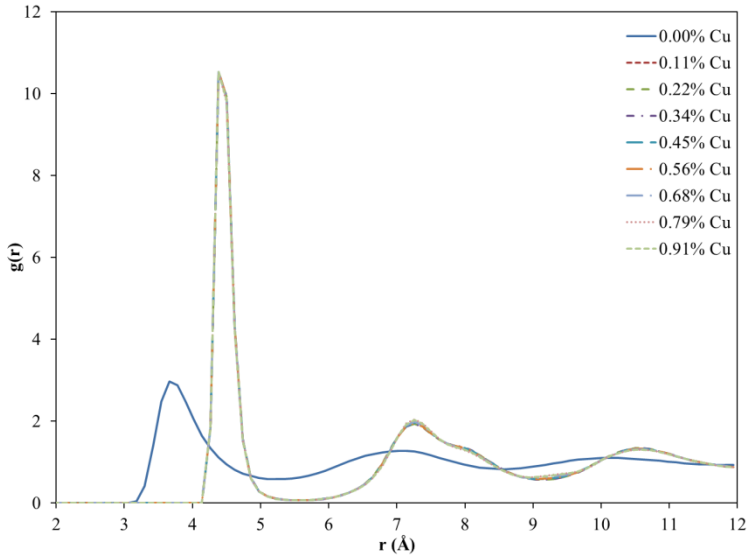

Figure C.1 Radial distribution function for argon with copper nanoparticle suspensions with a diameter of 0.5 nm.

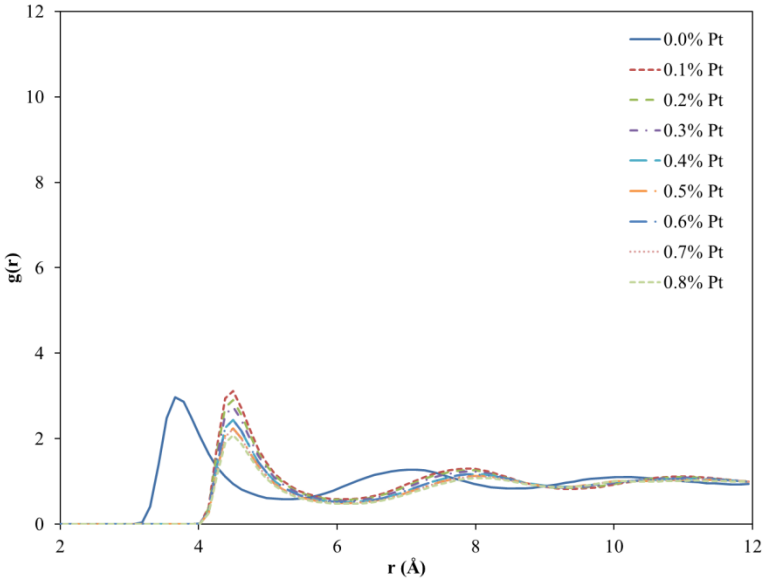

Figure C.2 Radial distribution function for argon with platinum nanoparticle suspensions with a diameter of 0.5 nm.

Appendix C (Continued)

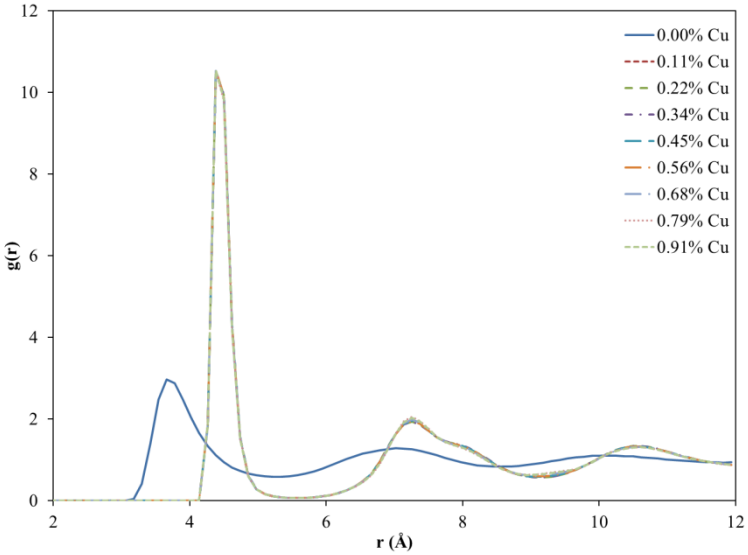

Figure C.3 Radial distribution function for argon with copper nanoparticle suspensions with a diameter of 0.6 nm.

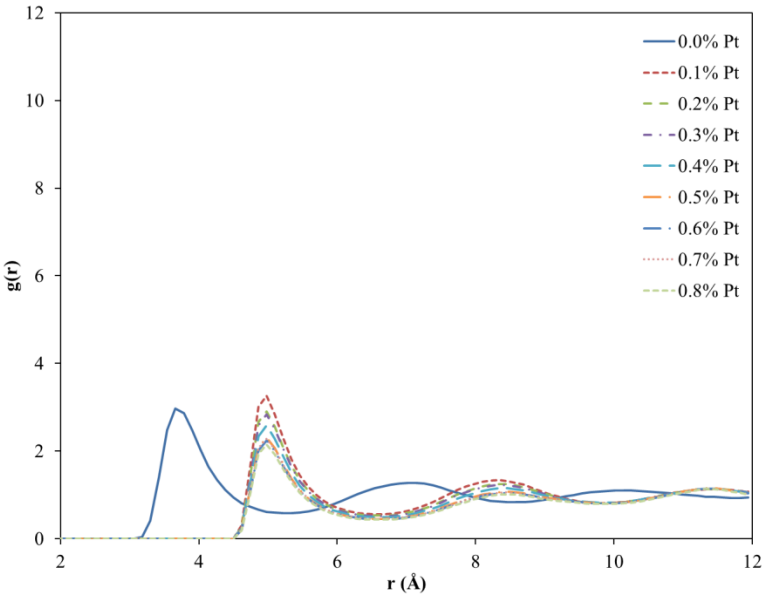

Figure C.4 Radial distribution function for argon with platinum nanoparticle suspensions with a diameter of 0.6 nm.

Appendix C (Continued)

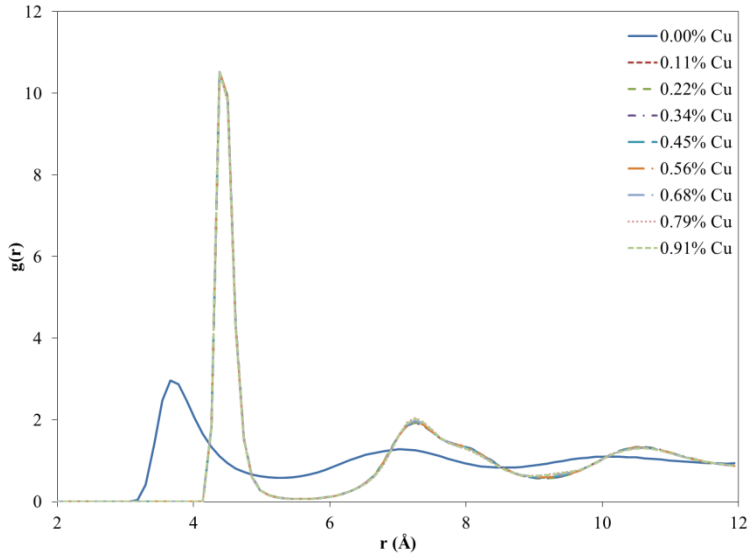

Figure C.5 Radial distribution function for argon with copper nanoparticle suspensions with a diameter of 0.7 nm.

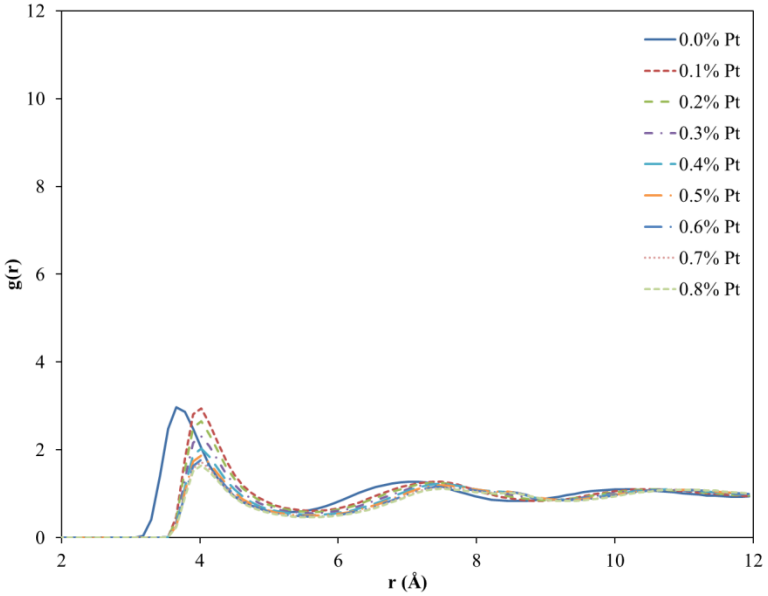

Figure C.6 Radial distribution function for argon with platinum nanoparticle suspensions with a diameter of 0.7 nm.

About the Author

John Shelton received his Bachelor's and Master's degree in Mechanical Engineering from North Carolina A&T State University in 2000 and 2005, respectively. In between degree programs, he went on to work as a Design Engineer at Ford Motor Company. He returned to school to study in the PhD program in the Mechanical Engineering at the University of South Florida in 2006.